The fabrication of chevrel phase superconductors and the origin of the irreversibility field

Ian James Daniel

Daniel, Ian James (1999) The fabrication of chevrel phase superconductors and the origin of the irreversibility field. Doctoral thesis, Durham University.

The Fabrication of Chevrel Phase Superconductors and the Origin of the Irreversibility Field

Ian James DANIEL

A thesis submitted in partial fulfilment of the requirements of the degree of
Doctor of Philosophy

Department of Physics
University of Durham
1999

The Fabrication of Chevrel Phase Superconductors and the Origin of the Irreversibility Field

Ian James DANIEL

Ph.D - 1999

Abstract

This thesis describes the fabrication and characterisation of high quality Chevrel phase superconductors and investigates the origin of the irreversibility field when measuring the magnetic moment of a superconductor using a Vibrating Sample Magnetometer.

A stoichiometry investigation into hot isostatically pressed (HIP'ed) lead molybdenum sulphide (PMS) across the compositional range $Pb_{1+y}Mo_6S_{8+x}$ where x=-0.5, 0, 0.5 and 1.0 and y=0.0 and 0.1 was completed. T_C, J_C, B_{IRR} and B_{C2} were measured for each sample and were similar to those reported for high quality bulk HIP'ed PMS.

A sample of tin molybdenum sulphide (SMS) was fabricated and the critical current density determined from dc magnetisation measurements. The reduced pinning force exhibited the Peak Effect and could be scaled in both the high and low field regimes using a Kramer dependence.

Three europium doped SMS samples of compositions $Eu_xSn_{1-x}Mo_6S_8$ with x = 0, 0.35 and 0.5 were characterised. The x = 0.35 sample exhibited the highest dB_{C2}/dT and $B_{C2}(0)$ of any tin based Chevrel phase material reported. The europium doped samples simultaneously exhibited paramagnetism and superconductivity.

The effect of the field inhomogeneity of the magnet used in a VSM system on the measurement of the magnetic moment of a superconductor was calculated. It was found that when the effective ac field caused by the movement of the sample is comparable to the self field of the sample, the voltage measured at the driver frequency does not represent the magnetic moment or the critical current density of the sample. The calculations show that the irreversibility field (B_{IRR}) occurs when the effective ac field penetrates the entire volume of the sample and *is not* when the critical current density falls to zero. Harmonics of the driver frequency were also calculated and it was shown that measurement of these harmonics allow the determination of the field at which the critical current density is zero. Harmonic measurements were performed and showed excellent agreement with the calculations.

Declaration and Copyright

I hereby declare that the work contained within this thesis is my own original work and nothing that is the result of collaboration unless otherwise stated. No part of this thesis has been submitted for a degree or other qualification at this or any other university.

Acknowledgements

Throughout the course of this study many people have provided invaluable assistance and I would like to take this opportunity to express my gratitude.

Firstly the Engineering and Physical Sciences Research Council and Oxford Instruments Plc. for providing financial support through the CASE award scheme and Prof. B. K. Tanner for allowing me the use of the Department of Physics facilities. My academic supervisor Dr. Damian Hampshire has provided an excellent working environment and the inspiration and motivation that has allowed me to perform the work contained in this thesis. I would like to thank him for making this Ph.D both challenging and enjoyable and I would like to thank his family for loaning him to me for the duration of this study. I would also like to thank my industrial supervisor Dr. Nick Kerley for his interest in this research.

I also wish to thank Dr. Christian Lehmann and Dr. Andreas Goeta from Durham University Chemistry Department for their help with the x-ray diffraction measurements, all the staff at Oxford Instruments Measurement Systems Group who looked after me on my placement there, Dr. C Dewhirst of the I.R.C. in Cambridge and Dr. G Yang and Prof. C Gough at Birmingham University for the use of their VSM systems.

This Ph.D would not have been possible without the assistance of the non-academic staff at the Department of Physics who were always willing to help when I asked the impossible. The staff of the mechanical workshop; Phil Armstrong, Michael Greener, Bill Hogg, Steve Lishman, Peter Luke, Ian Milne, Paul Moorhead, Kevin McGee, Ken Parkin, Malcom Robertshaw, Phil Robson and George Teasdale for turning my scribbled drawings into useful apparatus. The electronics workshop; Andrew Hunter, Tom Jackson, Chris Moore and Chris Mullaney for fixing the things I broke. The reprographics staff; Vicki Greener, Mike Lee, and Pauline Russell for always smiling when I asked for things doing by yesterday. The secretarial staff; Julie Bell, Nikki Bingham, Penny Carse, Claire Davies, Angela Healer, Joanne Pallister, Rebbeca Siddle and Linda Wilkinson for keeping me informed of who is who and what is what. Thanks also go to Norman Thompson and Davey Pattison for technical support around the lab, John Dobson for his advice, encouragement and for having enough fingers in enough pies to solve almost anything, Dave Stockdale for answering many ridiculous IT questions, the teaching lab staff for lending me things and Pat Monkhouse for keeping me fed and watered throughout my studies.

A special thanks must go to Karen Brazier from the University ITS who could not have been more helpful in explaining the workings of Maple and saving countless hours of exasperation.

I have had the pleasure of working with many others within the department including Dr. Salamat Ali, Gwyn Ashcroft, Dr. Najib Cheggour, John Clarke who quite literally took his life in his hands teaching me to rock climb, Stuart Dailey, Dr. James Egglestone, Brian Fulthorpe, Tom Hase, Dr. Hamidi Hamid, Dr. Peter Hatton, Dr. Alton Horsfall, Simon Keys, Nigel Leigh, Dr. Chris Leighton who knows all the answers, Andrea Li-Bassi, Dr. Jon Makar, Dr. Caroline Moore who added the female touch to the office, Dr. Ian Pape, Dr. Harry Ramsbottom who started me off on the Ph.D road, Dan Read who improved my musical taste no end, Dr. Toni Rogers, Dr. Dirk Rose, Adrian Sneary, Dr. Ian Terry, and Dr. Dong Ning Zheng. I wish to thank all of them for their contribution to my enjoyment of my time in Durham.

Outside the department I have been fortunate enough to have many good friends to maintain my sanity and to try and prevent me working too hard. Thanks go to Helen Bell, Jeremy Bull, Becky Bynon, Elena Donadio, Adele Duperuzel, Nancy Ann Hackman, Roy Jacques, Isobel Johnson, Anne Ketelaar, Helen Lofthouse, Alan Poulter, Michael and Rachel Swinhoe, Anna Tarrant and Colin Weir.

Finally I would like to thank my family who have always given their support and encouragement through out all of my studies. Without them, none of this would have been possible.

Contents

Appendix 1

Appendix 2

Chapter 1
Introduction

1.1 Motivation for Research

Superconductivity is a fascinating field of study, with materials exhibiting many amazing properties such as zero electrical resistance and the complete exclusion of magnetic field. They also have many commercial applications including the generation of magnetic fields, the construction of sensitive voltage detectors and the fabrication of resonance cavities for microwave transmitters[**1**].

This thesis is primarily concerned with the high field magnetic properties of superconductors, in particular, the fabrication of materials with potential for high field applications and the origin of the irreversibility field found in many superconducting materials.

The class of materials investigated are the Chevrel phase materials which are ceramic low temperature superconductors with upper critical fields of over 50T[**2**]. This makes them a suitable class of materials for the generation of static high magnetic fields markedly in excess of 20T[**3**], which is almost impossible with the current commercial materials.

One of the common measurement techniques used to determine the high field magnetic properties of superconductors is the vibrating sample magnetometer. This involves measuring the magnetic moment of the sample by moving it in a dc magnetic field. Before this work, the effect of the homogeneity of the magnetic field in which the sample moves on the measurement of the magnetic moment has not been considered. In this work it will be shown that the field homogeneity has a significant effect on the measurement of the irreversibility field and critical current density using a vibrating sample magnetometer unless care is taken with the experimental arrangement.

1.2 Thesis Structure

Chapter 2 will give a basic introduction to some of the fundamentals of superconductivity, including the important parameters used to characterise a superconducting material. A brief summary of the important theories used to describe the superconducting state will also be presented, and the applications of superconductivity discussed. Chapter 3 will review the literature relevant to the two main themes of this thesis. Firstly the fabrication of Chevrel phase superconductors will be considered, concentrating on lead molybdenum sulphide (PMS) and tin molybdenum sulphide (SMS), as these have the best high field properties. Following this the phenomenon of the irreversibility field will be introduced and a summary of the current understanding and interpretation of it presented.

The properties of lead molybdenum sulphide have been intensively studied since the discovery of its high upper critical field, of over 50T**[2]**. In chapter 4 an investigation into the effect of stoichiometry on the properties of PMS fabricated using a hot isostatic press will be presented, for a series of eight samples. The trends found within the series will be outlined and the implications discussed.

Chapter 5 concentrates on tin molybdenum sulphide, and in particular on the behaviour of the critical current density, which is known to exhibit the Peak Effect at fields close to the upper critical field**[4]**. The Peak Effect is an increase in critical current density, and hence pinning force, with increasing applied magnetic field. The scaling of the pinning force with field and temperature will be analysed and a functional form proposed, following that proposed by Kramer**[5]**. The doping of SMS with the rare earth metal europium is the subject of chapter 6. A series of three samples has been fabricated by Dr D N Zheng at a temperature of 1500°C. The series is characterised in this chapter where the doped system allows the investigation of the coexistence of magnetism and superconductivity.

The next three chapters are concerned with the measurement of the magnetic moment of a superconductor using a vibrating sample magnetometer. Chapter 7 details the design modifications made to the in-house system in Durham which have produced improvements in both sensitivity and noise level. In chapter 8 the measurement of the magnetic moment using a vibrating sample magnetometer is modelled with particular care being taken to include the effect of moving the sample in a inhomogeneous magnetic field. It is found that the measured critical current density and irreversibility field are incorrect if the sample self field is comparable to the effective ac field caused by the sample moving in an inhomogeneous magnetic field. Chapter 9 goes on to show experimental measurements performed on the VSM system described in chapter 7 which support the predictions of the calculations presented in chapter 8. Measurements were performed on the high field superconductors PMS and SMS, along with commercial NbTi multifilamentary wire, for various field inhomogeneities and temperatures. Chapter 10 then provides a summary of the work presented in this thesis and some ideas for future work..

Included in the appendices is a list of courses and conferences attended, a list of computer programs written throughout the course of study and a report on the development of an ac calorimeter from a commercial relaxation calorimetry system. This project was part of a three month industrial placement with Oxford Instruments Plc as part of the E.P.S.R.C. CASE award scheme.

1.3 References

[1] Buckel W *Superconductivity* V.C.H. 223 (1991)

[2] Foner S, McNiff Jr. E J and Alexander E J *Physics Letters* **49A** 269 (1974)

[3] Flukiger R and Seeber B *Europhysics News* **22** 2 (1991)

[4] Karasik V R, Karyaev E V, Zakosarenko V M, Rikel M O and Tsebro V I *Sov. Phys. JETP* **60** 1221 (1984)

[5] Kramer E J *J. Appl. Phys.* **44** 1360 (1973)

Chapter 2
Introduction to Superconductivity

2.1 Introduction to Chapter 2

In this chapter, the fundamental principles behind superconductivity are introduced and discussed. Firstly a brief chronology of the field of superconductivity is given and the definition of superconductivity presented. Critical parameters for superconductors are defined, explained and some of the fundamental measurements are discussed. The three main theories of superconductivity are presented next and their relative merits and predictions discussed. Finally superconductors are considered in the context of present and potential applications.

2.2 A Brief History of Superconductivity

At the beginning of this century H. Kamerlingh Onnes succeeded in liquifying Helium, giving access to a whole new range of physics, only observable at low temperatures. At the time, one of the most debated questions was what happens to the resistivity of metals at absolute zero? In order to seek an answer to this question, the resistivity of mercury was measured as a function of temperature. Mercury was chosen as it was readily available in a very pure state. This experiment led to the first observation of superconductivity in 1911 by Onnes when at about 4 Kelvin the resistivity of the mercury sharply dropped to zero[1].

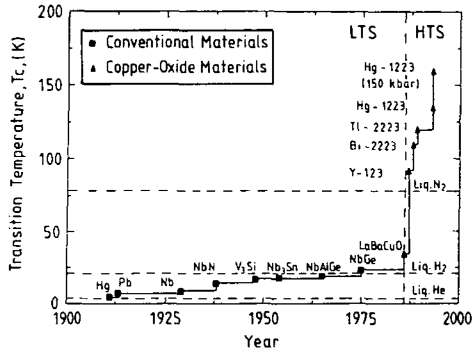

Figure 2.1 Chronological development of superconducting materials.

Since this initial discovery many other elements and compounds have been found to be superconductors at low temperatures, figure 2.1. The temperature at which these materials start to superconduct varies from a few millikelvin for Tungsten[2] to approximately 20 K for Nb_3Ge [3] which has the highest critical temperature for so called conventional superconductors. In 1986 a completely new class of superconductors was found[4], which contain layers of copper oxide within more complicated crystal structures. The race was then on to see who could raise the superconducting temperature the highest. An important goal was to obtain superconductivity above the boiling point of liquid nitrogen and hence open up the possibility of many applications. This happened in 1987 with the discovery of $YBa_2Cu_3O_{7-\delta}$ (YBCO) which became superconducting at around 95 Kelvin[5], rapidly surpassed in 1988 by $Bi_2Sr_2Ca_2Cu_3O_{10}$ (BISCCO 2223) at 110 Kelvin[6]. The present record for superconductivity at atmospheric pressure is held by $Hg_{0.8}Pb_{0.2}Ba_2Ca_2Cu_3O_{8+\delta}$ with a critical temperature of 133K.

2.3 What is a Superconductor?

An ideal superconductor is a material that, when cooled below a critical temperature (T_C), has zero electrical resistance and is a perfect diamagnet. It is possible for extrinsic factors such as microstructure and chemical stoichiometry to give non-ideal behaviour however ideal properties are found in most superconducting materials.

2.3.1 Zero Resistance

As discussed in section 2.2, when a superconductor is cooled below its critical temperature, its electrical resistance drops to zero, i.e. a current can flow and generate no voltage and hence flow indefinitely. Experiments have been performed to place an upper bound on the resistance of the superconducting state by setting up a current in a superconducting ring and measuring its decay over a period of years. This gave an upper bound for the resistivity of the superconducting state to be approximately $10^{-23}\,\Omega$cm, at least 11 orders of magnitude lower than that of copper[7].

2.3.2 Meissner Effect

This is the second property of superconductors and distinguishes superconductors from perfect conductors. The Meissner effect is the total exclusion of magnetic field from the bulk of the material, when cooled below the critical temperature, i.e. superconductors are perfect diamagnets.

2.3.3 Critical Parameters of Superconductors

There are three main external parameters that can determine whether a superconductor is in the superconducting state or the normal state. The first which we have already seen is temperature, with the critical parameter called the critical temperature (T_C), below which a material will superconduct. The next is the magnetic field applied to the material which must be below a value called the critical field for the material to superconduct. The final parameter is the amount of current flowing through the superconductor which again must be smaller than a critical value called the critical current density(J_C).

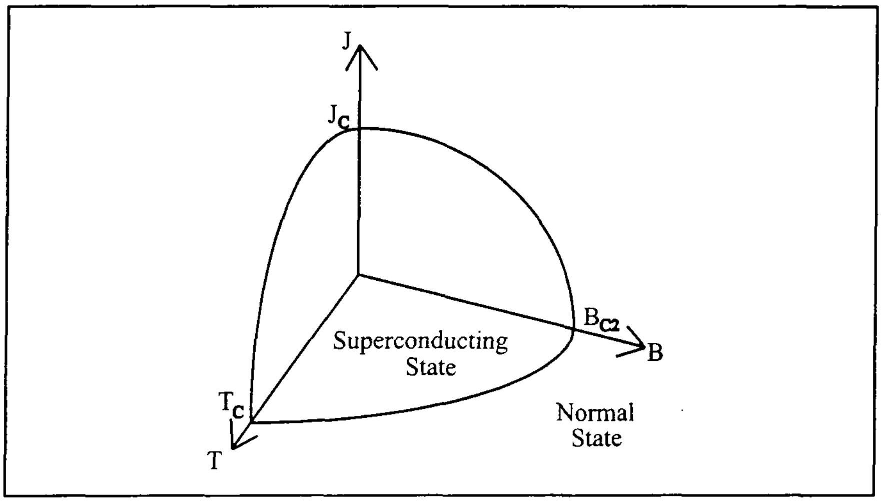

Figure 2.2 Superconducting state limited by critical field, critical current and critical temperature.

These three parameters are all interdependent and lead to a critical surface for superconductors, within which the material superconducts and outside which it is in the normal state. This is represented schematically in figure 2.2.

2.4 Magnetisation Curves For Superconductors

Superconductors can be divided into two classes by examining their behaviour in a magnetic field. These two classes, known as Type I and Type II superconductors, have quite different properties and will each be examined in turn in this section. The magnetisation curve shows how the magnetic moment of the sample changes with applied field.

2.4.1 Type I Superconductors

A Type I superconductor is a material that exhibits perfect diamagnetism up to a critical field (B_C), above which it stops superconducting and returns to the normal state. A magnetisation graph for a Type I superconductor is shown in figure 2.3. Most superconducting elements with the notable exception of niobium, vanadium and molybdenum are Type I superconductors.

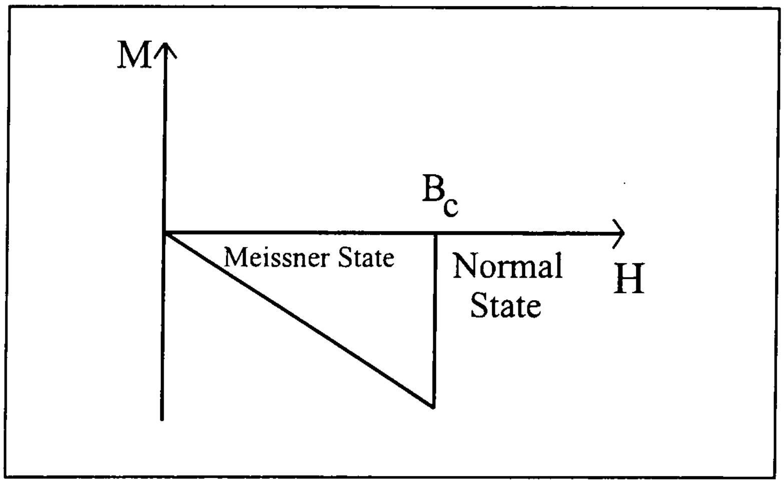

Figure 2.3 Magnetisation curve for a Type I superconductor

2.4.2 Type II Superconductors

These materials have a more complicated magnetic phase diagram as shown in figure 2.4. As the applied field is increased, the material remains in the Meissner state until the lower critical field (B_{C1}). At this point magnetic field penetrates into the bulk of the material in the form of quantised units called fluxons (see section 2.4.3).

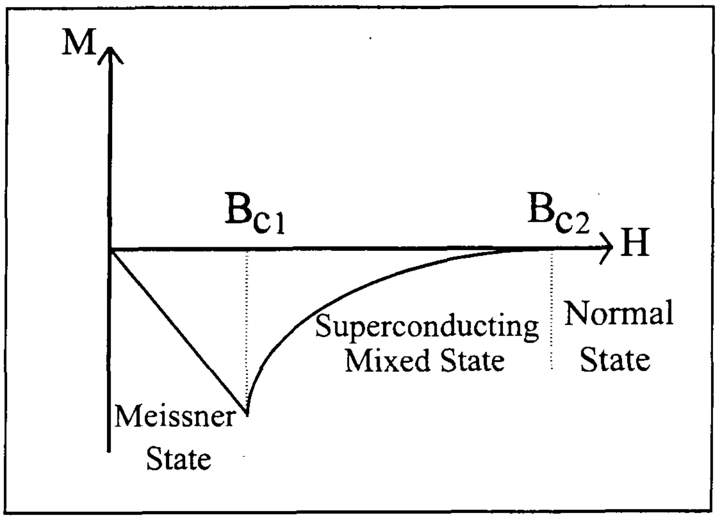

Figure 2.4 Magnetisation curve for a Type II superconductor.

This mixed state as it is called, is a lower energy state for the material and has a mixture of superconducting and normal material. As the fluxons enter the sample each one has its own screening current. The fluxon screening currents and the surface currents give the magnetic moment of the sample which can give useful information about the material. The mixed state exists until some upper critical field (B_{C2}) at which field the entire material becomes normal. Most commercially useful materials are Type II superconductors, as are the materials in this thesis.

2.4.3 Fluxons and the Flux Line Lattice

When magnetic field enters into the bulk of a superconductor it does so in the form of flux tubes called fluxons.

$$\Phi_0 = \frac{h}{2e} \qquad (1)$$

These are a normal region of material containing an integer multiple of field quanta given by equation 2.1 in which h is Planck's constant and e is the charge on an electron. It was predicted by Abrikosov [8] that when fluxons entered into a superconductor they would repel each other.

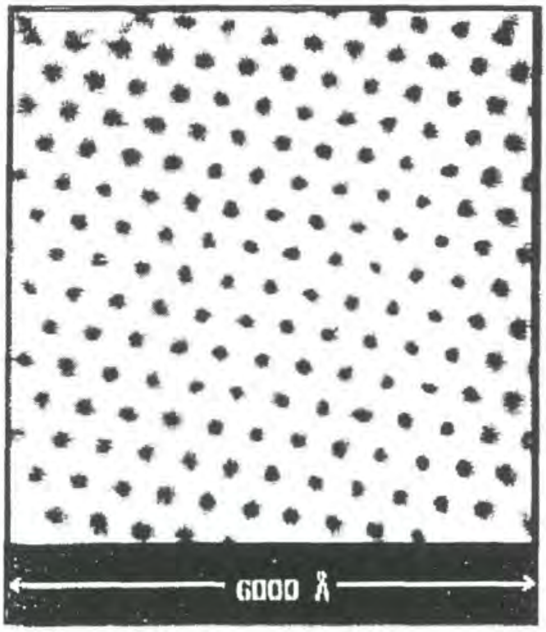

Figure 2.5 **S.E.M. picture of the flux line lattice in a superconductor.**

Abrikosov predicted these fluxons would form a square lattice arrangement however it was found by Kleiner et al**[9]** that a triangular arrangement was in fact a lower energy configuration. This has been confirmed experimentally and can clearly be seen in figure 2.5. The behaviour of fluxons within a superconducting material and in particular the form of the flux line lattice has been extensively investigated and will be discussed further in Chapter 3.

2.5 Pinning in Type II superconductors

Imagine a superconductor in the mixed state and therefore having fluxons running through it. If we now attempt to pass a current through the superconductor, these fluxons will feel a Lorentz force and move. The movement of flux lines causes dissipation and hence the current will not be a supercurrent. How is it possible for a superconductor in the mixed state to carry a lossless current? This is possible due to pinning of the fluxons within the superconductor, preventing them from moving under the Lorentz force.

2.5.1 Introduction to Pinning and Pinning Wells

As explained in section 2.4.3, fluxons enter the body of a Type II superconductor above B_{C1}, and are normal regions of material containing magnetic flux.

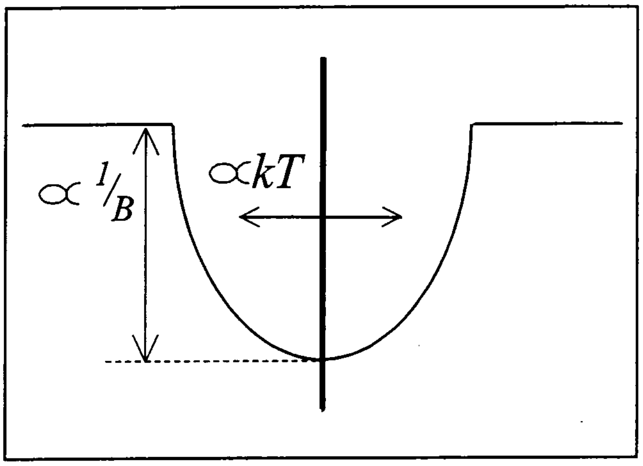

Figure 2.6 Representation of a pinned fluxon.

A pinning site is the name given to any point in the material to which the fluxon feels an attractive force. These are usually regions of weak superconductivity that can be driven normal using less energy than the bulk of the material and hence this site is energetically favoured by the fluxon.

The pinning of fluxons is crucial for achieving high critical current densities as will be shown in section 2.5.2. A representation of a pinned fluxon is given in figure 2.6. It can be seen that an increase in either applied field or in temperature can cause the fluxon to escape the pinning site and hence become unpinned.

2.5.2 The Bean Model

This model, **[10]**, describes how, for a material with random pinning, the fluxons distribute within the sample. It assumes that the current density at any point in the sample is the critical current density or zero. This implies that the field gradient within the sample can be described by equation 2.2.

$$\nabla\times\boldsymbol{B} = \pm\ \mu_0 J_c\ ,\ 0 \qquad (2)$$

This leads to the construction of Bean Profiles which show the distribution of magnetic field within a superconductor. As the applied field increases above B_{C1} the fluxons penetrate the body of the superconductor but are pinned as they enter. They are pinned in such a way as to produce a field gradient that causes a current to flow that is ± J_C or zero.

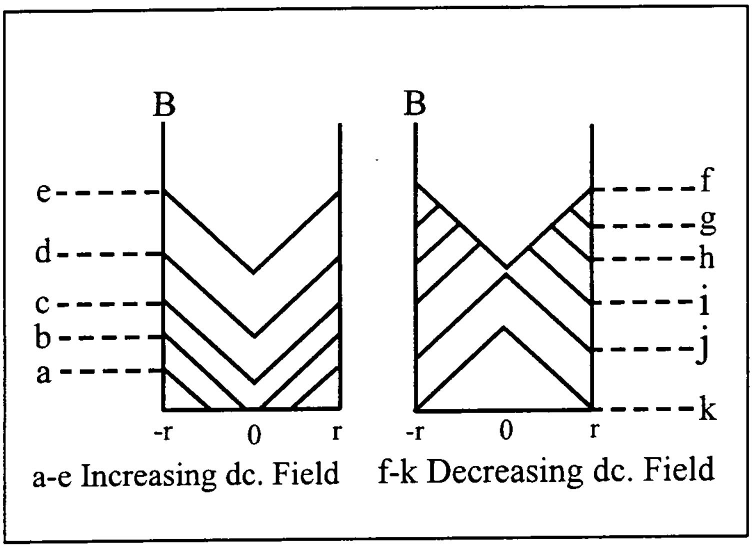

Figure 2.7 **Bean profile within a superconductor.**

This is shown in figure 2.7, lines a to e for an increasing applied field. As the field is decreased the same conditions on the field gradient within the sample still hold, as does the condition on the current density, shown in figure 2.7 lines f to k. Note that when the applied field is zero there is still field within the superconductor. This field is known as remnant field. The size of the currents flowing when the fluxons are pinned is always the critical current density and this in most cases is considerably larger than the screening currents flowing around the outside of the sample. This means that the magnetisation curves for a Type II superconductor with pinning are very different from those without pinning.

2.5.3 Irreversibility Fields

The magnetisation curve of a superconductor which has some pinning will be quite different to one without. The size of the hysteresis is related to the critical current density of the sample by a geometrical factor and hence when the critical current density is zero the magnetisation curve becomes reversible. This point on an hysteresis curve is known as the Irreversibility Field (B_{IRR}). The measurement and interpretation of magnetisation curves will form a large part of this thesis and will be discussed in more detail in chapters 3 and 8.

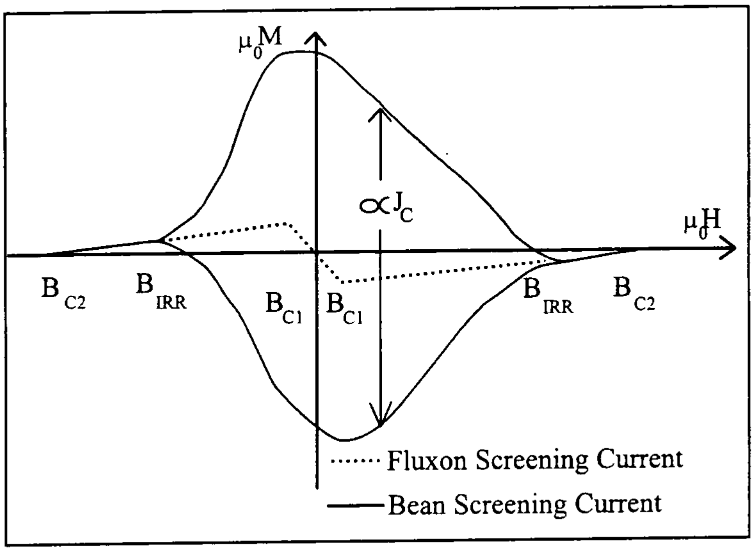

Figure 2.8 Magnetisation curve for a Type II superconductor with pinning.

A magnetisation curve for a superconductor with pinning, is shown in figure 2.8

2.6 Thermodynamics of Superconducting State

In this section the thermodynamics of the superconducting state will briefly be reviewed, giving some justification as to why materials become superconducting.

2.6.1 Free Energy Considerations

The Gibbs free energy in a fixed magnetic field is given by:

$$G = U - T\Sigma - H.M \tag{3}$$

where U is the internal energy, T is the temperature, Σ is the entropy, H is the applied field and M is the magnetisation. For a process at a fixed temperature we therefore have:

$$G(H) = G(0) - \int_0^H M.dH$$

At a superconducting to normal state transition the Gibbs free energy must be the same in both states.

Now using the fact that in the superconducting state M = 0, and in the normal state M=-μ_0H, hence:

$$G_n(0) - G_s(0) = \frac{\mu_0 H_c^2}{2} \tag{5}$$

As this difference is always positive, then superconductivity is the lowest energy state. The entropy difference is then given by:

$$s_n - s_s = \mu_0 H_c \frac{dH_C}{dT} \tag{6}$$

and the specific heat difference is given by:

$$c_n - c_S = -\mu_o T\left(H_c \frac{d^2 H_c}{dT^2} + \left(\frac{dH_c}{dT} \right)^2 \right) \tag{7}$$

Measurement of specific heat jumps at the superconducting normal state transition can be made and agree well with theoretical predictions.

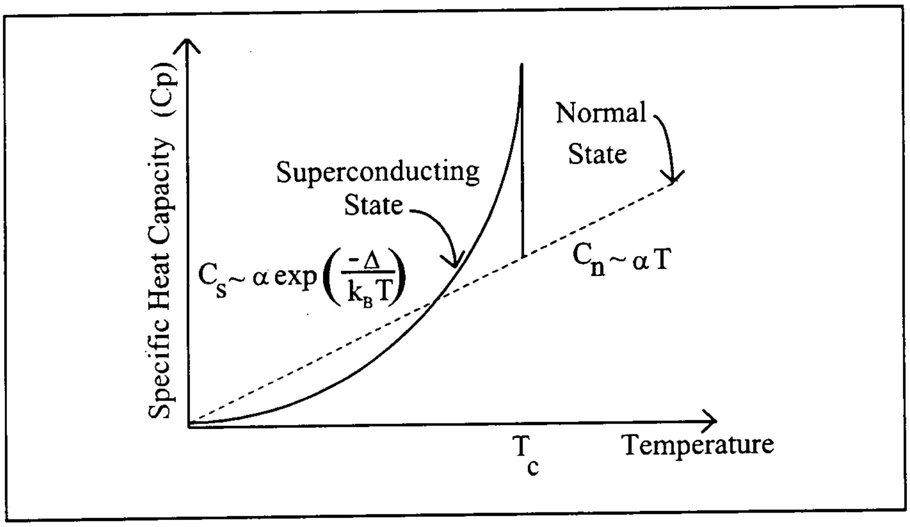

Figure 2.9 **Representation of the electronic contribution to the specific heat jump at a superconducting - normal state phase transition.**

Figure 2.9 shows an idealised transition, with the associated jump in specific heat capacity.

2.7 Theories of Superconductivity

Since the discovery of superconductors, many people have tried to produce a theoretical explanation of their properties. In this section three of the more successful will be presented and their predictions and limitations discussed.

2.7.1 London Equations

Postulated by the London brothers in 1935**[11]**, their equations describe the electromagnetic properties of the superconducting state. These are phenomenological equations, produced as they correctly give the already measured results.

The first equation describes the zero resistance aspect of superconductivity as:

$$\boldsymbol{E} = \mu_0 \lambda_L^2 \frac{\delta \boldsymbol{J}}{\delta t} \qquad \textbf{(8)}$$

where:

$$\lambda_L^2 = \frac{m^*}{\mu_0 n_{se}^* e^*} \qquad \textbf{(9)}$$

with m^*, n^*_{se}, e^* being the mass, number per unit volume and charge of the charge carrier. The second equation describes the Meissner effect as:

$$\boldsymbol{B} = -\mu_0 \lambda_L^2 \ \nabla \times \boldsymbol{J} \qquad \textbf{(10)}$$

where λ_L is as defined in equation 2.9 and J is the screening current flowing. To produce the Meissner Effect from equation 2.10, a substitution into Maxwell's equation:

$$\nabla \times \boldsymbol{B} = \mu_0 \boldsymbol{J} \qquad \textbf{(11)}$$

leads to the result:

$$\nabla^2 \boldsymbol{B} = \frac{1}{\lambda_L^2} \boldsymbol{B} \qquad \textbf{(12)}$$

where λ_L is called the London Penetration Depth and is as defined in equation 2.9.

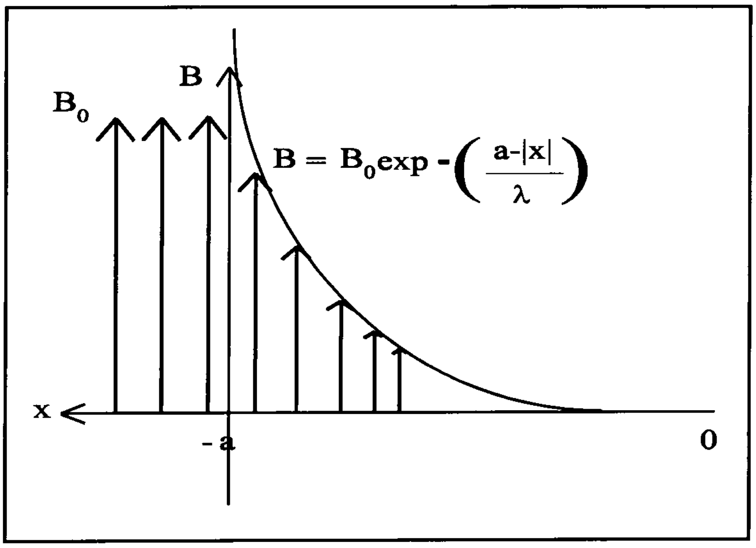

Figure 2.10 Decay of the field inside a superconductor.

This has the solution of an exponential decay in field over a distance λ_L from the edge of the material as is shown in figure 2.10. The London Equations do not attempt to explain any of the mechanisms causing these effects but succeed rather well in modelling the electromagnetic behaviour of superconducting materials.

2.7.2 Ginzburg Landau Theory

This is another phenomenological theory and was produced in 1950 by Ginzburg and Landau**[12]**. It describes the superconducting state using a complex order parameter ψ which is defined such that $|\psi|^2$ is equal to the superconducting electron density. This theory works incredibly well considering the simplicity of its assumptions and predicts a wide range of superconducting phenomena

By considering minimising the Gibbs free energy at T_C with respect to changes in the order parameter defined by:

$$f = f_{n0} + \alpha|\psi|^2 + \frac{\beta}{2}|\psi|^4 + \dots \qquad \textbf{(13)}$$

and with respect to the vector potential A, defined as:

$$\boldsymbol{B} = \nabla\times A \tag{14}$$

the Ginzburg Landau equations can be derived, which in variational form are given by:

$$\frac{1}{2m^*}(i\hbar\nabla + e^*A)^2\psi + a\psi + b|\psi|^2\psi=0 \tag{15}$$

and:

$$\nabla\times(\nabla\times A) + \frac{i\hbar e^*}{2m^*}(\psi^*\nabla\psi-\psi\nabla\psi^*)+\frac{e^{*^2}}{m^*}A|\psi|^2 = 0 \tag{16}$$

These are two coupled differential equations for the order parameter (ψ) and the vector potential (A). These equations are usually only solvable numerically except for a few special cases. They do however describe the electromagnetic properties of superconductors well, predicting many observed features of superconductors, and producing the London Equations, the penetration depth, the coherence length and fluxons as natural parameters.

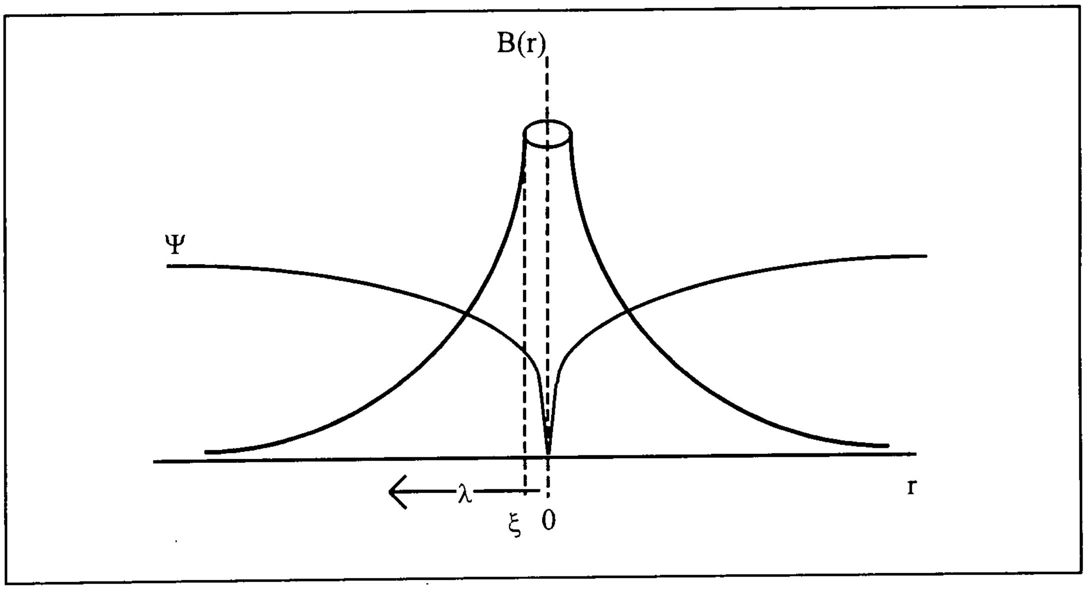

Figure 2.11 **Fluxon, with field decaying over penetration depth and radius of coherence length as predicted by Ginzburg Landau Theory.**

The fluxon described by Ginzburg Landau is shown in figure 2.11. These equations do not however postulate any microscopic explanation of the phenomenon of superconductivity.

2.7.3 BCS Theory

In 1957 Bardeen, Cooper and Schrieffer developed the first microscopic theory of superconductivity, BCS theory **[13]**.

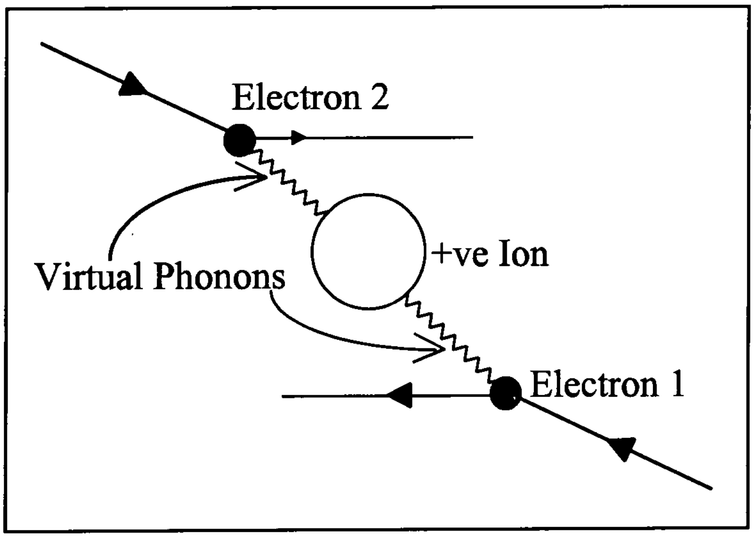

Figure 2.12 Attraction of two electrons via the crystal lattice to form a Cooper pair.

They postulated that the electrons within a superconductor formed pairs, called Cooper pairs by exchanging a virtual phonon via the crystal lattice. The Cooper pairs having zero momentum and zero spin no longer obey Fermi statistics. Instead they must be considered as bosons and hence all occupy the same quantum mechanical state. This requirement means that any one pair cannot exchange momentum with the lattice as this would change its quantum mechanical state. Hence the Cooper pairs do not interact with the lattice, they pass through it with no scattering and hence no resistance. The theory goes on to predict many observable features of the superconducting state, including Ginzburg Landau theory, which can be derived from BCS. theory. The discovery of high temperature superconductors and heavy fermion superconductors produced a new series of experimental results with which to compare the predictions of BCS theory and so far the theory and experimental evidence remain consistent.

2.8 Applications

The potential applications for superconductors are vast, and expanding all the time with the discovery of new materials with ever higher critical parameters. The current applications will be presented first and then a taste of some of the potential applications will be given.

2.8.1 Current Applications

By far the biggest use of superconductors at present is in producing superconducting magnets. These allow access to magnetic fields that are almost impossible to reach without the use of superconductors. As well as being used in research laboratories to allow measurement of materials at high fields, they can also be used as measurement techniques in their own right. **N**uclear **M**agnetic **R**esonance relies on the production of an incredibly stable and homogenous magnetic field that is only possible using superconducting magnets and allows the measurement of nuclear structure of materials. The most widespread of magnetic measurements is the **M**agnetic **R**esonance **I**maging technique. This is now widely used in hospitals to allow the imaging of tissue in the same way that x-rays are used for the imaging of bone. It allows 3D imaging of a patient, giving doctors vital information before operations.

A different application of superconductors is in the construction of Superconducting **Q**uantum **I**nterference **D**evices, allowing the measurement of tiny magnetic signals. Using a SQUID, it is possible to detect the heart beat of an unborn baby to monitor foetal development throughout a pregnancy. In an altogether different area, SQUIDs are also used to detect the magnetic signature of ships and submarines for military purposes.

2.8.2 Potential Applications

The potential applications for a material with no electrical resistance are vast, including superconducting magnets, energy storage devices, and power transmission lines. Another property of superconductors, the Josephson Effect, which will not be discussed here, opens the possibility of superconducting computers, running at speeds unobtainable using existing silicon based technology. The expulsion of a magnetic field gives the possibility of floating objects using magnetic fields. This is being investigated by the Japanese who have produced a train that floats on magnetic fields produced by superconductors. Also superconducting motors and frictionless bearings would produce untold improvements in performance over conventional techniques.

2.9 Summary

This chapter has given a very brief introduction into a few of the fundamentals of superconductivity, from its discovery, to the possible future applications. The parameters used to characterise superconductors, critical temperature, fields and current have been introduced and the main theories used to describe superconductors have been examined and the general principles behind them explained. The uses of superconductor presently and the potential for future applications make this an important and exciting field of research.

2.10 References

[1] Onnes H K *Comm. Leiden* **120B** (1911)

[2] Rosenberg H M *The Solid State* Oxford Science Publications 232 (1992)

[3] Buckel W *Superconductivity, Fundamentals and Applications* V.C.H. (1991)

[4] Bednorz J G and Muller K A *Z. Phys. B* **64** 189 (1986)

[5] Wu M K, Ashburn J R, Torng C J, Hor P H, Meng R L, Gao L, Huang Z J, Wang Y Q and Chu C W *Phys. Rev. Lett.* **58** 908 (1987)

[6] Maeda H, Tanaka Y, Fukutomi M and Asano T *Jpn. J. Appl. Phys.* **27** L209 (1988)

[7] Poole C P, Farach H A and Creswick R J *Superconductivity* Academic Press (1995)

[8] Abrikosov A A *Sov. Phys. JETP* **5** 1174 (1957) [Translation of *Zh. Eksp. Teor. Fiz.* **32** 1442 (1957)]

[9] Kleiner W H, Roth L M and Autler S H *Phys. Rev.* **133** A1226 (1964)

[10] Bean C P *Rev. Mod. Phys.* **36** 31 (1964)

[11] London F and London H *Proc. Roy. Soc.* **A149** 71 (1935)

[12] Ginzburg V L and Landau L D *Zh. Eksp. Teor. Fiz* **20** 1064 (1950)

[13] Bardeen J, Cooper L N and Schriefer J R *Phys. Rev.* **108** (5) 1175 (1957)

Chapter 3

Review of Chevrel Phase Fabrication and the Irreversibility Field

3.1 Introduction to Chapter 3

This thesis contains work on the fabrication and characterisation of Chevrel phase superconductors and the measurement of the irreversibility field. In this chapter the literature relevant to each will be reviewed in turn. Section 3.2 will introduce Chevrel phase superconductors and section 3.3 will cover some of the fabrication processes available and discuss their relative merits. Section 3.4 will summarise the properties of Chevrel phase superconductors and the figures of merit that allow the determination of sample quality, concentrating on $SnMo_6S_8$ and $PbMo_6S_8$ as these are the most likely to have commercial applications. Section 3.5 will describe the pinning within Chevrel phase materials and the properties of the flux line lattice will be discussed in section 3.6. This chapter will then be summarised in section 3.7.

3.2 Chevrel Phase Superconductors

In this section Chevrel phase(CP) superconductors will be introduced and some of their general properties described. The main methods for fabricating Chevrel phase materials will be discussed and the important factors in the fabrication process highlighted.

3.2.1 What is a Chevrel Phase Superconductor

Chevrel phase materials were first fabricated in 1971 by Chevrel et al**[1]** and have the chemical formula MMo_6X_8 where M is a metal and X is a chalcogen, usually sulphur or selenium. Superconductivity was discovered in this class of materials by Matthias et al in 1972**[2]** with the highest T_C for a Chevrel phase superconductor being approximately 15K for $Pb_1Mo_6S_8$**[3]**. The most interesting feature of the Chevrel phase is the high upper critical fields of over 50T for $Pb_1Mo_6S_8$**[4]** and over 30T for $Sn_1Mo_6S_8$**[5]**, making these materials of particular interest for commercial applications.

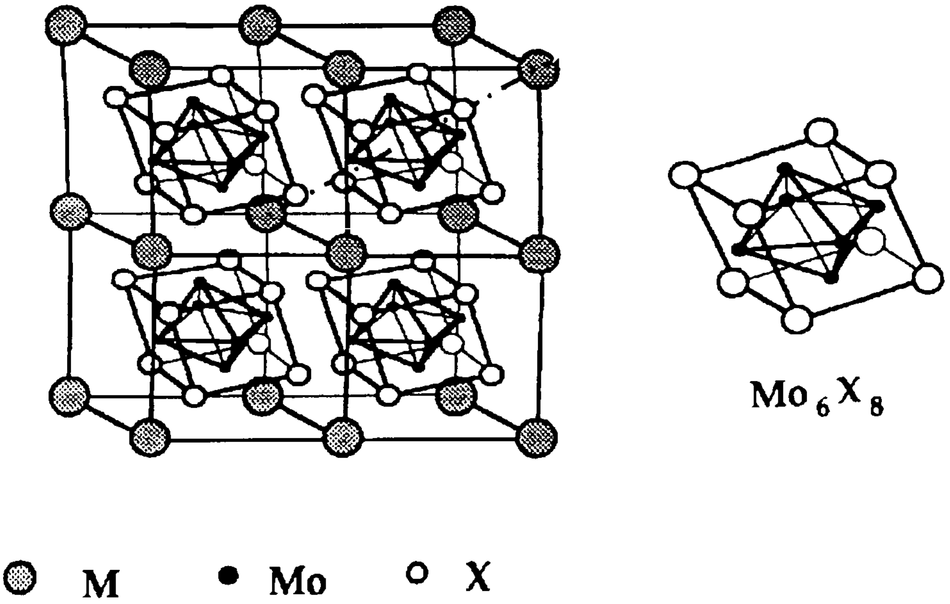

Figure 3.1 Crystal structure for a Chevrel phase compound[6].

The crystal structure of the Chevrel phase is a cubic arrangement of chalcogen atoms with a molybdenum atom at the centre of each face, surrounding the metal atom, as shown in figure 3.1. It is this structure that separates the metal atoms from the molybdenum atoms which contain the superconducting electrons, allowing magnetic metal atoms to coexist in the crystal lattice without destroying the superconductivity, discussed further in chapter 6.

3.3 Fabrication of Chevrel Phase Superconductors

Numerous methods have been used for fabricating Chevrel phase superconductors [3][7], however this review will be restricted to the process used in the fabrication of the materials used in this thesis, i.e. solid state sintering, and the technique which has provided the highest critical current densities in wires to date[8], i.e. the Mo_6S_8 route.

3.3.1 Solid State Sintering

Solid state sintering relies on the interdiffusion and reaction of precursors to form the required material. The nature of the material produced, in particular its microstructure, is strongly dependent on the reaction conditions used, which in the case of Chevrel phase materials are normally quite aggressive, with temperatures of between 900°C and 1600°C used for times of between 1 and 100 hours**[9][10]**. It is essential that the precursors for the reaction be mixed thoroughly in order to produce a homogenous material as the interdiffusion process is in general a slow one. The advantage of this technique is that it is relatively straight forward, contains a minimum of steps and can easily produce large quantities of material. The problems with this method are that the grain size of the material produced is usually of the order of a few microns **[7]**. If the times and temperatures are reduced to produce smaller grains, problems occur with homogeneity and incomplete reactions.

3.3.2 Mo_6S_8 Route

The critical current density of Chevrel phase materials have been seen to exhibit a strong dependence on grain size, with smaller grains giving higher critical current densities**[11]**. In order to achieve smaller grain size a novel fabrication route has been developed**[12]**. This technique involves producing a precursor Chevrel phase material, usually $LiMo_6S_8$ or $NiMo_6S_8$, and removing the metal cation using an aqueous solution of HCl, causing the crystal lattice to collapse but leaving the Mo_6S_8 clusters intact. These Mo_6S_8 cluster are now fine grained and free from impurities and can be reacted with lead sulphide at 440°C under a continuous flow of hydrogen gas to remove any excess sulphur. The resulting powder can then be heat treated at relatively low temperatures (<800°C) to produce homogenous, single phase, fine grained $PbMo_6S_8$. The advantages of this method are that the resulting material has small grains and the reaction temperatures required are easily achievable in a industrial environment, however the technique is more complicated than the solid state sintering technique.

3.3.3 Hot Isostatic Pressing

Sintered Chevrel phase materials suffer from poor connectivity of the grains (granularity) which degrades the superconducting properties of the material, in particular the critical current density. Hot isostatic pressing is a method for improving the connectivity of the grains and hence improving the properties of the material as a whole.

An improvement of over factor 20 has been found in the critical current density of $PbMo_6S_8$ by the use of hot isostatic pressing**[13]**.

The technique involves sealing the sample in a thin walled billet, typically stainless steel, and applying pressures of up to 2000 bar using compressed gas, usually argon. This is typically performed at temperatures of around 1000°C for a few hours. The density of the sample has been found to increase to greater than 90% theoretical density **[13][3]** and the sample also becomes far more metallic in nature.

3.3.4 General Points on Chevrel Phase Fabrication

In the fabrication of Chevrel phase materials, several considerations are common to all techniques. It was shown by Hinks et al**[14]**, and later by Foner et al**[15]** that contamination with oxygen could produce large variations in the superconducting properties of Chevrel phase materials. In light of this discovery in 1983, all results derived from samples fabricated before this date should be reevaluated to ensure the determining feature was not oxygen contamination. Since 1983 most processes have been adapted to reduce the amount of oxygen contamination, with the use of glove boxes for sample handling and oxygen getters in the reaction vessels. It was also found that the quartz tubes commonly used to fabricate Chevrel phase materials introduced both oxygen and, in the case of high temperature reactions, silicon was found within the materials**[7]**. To avoid this problem there has been a move towards the use of inert crucibles for high temperature reactions. The crucibles used have been either molybdenum, which becomes inert after a few reactions as the inner surfaces of the crucible are coated with a Chevrel phase layer or Boron-Nitride which was also found to be inert and able to withstand the high temperatures required for the reactions**[16]**.

3.4 Characteristics of Chevrel Phase Superconductors

In this section the superconducting properties of Chevrel phase superconductors will be reviewed, concentrating on lead molybdenum sulphide (PMS) and tin molybdenum sulphide (SMS), as these are the materials studied in the rest of the thesis.

3.4.1 Critical Temperatures

These range from non-superconducting up to 15K for PMS. There is no simple relation between the metal atom M and the critical temperature of the Chevrel phase material. The superconductivity is thought to occur in the molybdenum electrons which are only weakly coupled to the metal atom M. The superconducting properties are therefore determined by the volume of the unit cell and the electronic structure around the molybdenum cluster. Hence when the metal M is changed, both of these values vary and a simple relationship cannot be expected. Another compliction in Chevrel phase materials is the degredation of properties by contamination with oxygen as mentioned in 3.2.4. For samples of $PbMo_6S_8$ and $SnMo_6S_8$ transition temperatures of close to 15K and 14K respectively are expected for uncontaminated samples. Chemical stoichiometry has also been shown to have an effect on the critical temperature in both $PbMo_6S_8$**[17][18]** and $SnMo_6S_8$**[19]**, again making it difficult to determine any relation between critical temperature and material properties.

3.4.2 Upper Critical Fields

The main reason for the interest in Chevrel phase superconductors is the high upper critical fields found in the lead and tin compounds**[4][5]**, which make them potential materials for the production of static magnetic fields greater than 20T**[20]**. Again the upper critical fields of the materials are effected by oxygen contamination within the sample and hence there is a large spread of data in the literature. Values for PMS are between 50T and 60T while for SMS the values are between 30T and 35T.

3.4.3 Fundamental Parameters

Chevrel phase materials are also of interest from a more fundamental point of view. They have a Ginzburg Landau coherence length of approximately 2nm for PMS and 4nm for SMS, making them intermediate between the low T_C materials and High T_C cuprates, allowing easier investigation of the mechanisms in both classes of material. The other fundamental property is kappa (κ), the ratio of the penetration depth over the coherence length, which is approximately 130 for lead molybdenum sulphides**[21]**.

3.4.4 Critical Current Densities

The properties discussed so far appear to make Chevrel phase materials ideal for the production of high field magnets. Preventing this from occurring is the critical current densities available in these materials. Chevrel phase materials suffer from granularity, that is the grains of superconducting material with high critical current density are joined together by grain boundaries with much lower critical current density**[22]**. The grain boundaries are thought to be the limiting factor preventing the achievement of the current densities required**[23]**. Improvements in fabrication techniques including the removal of oxygen impurities and more recently the production of incredibly fine grain powders using the Mo_6S_8 route described in section 3.3.2. have resulted in improvements in the critical current density, particularly in wires. Recently values of 236 Amm^{-2} have been achieved at 4.2K and 20T**[8]** in PMS wires, which is within a factor 2 of becoming a viable material for production of high fields. The upper critical fields for these wires however were less than 40T. This is compared to typical bulk values for PMS of 100 Amm^{-2} at 4.2K and 10T[9]**[24]** for the critical current density and over 50T for the upper critical field. SMS has higher critical current densities reported of 770 Amm^{-2} at 10T, 4.2K and 170 Amm^{-2} at 20T, 4.2K**[25]**for bulk samples. There is still room for improvement, with the intragranular current density being estimated at 2000Amm^{-2} at 4.2K and 10T for PMS**[22]**.

3.5 Pinning Within Chevrel Phase Materials

Crucial to the achievement of higher critical current densities within Chevrel phase superconductors is an understanding of the pinning, introduced in section 2.5. In this section pinning mechanisms thought to operate in Chevrel phase materials will be introduced and their characteristic features will be summarised. Phenomena associated with pinning will then be explained, namely flux creep and the Peak Effect, both of which have been found in Chevrel phase materials.

3.5.1 Pinning Force Curves

The pinning force density in superconductors can be determined from the critical current density using:

$$F_P = J_C \times B \qquad (1)$$

Once the pinning force has been determined it can often be scaled using the reduced field B/B^*_{C2} and the reduced pinning force density F_P/F_P^{Max}. If the pinning force can be scaled it means that measurements taken at any temperature can be reduced to the same functional form as a function of the reduced field and reduced pinning force.

Once the functional form of the pinning force has been determined, this can usually be associated with a pinning mechanism, i.e. the cause of the pinning force within the material.

Type of Interaction	Geometry of Pins	Type of Pin	Functional Form of Pinning Force	Position of F_P^{Max}
Magnetic	Volume	Normal	$b^{1/2}(1-b)$	0.33
		$\Delta\kappa$	$b^{1/2}(1-2b)$	0.17,1
Core	Volume	Normal	$(1-b)^2$	-
		$\Delta\kappa$	$b(1-b)$	0.5
	Surface	Normal	$b^{1/2}(1-b)^2$	0.2
		$\Delta\kappa$	$b^{3/2}(1-b)$	0.6
	Point	Normal	$b(1-b)^2$	0.33
		$\Delta\kappa$	$b^2(1-b)$	0.67

Table 3.1 Pinning mechanisms and their functional forms as proposed by Dew-Hughes[26]

It is proposed that each functional form for the pinning force can be uniquely assigned to a pinning mechanism shown in table 3.1. The identifying feature of the pinning force curve is the position of the peak in the pinning force, usually allowing the mechanism to be determined. The situation becomes more complex if more than one mechanism is operating within a material. PMS has a functional form for the pinning force density of:

$$F_P = \alpha b^{1/2}(1-b)^2 \qquad (2)$$

where α is a constant and b is the reduced field, which is a normal surface pinning mechanism. This functional form is called the Kramer functional form and is considered to be due to the grain boundaries within the material acting as pinning sites. Further support is that the number of grain boundaries per unit volume is strongly correlated with the critical current density, for example in Nb_3Sn **[11]**

3.5.2 Flux Creep

In section 2.5 the critical state of a superconductor was introduced in which the fluxons were trapped within a pinning site, allowing a lossless supercurrent to flow which resulted in a field gradient across the sample.

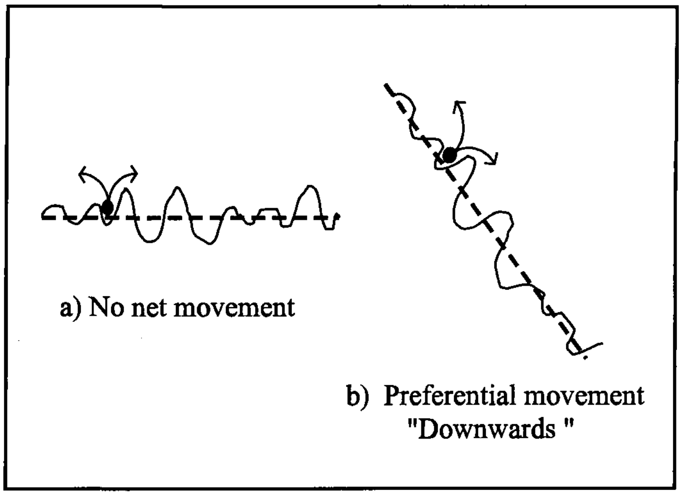

Figure 3.2 Illustration of flux creep within a superconductor.

Flux creep occurs when the thermal energy of the pinned fluxons allows them to migrate through the material to reduce the field gradient, first proposed by Anderson**[27]**. The equation for the motion of the fluxons was developed by Anderson and Kim**[28]** and states that:

$$R = \omega_0 e^{-U/k_B T} \qquad (3)$$

where R is the jump rate of the fluxons, ω is a characteristic attempt frequency of the flux line vibrations, U is the barrier energy, k_B is Boltzmann's constant and T is the temperature. It has been measured in Chevrel Phase materials by Zheng et al**[21]** and is between that of the low T_C superconductor NbTi and high T_C superconductors $YBa_2Cu_3O_7$, as would be expected given the coherence lengths of the three classes of material.

3.5.3 Peak Effect

This is a phenomenon found in many superconducting materials, including SMS, and is the increase in pinning force density with increasing magnetic field, close to the upper critical field for the material. Many causes of this effect have been postulated, a review of the important ones will now be given.

The first explanation of this effect is to consider two pinning mechanisms acting within the superconductor. Each of these mechanisms will have a field dependence and the total pinning force observed will be a summation of the two**[29]**. It can be seen from table 3.1 that it is possible to choose two pinning mechanisms that have peak strengths at different reduced field, one of which could be at high reduced field. If the two mechanisms are of comparable strength the total pinning force would show an increase in strength as the applied field increased, hence producing a peak at high reduced field.

The second explanation is that at high reduced fields the properties of the flux line lattice change. In particular the elastic constant fall to zero as the upper critical field is approached, proposed by Pippard**[30]**. The fact that the fluxons are more free to move will allow them to locate on pinning sites that were previously unavailable due to the rigidity of the flux line lattice and the pinning force density will therefore increase**[31]**. The peak effect will be examined in more detail in chapter 5.

3.6 Properties of the Flux Line Lattice

The behaviour of the flux line (vortex) lattice, particularly with respect to pinning has been greatly debated, even more so since the discovery of high temperature superconductors. Phenomena were observed that did not fit with the conventional understanding and so new explanations were required. One of the most investigated effects was the discovery of a region in the superconducting phase diagram in which there was superconductivity but no pinning and hence zero critical current density**[32]**. The field at which the critical current density becomes zero is called the irreversibility field. The irreversibility field has been extensively studied as it may prove a limiting factor for the application of high T_C superconductors. In this section the proposed causes for this region will be introduced, along with techniques by which it can be observed.

3.6.1 Possible Mechanisms for Zero Pinning Superconductivity

Before discussing mechanisms by which the pinning can disappear above the irreversibility field, it is important to understand the nature of the pinning and the arrangement of fluxons within the superconductor below the irreversibility field. There are two competing principles determining the arrangement of the flux line lattice in a superconductor containing pinning sites below the irreversibility field.

Firstly, if there were no pinning sites, the mutual repulsion of the fluxons would lead to the flux line lattice assuming its lowest energy arrangement of a hexagonal lattice[33] with long range order throughout the lattice. This arrangement however would not allow a lossless current to be passed as there is nothing preventing the entire flux line lattice moving without losing its ordering. At the other extreme, in a superconductor containing random pinning sites and no force between fluxons, all the fluxons would locate on pinning sites, with the lattice being totally disordered, however the fluxons would all be pinned. This would allow a lossless transport current to pass. The actual situation in most superconducting materials is a combination of the two extreme cases above where there is some pinning and some interaction between the fluxons. The relative strength of the pinning sites and the fluxon fluxon interaction determines the arrangement of fluxons within the material.

The irreversibility field has been discussed by many authors with the two most commonly accepted theories being lattice melting or giant flux creep. Yeshurun and Malozemoff[34] proposed that flux creep as discussed in section 3.5.2 can also lead to zero pinning superconductivity if the rate at which the fluxons move becomes sufficiently great that no field gradient exists within the sample. This effect is known as Giant Flux Creep and would give zero critical current density when:

$$1-t = \frac{8\pi f^2 B k_B T_C \ln\left(Bd\Omega/E_c\right)}{2.56 H^2_{c0}\Phi_0\xi_0} \qquad (4)$$

where t is the reduced temperature, f is approximately 6, B is the applied field, T_C is the critical temperature, d is the distance between pinning sites, Ω is the frequency of oscillation of a fluxon in a pinning site, E_C is a minimum measured voltage per metre,

H_{C0} is the thermodynamic critical field, Φ_0 is a flux quantum and ξ_0 is the Ginzburg Landau coherence length. This does not result from a phase transition of the flux line lattice from solid to liquid. Tinkham et al[35] used the idea of giant flux creep to explain the broadening of the resistance transitions with applied field. This flux creep theory does not hold for all materials as was found by various authors[36][37][38]. These discrepancies were overcome by Hagen and Griessen[39] who included a distribution in the strength of the pinning potential. Various other forms of the activation energies have been proposed by different authors, each holding in a particular temperature or field regime, for a particular material[40][41][42]. No one of these theories can be applied to any sample across the whole field and temperature range.

An alternative explanation for the reversible region is that proposed by Nelson et al[43] in which the flux line lattice undergoes a phase transition and becomes a liquid. The elastic constants of the flux line lattice decrease with increasing field[30] allowing the fluxons greater movement. It is proposed by Nelson et al that the flux line lattice will melt when the amplitude of the thermal motion of the flux lines is greater than ten percent of the lattice spacing, i.e.

$$\sqrt{<u>^2} \gg c_L a_0 \qquad (5)$$

where u is the thermal motion of the fluxons, $c_L = 0.1$ (the Lindemann criteria) and a_0 is the fluxon lattice spacing. This theory has been supported experimentally by Gammel et al[44] in thin films. The theory was extended by Nelson and Seung[45] to a 3D system in which the fluxons can become entangled, with supporting experimental evidence for Gammel et al[46]. The melting line was first calculated as a function of field and temperature by Houghton et al[47] and is given by:

$$B_{3D}(T_m) \approx \frac{1}{\left(4\left(\sqrt{2}-1\right)+1\right)^2 \pi \mu_0^2} \times \left[\frac{\Phi_0^5 c_L^4}{\left(\gamma k_B T_C \lambda_{ab}^2(0)\right)^2}\right] \times \left[\frac{1-(T_m/T_C)^n}{T_m/T_C}\right]^2 \qquad (6)$$

where c_L is the Lindemann parameter, T_m is the melting temperature, γ^2 is the effective mass anisotropy, $\lambda_{ab}(0)$ is the zero temperature value of the London penetration depth, Φ_0 is the flux quantum for the two fluid model and n = 4**[48]**. Good agreement was found with the results of Gammel et al**[46]** and Cubitt et al**[48]**. The question of whether a 3D model can be applied to the planar structure that occurs in high T_C materials has been addressed by Clem**[49]** who considered the fluxons as columns of 2D "flux pancakes" which are coupled at low temperatures but become decoupled with increasing field and temperature, as observed by Cubitt et al**[48]** in BISCCO 2212 using neutron diffraction. The field at which the dimensionality of the flux line lattice changes is given by:

$$B_{2D} \approx \frac{\Phi_0}{(s\gamma)^2} \tag{7}$$

where s is the interplane separation of the CuO_2 planes and γ^2 is the effective mass anisotropy.

The lattice melting theories discussed above ignore the pinning within the material, as pointed out by Brandt**[50]**. He noted that as there was no long range order in a vortex glass anyway, the disorder would just increase continuously, with no distinct phase transition. Experimental evidence from Xu et al**[51]** also supports the irreversibility field being a depinning line rather than a melting line.

A model for a flux line lattice combined with pinning sites was described by Fischer et al**[52]** and is known as the vortex glass which uses collective pinning arguments to combine the pinning sites and the fluxon fluxon forces. Collective pinning**[53]** occurs when the density of flux lines is greater than the density of pinning sites. A fluxon that is close to a pinning site is attracted to it and becomes pinned. The fluxons neighbouring this pinned fluxon rearrange to give the hexagonal Abrikosov lattice arrangement in order to minimise the energy of the lattice, and are held stationary by the fluxon fluxon forces. This leads to a situation where there is local ordering around each pinned fluxon but no long range order throughout the material, as the lattice ordering must change in between pinning sites and hence the name vortex glass. The melting field for a vortex glass is given by:

$$B_M \sim \frac{\Phi_0}{\lambda_\perp^2 \ln^2(\Lambda_T/\lambda_\perp)} \tag{8}$$

where Λ_T is the thermal length defined as:

$$\Lambda_T = \frac{\Phi_0^2}{16\pi^2 T} \tag{9}$$

and $\lambda_\perp$is the mean field magnetic penetration length given by:

$$\lambda_\perp = \left[\frac{mc^2\beta}{16\pi|\alpha|e^2}\right]^{1/2} \tag{10}$$

where α and β are parameters from the Ginzburg Landau equations. This model has been supported experimentally by Koch et al**[54]**, Gammel et al**[55]** and Sandvold et al**[56]**, however it is suggested by Coppersmith et al**[57]** that the data of Koch could also be described using a flux creep argument.

Finally another explanation has been suggested by Yamafuji and Kiss**[58][59]** in which they combine the melting transition from vortex glass to vortex liquid with a distribution of critical current density and find excellent scaling of transport measurements for YBCO and TISCCO (2223).

3.6.2 Experiments Allowing the Observation of the Flux Line Lattice

One of the most simple methods of observing the flux line lattice is a decoration experiment, in which small magnetic particles are place on the surface of a superconductor in the mixed state. The magnetic particles then nucleate on the fluxons, allowing the flux line lattice to be seen using an SEM. This is however of limited use as it only shows the fluxons at the surface and is limited in resolution. At low temperatures the fluxons are observed to form a triangular lattice, and at higher temperatures this lattice disappears. This may be evidence for lattice melting or the lattice may just be finer than the resolution of the technique.

One of the earliest measurements of lattice melting is the vibrating reed technique. Here a sample is attached to a thin silicon reed that is vibrated at resonance. A magnetic field is applied and the resonance condition achieved again. If the temperature is now raised and the resonance frequency measured, the melting of the flux line lattice can be observed as a change in resonance frequency of the reed due to the speed at which the lattice responds within the sample being greater when the lattice is a liquid. This allows the measurement of lattice melting as a function of both field and temperature, but does not give any insight into the mechanisms behind the melting.

The measurement of resistivity as a function of temperature has also been found to show features indicative of a change in the flux line lattice**[60]**. Consider measuring the resistive transition in a high temperature superconductor in non-zero applied field. As the temperature is increased, initially there is an increase in resistance which during the transition slows down. The transition then continues at this slow rate until very close to the critical temperature when the resistance increases quickly up to its normal state value. The behaviour of this intermediate range has been attributed to the properties of the flux line lattice**[61]**.

Another method of direct observation of the flux line lattice is with the use of small-angle neutron scattering (SANS) e.g. **[48]**. This allows the flux line lattice to be observed as a function of temperature and field by the scattering of neutrons by the periodic lattice. Hence if the order of the lattice is destroyed, the scattering goes to zero. Single crystal niobium measurements**[62]** have shown no evidence for a simple melting transition, but instead suggest a more complicated phase transition. It is also not clear how these results relate to high temperature superconductors, and experiments are made difficult by the higher temperatures involved.

One of the most commonly used techniques for measuring the properties of the flux line lattice is dc magnetometry, either using a SQUID magnetometer or a vibrating sample magnetometer. Both of these techniques allow the measurement of the critical current density of a superconductor which is directly related to the pinning of the fluxons within the material. As discussed in section 2.5, when the magnetisation curve becomes reversible, this is the point at which the pinning is considered to be zero. It is from this technique that the point at which the flux line lattice becomes unpinned acquired the name of the Irreversibility Field.

The final technique is Lorentz Force Microscopy e.g. [63]. This allows real time observation of the motion of flux lines. The principle behind the technique is to shine high energy electron beams through a sample orientated at 45 degrees to the beam and at 45 degrees to a magnetic field. As the electrons pass through the sample they are deflected by the fluxons allowing their imaging. The fluxons appear as small bumps and have been observed to hop between pinning sites and to exhibit flux creep. Unfortunately the resolution of this technique is temperature dependent, decreasing with increasing temperature. If the resolution can be improved this will allow the observation real time of the phase transition of the flux line lattice.

3.6.4 Summary of the Properties of the Flux Line Lattice

In this section numerous explanations for the magnetic phase diagram of superconductors and the experimental techniques by which it has been investigated have been presented. All the explanations of a zero pinning superconducting region close to the upper critical field have some merit, can be supported by some of the experimental evidence and can be modelled by some choice of parameters in the proposed theories. So far there has been no single theory that can explain all the observed phenomena. Because of this uncertainty, it is important that the experimental evidence is correctly interpreted in terms of its relation to the behaviour of the flux line lattice to avoid any misleading results.

3.7 Summary

In this chapter the relevant literature for the two themes within this thesis has been presented. Chevrel phase materials have been introduced and have been shown to be an important area of research, having great potential for use in the next generation of high field magnets as well as having fundamental properties intermediate between those of the low temperature superconductors and the high temperature superconductors. Secondly the properties of the flux line lattice and in particular the region of zero pinning superconductivity above the irreversibility field on the magnetic phase diagram have been discussed. The understanding of this region could prove critical for the applications of high temperature superconductors and the number of possible explanations means that the correct interpretation of the experimental results is critical for the development of a full understanding of this phenomenon.

3.8 References

[1] Chevrel R, Sergent M and Prigent J *J. Solid State Chem.* **3** 515 (1971)

[2] Matthias B T, Marezio M, Barz H E, Corenzwit E and Cooper A S *Science* **175** 1465 (1972)

[3] Decroux M, Selvam P, Cors J, Seeber B, Fischer O, Chevrel R, Rabiller P and Sergent M *IEEE Trans. on Appl. Supercon.* **3** 1502 (1993)

[4] Foner S, McNiff Jr. E J and Alexander E J *Physics Letters* **49A** 269 (1974)

[5] Odermatt R, Fischer O, Jones H and Bongi G *J. Phys. C* 7 L13 (1974)

[6] Chevrel R, Sergent M, Le Lay L, Padoui J, Pena O, Dubots P, Genevey P, Couach M and Vallier J -C *Revue Phys. Appl.* **23** 1777 (1988)

[7] Selvam P, Cattani D, Cors J, Decroux M Neidermann Ph, Ritter S, Fischer O, Rabiller P, Chevrel R, Burel L and Sergent M *Mat. Res. Bull.* **26** 1151 (1991)

[8] Cheggour N, Decroux M, Gupta A, Fischer O, Perenboom J A A J, Bouquet V, Sergent M and Chevrel R *J. Appl. Phys.* **81** 6277 (1997)

[9] Cattani D, Cors J, Decroux M and Fischer O, *IEEE Trans. on Mag.* **27** 950 (1991)

[10] Kimura Y *Phys. Stat. Sol.* **69** K189 (1982)

[11] Rossel C and Fischer O *J. Phys. F* **14** 455 (1984)

[12] Rabiller P, Rabiller-Baudry M, Even-Boudjada S, Burel L, Chevrel R, Sergent M, Decroux M, Cors J and Maufras J L *Mat. Res. Bull.* **29** 567 (1994)

[13] Ramsbottom H D and Hampshire D P *Physica C* **274** 295 (1997)

[14] Hinks D G, Jorgensen J D and Li H -C *Phys. Rev. Lett.* **51** 1911 (1983)

[15] Foner S, McNiff Jr. E J, Hinks D G *Phys. Rev. B* **31** 6108 (1985)

[16] Selvam P, Cors J, Decroux M and Fischer O *Appl. Phys. A* **60** 459 (1995)

[17] Yamasaki H and Kimura Y, *Mat. Res. Bull* **21** 125 (1986)

[18] Yamamoto S, Wakihara M, and Taniguchi M, *Mat. Res. Bull.* **20** 1493 (1985)

[19] Sato K, Hinode H, Wakihara M and Taniguchi M *Mat. Res. Bull.* **23** 993 (1988)

[20] Flukiger R and Seeber B *Europhysics News* **22** 2 (1991)

[21] Zheng D N, Ramsbottom H D and Hampshire D P *Phys. Rev. B* **52** 12931 (1995)

[22] Cattani D, Cors J, Decroux M and Fischer O *Physica B* **165&166** 1409 (1990)

[23] Decroux M, Cattani D, Cors J, Ritter S and Fischer O *Presented at Int. Conf. Low Temp. Phys. Brighton* (1990)

[24] Gupta A, Decroux M, Selvam P, Cattani D, Willis T C and Fischer O *Physica C* **234** 219 (1994)

[25] Bonney L A, Willis T C and Larbalestier D C *J. Appl. Phys.* **77** 6377 (1995)

[26] Dew-Hughes D *Phil. Mag.* **30** 293 (1974)

[27] Anderson P W *Phys. Rev. Lett.* **9** 309 (1962)

[28] Anderson P W and Kim Y B *Rev. Mod. Phys.* **36** 39 (1964)

[29] Kramer E J *J. Appl. Phys.* **44** 1360 (1973)

[30] Pippard A B *Phil. Mag.* **19** 217 (1969)

[31] Brandt E H *Superconductivity* **6** 201 (1993)

[32] Muller K A, Takashige M and Bednorz J G *Phys. Rev. Lett.* **58** 1143 (1987)

[33] Abrikosov A A *Sov. Phys. JETP* **5** 1174 (1957) [Translation of *Zh. Eksp Teor. Fiz.* **32** 1442 (1957)]

[34] Yeshurun Y and Malozemoff A P *Phys. Rev. Lett.* **60** 2202 (1988)

[35] Tinkham M *Phys. Rev. Lett.* **61** 1658 (1988)

[36] Safar H, Duran C, Guimpel J, Civale L, Luzuriage J, Rodriguez E, de la Cruz F, Fainstein C, Shhneemeyer L F and Waszczak J V *Phys. Rev. B* **40** 7390 (1989)

[37] Thompson J R, Sun Y R and Holtzberg F *Phys. Rev. B* **44** 458 (1991)

[38] Xue Y Y, Huang Z J, Hor P H and Chu C W *Phys. Rev. B* **44** 113598 (1991)

[39] Hagen C W and Griessen R *Phys. Rev. Lett.* **62** 1674 (1989)

[40] Zeldov E, Amer N M, Koren G Gupta A, McElfresh M W and Gambino R J *Appl. Phys. Lett.* **56** 680 (1990)

[41] Vinokur V M, Fiegel'man M V and Geshkenbein V B *Phys. Rev. Lett.* **67** 915 (1991)

[42] Fiegel'man M V Geshkenbein V B, Larkin A I and Vinokur V M *Phys. Rev. Lett.* **63** 2303 (1989)

[43] Nelson D R *Phys. Rev. Lett.* **60** 1973 (1987)

[44] Gammel P L, Hebard A B and Bishop P J *Phys. Rev. Lett.* **60** 144 (1988)

[45] Nelson D R and Seung H S *Phys. Rev. B* **39** 9153 (1989)

[46] Gammel P L, Schneemeyer L F, Wasczak J V and Bishop D J *Phys. Rev. Lett.* **61** 1666 (1988)

[47] Houghton A, Pelcovits R A, Sudbø A *Phys. Rev. B* **40** 6763 (1989)

[48] Cubitt R, Forgan E M, Yang G, Lee S L, Paul D McK, Mook H A, Yethiraj M, Kes P H, Li T W, Menovsky A A, Tarnawski Z and Mortenson K *Nature* **365** 407 (1993)

[49] Clem J R *Phys. Rev. B* **43** 7837 (1991)

[50] Brandt E H *Phys. Rev. Lett.* 63 1106 (1989)

[51] Xu Y, Suenaga M, Moodenbaugh A R and Welch D O *Phys. Rev. B* **40** 10882 (1989)

[52] Fisher D S, Fisher M P A and Huse D A *Phys. Rev. B* **43** 130 (1991)

[53] Larkin A I and Ovchinnikov Y N *J. Low Temp. Phys.* **34** 409 (1979)

[54] Koch R H, Fuglietti V, Gallagher W J, Koren G, Gupta A and Fisher M P A *Phys. Rev. Lett.* **63** 1511 (1989)

[55] Gammel P L, Schneemeyer L F and Bishop D J *Phys. Rev. Lett.* **66** 953 (1991)

[56] Sandvold E and Rossel C *Physica C* **190** 309 (1992)

[57] Coppersmith SU, Inui M and Littlewood P B *Phys. Rev. Lett.* **64** 2585 (1990)

[58] Yamafuji K and Kiss T *Physica C* **258** 197 (1997)

[59] Yamafuji K and Kiss T *Physica C* **290** 9 (1997)

[60] Kwok W K, Fendrich J A, van der Beck C J and Crabtree G W *Phys. Rev. Lett.* 73 2614 (1994)

[61] Jackson D J C and Das M P *Supercond. Sci. and Tech.* **9** 713 (1996)

[62] Lynn J W, Rosov N, Grigereit T E, Zhang H and Cinton T W *Phys. Rev. Lett.* **72** 3413 (1994)

[63] Harada K, Matsuda T, Bonevich J, Igarashi M, Kondo S, Pozzi G, Kawabe U and Tonomura A *Nature* **360** 51 (1992)

Chapter 4

Stoichiometry Study on Hot Isostatically Pressed Lead Molybdenum Sulphide

4.1 Introduction to Chapter 4

The critical temperature of the Chevrel phase superconductor lead molybdenum sulphide(PMS) has previously been found to vary with the stoichiometry. It was found that increasing the lead and sulphur content increases the critical temperatures of the materials**[1][2][3]**. In this study PMS samples were fabricated at 1100°C under 2000 bar of argon using a hot isostatic press, in the lead rich, sulphur rich region of the phase diagram. The hot isostatic press is used as it has been shown to increase the critical current density in PMS by more than a factor 20 compared to standard sintering techniques**[4]**. A series of samples was fabricated with varying proportions of the starting elements given by $Pb_{1+y}Mo_6S_{8+x}$ where $y = 0$ or 0.1 and $x = -0.5$, 0.0, 0.5 and 1.0, described further in section 4.2. These samples were then characterised using transport and magnetic measurements to investigate the variation in superconducting properties. X-ray powder diffraction measurements were performed by Dr C Lehmann to determine phase composition. The details of these experiments are given in section 4.3. Section 4.4 covers the analysis and interpretation of the results which are discussed in section 4.5. Section 4.6 provides a summary of the chapter.

4.2 Sample Fabrication

In this section the detail of the sample fabrication will be given for the series of samples produced. The technique used was a solid state sintering technique as described in section 3.3.1. To avoid contamination with oxygen, all sample handling was performed in an inert argon atmosphere, with oxygen and water content of less than 10 p.p.m. and all tubes were thoroughly cleaned and degassed prior to use.

4.2.1 Formation of Precursors from Elements

In order to form the Chevrel phase, precursors were formed from elemental constituents. Lead (99.9999%), sulphur(99.999%) and molybdenum (99.95%) were weighed in the correct proportions for the required stoichiometry and sealed under vacuum in quartz tubes. These precursors were subjected to a heat treatment of:

$$\mathit{Room\ Temperature} \xrightarrow{400^\circ C/Hour} 450^\circ C \xrightarrow{8Hours} 450^\circ C \xrightarrow{33^\circ C/Hour} 650^\circ C \xrightarrow{6Hours} 650^\circ C \xrightarrow{Furnace\ Cooled} \mathit{Room\ Temperature}$$

The heat treatment was performed in a tube furnace under a continuous flow of argon gas.

4.2.2 Precursor Reaction to Form the Chevrel Phase

The resulting precursors were removed from the quartz tubes, hand ground using a mortar and pestle for approximately 30 minutes to ensure homogeneity. The powders were pressed into pellets and again sealed under vacuum in quartz tubes. The samples were then heat treated to fabricate the Chevrel phase, the heat treatment being:

$$\mathit{Room\ Temperature} \xrightarrow{1000^\circ C/Hour} 1050^\circ C \xrightarrow{24Hours} 1050^\circ C \xrightarrow{Furnace\ Cooled} \mathit{Room\ Temperature}$$

Again the heat treatment was performed in a tube furnace under a continuous flow of argon gas.

4.2.3 Hot Isostatic Pressing

The final stage in the processing was the use of a hot isostatic press to increase the density of the samples. The sintered Chevrel phase samples were removed from the quartz tube, wrapped in molybdenum foil and sealed under vacuum in thin walled stainless steel tubes. These billets were then hot isostatically pressed for 8 hours at 2000 bar and 1100°C. Following the hot isostatic pressing small holes were noticed in the steel walls of some of the billets though the molybdenum foil was still intact. The samples were still properly densified and no variation was found in T_C of the parts of the sample located close to the holes. The holes were caused by the high temperature of the reaction as they were not seen in similar reactions at slightly lower temperatures.

4.3 Experimental Characterisation

In this section the experimental characterisation of the samples will be described and results presented for the sample of stoichiometric composition, to show the quality of the data obtained.

4.3.1 X-ray Powder Diffraction

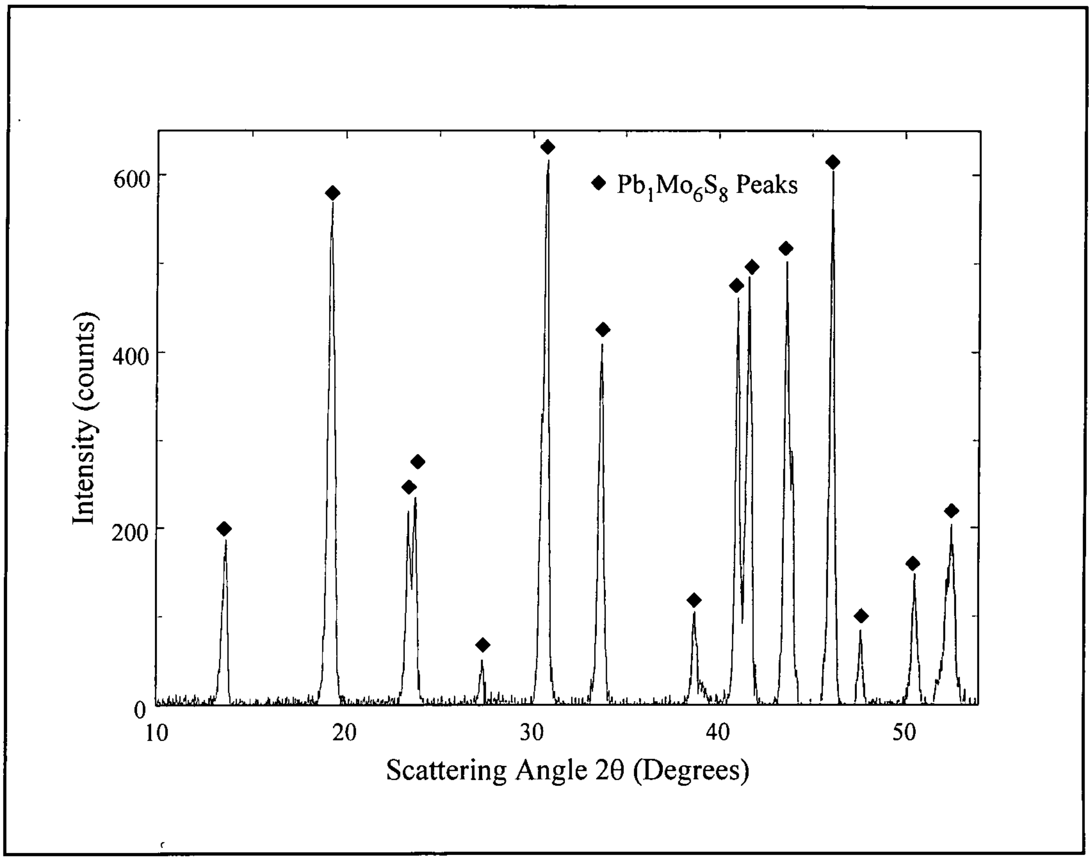

Figure 4.1 **X-ray powder diffraction trace for $Pb_1Mo_6S_8$ showing the sample to be single phase to the resolution of the technique.**

The phase composition of the sample was determined using x-ray powder diffraction performed by Dr C Lehmann from The Department of Chemistry at Durham University. A small amount of the sample was ground to a fine powder and dispersed on a perspex sample holder. The measurements were performed using a Philips PW1050 with a graphite secondary monochromator using Cu K_α at 1.5418Å, produced by a HiltonBrooks Generator. The data was taken at 0.02 degree intervals, counting for 2 seconds at each step.

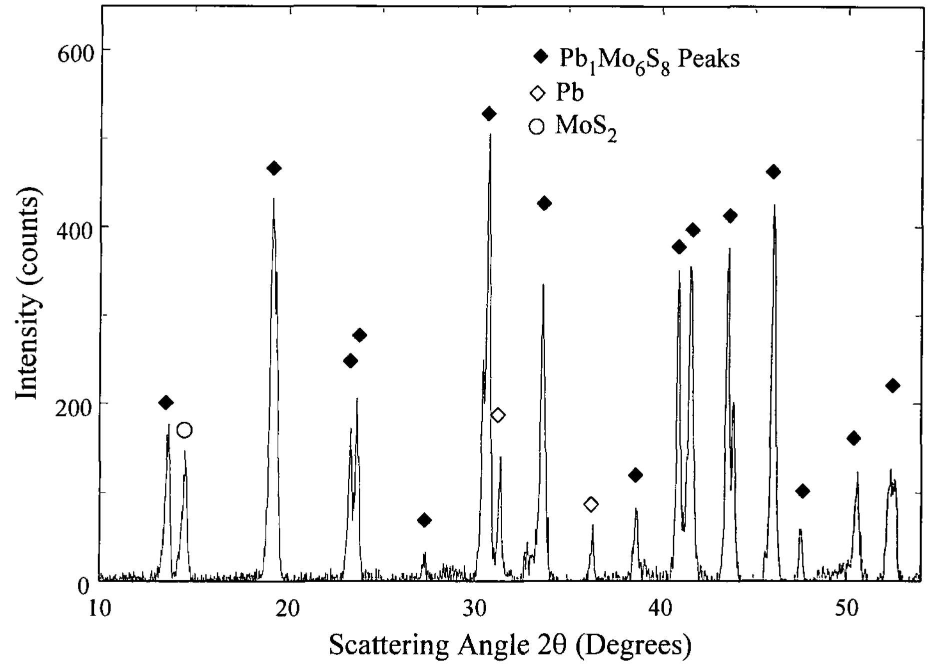

Figure 4.2 **X-ray powder diffraction trace for $Pb_{1.1}Mo_6S_9$ showing the sample contains second phase material in the form of MoS_2 and Pb.**

It can be seen from figure 4.1 that the stoichiometric sample is single phase, to the limit of this technique, and in figure 4.2 second phase impurities can be seen in one of the non stoichiometric sample when additional lead and sulphur is added. The height of the peaks for the second phase impurities was systematic with the nominal compositions of the sample.

4.3.2 Ac. Susceptibility and Ac. Resistance Measurements

In order to characterise the superconducting properties of the samples a study of their ac. resistance and ac. susceptibility was performed. Measurements were performed as a function of temperature, from 7.0 K to $T>T_C$ in dc fields up to 14T using a system developed in-house. The temperatures are accurate to 0.1K, determined from the measurement of a lead sample and the fields to better than 0.1%. The ac. resistance measurements were performed using a standard 4 terminal technique, with an excitation current of 3.3mA at 76 Hz. For the ac. susceptibility measurements, an ac. field of approximately 100μT was used at a frequency of 330 Hz.

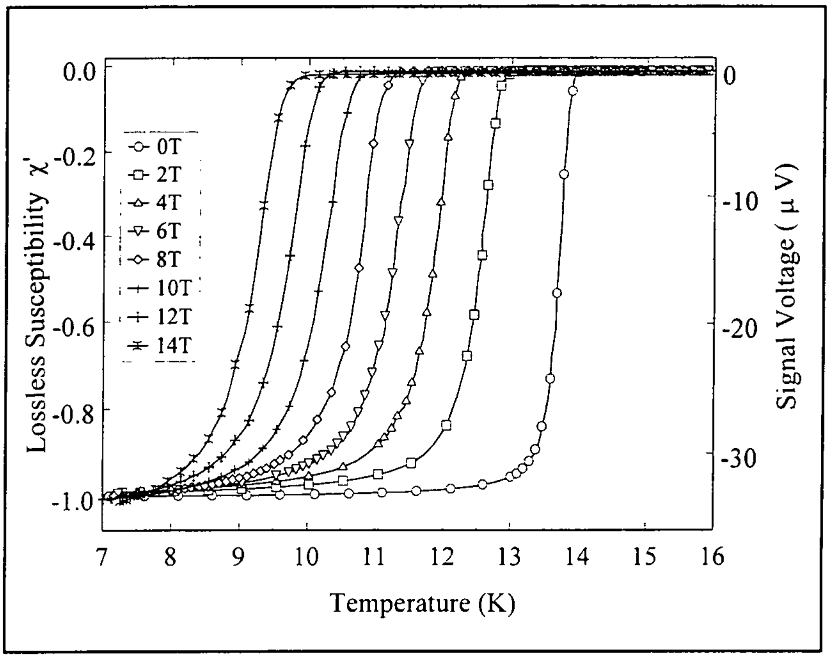

Figure 4.3 **Ac. susceptibility data for $Pb_1Mo_6S_8$ showing the lossless component of the superconducting transition.**

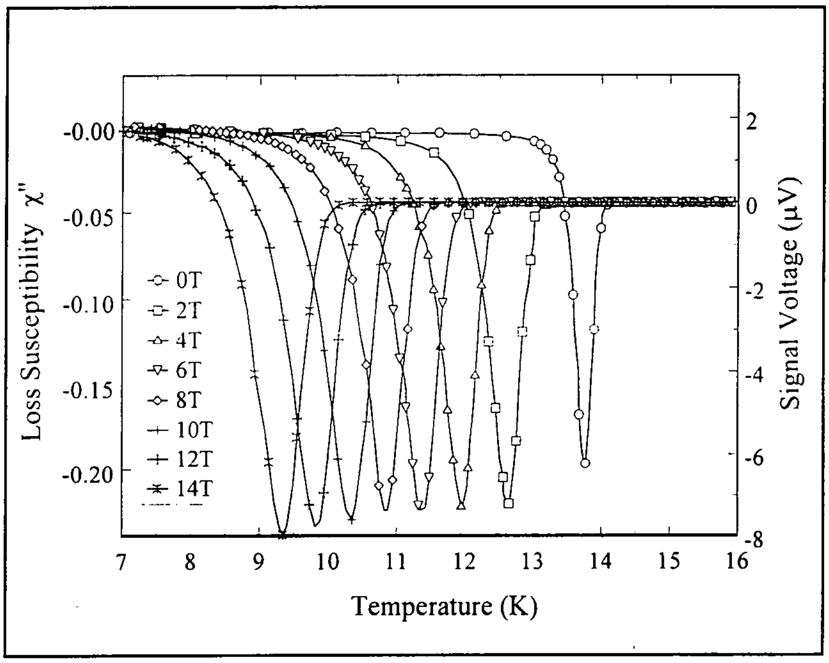

Figure 4.4 **Ac. susceptibility data for $Pb_1Mo_6S_8$ showing the loss component of the superconducting transition.**

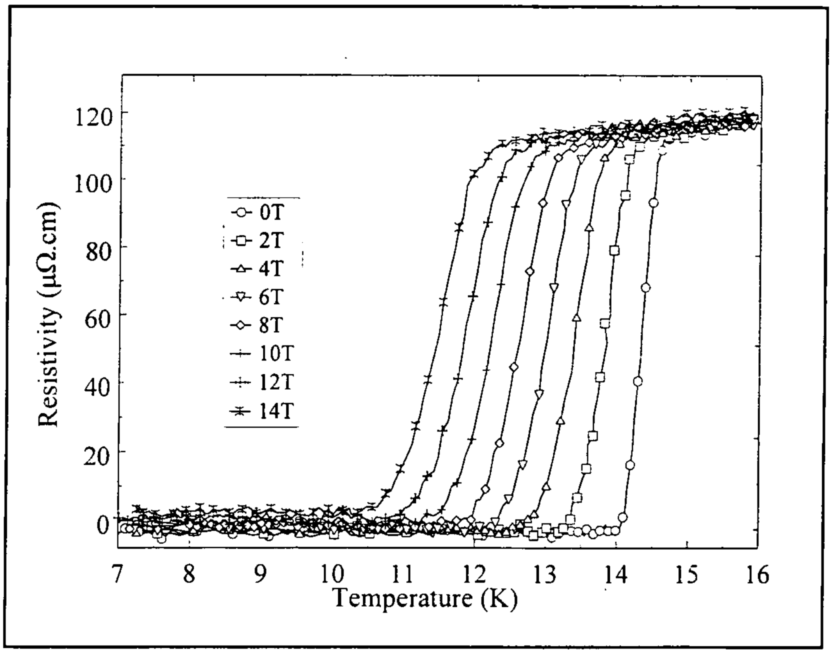

Figure 4.5 **Ac. Resistivity data for $Pb_1Mo_6S_8$ showing the superconducting transition.**

Figures 4.3 to 4.5 show a typical data set obtained for the stoichiometric sample, similar data was obtained for each sample. Traces labelled zero field were performed in the remnant field of the magnet which may be up to 100mT, but produces changes of less than 0.2K in the values obtained. χ' is assumed to be -1 in the low temperature regime, and a background has been subtracted, χ'' is normalised relative to χ' and a background has been subtracted.

4.3.3 Dc Magnetisation Measurements

In order to measure the critical current densities, irreversibility fields and upper critical fields of the samples dc magnetisation measurements were performed. The samples were measured using an Oxford Instruments Vibrating Sample Magnetometer, the stoichiometric sample was measured by Dr. D P Hampshire at Birmingham University and the remaining samples were measured by the author, with the aid of Dr. D N Zheng at Cambridge University. For each measurement the longest dimension of the sample was aligned parallel to the applied field except for the stoichiometric sample measured in Birmingham where it was perpendicular to the applied field.

Stoichiometry	Length (mm)	Width (mm)	Thickness (mm)
$Pb_1Mo_6S_{7.5}$	4.3	2.2	0.95
$Pb_1Mo_6S_8$	4.9	3.0	0.74
$Pb_1Mo_6S_{8.5}$	3.8	2.35	1.0
$Pb_1Mo_6S_9$	2.75	2.75	0.6
$Pb_{1.1}Mo_6S_{7.5}$	3.2	2.65	0.6
$Pb_{1.1}Mo_6S_8$	3.4	1.9	0.6
$Pb_{1.1}Mo_6S_{8.5}$	4.0	2.0	0.6
$Pb_{1.1}Mo_6S_9$	3.3	1.85	0.3

Table 4.1 Sample dimensions for the dc magnetisation measurements.

The dimensions of the samples used in the dc magnetisation measurements are summarised in table 4.1. It will be shown in chapter 8 that for a VSM experiment it is important that the self field of the sample is at least an order of magnitude larger than the effective ac. field caused by the sample moving in an inhomogeneous dc field. In light of this, the effective ac. field from the sample moving in a dc magnetic field was determined for the Oxford Instruments VSM and hence a critical current criteria found above which the effect of the ac. field is small enough to be neglected for these samples. In order to determine this it is necessary to calculate the parameter γ defined as:

$$\gamma = \frac{B_{ac}}{\mu_0 J_c r_m} \qquad (1)$$

where B_{ac} is the effective ac. field produced by the field inhomogeneity and is calculated to be 0.06mT for a dc field of 2T, explained in more detail in chapter 9. From this, assuming an average sample dimension of 1mm, and knowing that $\gamma < 0.1$ means that the measured critical current density is within 25% of the actual current density (where γ is as defined in equation 4.1) then:

$$J_c > 5\times10^5 Am^{-2} \qquad \textbf{(2)}$$

for the ac. field effect to be unimportant in the rest of this chapter.

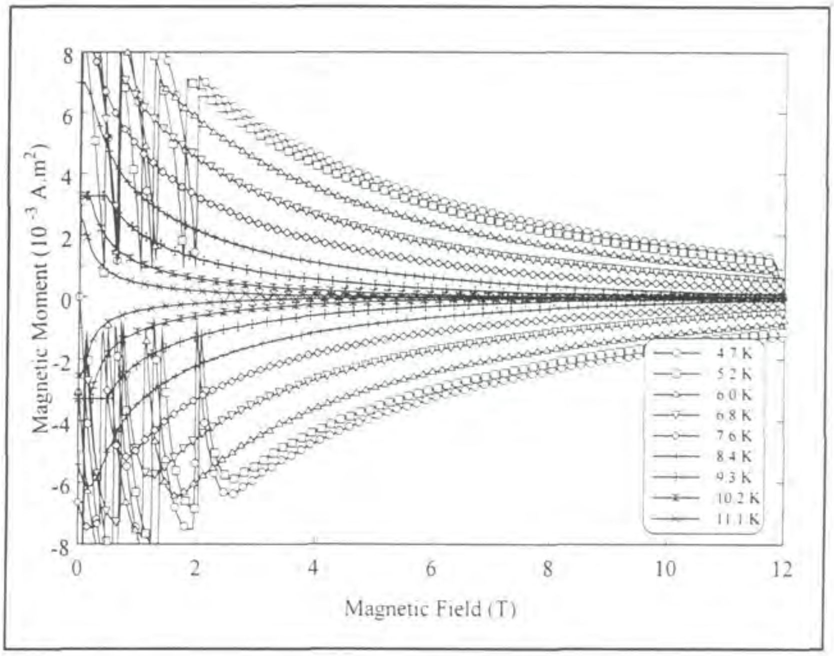

Figure 4.6 Dc magnetisation data for $Pb_1Mo_6S_8$ at low temperatures, with flux jumping in the sample at low fields.

Figure 4.6 shows the magnetisation loop for the lower temperatures measured and figure 4.7 shows the higher temperatures

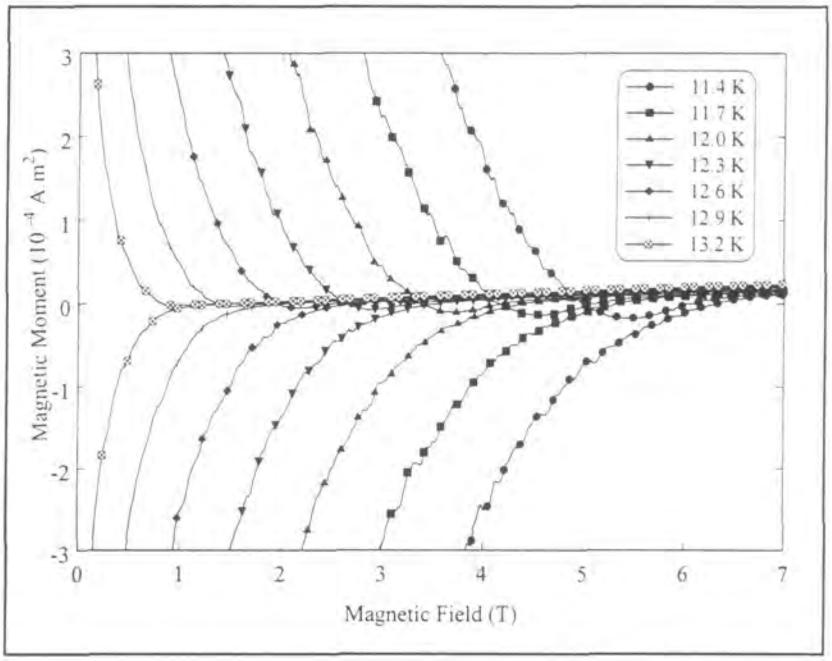

.**Figure 4.7** Dc magnetisation data for $Pb_1Mo_6S_8$ at higher temperatures showing the irreversibility fields.

From the magnetisation curves it is possible to calculate the critical current density using:

$$J_C = \frac{2\Delta M}{Volume.Thickness\left(1-\frac{Thickness}{3.Width}\right)} \qquad \textbf{(3)}$$

as proposed by Bean[**5**].

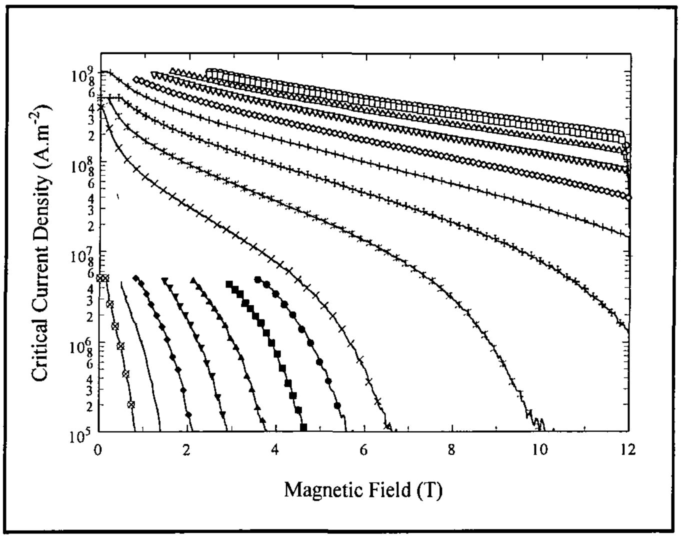

Figure 4.8 **Critical current density derived from the magnetisation loop using Bean's analysis. For legend see figure 4.6 and figure 4.7.**

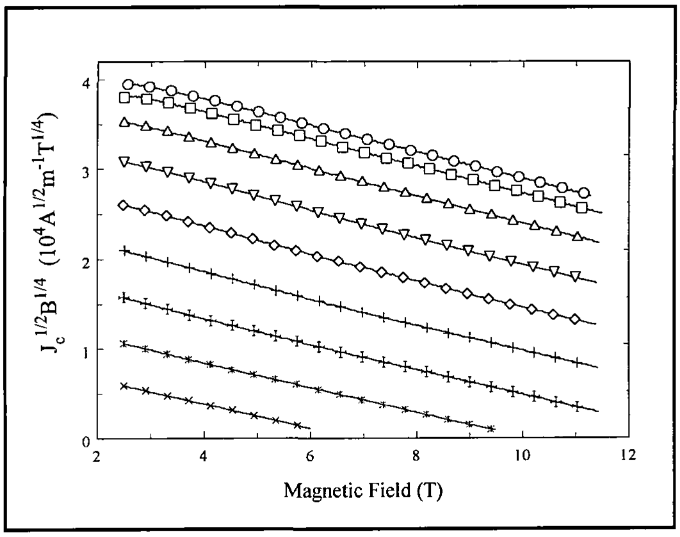

Figure 4.9 **Kramer plots of the critical current densities, see figure 4.6 for legend.**

The critical current density for the stoichiometric sample is shown in figure 4.8 where it can be seen that the values measured are above the criteria that allows the neglecting of the ac. field effect. In order to assess the pinning mechanism operating in these materials the data in figure 4.8 was replotted in the form of Kramer plots**[6]**. These lines, shown in figure 4.9, allow the determination of an irreversibility field by linear extrapolation to zero. The plots also show that the pinning within the material has a functional form for the field dependence of:

$$F_P = F(T).b^{1/2}(1-b)^2 \qquad \textbf{(4)}$$

by the fact that they are straight lines. This functional form is thought to be produced by grain boundary pinning within the material[7].

4.4 Results

In this section the results of the experiments described in section 4.3 will be presented for all the samples fabricated, allowing the variations with stoichiometry to be seen.

4.4.1 X-ray Powder Diffraction

Table 4.1 shows a summary of phase compositions for all the samples fabricated determined from the x-ray powder diffraction measurements.

1.1	PMS Pb Mo	PMS Pb	PMS Pb MoS_2	PMS Pb MoS_2
1.0	PMS Pb Mo	PMS	PMS Pb MoS_2	PMS Pb MoS_2
Pb S	7.5	8.0	8.5	9.0

Table 4.1 **Phase composition as determined by x-ray powder diffraction for the eight samples fabricated.**

The stoichiometric sample is single phase, and second phase impurities are introduced for all other compositions. The amounts of the second phase impurities increases systematically with the addition of excess sulphur and lead.

4.4.2 Ac. Resistance and Susceptibility Measurements

In this section the results of the ac. resistance and ac. susceptibility measurements will be presented for the eight samples fabricated.

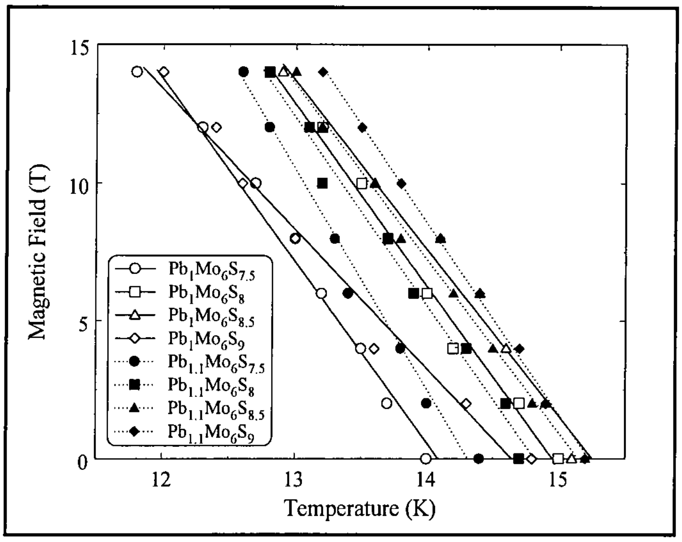

Figure 4.10 Onset of the resistive transition for the eight samples at various fields allowing the determination of dB^*_{C2}/dT and $B^*_{C2}(0K)$

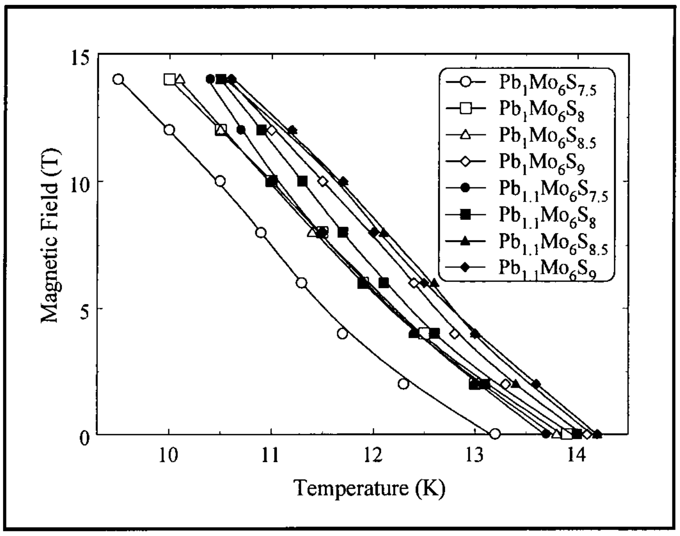

Figure 4.11 Zero resistance point for the eight samples as a function of magnetic field.

The onset of the resistivity transition for each of the samples as a function of dc field is shown in figure 4.10. It can be seen that the gradients of the line are all similar with the exception of $Pb_1Mo_6S_9$ which has a smaller slope than the others. The zero resistance point is shown as a function of magnetic field for all eight samples in figure 4.11. The trend in T_C in figure 4.11 shows increasing the lead content increases T_C for all sulphur contents fabricated. The resistivity measurement is not considered to give a good representation of the bulk of the sample as it only requires a percolative path to show zero resistance. Ac. susceptibility measurements measure the bulk of the material and represent the average properties of the material. The onset of the susceptibility transition is considered to occur when the grains become superconducting and the shape of the transition and the peak in the loss component is considered to be indicative of the properties of the grain boundaries within the material.

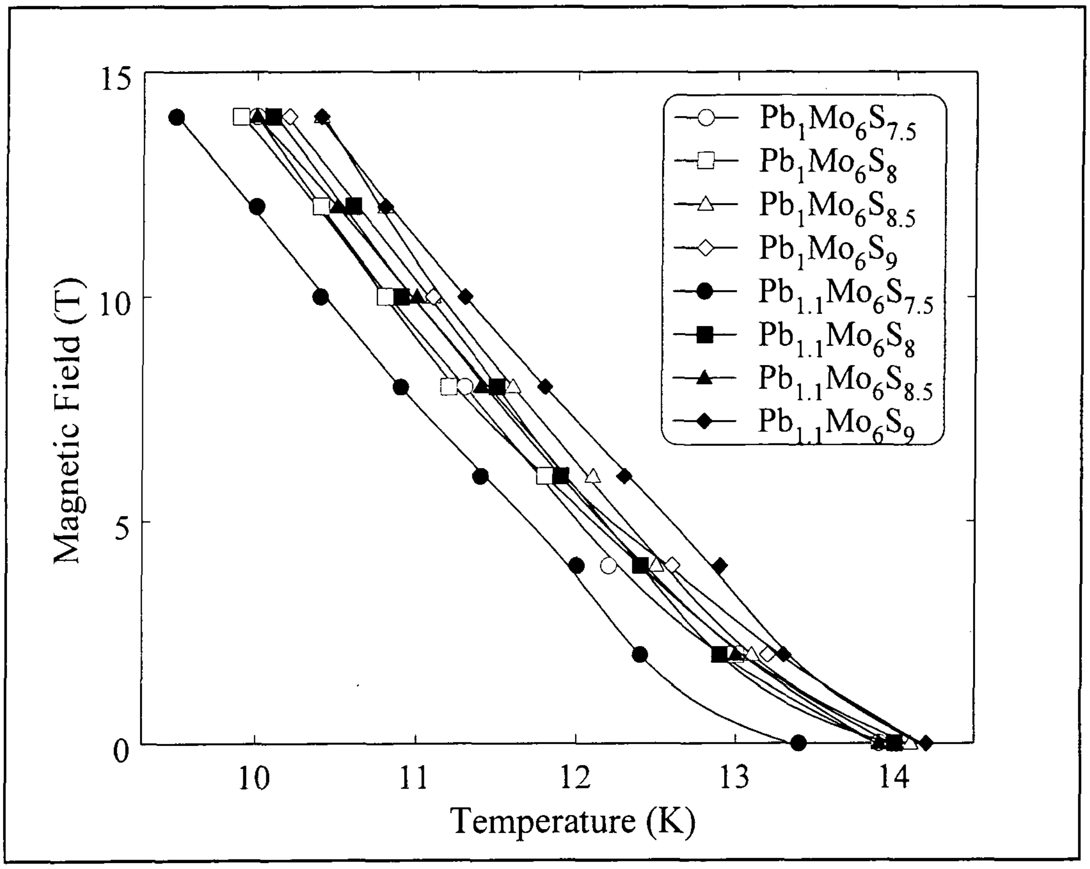

Figure 4.12 **Onset of the susceptibility transition showing the average properties of all the grains.**

It can be seen from figure 4.12 that there is a variation across the whole range of stoichiometries studied of less than 1K for all magnetic fields, with the field dependence being approximately the same for all stoichiometries.

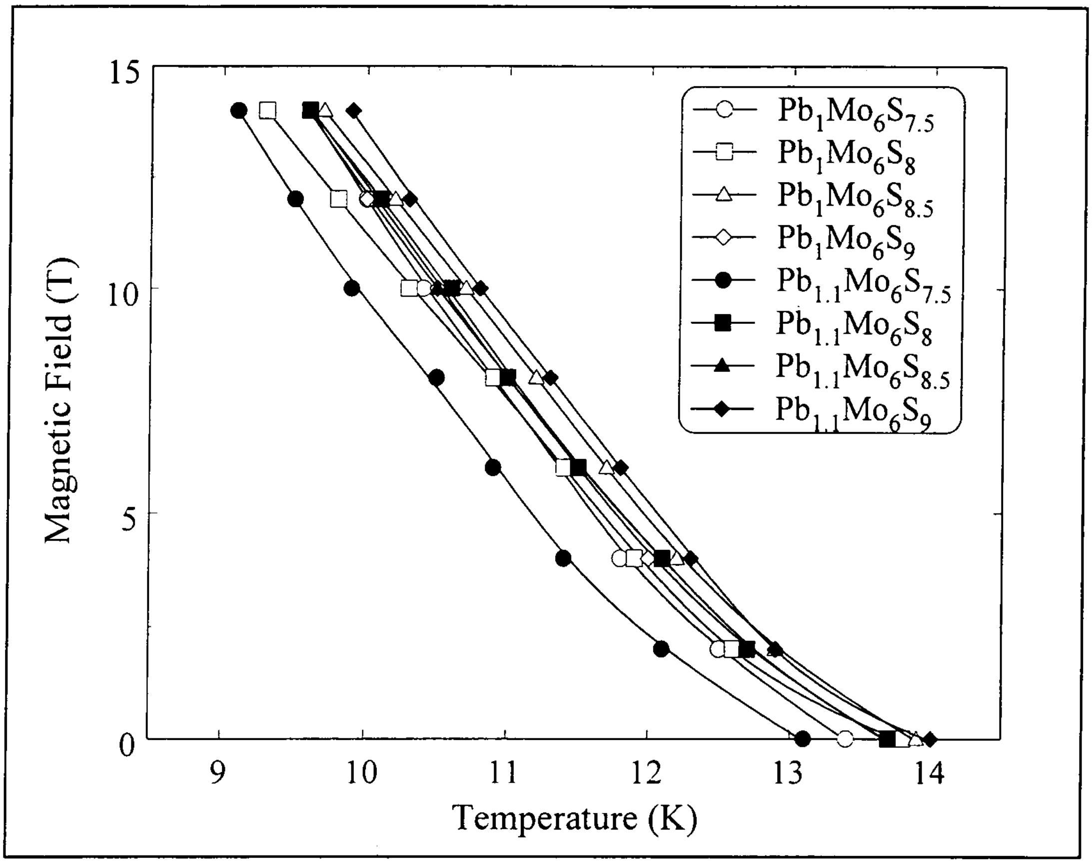

Figure 4.13 The magnetic phase diagram produced from the peak in the loss component of the susceptibility transition.

The results shown in figure 4.13 show the field dependence of the peak in the loss component. For all stoichiometries fabricated there is only a small variation in properties suggesting that the grain boundaries in all these materials are similar.

4.4.3 Dc Magnetisation Results

The results obtained from the dc magnetisation measurements will be presented in this section, allowing the comparison of critical current density, irreversibility field and upper critical field for the all the samples fabricated.

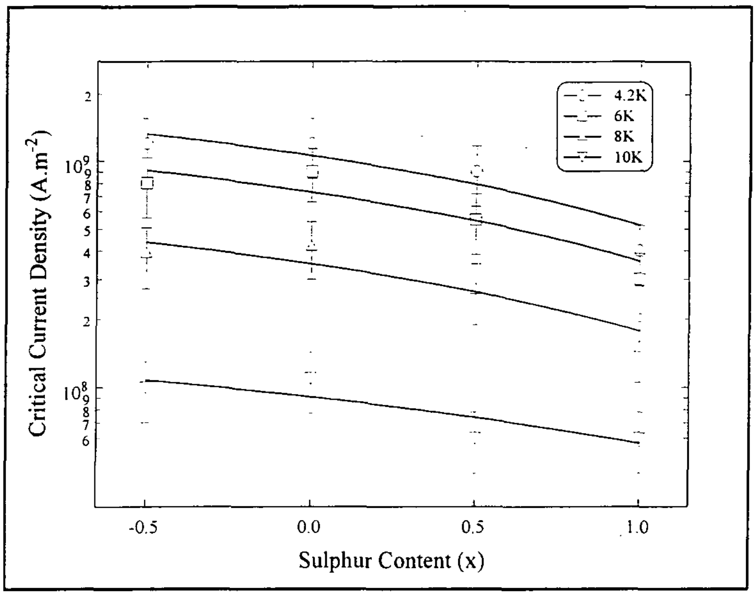

Figure 4.14 **The critical current density measured at 2T as a function of sulphur content for the stoichiometric lead samples at 4 temperatures from 4.2 K to 10 K.**

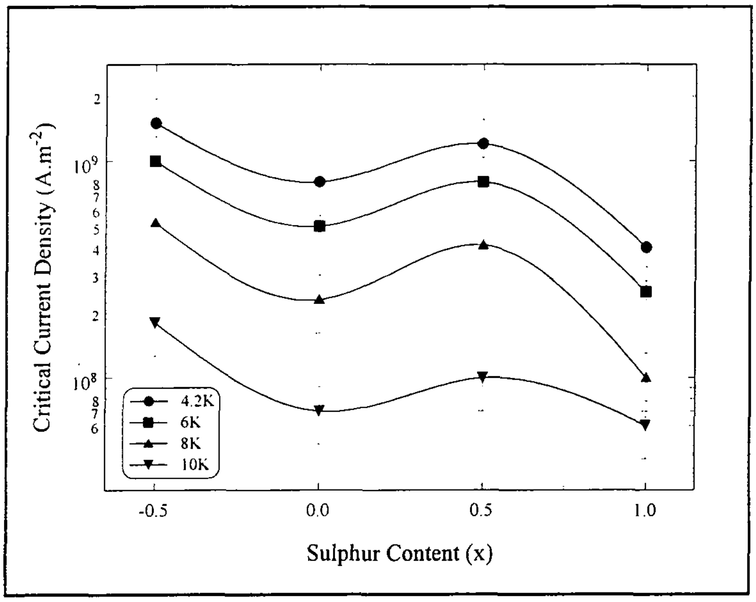

Figure 4.15 **The critical current density measured at 2T as a function of sulphur content for the lead rich samples at 4 temperatures from 4.2 K to 10 K. The lines are intended as guides to the eye.**

The critical current density is the first property to be investigated. Figure 4.14 shows the variation with sulphur content for the stoichiometric lead samples. The values for the stoichiometric sample at the temperatures shown have been determined from values at intermediate temperatures due to differing thermometry calibrations at the time of measurement. The values were taken at 2T and the lines are a linear fit for each temperature, showing a decreasing trend in J_C with increasing sulphur content.

For the lead rich samples the critical current density showed no systematic variation with sulphur content as shown in figure 4.15, again the values are at 2T, and the variations with sulphur content are almost a factor of 3. By a comparison of figure 4.14 and figure 4.15 it can be seen that for $Pb_{1+y}Mo_6S_8$ increasing the lead content decreases J_C whilst for $Pb_{1+y}Mo_6S_{7.5}$ and $Pb_{1+y}Mo_6S_{8.5}$ increasing the lead content increases J_C. For $Pb_{1+y}Mo_6S_9$ the variation with y in J_C is within the uncertainty of the measurement.

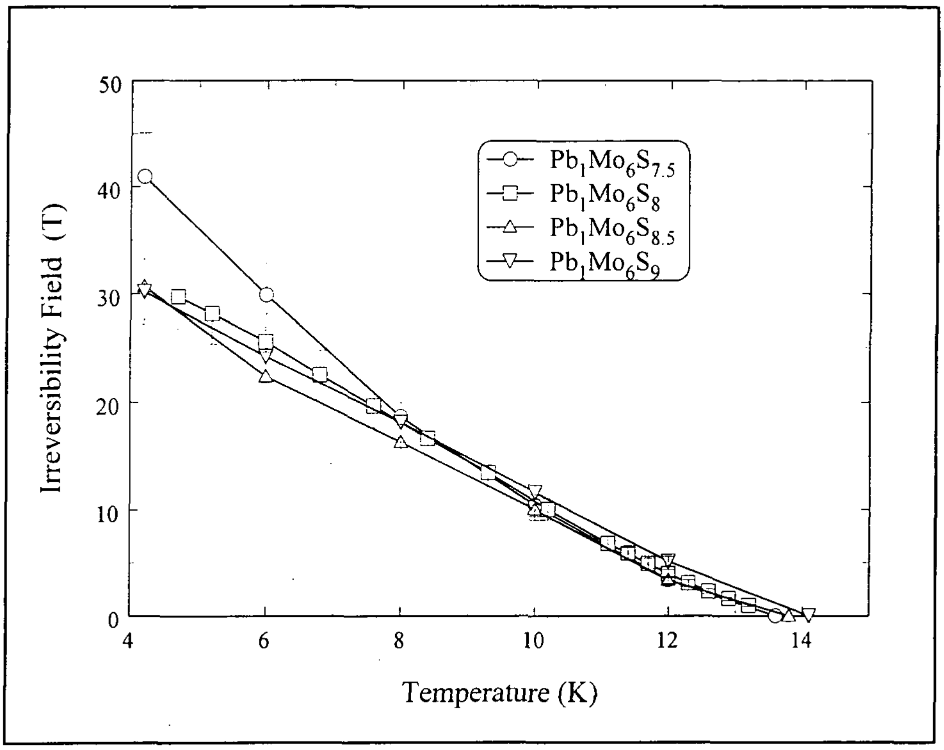

Figure 4.16 Irreversibility fields determined from the extrapolation of Kramer plots for the stoichiometric lead samples.

The irreversibility fields, determined by extrapolation of the Kramer plots, are important parameters for the possible applications of superconductors as they represent the point at which the critical current density falls to zero. The values for the stoichiometric lead samples are shown in figure 4.16, where the error bars are determined from the estimated error on the gradient used for the extrapolation. It can be seen the distribution in values for the various sulphur contents is within the experimental error of the measurement except at lower temperatures when the sulphur deficient sample has a higher value.

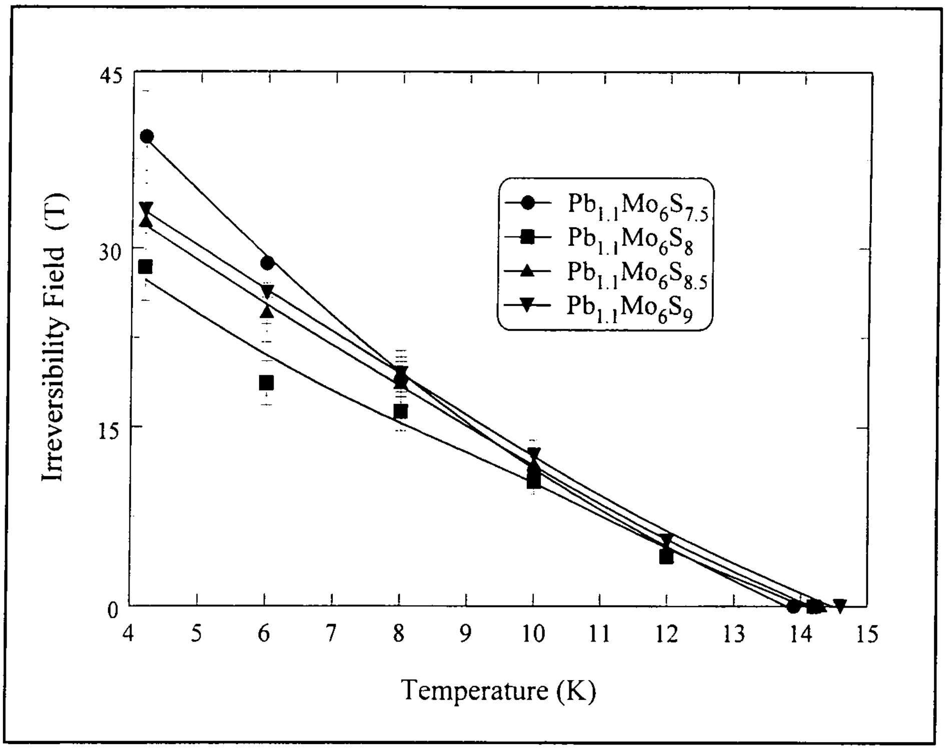

Figure 4.17 Irreversibility fields determined from the extrapolation of Kramer plots for the lead rich samples.

For the lead rich samples shown in figure 4.17 the uncertainty in the measurement prevents the samples being distinguished except at low temperatures where the sulphur deficient sample has a higher irreversibility field than the stoichiometric sulphur sample. Next the upper critical fields determined from the magnetisation measurements will be presented. The values are taken as the point at which the reversible magnetisation curve falls onto a background, determined from a measurement just above T_C. This was not possible for the sample $Pb_{1.1}Mo_6S_8$ as the background was not reproducible.

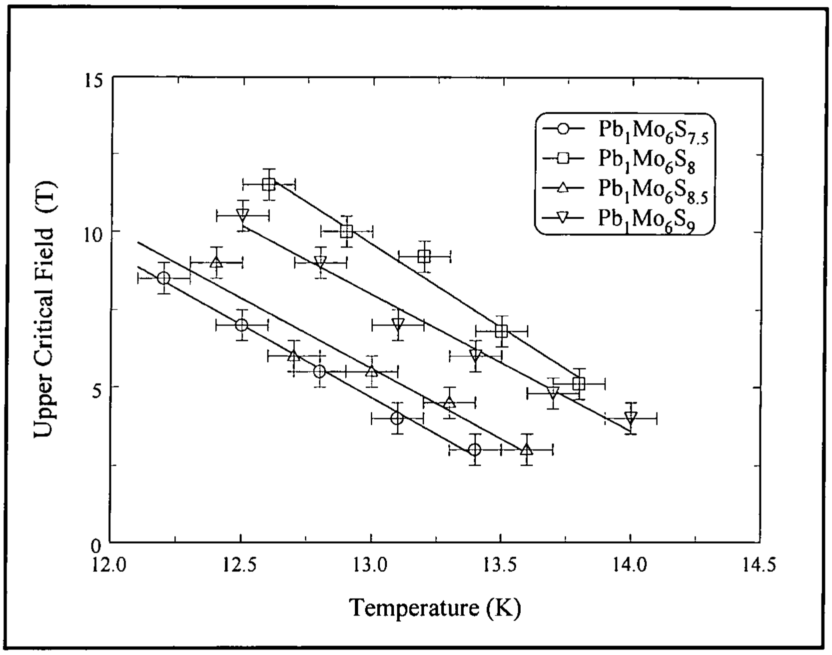

Figure 4.18 Upper critical fields determined from magnetisation curves for the samples of stoichiometry $Pb_1Mo_6S_{8+x}$.

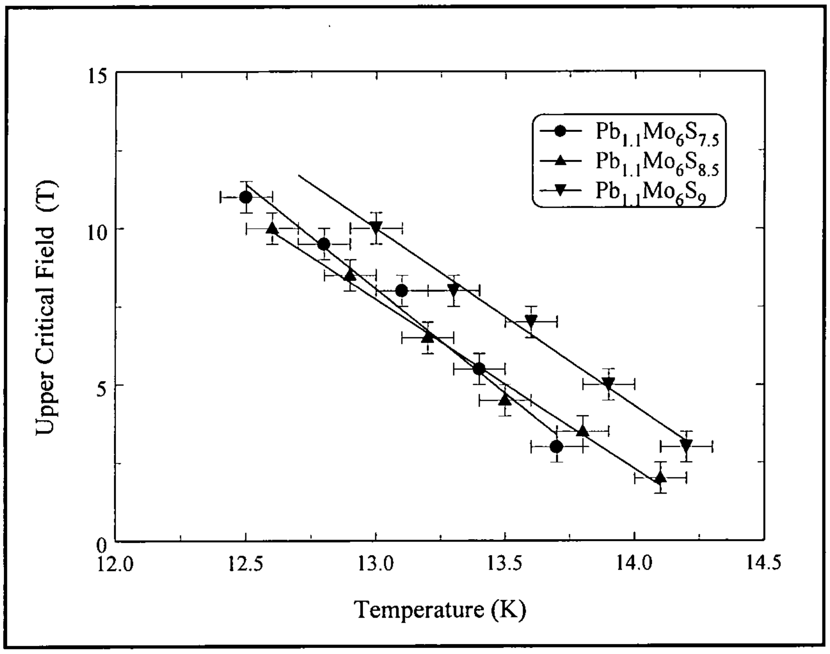

Figure 4.19 Upper critical fields determined from magnetisation curves for the samples of stoichiometry $Pb_{1.1}Mo_6S_{8+x}$.

The first set of upper critical fields are for the stoichiometric lead samples, shown in figure 4.18 and show no systematic trend for varying sulphur contents. The highest values are obtained for the single phase stoichiometric sample. For the lead rich samples, the upper critical fields shown in figure 4.19 show no systematic trend with sulphur content, however the lead rich samples do have higher upper critical fields than the stoichiometric samples for all sulphur compositions in this study.

4.4.4 Summary of Electromagnetic Properties

The variety of measurements performed on each of the samples allow a comparison to be made between different techniques of measurement. The variation with stoichiometry of the field dependence of the critical temperature has been determined from four different techniques. The onset of the resistive transition is considered to represent the upper critical field of the sample**[8]** which can also be determined from the dc magnetisation measurement. The loss susceptibility peak is considered to be indicative of the irreversibility field**[9]**, the point at which the critical current density falls to zero, which can also be determined from the extrapolation of the Kramer plots to zero.

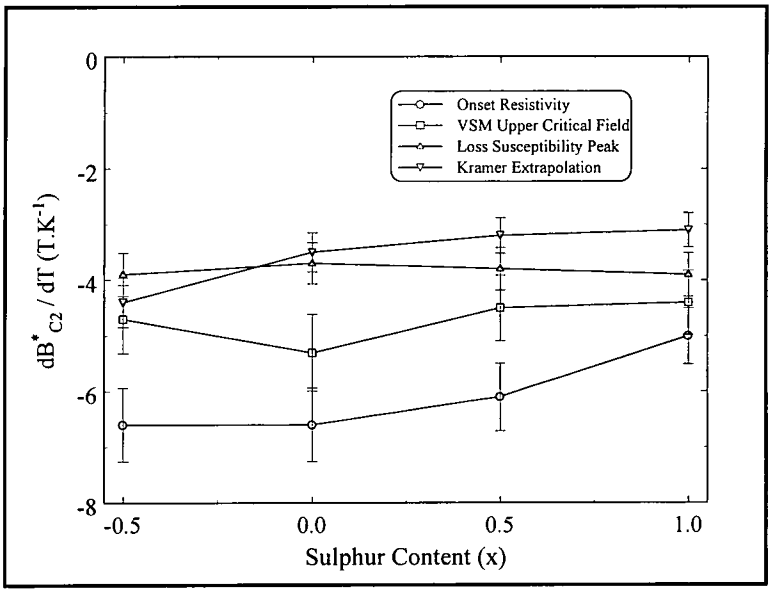

Figure 4.20 **dB^*_{C2}/dT as a function of stoichiometry, as determined from ac. resistivity, ac. susceptibility and dc magnetisation measurements for $Pb_1Mo_6S_{8+x}$**

Firstly considering the stoichiometric lead samples for the four sulphur contents investigated. Figure 4.20 shows the variation with stoichiometry of the field dependence of the critical temperature measured by the four techniques mentioned above. It can be seen that the values obtained by resistivity onset and dc magnetisation are comparable, and that the values obtained from the Kramer extrapolation and the loss peaks are also comparable. The average values for dB^*_{C2} / dT determined by the various techniques are $-6T.K^{-1}\pm0.6T.K^{-1}$ from the resistivity onset, $-4.7T.K^{-1}\pm0.6T.K^{-1}$ from the VSM measurements, and $-3.8T.K^{-1}\pm0.4T.K^{-1}$ from both the loss susceptibility peaks and the Kramer extrapolations.

The trend with increasing sulphur content across the range studied for the resistivity onset determined values of dB^*_{C2}/dT is $+1.0T.K^{-1}(\text{sulphur atom})^{-1}\pm1.0T.K^{-1}(\text{sulphur atom})^{-1}$, for the VSM determined values is $+0.3T.K^{-1}(\text{sulphur atom})^{-1}\pm0.6T.K^{-1}(\text{sulphur atom})^{-1}$, for loss peak determined values is $0T.K^{-1}(\text{sulphur atom})^{-1}\pm0.47T.K^{-1}(\text{sulphur atom})^{-1}$ and for the Kramer extrapolation determined values is $+0.6T.K^{-1}(\text{sulphur atom})^{-1}\pm0.6T.K^{-1}(\text{sulphur atom})^{-1}$.

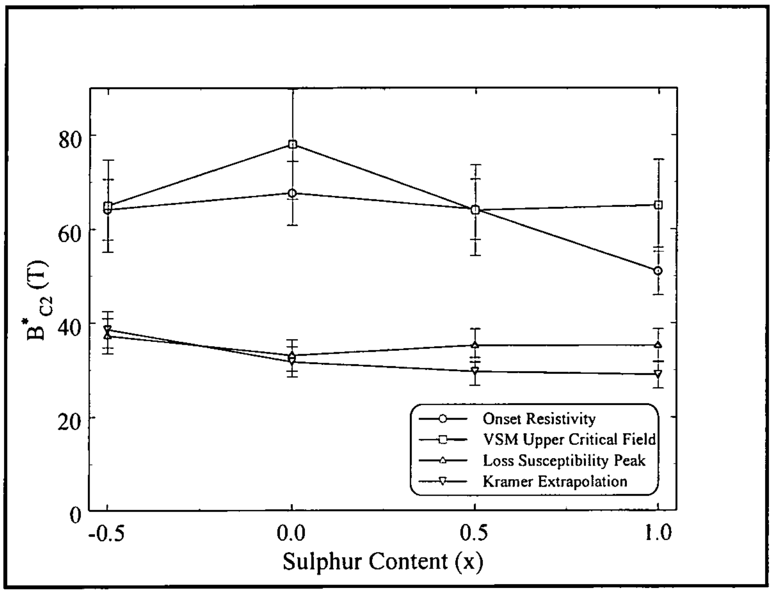

Figure 4.21 **The upper critical field extrapolated using WHH dirty limit[10] as a function of stoichiometry, determined from ac. resistivity, ac. susceptibility and dc magnetisation measurement for $Pb_1Mo_6S_{8+x}$**

From the values of dB^*_{C2} / dT shown in figure 8.20 it is possible to determine values for $B^*_{C2}(0)$ using an expression derived from WHH theory[10] for a dirty superconductor that states:

$$B_{C2}(0) = 0.69T_C\left[\frac{dB_{C2}(T)}{dT}\right]_{T = T_C} \qquad (5)$$

The values shown in figure 4.21 are calculated using equation 4.5 and the values for each of the measurement techniques shown in figure 4.20. The validity of applying equation 4.5 to the values obtained from the loss peaks and the Kramer extrapolations is uncertain as equation 4.5 was derived as a result for the thermodynamic upper critical field, and not for the irreversibility field. The values are calculated to allow a direct comparison of the four techniques without the introduction of a different extrapolation technique. For the resistivity onset measurement the average value is 62T±7T and for the VSM measurement the average value is 68T±9T. Both of these values are considered to represent the upper critical field for the samples. The average value calculated from the loss peaks is 35T±4T and from the Kramer extrapolations is 33T±4T.

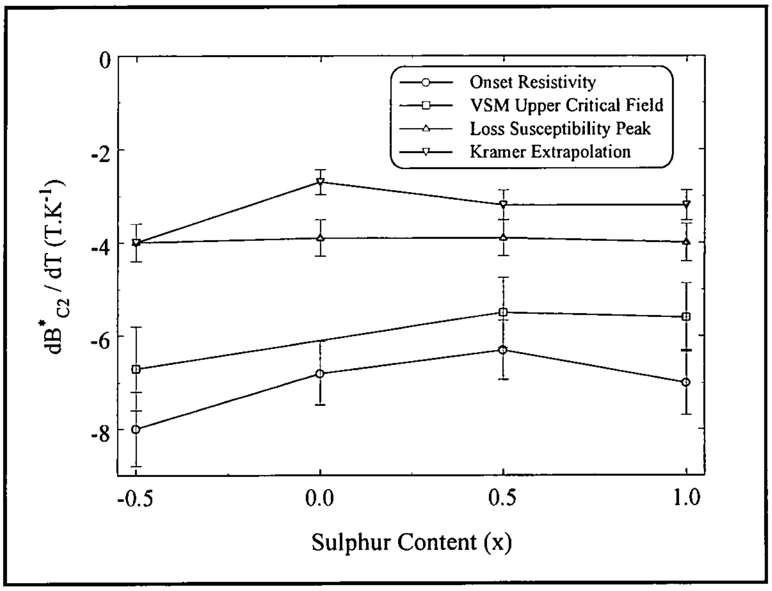

Figure 4.22 **dB^*_{C2}/dT, as a function of stoichiometry determined from resistivity, susceptibility and dc magnetisation measurements for $Pb_{1.1}Mo_6S_{8+x}$**

Now repeating the analysis on the lead rich samples, again for four sulphur contents. Figure 4.22 shows the variation with stoichiometry of the field dependence of the critical temperature again measured by four techniques. It can be seen that the values obtained by resistivity onset and dc magnetisation are comparable, and that the values obtained from the Kramer extrapolation and the loss peaks are also comparable. The average values for dB^*_{C2}/dT determined by the various techniques are $-7T.K^{-1}\pm0.7T.K^{-1}$ from the resistivity onset, $-5.9T.K^{-1}\pm0.8T.K^{-1}$ from the VSM measurements, $-4.0T.K^{-1}\pm0.4T.K^{-1}$ from the loss susceptibility peaks and $-3.3T.K^{-1}\pm0.4T.K^{-1}$ from the Kramer extrapolations.

The trend with increasing sulphur content across the range studied for the resistivity onset determined values of dB^*_{C2}/dT is $+0.47T.K^{-1}(\text{sulphur atom})^{-1}\pm0.87T.K^{-1}(\text{sulphur atom})^{-1}$, for the VSM determined values is $+0.6T.K^{-1}(\text{sulphur atom})^{-1}\pm1.0T.K^{-1}(\text{sulphur atom})^{-1}$, for loss peak determined values is $0T.K^{-1}\pm0.47T.K^{-1}(\text{sulphur atom})^{-1}$ and for the Kramer extrapolation determined values is $+0.4T.K^{-1}(\text{sulphur atom})^{-1}\pm0.4T.K^{-1}(\text{sulphur atom})^{-1}$.

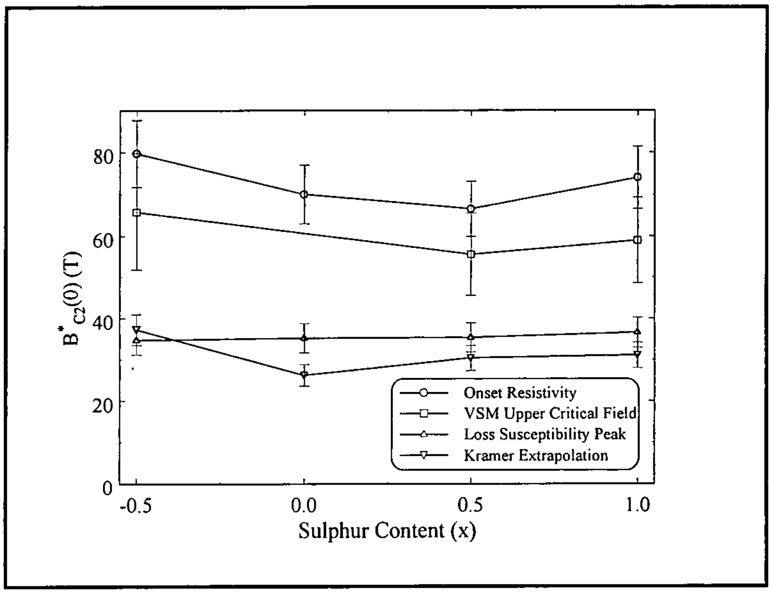

Figure 4.23 The upper critical field extrapolated using WHH dirty limit[10] as a function of stoichiometry for $Pb_{1.1}Mo_6S_{8+x}$

The values shown in figure 4.23 are calculated using equation 4.5 and the values for each of the measurement techniques shown in figure 4.22. For the resistivity onset measurement the average value is 72T±7T and for the VSM measurement the average value is 60T±8T. Both of these values are considered to represent the upper critical field. The average value calculated from the loss peaks is 35T±4T and from the Kramer extrapolations is 31T±4T.

4.5 Discussion

The superconducting properties of lead molybdenum sulphide are known to be affected by both oxygen content[**11**] and stoichiometry [**1-3**]. The effect of oxygen was found to be detrimental to the superconducting properties, however variations with stoichiometry were found to improve the critical temperature. The effect of stoichiometry on various properties of PMS has been investigated previously and the results of this study will be compared to the results in the literature for each in turn.

4.5.1 Phase Composition and Critical Temperatures

Krabbes et al investigated the phase diagram of PMS fabricated at 1250K under vacuum and found that the single phase compound was formed within the compositional range for $Pb_yMo_6S_x$ where y varies between 0.9 and 1.1 and x varies between 7.6 and 7.9. They also measured the critical temperature and found that the high lead, high sulphur region of the samples investigated had the highest critical temperatures. The transition temperatures varied from 13K to 10K and had an average width of 1K.

Yamamoto et al fabricated samples at 1000°C under vacuum in the composition range $Pb_yMo_6S_x$ where y varies between 0.95 and 1.05 and x varies between 7.55 and 7.8. They found a single phase region around y = 0.9 to 1.05 and x = 7.55 to 7.8. They found that the critical temperature was increased by increasing the lead content and that the effect of sulphur content was dependent on the lead content. The samples fabricated had T_C's ranging from 11.4K to 15.5K with a transition width of up to 6.4K, determined using a four terminal resistance technique.

No mention is made in these first two papers of any attempts being made to control the oxygen contamination in the samples, which is known to cause variations in the superconducting properties of Chevrel phase compounds[**11**].

The first study performed where oxygen content was controlled was performed by Yamasaki et al who fabricated samples at 900°C under vacuum in the composition range $Pb_yMo_6S_x$ where y varies between 0.8 and 1.1 and x varies between 7.0 and 8.0. They found a single phase region around y = 0.9 to 1.0 and x = 7.4 to 7.6. They measured the critical temperature using an inductive technique and found broad transitions of over 6K width with an onset T_C of 13.9K. The samples were then annealed at 900°C for 48 hours under 150-200 Torr Ar gas, causing the transition to sharpen to a width of <0.25K, though the onset values were lower, around 13K. The critical temperature varied with stoichiometry from 11.65K to 13.7K with the highest values being found in the lead rich, sulphur rich region of the compositions investigated. The samples were handled in an inert argon atmosphere to reduce oxygen contamination, however the critical temperatures are low compared to oxygen free samples where the critical temperature is around 15K.

Of the samples fabricated in this study, only one was single phase by x-ray powder diffraction and this was the stoichiometric sample $Pb_1Mo_6S_8$, all other samples contained some second phase material. This is in contrast to the results of previous authors who found sulphur deficient samples to be single phase. This can be attributed to the oxygen substituting on to the sulphur sites in the previous studies, thus reducing the T_C's and reducing the sulphur required to produce single phase samples. The relative amounts of second phase materials in the samples fabricated in this study were systematic with the nominal composition.

The critical temperatures as determined from the onset of the resistive and susceptibility transitions varied from 14.0K to 15.3K and from 13.4K to 14.2K respectively across the range of stoichiometries investigated suggesting high quality samples with little or no oxygen contamination. The widths of the zero field transitions from the 10% value to the 90% value were small, for the resistive transition 0.4K, and for the susceptibility 0.5K, again indicative of high quality samples.

4.5.2. Upper Critical Fields

There are numerous ways to determine the upper critical field of superconductors. The most common are heat capacity measurements, magnetisation measurements and ac. resistivity measurements. The upper critical field for PMS has been measured previously using heat capacity measurements**[12]**, giving values of between 55T and 58T, with values for dB^*_{C2}/dT of between $-5.5T.K^{-1}$ and $-6.0T.K^{-1}$. Dc magnetisation measurements for the upper critical fields have given values of 56T for $B^*_{C2}(0)$ and $-5.8T.K^{-1}$ for dB^*_{C2}/dT**[13]**. Early resistivity measurements have given values of between 36T and 45T for $B^*_{C2}(0)$ and $-5.7T.K^{-1}$ for dB^*_{C2}/dT.

In this study the average values obtained for dB^*_{C2}/dT for the lead rich samples were $-7.0T.K^{-1}\pm0.7T.K^{-1}$ by resistivity onset and $-5.9T.K^{-1}\pm0.8T.K^{-1}$ from magnetisation measurements which are higher than the average values for the stoichiometric lead samples with values of $-6.0T.K^{-1}\pm0.6T.K^{-1}$ by resistivity onset and $-4.7T.K^{-1}\pm0.6T.K^{-1}$ from magnetisation measurements. There is a weak trend of increasing values of dB^*_{C2}/dT with increasing sulphur content for both lead contents of $+0.6T.K^{-1}$(sulphur atom)$^{-1}\pm0.87T.K^{-1}$(sulphur atom)$^{-1}$ across the range of sulphur contents studied.

The values of the upper critical fields for the stoichiometries measured range between 62T±7T and 72T±7T and the variations with both lead and sulphur content are within the experimental uncertainty on the measurements suggesting all the samples are high quality regardless of the amount of second phase impurities present.

4.5.3 Irreversibility Fields

The irreversibility field has been observed in PMS to be well below the upper critical field**[13][14]** and is found to give values of between 30 and 35T**[15]** at zero Kelvin. The irreversibility field is a limiting factor for the applications of materials as above this field a lossless current can no longer flow. The irreversibility field as discussed in section 2.5.3 is the field at which the critical current density falls to zero and can therefore be determined by the extrapolation of the Kramer plots to zero. Another measurement thought to represent the irreversibility field is the peak in the loss component of a susceptibility measurement**[9]** and both of these techniques for determining the irreversibility field have been used in this study.

The irreversibility fields, derived from both the extrapolations of the Kramer plots and the peaks in the loss components give average values of between 31T and 35T for all the samples studied, and variations with sulphur and lead content are within the experimental error on the measurement. The variation in values determined for dB^*_{C2}/dT with lead content is within the errors on the measurement and have a weak dependence on sulphur content of +0.3T.K^{-1}±0.6T.K^{-1}(sulphur atom)$^{-1}$. The average value across all compositions is -3.7T.K^{-1}±0.5T.K^{-1}, which can be compared with values in the literature varying from -2.9T.K^{-1} for unHIP'ed samples[16] to -6.0T.K^{-1} for hot pressed materials[17], with values for HIP'ed bulk samples being -3.7T.K^{-1}[13][17].

4.5.4 Critical Current Densities

The critical current density of Chevrel phase materials is the limiting factor preventing the use of this class of materials for high field applications. Previous work on the effect of stoichiometry on critical current density in bulk unHIP'ed samples has found that increasing the lead content can increase the critical current density[18]. In other work on wires it was also found that increasing the lead content could increase the critical current density[19]. This has been attributed to the additional lead improving the connectivity between the grains.[19].

The results of the previous section show that the effect of additional lead is dependent on the sulphur content of the samples, with additional lead increasing the critical current densities for $Pb_yMo_6S_{7.5}$ and $Pb_yMo_6S_{8.5}$. For $Pb_yMo_6S_9$ the variation with lead content is within the errors on the measurement and for $Pb_yMo_6S_8$ additional lead decreases the critical current density. Variations of more than a factor 3 being seen in the lead rich samples for different sulphur content and a decreasing trend in J_C being seen in stoichiometric lead samples with increasing sulphur content. Values of the critical current density for bulk PMS have been previously measured. Karasik et al[20] measured values between 4x10^{8}Am^{-2} and 1.0x10^{9}Am^{-2} at 4.2K and 2T depending on heat treatment for hot pressed samples. Cattani et al[16] measured values of 2.5x10^{8}Am^{-2} at 4.2K and 2T also for hot pressed samples. Gupta et al[17] found that for HIP'ed bulk samples $J_C \approx$ 3x10^{8}Am^{-2} at 5.5K and 8T, while values for hot pressed samples were around 2x10^{8}Am^{-2} depending on the pressing temperature. Zheng et al found a value of 6x10^{8}Am^{-2} at 4.2K and 2T also for HIP'ed bulk samples.

For the samples in this study values for the critical current density varied between 4x10^{8}Am^{-2} and 1.5x10^{9}Am^{-2} at 4.2K and 2T depending on stoichiometry which are within the range of values in the literature for high quality bulk samples.

4.5.5 Summary

All of the data presented in this chapter are consistent with high quality samples measured in the literature. The quite large range of stoichiometries investigated has shown that the single phase sample is not considerably different in properties from the samples containing second phase materials and that across all the compositions studied, the superconducting properties are all within the expected values for high quality material, suggesting second phase impurities do not significantly degrade the superconducting properties. This is in contrast to the reports of Selvam et al**[21]**on hot pressed samples who state that second phases degrade the critical current density and that highest T_C comes from stoichiometric composition.

4.6 Conclusions

The aim of this study was to investigate the effect of stoichiometry on the superconducting properties, including T_C, B_{C2}, J_C and B_{IRR} in samples that were fabricated so as to avoid contamination with oxygen. The samples were all hot isostatically pressed as this produces samples with higher critical current densities than sintering alone. Previous studies in bulk samples have investigated only the variation in critical temperature of unHIP'ed material with stoichiometry, and have not considered hot isostatically pressed samples.

Eight samples have been fabricated using a hot isostatic press across a range of stoichiometries described by $Pb_{1+y}Mo_6S_{8+x}$ where y = 0 or 0.1 and x = -0.5, 0.0, 0.5 and 1.0. The stoichiometric composition gives a single phase sample by x-ray and systematic increases in the second phases of MoS_2, Mo and Pb are seen for other compositions. The samples are all of high quality, having onset T_C's in the range of 14.0 K to 15.2 K, upper critical fields at zero Kelvin of approximately 60T±10T and irreversibility field at zero Kelvin, of 32T±3T. The critical current densities for all the samples are also within the range of values in the literature for high quality bulk samples with values between $4\times10^8Am^{-2}$ and $1.5\times10^9Am^{-2}$ at 4.2K and 2T. The Chevrel phase superconductor $Pb_{1+y}Mo_6S_{8+x}$ is reasonably sensitive to variations in stoichiometry or second phase impurities and some trends have been experimentally measured for samples fabricated at 2000 bar.

4.7 References

[1] Krabbes G and Opperman H *Crys. Res. and Tech.* **16** 777 (1981)

[2] Yamamoto S, Wakihara M, and Taniguchi M *Mat. Res. Bull.* **20** 1493 (1985)

[3] Yamasaki H and Kimura Y *Mat. Res. Bull.* **21** 125 (1986)

[4] Ramsbottom H D and Hampshire D P *Physica C* **274** 295 (1997)

[5] Bean C P *Rev. Mod. Phys.* **36** 31 (1964)

[6] Kramer E J *J. Appl. Phys.* **44** 1360 (1973).

[7] Dew-Hughes D *Phil. Mag.* **30** 293 (1974)

[8] Gupta A, Decroux M, Willis T C and Fischer O *Physica C* **235-240** 2541 (1994)

[9] Ramakrishman S, Kumar R, Paulose P L, Grover A K and Chaddah P *Phys. Rev. B* **44** 9514 (1991)

[10] Werthamer N R, Hefland E and Hohenberg P C *Phys. Rev.* **147** 295 (1966)

[11] Foner S, McNiff Jr E J and Hinks D G *Phys. Rev. B.* **31** 6108 (1985)

[12] Cors J, Cattani D, Decroux M, Stettler A and Fischer O *Presented at LTR-19, Brighton, UK.*(1990)

[13] Zheng D N, Ramsbottom H D and Hampshire D P *Phys. Rev. B* **52** 12931 (1995)

[14] Rossel C, Sandvold E, Sergent M, Chevrel R and Potel M *Physica C* **165** 233 (1990)

[15] Decroux M, Selvam P, Cors J, Seeber B, Fischer O, Chevrel R, Rabiller P and Sergent M *IEEE Trans. on Appl. Supercon.* **3** 1502 (1993)

[16] Cattani D, Cors J, Decroux M and Fischer O *IEEE Trans. on Magn.* **27** 950 (1991)

[17] Gupta A, Decroux M, Selvam P, Cattani D, Willis T C and Fischer O *Physica C* **234** 219 (1994)

[18] Alekseevskii N E, Dobrovol'skii N M, Eckert D and Tsebro V I *J. Low Temp. Phys.* **29** 565 (1977)

[19] Yamasaki H and Kimura Y *MRS Int'l Mtg on Adv. Mats.* **6** 109 (1989)

[20] Karasik V R, Karyaev E V, Rikel M O and Tsebro V I *Sov. Phys. JETP* **56** 881 (1982)

[21] Selvam P, Cattani D, Cors J Decroux M, Junod A, Niedermann Ph, Ritter S and Fischer O *J. Appl. Phys.* **72** 4232 (1992)

Chapter 5
An Investigation of the Peak Effect in the Chevrel Phase Superconductor Tin Molybdenum Sulphide.

5.1 Introduction

In this chapter, the high field properties of $SnMo_6S_8$ will be studied in detail. In particular the dependence of the critical current density on field will be investigated as $SnMo_6S_8$ is known to exhibit the Peak Effect, i.e. an increase in critical current density with increasing applied field, discussed in more detail in section 3.5.3. Understanding the mechanism causing this increase in flux pinning with increasing field may give the possibility of increasing the critical current density in other materials, including Chevrel phase and high T_C superconductors, for high field applications.

Kramer investigated the peak in the pinning force density**[1][2]**and found it to be a general phenomenon among superconducting materials that was dependent on microstructure. He proposed a parameterisation of the pinning force (F_P) of the form:

$$F_P(T) = \alpha . B_{C2}^{*\,n}(T) . b^{1/2} . (1-b)^2 \qquad \textbf{(1)}$$

where α is a scaling prefactor, n is determined experimentally and is approximately 2.5 and b is reduced magnetic field. In this work we parameterise the field and temperature dependence of the pinning force using Kramer's functional form over the whole field range, for temperatures from 4.2K to just below T_C.

In order to investigate the Peak Effect, a sample of $SnMo_6S_8$ was fabricated using a hot isostatic press, as described in section 5.2. The sample was then characterised using x-ray powder diffraction, performed by Dr C Lehmann of Durham University Chemistry Department. The author performed ac resistivity, ac susceptibility and dc magnetisation measurements. The details of the characterisation are described in section 5.3. From the dc magnetisation measurements, the critical current density was calculated using the Bean model**[3]** and from this the pinning force was deduced using:

$$F_P = J_C \times B \qquad \textbf{(2)}$$

The scaling of the pinning force as a function of temperature and magnetic field was then determined as is shown in section 5.3 and is discussed in section 5.4. This chapter is then summarised in section 5.5.

5.2 Sample Fabrication

A solid state sintering reaction route was chosen for the fabrication of this sample, with elemental starting materials being used to fabricate precursors where possible in order to reduce impurities. To avoid contamination with oxygen and water, all sample handling was performed in a glove box with water and oxygen content at less than 10 p.p.m. Also a molybdenum crucible, as described in chapter 6, was used for the high temperature reaction to avoid any contamination from the quartz tubing which is more usually used for these reactions.

To fabricate the precursors, molybdenum powder (< 8μm mesh, 99.95%) and sulphur chips (99.999%) were reacted to form MoS_2 using a heat treatment of:

$$Room\ Temperature \xrightarrow{400\,^{\circ}C/Hour} 450\,^{\circ}C \xrightarrow{6Hours} 450\,^{\circ}C$$

$$\xrightarrow{33\,^{\circ}C/Hour} 650\,^{\circ}C \xrightarrow{8Hours}$$

$$650\,^{\circ}C \xrightarrow{Furnace\ Cooled} Room\ Temperature$$

This reaction was performed inside evacuated quartz tubes inside a tube furnace under a continuous flow of argon gas. The precursors were then hand ground using a mortar and pestle for 30 minutes, combined with Sn(II)S (<8μm mesh, 99.5%) in the appropriate proportions, sealed in the molybdenum crucible and reacted at 1100°C for 24 hours in a tube furnace under a continuous flow of argon gas. The sample was then removed from the crucible, hand ground again for 30 minutes, pressed into pellets, wrapped in molybdenum foil and sealed under vacuum in a thin walled stainless steel tube. This billet was then hot isostatically pressed at 800°C and 2 kbar argon gas for 8 hours.

5.3 Experimental Characterisation

5.3.1 X-ray Powder *Diffraction*

The phase composition of the samples was determined using x-ray powder diffraction performed by Dr C Lehmann from The Department of Chemistry at Durham University. A small amount of the sample was ground to a fine powder and dispersed on a perspex sample holder. The measurements were performed using a Philips PW1050 with a graphite secondary monochromator using Cu K_α at 1.5418Å, produced by a HiltonBrooks Generator. The data was taken at 0.02 degree intervals, counting for 2 seconds at each step.

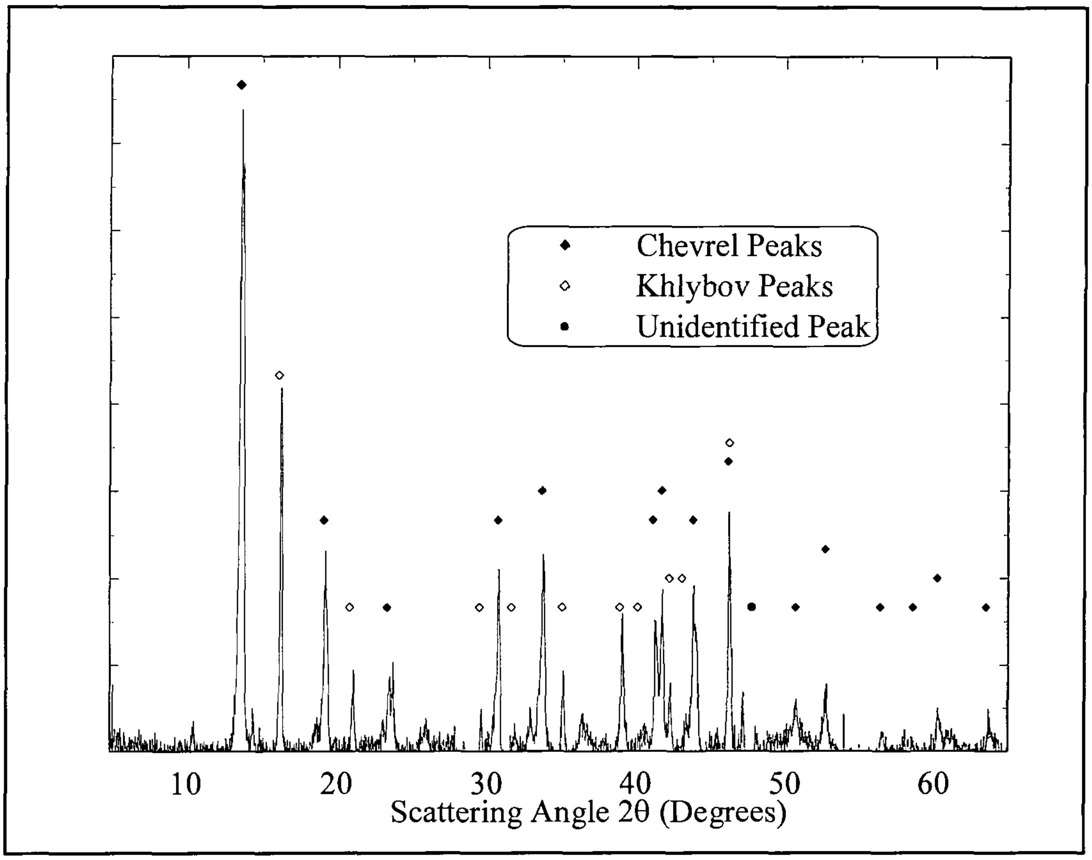

Figure 5.1 X-ray powder diffraction trace for $SnMo_6S_8$ after the subtraction of a background.

The samples were found to be predominantly $SnMo_6S_8$ in two structural phases, rhombohedral and monoclinic as identified by Chevrel[4] and Khlybov[5] respectively.

5.3.2 Ac Susceptibility and Ac Resistivity Measurements

In order to characterise the superconducting properties of the sample a study of its ac resistivity and ac susceptibility was performed. Measurements were performed as a function of temperature, from 5.5 K to $T>T_C$ in dc fields up to 14T using the system developed in-house. The temperatures are accurate to 0.1K and the fields to better than 0.1%. The ac resistivity values were determined using a standard 4 terminal technique, with an excitation current of 3.3mA at 76 Hz . For the ac susceptibility measurement, an ac field of approximately 100μT was used at a frequency of 330 Hz.

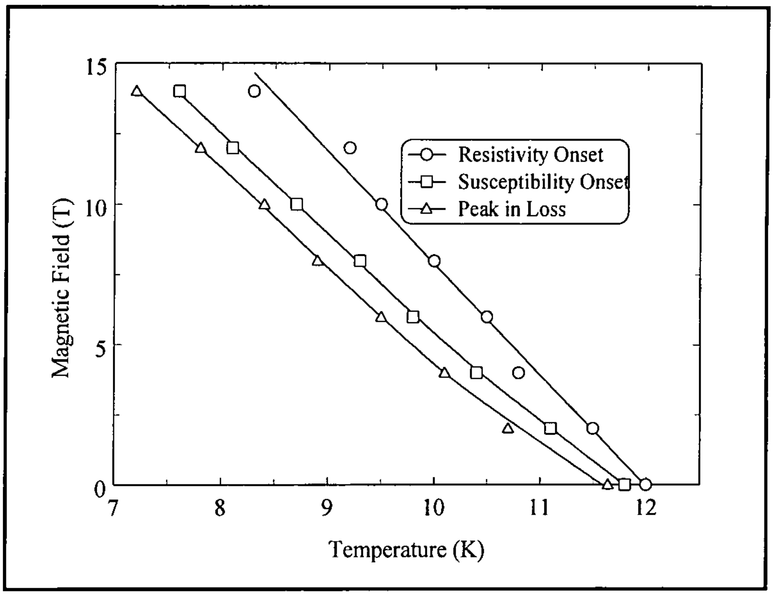

Figure 5.2 Magnetic phase diagram for $SnMo_6S_8$ determined using ac susceptibility and ac resistivity measurements.

The results are summarised in the magnetic phase diagram shown in figure 5.2. The transitions were sharp, with a width of 0.2K for the zero field susceptibility transition and 0.1K for the zero field resistive transition. The transitions were broadened to 0.4K for the 14T susceptibility transition and 0.3K for the 14T resistivity transition. The critical temperature measured for this sample, 11.8K from the onset of the susceptibility transition, is within the values found in the literature for $SnMo_6S_8$ fabricated without using an oxygen getter, i.e. 10.8 K to 13.66 K[**6**]. dB^*_{C2}/dT was determined to be $4T.K^{-1}$ from the onset of the resistivity transition and hence the upper critical field at zero Kelvin was calculated using:

$$B_{C2}(0) = 0.69T_C\left[\frac{dB_{C2}(T)}{dT}\right]_{T\,=\,T_C} \qquad (3)$$

derived from WHH theory for a dirty superconductor[7]. This gives a value for $B_{C2}(0)$ of 33T, again similar those found in the literature[8][9][10]. The normal state resistivity was found to be 440μΩ.cm at room temp and 15μΩ.cm just above T_c at T = 12K.

5.3.3 Dc Magnetisation Measurements

In order to determine the critical current density of the samples and the pinning force density, dc magnetisation measurements were performed using the vibrating sample magnetometer described in chapter 7. Magnetisation measurements were performed at temperatures from 4.2 K to above T_C in fields up to 11.6T at a sweep rate of 0.9T.min^{-1} for a sample of dimensions 5.55mm x 2.45mm x 1.88mm with the longest dimension parallel to the applied field.

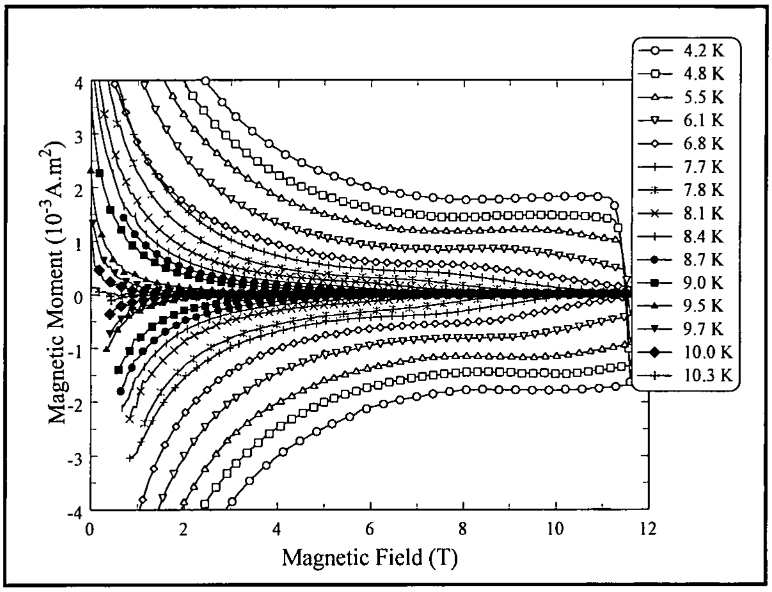

Figure 5.3 Magnetisation curves for $SnMo_6S_8$ for temperatures from 4.2K to 10.3K.

The magnetisation curves measured are shown in figure 5.3. Flux jumping has been removed from the data in the low field, low temperature measurement range and fewer data points are shown than were taken.

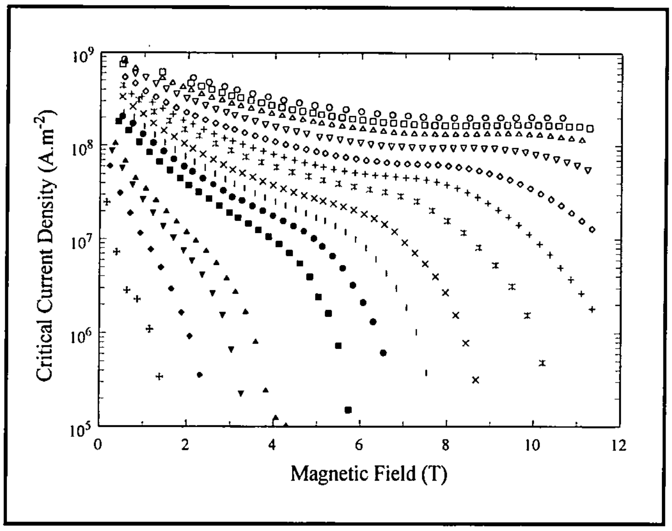

Figure 5.4 Critical current density for $SnMo_6S_8$ calculated from the magnetisation curves shown in figure 5.3, legend as in figure 5.3.

From Bean's critical state model [3], the size of the hysteresis(ΔM) was used to calculate the critical current density using the equation:

$$J_c = \frac{2\Delta M}{Volume.Thickness.\left(1 - \dfrac{Thickness}{3.Width}\right)} \qquad \textbf{(4)}$$

The critical current density is shown in figure 5.4, again more data points were taken than are shown.

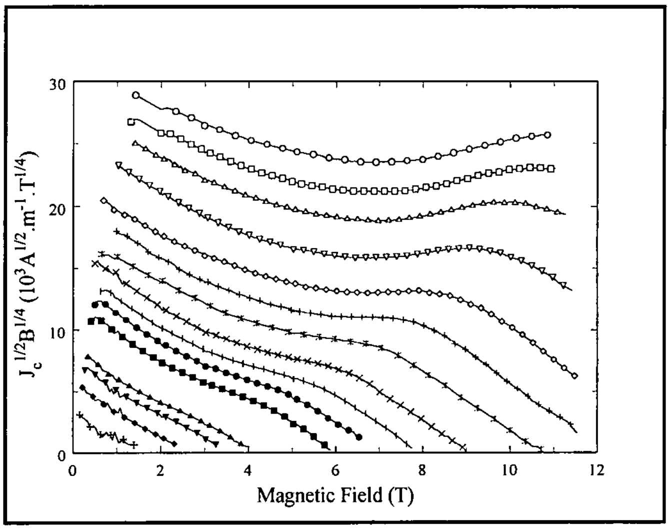

Figure 5.5 Kramer plots for $SnMo_6S_8$ calculated from the critical current density, legend as in figure 5.3.

Kramer plots are a useful tool in the analysis of the form of the critical current density. Considering again Kramer's analysis for the functional form of the pinning force:

$$F_P(T) = \alpha . B_{C2}^{*\,n}(T) . b^{1/2} . (1-b)^2 \qquad \textbf{(5)}$$

and knowing that:

$$F_P = J_C \times B \qquad \textbf{(6)}$$

it is possible to determine the validity of applying this model to the experimentally measured critical current density by plotting $J_C^{0.5} \times B^{0.25}$ against B. If the Kramer model is applicable then these plots, called Kramer plots, will be straight lines. This allows us to determine the region over which the Kramer model is valid. From figure 5.5 it can be seen that at low field for all temperatures the lines are straight. In the intermediate field range the lines deviate, the amount depending on the temperature, some even having positive gradient. As the upper critical field is approached, only possible in the measurements at higher temperatures, the lines become straight again. This suggests that the Kramer model for the pinning force is appropriate in two field regimes.

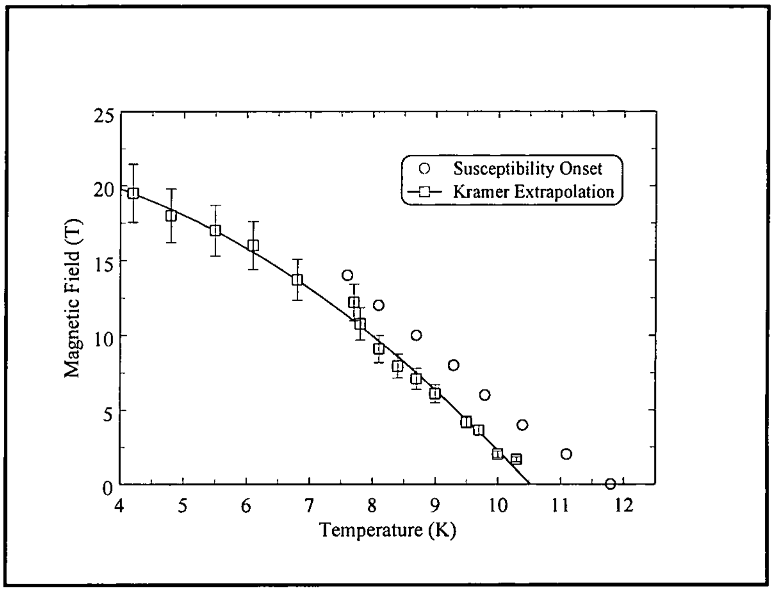

Figure 5.6 Irreversibility fields determined from extrapolations of the Kramer plots and the onset of the ac susceptibility transition. The solid line is a guide to the eye.

The high field straight lines were also extrapolated to $J_C^{0.5} \times B^{0.25} = 0$, allowing the determination of the irreversibility field. The values obtained are shown in figure 5.6 and are consistent with those determined from ac susceptibility measurements.

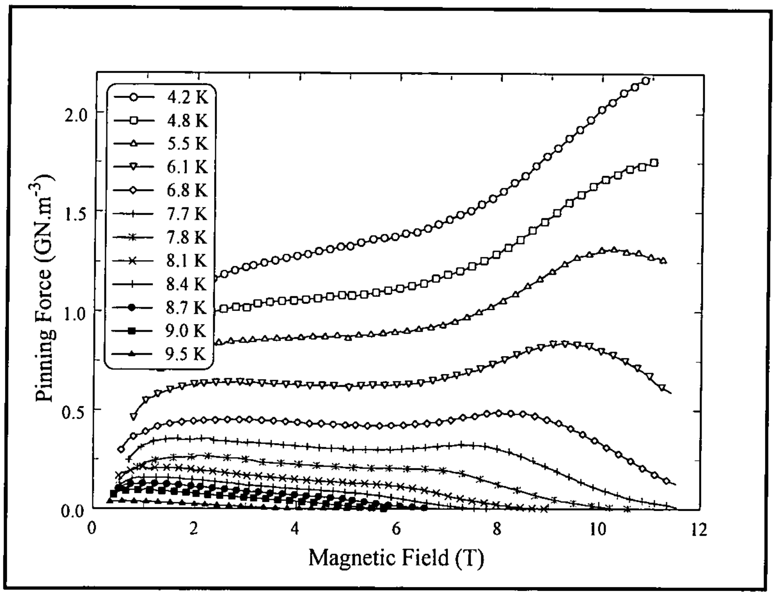

Figure 5.7 Pinning force density for $SnMo_6S_8$ for temperatures from 4.2K to 9.5K.

From the critical current density, the pinning force density can be calculated using equation 5.6 and is shown in figure 5.7. In this figure the increase in pinning with increasing field can clearly be seen and it is this that is named the Peak Effect. The relative strengths of the low field and the high field pinning can be seen to vary by approximately factor 4 with temperature. At 4.2K the high field pinning is approximately twice the strength of the low field pinning however at temperatures above 8K this situation is reversed, with the low field pinning being the stronger.

If the pinning force does indeed obey a scaling law, it is possible to reduce all the pinning force curves to a single functional form by normalising by the irreversibility field and the maximum pinning force. In the case of the pinning force shown in figure 5.7 it is clear that the pinning force cannot be scaled as a function of reduced field and reduced pinning force across the whole field and temperature range measured using a single scaling equation. Instead the pinning force has been scaled in two regions, low reduced field and high reduced field.

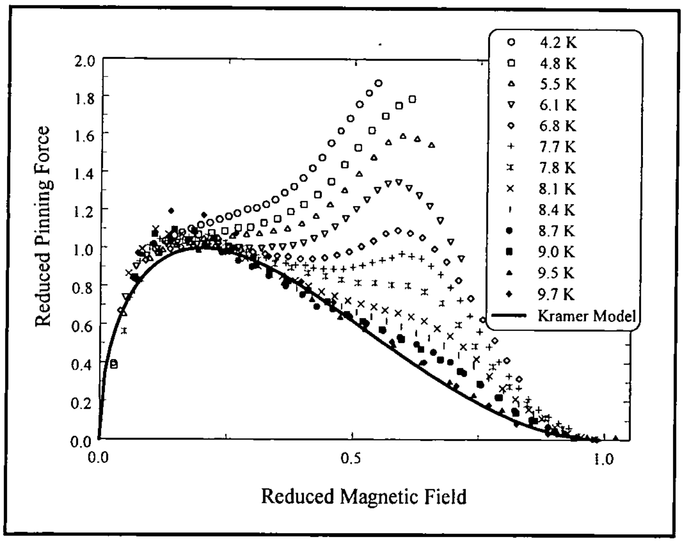

Figure 5.8 Scaling of the low reduced field pinning force using Kramer's scaling law

Firstly consider the low reduced field case, as shown in figure 5.8. The data has been normalised by the measured irreversibility field, and then scaled using the prefactor $(\alpha_L).(B^*_{c2})^n$ which is chosen so as to reduce all the pinning force curves to a single line at low reduced field. It can be seen that the Kramer functional form, shown as the solid line, represents the pinning force well at low reduced field, however the pinning force clearly does not scale with these parameters at high reduced field.

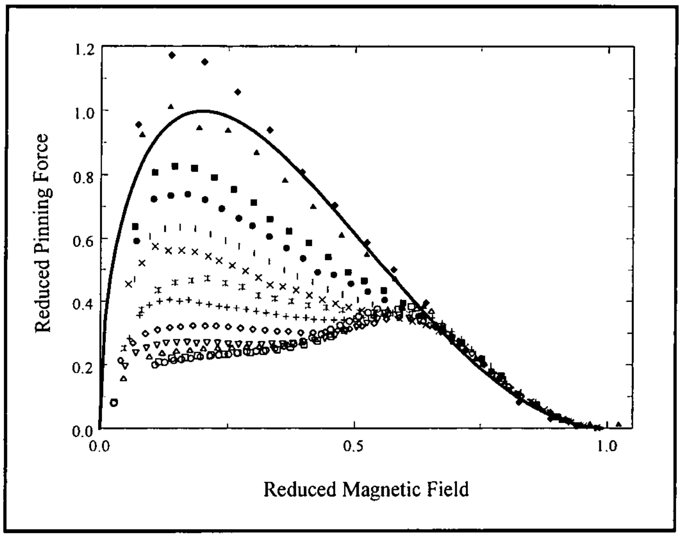

Figure 5.9 Scaling of the high reduced field pinning force using Kramer's scaling law, see figure 5.8 for legend.

It was found that the pinning force in the high reduced field region could also be reduced to a single curve using the same irreversibility fields as the low reduced field case but using a different prefactor $(\alpha_H).(B^*_{C2})^n$. It can be seen from figure 5.9 that the pinning in the high reduced field also reduces to the Kramer functional form.

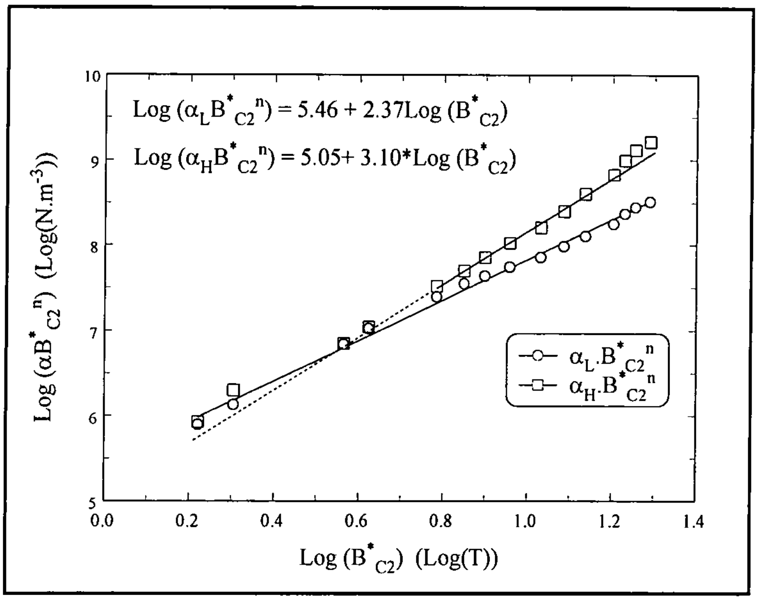

Figure 5.10 Log log plot of the prefactors from both low and high reduced field cases.

The prefactors used for the reduction of the pinning force are shown in a log log plot in figure 5.10, allowing the determination of α_L, α_H and n for both field regions. Hence in the low reduced field region the functional form of the pinning force is described by:

$$F_p = \alpha_L \times B_{C2}^{*\,2.37} b^{1/2}(1-b)^2 \tag{7}$$

and for the high reduced field is described by:

$$F_p = \alpha_H \times B_{C2}^{*\,3.10} b^{1/2}(1-b)^2 \tag{8}$$

where b is the reduced field, B_{C2}^* is the field at which the critical current density goes to zero, α_L=2.9x10^5 N.m^{-3}.T$^{-2.4}$ and α_H=1.1x10^5 N.m^{-3}.T$^{-3.1}$. The dotted line is a guide to the eye and is an extension of the high reduced field mechanism into the low reduced field regime where it is not observed.

5.4 Discussion

In this section the results presented in section 5.3 will be compared to studies already in the literature to determine the sample quality and to highlight the features of the pinning mechanism observed.

5.4.1 Sample Quality

The sample was found to contain only $SnMo_6S_8$ in two structural forms, with no impurities present to the resolution of x-ray powder diffraction. The critical temperature is low, indicative of oxygen contamination or off-stoichiometry. The sample was prepared with care to avoid oxygen contamination however the molybdenum crucible used was relatively new and therefore possibly affected the stoichiometry of the sample. Sulphur deficient samples have been shown to have lower critical temperatures**[11]** and the lower critical temperature is attributed to this cause.

5.4.2 Peak Effect

In 1969 Fietz and Webb**[12]** postulated that the pinning force within a superconductor could be parameterised by a product of two functions, one describing the field dependence and one describing the temperature dependence of the pinning force such that:

$$F_p = K \times B^*_{C2}(T)^{5/2} \times g(B/B^*_{C2}) \qquad \textbf{(9)}$$

where K is a constant, B^*_{C2} is the upper critical field of the sample and g is a function only of the reduced field B/B^*_{C2}. Kramer extended this work in 1973**[2]** by producing an empirically derived functional form for the field dependence of equation 5.9 in two different field regimes. He postulated that in low reduced fields the pinning force will be of the form:

$$F_p = K_p \times B^*_{C2}(T)^{5/2} \times \frac{b^{1/2}}{(1-b)^2} \qquad \textbf{(10)}$$

and that in high reduced fields the pinning force will be of the form:

$$F_S = K_S \times B_{C2}^{*}(T)^{5/2} \times b^{1/2}(1-b)^2 \qquad \textbf{(11)}$$

where b is the reduced field. The first of these functional forms is based on the principle of pin breaking and the second is based on shearing of the flux line lattice. As the two mechanisms have different causes, he proposed that their relative strength could change, thus moving the peak in the measured pinning force which is a sum of the two functions.

The work by Kramer was for a general hard high field superconductor. The pinning force in $SnMo_6S_8$ has previously been investigated, and attempts made to parameterise the pinning forces using Kramer-like models. Karasik et al**[13]** measured the effect of microstructure on the pinning in SMS and found that the low reduced field critical current density was strongly affected by microstructure however the high reduced field critical current density was relatively unchanged. They suggested that the low reduced field mechanism could be scaled using Kramer's functional form and proposed a high reduced field pinning force of the form:

$$F_p = \alpha(T)(1-b)^2 \qquad \textbf{(12)}$$

This functional form is attributed by Dew-Hughes to a normal volume pinning mechanism, suggesting large normal regions within the sample, though it was determined to be single phase according to x-ray powder diffraction measurements. More recently, investigations of the peak effect in $SnMo_6S_8$ **[14][15]**have considered the low reduced field pinning to be of the form:

$$F = \alpha \times B_{C2}^{*}(T)^{5/2} \times b^{1/2}(1-b)^2 \qquad \textbf{(13)}$$

where α is a microstructure dependent prefactor. This functional form has then been used to subtract the low reduced field pinning from the total pinning within the sample, leaving a high reduced field pinning mechanism that has a peak at a value of reduced field of approximately 0.6. Bonney et al. **[15]** went on to fit this high field peak using a generalised functional form for the pinning force of:

$$F = C \times b^{p}(1-b)^{q} \qquad \textbf{(14)}$$

where C is a constant and p and q took values of 1.6 to 4.0 and 1.4 to 3.1 respectively in order to have good fits. The values of p and q for the high field pinning mechanism were found by Bonney et al to be dependent on microstructure. They concluded from the two functional forms of the pinning force curves that the low reduced field pinning mechanism was a grain boundary pinning mechanism, similar to that seen in Nb_3Sn and that the high reduced field pinning mechanism was due to intragranular defects acting as pinning centres.

Gupta et al**[14]** also concluded that the relative strengths of the low reduced field and the high reduced field were dependent on microstructure, and then went on to propose that the low field pinning mechanism was dominated by flux line lattice shear model and the high reduced field pinning was a pin breaking mechanism, based on the functional form of the two pinning force curves when separated from each other.

Single crystal $SnMo_6S_8$ has been fabricated by Le Lay et al**[16]** which allows the study of the pinning without grain boundaries. The critical current density was found to show an increase with increasing field. The pinning force was calculated from the data of Le Lay et al by Rikel**[17]** with a suggested scaling with temperature at high reduced fields of the functional form:

$$F_p = \alpha(T) b^{5/2}(1-b) \qquad \textbf{(15)}$$

This functional form is not usually attributed to any mechanism for pinning and is postulated as a mathematical fit to the data.

It seems from the literature that the pinning in SMS is not well understood. In this chapter we have completed a detailed investigation of the scaling properties of $Sn_1Mo_6S_8$ as a function of temperature and magnetic field. Evidence for two separate mechanisms has been produced which operate in low reduced field and in high reduced field and have a functional form given by:

$$F^{*}_{pL} = \alpha_L B^{*\,2.4}_{C2}(T).b^{1/2}.(1-b)^2 \qquad \textbf{(16)}$$

for the low reduced field pinning mechanism and:

$$F^{*}_{pH} = \alpha_H B^{*\,3.1}_{C2}(T).b^{1/2}.(1-b)^2 \qquad \textbf{(17)}$$

for the high reduced field pinning mechanism, the prefactors being $\alpha_L = 2.9\text{x}10^5$ $\text{N.m}^{-3}.\text{T}^{-2.4}$ and $\alpha_H = 1.1 \text{ x } 10^5 \text{ N.m}^{-3}.\text{T}^{-3}$.

Both these equations have the same functional form for the field dependence of the pinning force. This field dependence is usually associated with the flux line lattice shear model and with grain boundary pinning. The different temperature dependencies of these two mechanisms are given by the different exponents n. The functional form of the two pinning force curves is dependent on how the two forces are separated. Work in the literature suggests the high reduced field pinning force is associated with pin breaking**[14]** and with intragranular pinning**[15]**. In neither case was good agreement and scaling with temperature found between the theoretical predictions and experimental curves. We have found good agreement with the Kramer functional form for the field dependence of the pinning force in both high and low reduced fields which scales well with temperature. We suggest that the increase in strength at high reduced fields is caused by the reduction of the elastic constants of the flux line lattice**[18]**, allowing the fluxons to move to pinning sites that were not previously available to the rigid flux line lattice. This proposal does not require two sources of pinning within the material, both peaks can be attributed to grain boundary pinning, which is thought to be the pinning mechanism in Chevrel phase materials. Alternatively, there may be a mechanism that is not simple grain boundary pinning which nevertheless gives the Kramer field dependence**[19]**. Finally we note that if the high field pinning mechanism could be continued into the low field regime then the critical current density achieved at 4.2 K would increase by factor 5 at intermediate low fields as can be seen from figure 5.9.

5.5 Conclusion

The Peak Effect in $Sn_1Mo_6S_8$ has been studied in detail using variable temperature high field magnetisation measurements on a well characterised sample, fabricated using a hot isostatic pressing technique. Scaling has been found in the pinning force density in both the high and the low reduced field regions. The relative strengths of the two mechanism are temperature dependent, but both have the functional form proposed by Kramer i.e.

$$F = \alpha \times B^{*}_{C2}(T)^{n} \times b^{1/2}(1-b)^{2} \qquad \textbf{(18)}$$

which is associated with grain boundary pinning. Previous work on $SnMo_6S_8$ proposed alternative mechanisms for the high reduced field pinning but found that the temperature scaling gave no physically meaningful functional form. In this work the Kramer field dependence is shown to scale the pinning force density well for all temperatures measured, in both low reduced field and high reduced field. We note that extending the high field mechanism throughout the entire superconducting phase may provide a means to increase J_C in Chevrel phase materials to those required for high field magnet applications.

5.6 References

[1] Kramer E J *J. Elec. Mat.* **4** 839 (1975)

[2] Kramer E J *J. Appl. Phys.* **44** 1360 (1973)

[3] Bean C P *Rev. Mod. Phys.* **36** 553 (1964)

[4] Chevrel R, Sergent M and Prigent J *J. Sol. Stat. Chem.* **3** 515 (1971)

[5] Khlybov E, Kuz'micheva G and Evdokimova V *Russ. J. Inorg. Chem (English Translation)* **31** 627 (1986)

[6] Miller W M and Ginsberg D M *Phys. Rev. B.* **28** 3765 (1983)

[7] Werthamer N R, Helfand E and Hohenberg P C *Physical Review* **147** 295 (1966)

[8] Gupta A, Decroux M, Willis T C and Fischer O *Physica C* **235-240** 2541 (1994)

[9] Hinks D G, Jorgensen J D and Li H -C *Phys. Rev. Lett.* **51** 1911 (1983)

[10] Meul H W *Helv. Phys. Acta.* **59** 417 (1986)

[11] Sato K, Hinode H, Wakihara M and Taniguchi M *Mat. Res. Bull.* **23** 993 (1988)

[12] Fietz W A and Webb W W *Physical Review* **178** 657 (1969)

[13] Karasik V R, Karyaev E V, Zakosarenko V M, Rikel M O and Tsebro V I *Sov. Phys JETP* **60** 1221 (1984)

[14] Gupta A, Decroux M, Selvam P, Cattani D, Willis T C and Fischer O *Physica C* **234** 219 (1994)

[15] Bonney L A, Willis T C and Larbalestier D C *J. Appl. Phys.* **77** 6377 (1995)

[16] Le Lay L, Willis T C and Larbalestier D C *IEEE Trans. on Magn.* **27** 954 (1991)

[17] Rikel M O *Presented at ASC 98*

[18] Pippard A B *Phil. Mag.* **19** 217 (1969)

[19] Hampshire D P *Physica C* **296** 153 (1998)

Chapter 6

Europium Doping in $SnMo_6S_8$

6.1 Introduction to Chapter 6

The relationship between superconductivity and magnetism has been of interest to physicists for many years. It was first noted by Ginzburg in 1957**[1]** that superconductivity and magnetic ordering did not both appear in any one material, which he thought strange, considering the number of materials that exhibit either of the phenomena. This led him to postulate that the two were mutually exclusive, and he calculated that the magnetisation of the magnetic ions would often be greater than the upper critical field of the superconductor. This led experimentalists to try to find materials in which the coupling between the magnetic ions and the superelectrons was strong enough to be non-zero but weak enough that the superconductivity was not destroyed. In 1975 Fischer et. al.**[2]** fabricated Chevrel phase materials which are both superconducting and contain rare earth magnetic ions in the crystal lattice. This coexistence is made possible by the spatial separation of the magnetic ions from the superelectrons. These materials have been extensively studied to try to develop an understanding of how the two competing mechanisms interact.

Chevrel phase materials not containing magnetic ions, $PbMo_6S_8$ and $SnMo_6S_8$, have high upper critical fields and critical current densities, making them potential materials for high field applications. In this work the effect of doping the non-magnetic Chevrel phase material $SnMo_6S_8$ with europium was investigated. The interaction between fluxons and the magnetic ions may provide a mechanism for increasing the critical current density within Chevrel phase superconductors via a magnetic pinning force.

Work previously done in this field was restricted to resistance measurements of the superconducting transition**[3]** and therefore not necessarily representative of the bulk of the sample. Further measurements were later performed on $Eu_{0.75}Sn_{0.25}Mo_6S_{7.73}Se_{0.27}$ using ac susceptibility and dc magnetometry techniques to give a better bulk measurement**[4]**. The introduction of selenium however reduced the critical temperature to around 4.0K and hence made this system difficult to study and of little importance for commercial applications. In this study, three samples were fabricated with varying europium concentrations as described in section 6.2. The sample fabrication was performed by Dr D N Zheng. The samples were then characterised using x-ray powder diffraction measurements, which were performed by Dr A E Goeta. The author completed ac resistance and susceptibility measurements and dc magnetisation measurements which will be discussed in section 6.3. Results confirm the coexistence of magnetism and superconductivity which will be discussed in section 6.4 and a summary of the chapter will be given in section 6.5

6.2 Sample Fabrication

This section gives a detailed account of the fabrication process used to produce the materials studied. It has been found that the addition of rare earth metals to Chevrel phase superconductors can provide changes in superconducting properties for one of two reasons. Firstly the addition of small amount of rare earth ions can form a second phase impurity which changes the superconducting properties of the material by acting as an oxygen getter. Secondly the magnetic ions can substitute into the crystal lattice of the Chevrel phase material giving access to new physics with the interaction of magnetism and superconductivity. The second of the two is the mechanism under investigation in this study. It has been found that high reaction temperatures, as high as 1500°C are necessary to incorporated Gd ions into $PbMo_6S_8$**[5]** and so this temperature was chosen for these reactions. The two mechanisms affecting the superconductor can be distinguished by measuring the magnetic moment of the sample in the normal state, where if the ions have been substituted correctly into the lattice, a strong paramagnetic response will be found. The sample fabrication was performed by Dr D N Zheng. To avoid contamination, all sample handling was performed within a glove box, where the water and oxygen content is less than 10 p.p.m. and all tubes used were thoroughly cleaned and degassed prior to use.

6.2.1 Formation of Precursors From Elements

The fabrication route chosen was a solid state sintering route in which elements were used to fabricate the required precursor for the reactions wherever possible to reduce impurities. Molybdenum powder (99.95%) and sulphur powder (99.999%) were reacted to form MoS_2. The heat treatment used was:

$$\mathit{Room\ Temperature} \xrightarrow{100^\circ C/Hour} 420^\circ C \xrightarrow{10Hours} 420^\circ C$$
$$\xrightarrow{33^\circ C/Hour} 450^\circ C \xrightarrow{15Hours} 450^\circ C \xrightarrow{33^\circ C/Hour} 650^\circ C$$
$$\xrightarrow{8Hours} 650^\circ C \xrightarrow{Furnace\ Cooled} \mathit{Room\ Temperature}$$

Europium chip (99.9%) and sulphur powder (99.999%) were reacted to form EuS. The heat treatment used was:

$$\mathit{Room\ Temperature} \xrightarrow{100^\circ C/Hour} 450^\circ C \xrightarrow{8Hours} 450^\circ C$$
$$\xrightarrow{33^\circ C/Hour} 650^\circ C \xrightarrow{10Hours} 650^\circ C$$
$$\xrightarrow{Furnace\ Cooled} \mathit{Room\ Temperature}$$

Both the above reactions were performed in evacuated sealed quartz tubes in a tube furnace under continuous flow of argon gas. After the reaction the quartz tubes were opened and the precursors were ground for approximately forty minutes using a mortar and pestle to ensure homogeneity.

6.2.2 Precursor Reaction to Chevrel Phase

To avoid oxygen contamination from the quartz tubes and to allow the use of high temperatures, a molybdenum crucible was used.

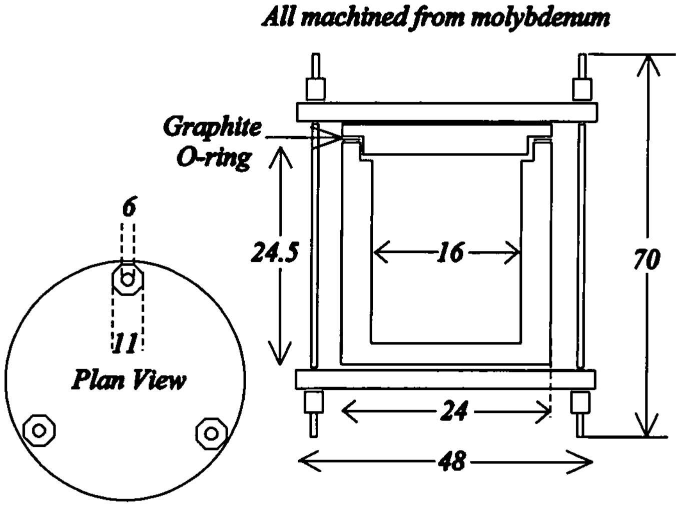

Figure 6.1 **Molybdenum crucible and clamp designed to work in a 50mm tube furnace at temperatures up to 1500°C, with no leakage.**

A frame was designed by the author to allow the crucible to be sealed within a 50mm tube furnace. The frame was constructed from molybdenum to avoid problems with differential thermal expansion. This allows the precursors to be sealed in a container that is inert to reaction with the sample and that can survive the high reaction temperatures required. The precursors produced were combined with SnS (99.5%) in the correct ratios to allow the fabrication of three samples of the composition $Eu_xSn_{(1-x)}Mo_6S_8$ for x = 0, 0.35 and 0.5. The x = 0 sample was fabricated to determine the effect of the high reaction temperature on the properties of $SnMo_6S_8$. The precursors were pressed into pellets and sealed in the molybdenum crucible. A conventional tube furnace was used for the heat treatments with a continuous flow of argon gas. The first heat treatment used was:

$$Room\ \ Temperature\xrightarrow{960^{\circ}C/Hour}1150^{\circ}C$$

$$\xrightarrow{45Hours}1150^{\circ}C\xrightarrow{Furnace\ \ Cooled}Room\ \ Temperature$$

The reacted precursors were removed from the crucible, ground using a mortar and pestle for approximately forty minutes to aid homogenisation, pressed into pellets and resealed in the crucible. Another heat treatment was then performed, differing slightly for the different samples. For the x = 0 and the x = 0.5 sample:

$$Room\ \ Temperature\xrightarrow{960^{\circ}C/Hour}1450^{\circ}C$$

$$\left(\frac{7Hours\ \text{-}\ x{=}0}{8Hours\ \text{-}\ x{=}0.5}\right)1450^{\circ}C\xrightarrow{Furnace\ \ Cooled}Room\ \ Temperature$$

For x = 0.35:

$$Room\ \ Temperature\xrightarrow{600^{\circ}C/Hour}1350^{\circ}C\xrightarrow{0.5Hours}$$

$$1350^{\circ}C\xrightarrow{120^{\circ}C/Hour}1450^{\circ}C\xrightarrow{7.5Hours}$$

$$1450^{\circ}C\xrightarrow{Furnace\ \ Cooled}Room\ \ Temperature$$

The high temperature reactions for all three of the samples were performed under a continuous flow of argon gas.

6.2.3 Hot Isostatic Pressing

After the high temperature reactions the samples were ground again using a mortar and pestle for forty minutes, pressed into pellets, wrapped in molybdenum foil and sealed under vacuum in thin walled stainless steel tubes. These tubes were then cold isostatically pressed under approximately 100 bar of argon to ensure the quality of the vacuum seals. The billets were then hot isostatically pressed at 800°C and 2000 bar for 2.75 hours after which time, due to a fault in the press the pressure reduced linearly at a rate of 300 bar per hour. The temperature was maintained at 800°C during this pressure drop so that the total time for the sample at 800°C was 8.5 hours.

The remaining pressure was released and the sample allowed to furnace cool to room temperature.

6.3 Experimental Characterisation

In this section the experimental results of the characterisation of the three samples will be presented. The mechanical differences in the material were clearly visible during the handling of samples for these experiments. The undoped material was hard, silvery and shiny, the $x = 0.35$ sample was also hard, light grey in colour though quite brittle and could be seen to be polycrystalline. The $x = 0.5$ sample was darker in colour, non-shiny and chalky in texture.

6.3.1 X-ray Powder Diffraction

The phase composition of the samples was determined using X-ray powder diffraction performed by Dr A E Goeta from The Department of Chemistry at Durham University. A small amount of the sample was ground to a fine powder and dispersed on an off-cut silicon wafer. The measurements were performed using a Philips PW1050 using Cu K_α at 1.5418Å, produced by a HiltonBrooks Generator. The data was taken at 0.02 degree intervals, counting for 10 seconds at each step. The results obtained are shown in figure 6.2, for all three of the samples. The peak markers are shown on each of the samples, taken from the 2 x-ray cards available for $SnMo_6S_8$ produced by Chevrel**[6]** and Khlybov**[7]**.

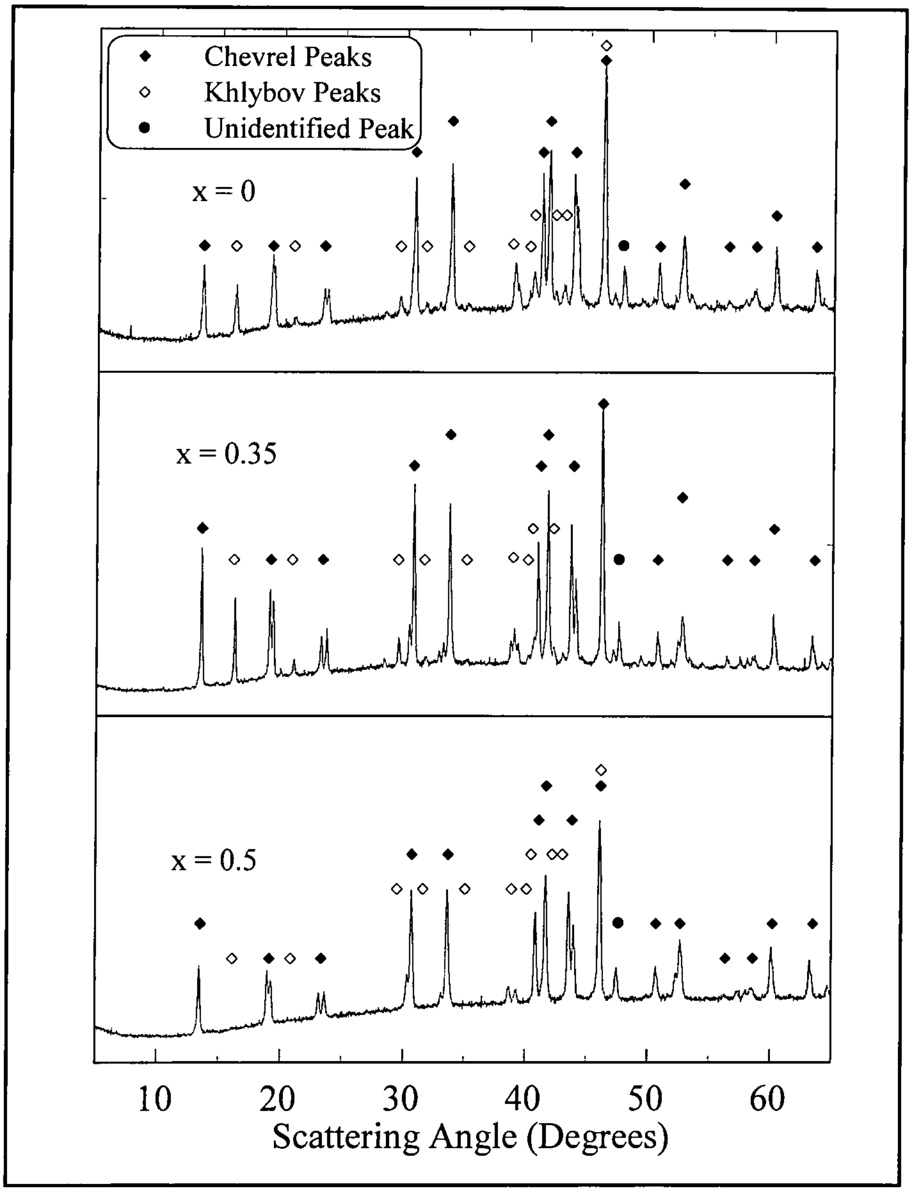

Figure 6.2 X-ray powder diffraction patterns for $Eu_xSn_{(1-x)}Mo_6S_8$ for x = 0, 0.35 and 0.5 with the major peaks being identified as $SnMo_6S_8$.

It can be seen that all the major peaks can by associated with one of the two structural forms of $SnMo_6S_8$ and that there are no other crystalline phases present, hence the materials are of high quality. With the increase in europium doping, a splitting of peaks can be seen e.g. at 18 degrees and at 24 degrees. This suggests a change in the unit cell dimensions as expected if the europium ions were being substituted on to the tin sites.

6.3.2 Ac Susceptibility and Ac Resistivity Measurements

In order to characterise the superconducting properties of the samples a study of the ac resistivity and ac susceptibility of the samples was completed.

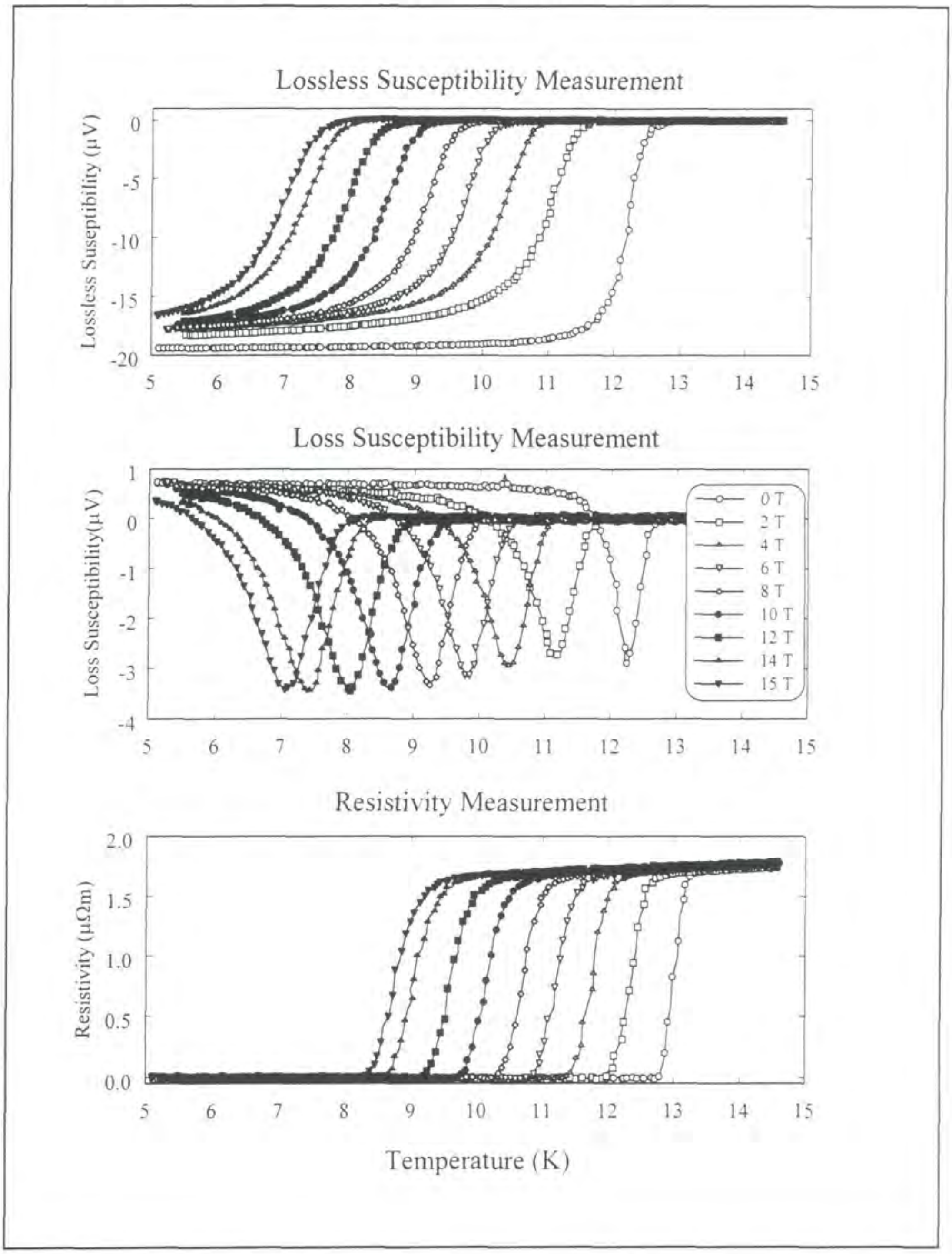

Figure 6.3 **Superconducting transitions in $SnMo_6S_8$ as a function of dc magnetic field.**

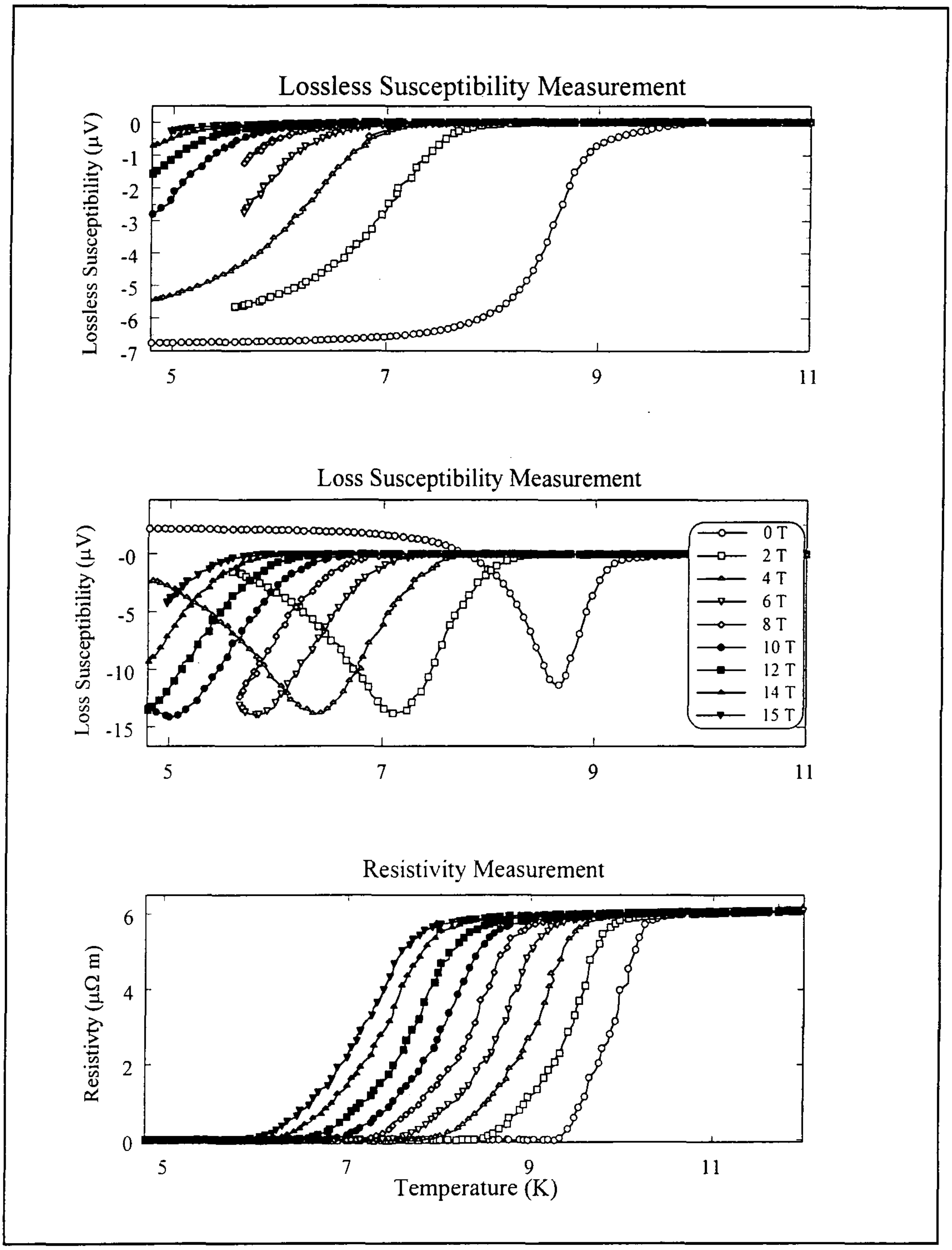

Figure 6.4 **Superconducting transitions in $Eu_{0.35}Sn_{0.65}Mo_6S_8$ as a function of dc magnetic field.**

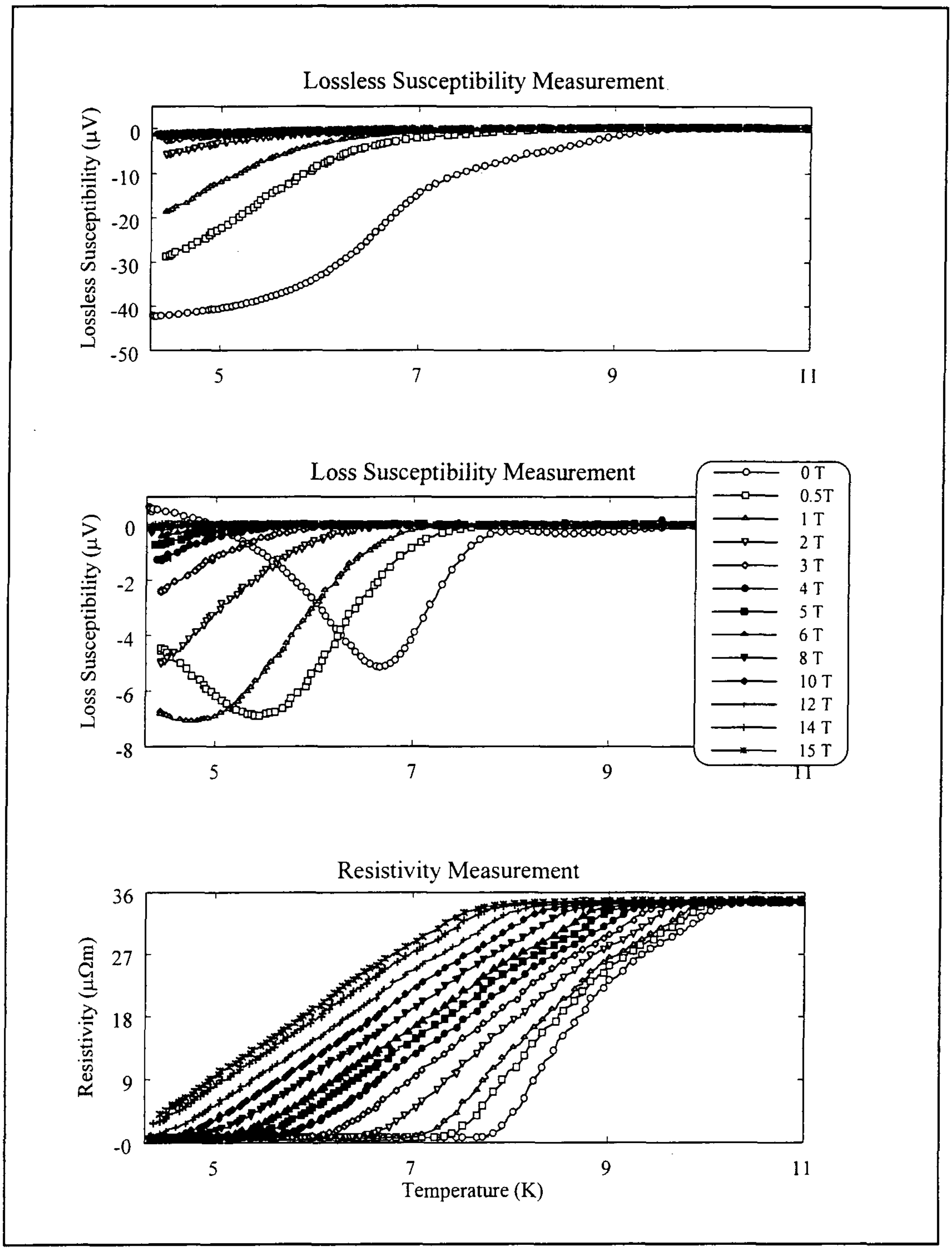

Figure 6.5 **Superconducting transitions in $Eu_{0.5}Sn_{0.5}Mo_6S_8$ as a function of dc magnetic field.**

Measurements were performed as a function of temperature, from 4.3 K to $T>T_C$ in dc fields up to 15T using a system developed in-house The temperatures are accurate to 0.1K, confirmed by the measurement of a pure lead sample and the fields to better than 0.1%.The ac resistivity values were determined using a standard 4 terminal technique, with an excitation current of 3.3mA at 76 Hz. For the ac susceptibility measurement, an ac field of approximately 100μT was used at a frequency of 330 Hz. The zero field data shown was measured in the remnant field of the magnet which is thought to be less than 0.1T, and comparison with results taken in a dewar suggest changes of less than 0.2K in the properties measured due to the remnant field. For the undoped sample the onset of the resistive transition in zero field is 13.4 K, and is sharp, with a width of 0.3K in zero field from the 90% to the 10% value of resistivity, indicating high quality homogenous samples. The ac susceptibility data contains only one transition, again suggesting single phase homogenous samples.

The introduction of europium reduces the onset of the resistive transition for the x = 0.35 sample to 10.4K. The transition is now quite broad, with a width of 0.7 K in zero field. The susceptibility measurement contains two transitions which is characteristic of a granular material, with the higher transition representing the grains and the lower transition representing the grain boundaries.

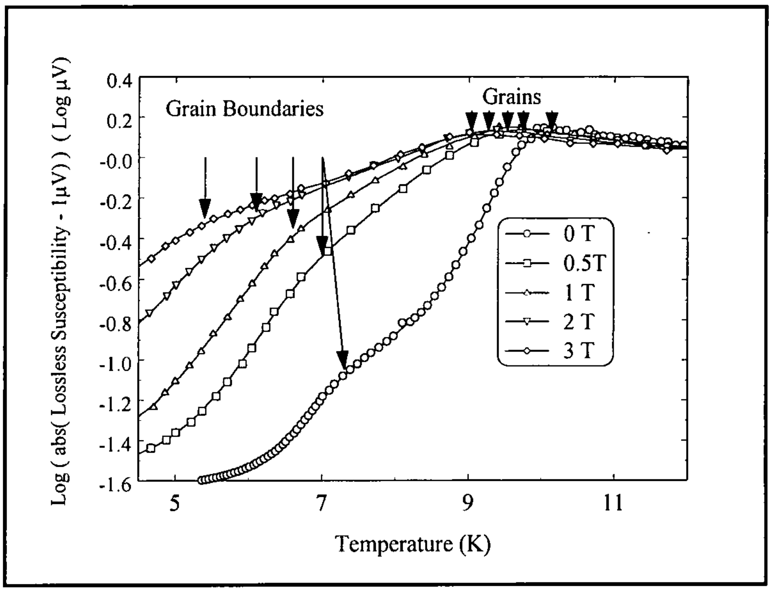

Figure 6.6 **Detail of the onset of the superconducting transition in $Eu_{0.5}Sn_{0.5}Mo_6S_8$ sample. The two phase transition can clearly be seen.**

The onset of the resistive transition for the 50% doped sample is at 10.0K in zero field, with the width of the transition now being approximately 2.2K. At low fields it is possible to see two distinct gradients within the transition, indicating granularity. The susceptibility measurement shows two transitions, in the lossless component, and two peaks in the loss component at low field. Figure 6.6 shows in more detail the two phase nature of the transition. The onset is sharp, when the grains begin to superconduct, indicated by the higher set of arrows. Then there is a distinct change in gradient during the transition as the grain boundaries start to superconduct, indicated by the lower set of arrows.

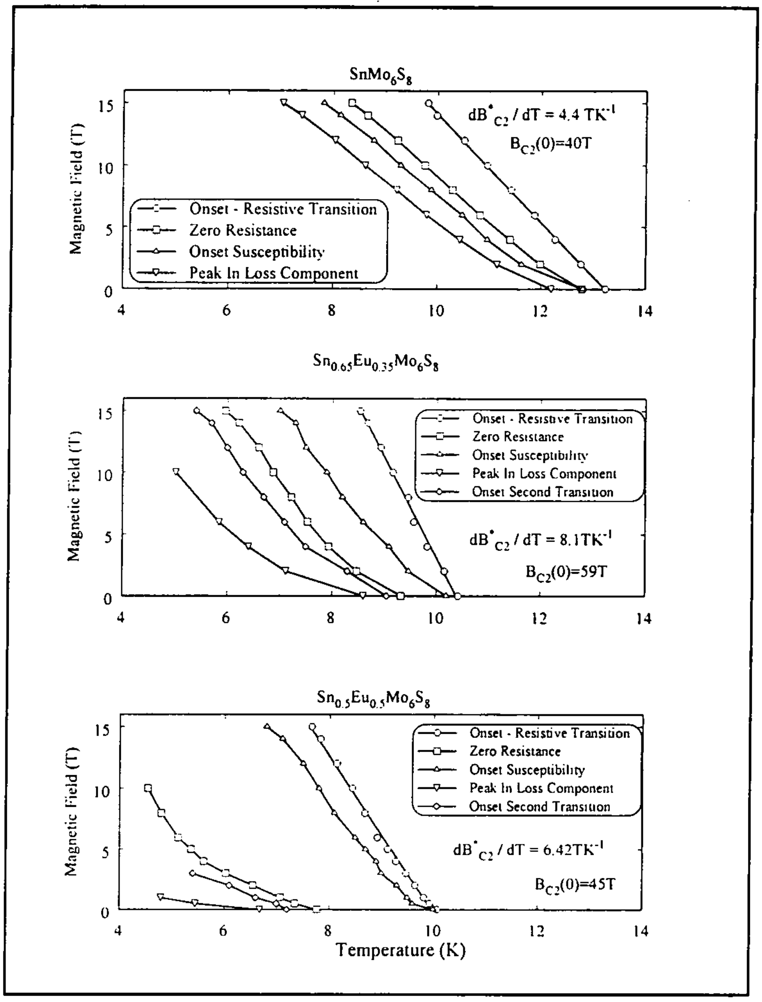

Figure 6.7 The magnetic phase diagrams for the three samples determined from the ac resistivity and ac susceptibility measurements.

The data shown in figure 6.3 to figure 6.6 allows the determination of a magnetic phase diagram for each of the samples, figure 6.7. The onset and zero resistance values are taken at the 90% and 10% levels respectively.

$$B_{C2}(0) = 0.69T_C\left[\frac{dB_{C2}(T)}{dT}\right]_{T = T_C} \qquad (1)$$

The gradients shown are for the onset of the resistive transition and the extrapolated upper critical field at zero Kelvin is determined using an equation (equation 6.1) derived from WHH theory for a dirty superconductor. To allow easy comparison of the three samples, the resistivity measurements are presented in figure 6.8. The onset of the transition is considered to represent the properties of the best grains and the zero resistance point is associated with $J_C \approx 0$, the Irreversibility Field[12].

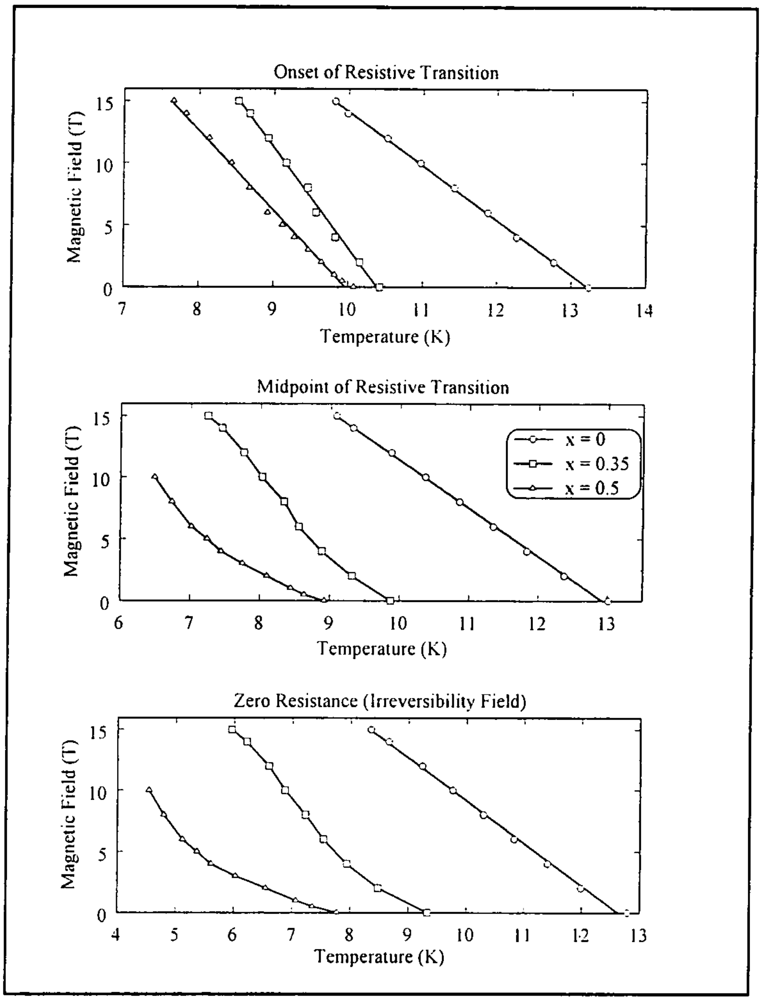
Onset of Resistive Transition

Midpoint of Resistive Transition

Zero Resistance (Irreversibility Field)

Figure 6.8 **Comparison of the resistive transition for the three samples for the nset, midpoint and the zero resistance point.**

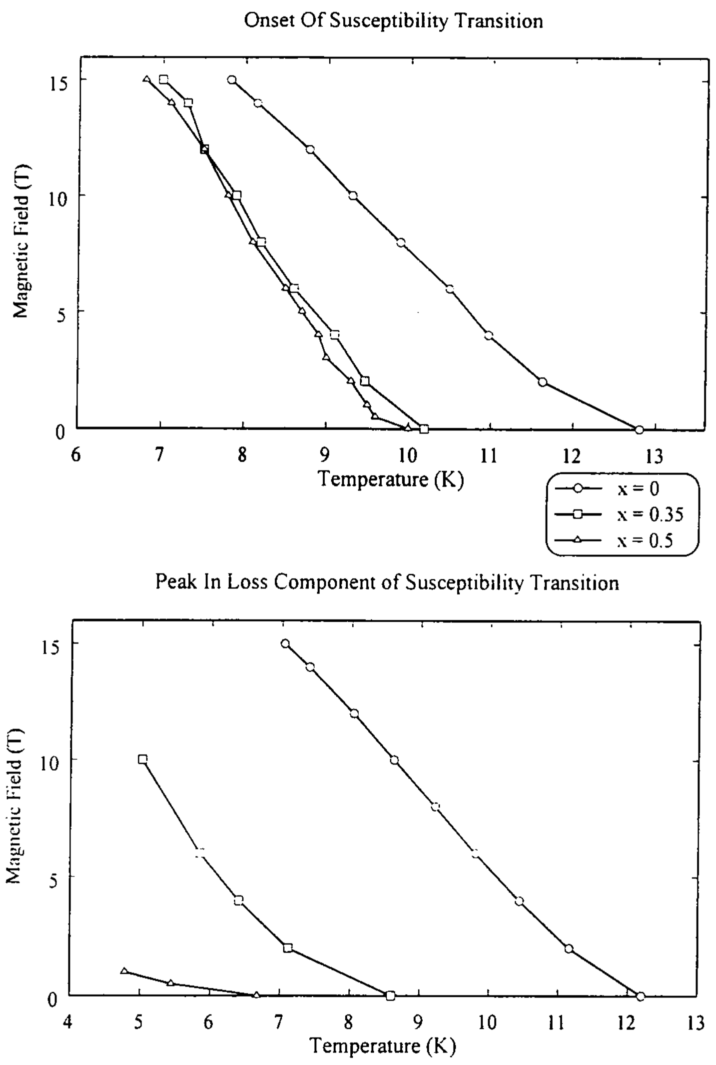

Figure 6.9 **Comparison of the susceptibility transitions for the three samples for both the onset of the lossless transition and the peak in the loss component.**

Similarly, the susceptibility measurements of the samples are compared in figure 6.9. In large grain materials the onset of the susceptibility is a measure of the average properties of the grains, where the two doped samples can be seen to have similar values across the whole field range. The peak in the loss component however shows a large difference, dependent on doping and is also representative of the irreversibility field[8].

Doping Level	Onset Of Zero Field Resistive Transition (K)	Width of Resistive Transition In Zero Field (K)	Zero Field Normal State Resistivity (μΩ.m)	dB^*_{C2}/dT ($T.K^{-1}$)	$B^*_{C2}(0)$ (T)
0%	13.2	0.3	1.73	4.4	40
35%	10.4	0.7	6.1	8.1	59
50%	10.0	2.2	35	6.4	45
0%(Chap. 5)	12.0	0.1	0.8	3.9	32
0%-Fischer	10.4	-	-	4.4	28
50%-Fischer	10.0	-	-	6.0	41

Table 6.1 **Summary of the parameters determined from the resistivity measurement for samples in this chapter, chapter 5 and from Fischer et al[9].**

Doping Level	Onset of Zero Field Susceptibility Transition (K)	Width of Susceptibility Transition In Zero Field (K)	dB^*_{C2}/dT ($T.K^{-1}$)	$B^*_{C2}(0)$ (T)
0%	12.8	1.0	3.3	29
35%	10.2	1.6	5.5	37
50%	10	3.1	5.2	35
0%(Chap. 5)	11.8	0.2	3.3	27
0%-Bonney[10]	14.3	0.3	2.8	27

Table 6.2 **Parameters determined from susceptibility measurements including data for the sample discussed in chapter 5 and the sample fabricated by Bonney et al[10].**

Tables 6.1 and 6.2 contain a summary of the parameters determined from the samples in this study. Also included are the results from chapter 5 for the sample fabricated at a lower temperature, the results found by Fischer et al[9] on for both an undoped and a sample doped at x = 0.5, and the results of Bonney et al for the sample with high J_C values.

6.3.3 Dc. Magnetisation Measurements

In order to determine the critical current density of the samples and to measure the doping level of the magnetic ions in the lattice, dc magnetisation measurements were performed using the vibrating sample magnetometer described in chapter 7. Magnetisation measurements were performed at 4.2 K in fields up to 15 T for the x = 0 and x = 0.35 samples and to 7 T for the x = 0.5 sample.

Sample Doping Level (x)	Sample Dimensions (mm)	Low Field Susceptibility	Zero Field Critical Current Density (Am^{-2})
0	1.5 x 2.2 x 4.6^*	-	3.4×10^8
0.35	2.3 x 0.8 x 5.1^*	0.04	8.4×10^7
0.5	1.0 x 3.5 x 5.0^*	0.029	6.8×10^6
0 - 1100°C Sample	2.5 x 1.9 x 5.6^*	-	1.6×10^9
Bonney et al[10].	1 x 1 x 3^*	-	$\sim 4 \times 10^9$

Table 6.3 Dimensions, low field susceptibility and the zero field critical current density for the dc magnetisation samples. The star denotes the sample dimension parallel to the applied field.

Table 6.3 gives the dimensions, the low field susceptibility and the zero field critical current density for the dc magnetisation measurements. Also included is the sample fabricated at 1100°C from chapter 5 and the sample fabricated by Bonney et al[10] with a high critical current density.

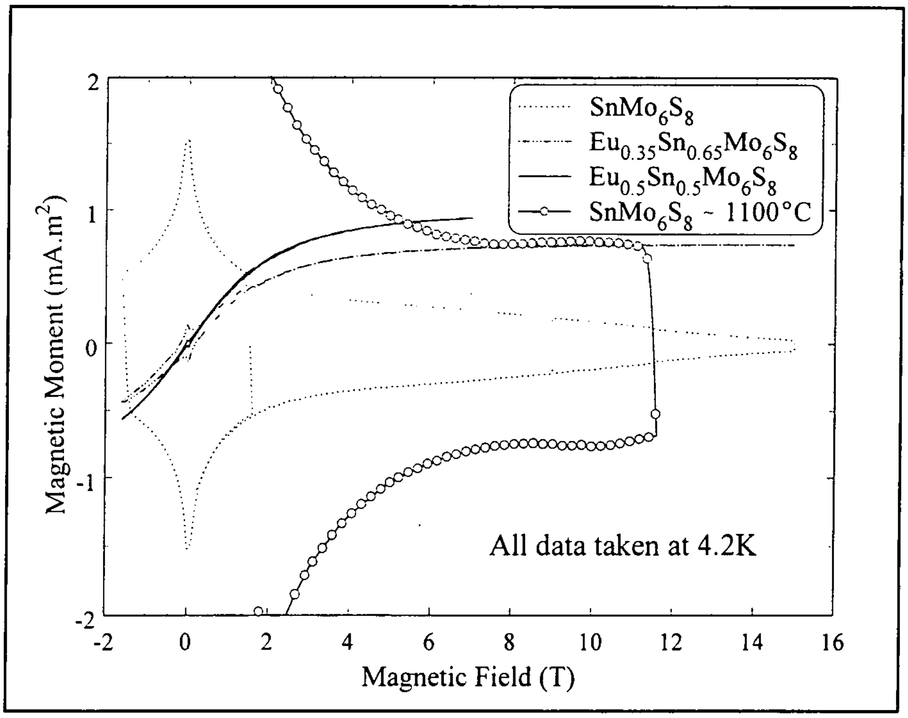

Figure 6.10 High field magnetisation data for the three samples investigated.

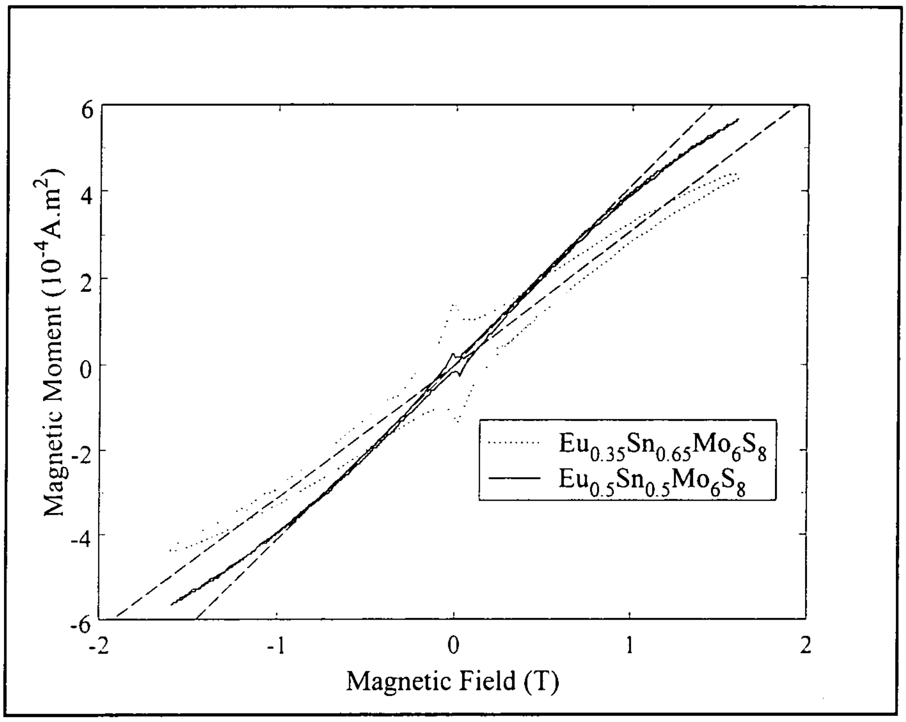

Figure 6.11 Low field magnetisation data for the doped samples showing the irreversible part of the magnetisation curve in more detail. The dashed straight lines are used to determine the doping level.

The results are shown in figure 6.10, for the three samples in this study. Also included is a magnetisation curve (scaled by a factor 1.9 to account for different sample volume and demagnetisation factor) for the $SnMo_6S_8$ sample discussed in chapter 5 to show the effect of the high temperature reaction on the x = 0 sample. The doped samples can be seen to have a paramagnetic background on top of which is superimposed the irreversible magnetisation representing the critical current density of the sample. The low field region is examined more closely in figure 6.11. Here it can be seen that both doped samples possess reversible and irreversible components of the magnetisation curve. The susceptibility is given by:

$$\chi_V = \frac{\mu_0 N_V g^2 \mu_B^2 J(J+1)}{3k_B T} \qquad (2)$$

where N_V is the number of magnetic ions per unit volume, g is the Landau g factor, and J is the angular momentum. The straight lines through the low field data in figure 6.11 allow the calculation of the doping level using Curies' Law (equation 2) to give χ and assuming the electron structure for europium is in the 2+ state which gives g = 2 and J = 7/2, N_V can be calculated to give the level of doping. The doping levels were determined to be 32% ± 3% for the nominal x = 0.35 sample and 23% ± 2% for the nominal x = 0.5 sample.

6.4 Discussion

In this section the results presented in section 6.3 will be discussed and compared with results in the literature.

6.4.1 X-ray Powder Diffraction

The results presented in section 6.3.1 demonstrate that high quality europium doped $SnMo_6S_8$ has been fabricated using high reaction temperatures and pressures. The x-ray measurements contains only peaks attributed to $SnMo_6S_8$, and show a splitting of peaks with increasing Europium concentration. This suggests the material contains no crystalline impurity phase and that the europium is being substituted on to the tin sites, causing a change in unit cell parameters and hence splitting the peaks

6.4.2 Ac Resistivity and Ac Susceptibility

The critical temperature for the x = 0 sample determined in zero field compares well with those in the literature, which range from 10.8 K to 13.66 K**[11]** and up to 14.5K for oxygen gettered samples**[12]**. This indicates that the samples fabricated for this study are both homogenous and of high quality.

The properties of the sample summarised in table 6.1 show clearly the effect of europium doping on $SnMo_6S_8$. The critical temperature systematically decreases, while the width of the transition, and the normal state resistivity systematically increase with increasing europium levels. The change in the onset of the resistive transition suggests that the europium is affecting the properties of the grains, however the broadening of the transition and the increase in normal state resistivity suggest that the sintering of the grains together is also degraded. The broadening of the transition and the increase in normal state resistivity could also be explained by the introduction of second phase material, caused by the presence of europium however this is not thought to be the case as the powder diffraction shows single phase samples. The upper critical fields determined for the x = 0 sample are higher than those presented in the literature **[11][12][13]**. This is attributed to reduced oxygen contamination in the samples in this study due to the use of a molybdenum crucible. The dB^*_{C2} / dT however fall within the values previously observed **[11]**.

The information in the literature on doped Chevrel phase superconductors is limited in validity due to the discovery of the importance of oxygen content in determining the superconducting parameters of a sample**[14]**. In work performed previous to this discovery, the oxygen content of samples prepared was not controlled. The introduction of rare earth metals could then change the superconducting properties of the sample by gettering the oxygen**[13]**. The oxygen content of a series of samples can be estimated from critical temperature of the undoped sample. Work done by Fischer et al in 1975 considered the series $Sn_{1.2(1-x)}Eu_xMo_{6.35}S_8$ however the x = 0 sample had a critical temperature of only 11K, suggesting a high degree of oxygen contamination. They found the effect of adding europium was negligible for concentrations up to x=0.3 suggesting that europium does not in fact act as an oxygen getter. As can be seen from table 6.1, good agreement is found between the x = 0.5 sample in this study and that of Fischer et al. More recent work by Meul**[15]** on the series $Eu_xSn_{1-x}Mo_6S_8$ also has a low critical temperature, defined as the mid point of the resistive transition, for the x = 0 sample of approximately 11K and they find critical temperature to be nearly independent of europium concentration up until x = 0.6.

The samples studied in this chapter show a marked decrease in the onset of the resistive transition between x = 0 and x = 0.35 of approximately 3K, the difference between x= 0.35 and x = 0.5 is small, approximately 0.5K. The midpoints of the resistive transitions are 9.9 K and 8.9K for the x = 0.35 and the x = 0.5 samples respectively. The critical temperatures for the doped samples are therefore lower than those measured by Meul of approximately 10.5K for $0.3 < x < 0.6$.

The effect of magnetic field on europium doped samples (x = 0.5, 0.7 and 0.8) was measured by Fischer et. al. and it was found that the doping changed the dependence of the upper critical field as a function of temperature and increased the extrapolated upper critical field at zero Kelvin, attributed to the compensation effect, proposed by Jaccarino and Peter in 1962**[16]**. Fischer found that for x = 0.5 dB^*_{C2} / dT was 5.7 TK^{-1} and the extrapolated upper critical field at zero Kelvin was 41T. This is comparable with results shown in table 6.1 for the x = 0.5 sample. Meul et. al. went on to study magnetic field induced superconductivity on $Eu_{0.75}Sn_{0.25}Mo_6S_{7.73}Se_{0.27}$ and did not present further work on the low level doped samples.

The low level doped sample (x = 0.35) shows a large increase in dB^*_{C2} / dT and $B^*_{C2}(0)$, as determined from the onset of the resistive transition, shown in table 6.1. These are the highest values recorded for any tin based Chevrel phase compound, almost a factor 2 larger than the average values in the x = 0 samples.

So far only the resistive measurement of the superconducting transition has been discussed as this is the measurement found in the literature. It is however limited in that it does not measure the bulk properties of the material, though is thought to give a good measurement of the properties of the grains with the onset of the transition being associated with the thermodynamical upper critical field and the zero resistance point being associated with the irreversibility field**[13]**.

By using an ac susceptibility technique to measure the superconducting transition, a better measure of the bulk of the sample can be obtained. This is the first characterisation of a series of the form $Eu_xSn_{(1-x)}Mo_6S_8$ using an ac susceptibility measurement. The onset of the superconducting transition can be associated with the onset of superconductivity within the grains, followed by the onset of superconductivity of the grain boundaries at lower temperatures. The analysis of the susceptibility signal is complicated by the fact that it is affected by the size of the ac field used[**17**]. The field used for all the samples in this study was the same, allowing relative comparisons to be made, however the values produced are not necessarily intrinsic to the materials. The onset of diamagnetism associated with the grains is however thought to be broadly independent of the ac field used in high dc fields and therefore can be considered intrinsic. It can be seen that the properties of the grains for both the doped samples are in fact the same to within the experimental accuracy available, which is consistent with other reports in the literature[**15**]. The position of the peak in the loss component for the $x = 0.5$ sample is however significantly lower than the $x = 0.35$ sample indicating the reduced connectivity of the grains in the higher doped sample. This is in agreement with the increase in normal state resistivity found for the higher doping level. It should be noted which ever measurement of the superconducting properties is chosen, it is predicted that at 4.2 K the $x = 0.35$ sample will be superconducting up to approximately 15 T and the $x = 0.5$ sample will be superconducting up to approximately 2 T.

6.4.3 Dc. Magnetisation Measurements

Comparing the undoped samples fabricated at two different reaction temperatures, clearly the higher reaction temperature reduces the critical current density. The critical current density in all cases is calculated assuming macroscopic screening currents. The reduction in the undoped sample can be attributed to larger grain size produced by the higher reaction temperature. For the doped samples, the grains appear to be less well connected, hence the samples are more granular and macroscopic screening currents may not be present. It is not necessarily the case that the europium doping reduces the intragranular critical current density. If the connectivity of the grains can be improved to that of the undoped sample, whilst still including the europium, perhaps by using a different heat treatment, then these materials would be of great interest. The doped samples have irreversibility fields of approximately 3T for the $x = 0.35$ sample and 0.5T for the x = 0.5 sample. The shape of the background magnetisation suggests that the samples are paramagnetic, and since the results of section 6.3.2 show that the x = 0.35 sample is superconducting up to fields of approximately 15T and the x = 0.5 sample is superconducting up to fields of approximately 2T, then these sample exhibit a coexistence of superconductivity and paramagnetism. The paramagnetism of the samples also supports the fact that the europium has been substituted into the lattice and is not present as a second phase. The calculation of the doping level from the magnetisation measurement suggest the doping level is higher in the x=0.35 sample than in the x=0.5 sample. It is not possible to determine whether this is true without a more detailed investigation using TEM. An alternative is that the higher doping level allows some magnetic ordering to take place, hence Curies' Law is no longer applicable.

6.4.4 Effect of Doping with Magnetic Ions

The changes in the critical temperature and critical field with the introduction of magnetic ions into the crystal lattice that have been seen can be explained by considering the effect of a magnetic ion on the paired electrons. The magnetic ions will try to align the electrons parallel to the applied field, hence destroying the Cooper pair. Therefore less energy is required to destroy the Cooper pair, and hence the critical temperature of the doped samples is lower than that of the undoped sample. To discuss the effect on the upper critical field it is necessary to consider an equation derived from Ginzburg Landau theory:

$$B_{C2} = 3\times10^{3}\gamma\rho_{N}T_{C}$$

where γ is the Sommerfeld constant, ρ_N is the normal state resistivity and T_C is the critical temperature. The derivation of this result is beyond the scope of this work and it will be used without proof. It has been seen that the normal state resistivity of the samples has increased with increasing doping and although this is partly due to poor connectivity, it is expected that the addition of magnetic ions will increase the scattering of electrons within the normal state and hence increase the intrinsic normal state resistance. The effect of the magnetic ions on the Sommerfeld constant is unknown and the critical temperature is only changed by approximately fifty percent. However the overall effect of the introduction of magnetic ions is an increase in upper critical field.

6.5 Conclusions

A series of europium doped tin molybdenum sulphide samples has been fabricated at high temperatures to investigate the coexistence of superconductivity and magnetism. The samples have been fully characterised using x-ray powder diffraction, ac resistivity, ac susceptibility and dc magnetometry. X-ray measurements show only peaks for $SnMo_6S_8$, with no impurity phase being seen, though there appears to be two structural phases of $SnMo_6S_8$. The unit cell dimensions can be inferred to change from the splitting of peaks with the addition of europium. This suggests the europium has successfully been incorporated in to the Chevrel phase lattice and is not present as a second phase within the sample. The doping levels have also been determined from the magnetisation measurements of the sample using Curies Law and were found to be 32% ± 3% for the nominal 35% sample and 23% ± 4% for the nominal 50% sample.

The addition of europium increases the normal state resistivity of the sample and also changes the metallurgical properties of the samples, becoming less well sintered for increasing europium levels and hence more granular. This can also be seen in the electromagnetic measurements as a broadening of the superconducting transition, allowing the transitions of the grains and the grain boundaries to be distinguished in the ac susceptibility measurement.

The variation in superconducting properties of the samples has been measured and the addition of europium at the levels used strongly affects the properties compared to the $x = 0$ sample, in contrast to previous studies in the literature where the addition of europium had little effect until $x = 0.6$. This is attributed to the fact that the $x = 0$ sample in this study has a higher T_C than those in the literature, suggesting that previous studies were affected by oxygen contamination.

The $x = 0.35$ sample has a lower critical temperature of 10.4K (resistivity onset) than the $x = 0$ sample (13.4K - resistivity onset) however $B^*_{C2}(0)$ and dB^*_{C2} / dT are considerably enhanced to 59T and 8.1 $T.K^{-1}$ respectively which are the highest values ever reported for a tin based Chevrel phase material. The $x = 0.5$ sample has values for

T_C (resistivity onset), $B^*_{C2}(0)$ and dB^*_{C2} / dT of 10.0K, 45T and 6.4T.K^{-1} which are similar to those reported by Fischer et al of 10K, 41 T and 6.1T.K^{-1}.

It was hoped that the introduction of magnetic ions may increase the pinning within the samples via an attractive force between magnetic ions and fluxons, and hence increase the critical current density. It was found however that even after allowing for the decrease in critical current density due to the higher reaction temperature, the addition of europium at the levels used reduced the critical current density by approximately factor 4 for the x = 0.35 sample and by approximately factor 50 for the x = 0.5 sample, measured at 4.2K and zero field. The irreversibility field was also dramatically reduced from greater than 20 T at 4.2K for the x = 0 sample to approximately 3T for the x = 0.35 sample and 0.5T for the x = 0.5 sample. These samples are however clearly granular and it is likely that this is the cause of the degradation and doping with europium may not necessarily decrease the critical current density. Further investigation is required to find a heat treatment that will result in well connected grains.

In summary, the addition of europium to $SnMo_6S_8$, at the levels used in this study, with the heat treatment described increases B^*_{C2}, and dB^*_{C2} /dT, decreases T_C, J_C and B_{IRR}, and produces a material in which the coexistence of paramagnetism and superconductivity has been found.

6.6 References

[1] Ginzburg V L, *Sov. Phys. -JETP* **4** 153 (1957)

[2] Fischer O, Treyvaud A, Chevrel R and Sergent M *Sol. Stat. Comm.* **17** 721 (1975)

[3] Meul H W, Rossel C, Decroux M, Fischer O, Remenyi G and Briggs A *Physica B* **126** 44 (1984)

[4] Remenyi G, Welp U, Tholence J L, Meul H W, Triscone J M, Kargut M G, Rossel C, Fischer O and Maki K *Physica B* **135** 339 (1985)

[5] Zheng D N, Sneary A B and Hampshire D P *Inst. Phys. Conf. Ser.* **158** 1005 (1997)

[6] Chevrel R, Sergent M and Prigent J *J. Sol. Stat. Chem.* **3** 515 (1971)

[7] Khlybov E, Kuz'micheva G and Evdokimova V *Russ. J. Inorg. Chem. (English Translation)* **31** 627 (1986)

[8] Ramakrishman S, Kumar R, Paulose P L, Grover A K and Chaddah P, *Phys. Rev. B* **44** 9514 (1991)

[9] Fischer O, Decroux M, Roth S, Chevrel R and Sergent M *J. Phys. C Sol. State Phys.* **8** L474 (1975)

[10] Bonney L A, Willis T C and Larbalestier D C *J. Appl. Phys.* 77 6377 (1995)

[11] Miller W M and Ginsberg D M *Phys. Rev. B* **28** 3765 (1983)

[12] Foner S, McNiff Jr E J and Hinks D G *Phys. Rev. B* **31** 6108 (1985)

[13] Gupta A, Decroux M, Willis T C and Fischer O *Physica C* **235-240** 2541 (1994)

[14] Hinks D G, Jorgensen J D and Li H -C *Phys. Rev. Lett.* **51** 1911 (1983)

[15] Meul H W *Helv. Phys. Acta.* **59** 417 (1986)

[16] Jaccarino V and Peter M *Phys. Rev. Lett.* **9** 290 (1962)

[17] Selvam P, Cattani D, Cors J, Decroux M, Junod A, Niedermann Ph, Ritter S and Fischer O *J. Appl. Phys.* 72 4232 (1992)

Chapter 7
Sensitivity Improvements to a Vibrating Sample Magnetometer

7.1 Introduction to Chapter 7

The vibrating sample magnetometer is an incredibly powerful tool for characterising magnetic properties of materials. It allows the magnetisation of samples to be measured as a function of applied field and usually also as a function of temperature. In this chapter magnetometry will be reviewed, then the principle of operation of the vibrating sample magnetometer will be explained along with the relevant design considerations. The VSM system in Durham will be introduced, with its limitations explained. Alterations made to improve the operation of the VSM in Durham will be presented and the resulting system compared to commercially available equipment.

7.2 Review of Magnetometry

There are many techniques for the measurement of magnetic moment, each with its own advantages and disadvantages. In this section a summary of those most used for the measurement of the magnetic moment of superconductors will be reviewed**[1]**, their principle of operation explained and their relative merits discussed**[2]**.

7.2.1 Dc. Extraction Technique

Possibly one of the most simple techniques, this involves completely removing the sample from a set of sense coils. This moving magnetic moment produces a total flux change in the coils that is directly related to the magnetic moment of the sample. This process is then repeated for different values of dc field to produce a magnetisation curve. As this technique uses incremental increases in field, it is a relatively slow technique, but with sensitivities around $1\mathrm{x}10^{-8}\mathrm{Am}^2$ operating from 4.2 K to room temperature.

7.2.2 Ac. Susceptometer

The measurement of susceptibility gives easy access to the magnetic moment of a sample. Two coils (primary coils) are connected in series to produce an ac magnetic field. Inside each of these coils is a smaller sense coil (secondary coils). The secondary coils are wound in opposition and carefully balanced to give no signal when the ac field is applied by the primary coil. The sample can then be placed inside one of the secondary coils so that the signals from the two coils no longer cancel, the difference being proportional to the susceptibility of the sample. This is a simple technique which requires no moving parts and gives sensitivities of approximately 1×10^{-11}Am^2 for equivalent magnetic moment and can be used at variable temperatures. In this measurement the dc field can be swept continuously giving a much faster measurement than the incremental field techniques.

7.2.3 Cantilever Magnetometer

This measurement is slightly different from the other techniques discussed in this chapter as it is a "force" technique in which a sample is placed in an inhomogeneous field and the force on the sample is measured. This force can be used to determine the magnetic moment of the sample. The experiment is usually performed using a micro-machined silicon cantilever beam. As the force on the sample increases, the beam bends and the motion of the end of the beam can be detected by measuring the change in capacitance of the gap between the end of the beam and a fixed plate underneath it. The sensitivities available vary from 1×10^{-8}Am^2 to 1×10^{-12}Am^2 depending on the size of the dc field, with the higher sensitivity being at high field. As with the ac susceptometer the field can be swept continuously giving a faster measurement speed.

7.2.4 *S*uperconducting *QU*antum *I*nterference *D*evice Magnetometer

SQUID magnetometry uses a feature of superconductors to allow incredibly sensitive measurement of magnetic moment. The Josephson Effect is used to measure, at the single fluxon level, the field within a set of sense coils. The technique is similar to a dc extraction technique, (section 7.2.1) but the sample is moved from one coil into another. This moving magnetic moment produces a change in field in the coils that is accurately determined using a SQUID. The sensitivity is around 1×10^{-10}Am^2 however the fact that the SQUID relies on a superconducting coils limits the field range within which this technique can be successfully utilised. As with the dc extraction technique the dc field must be changed incrementally and a point taken at each value, making this a relatively slow measurement.

7.2.5 Vibrating Sample Magnetometer (VSM)

This is one of the most well established techniques for measuring magnetic moment. Sensitivities are around the 1×10^{-10} Am^2 level, with measurements being possible easily as a function of field and temperature. The field may be swept continuously, giving high measurement speeds. The design considerations for a VSM will form the basis of the rest of this chapter and so will not be discussed further here.

7.3 The Vibrating Sample Magnetometer

The Vibrating Sample Magnetometer (VSM) was conceived by Simon Foner in 1956[3] and has become a widespread measurement system to allow the determination of magnetic moment as a function of both field and temperature[4][5]. In this section the principle of operation will be explained and some of the design considerations when constructing a VSM introduced.

7.3.1 Principal of Operation

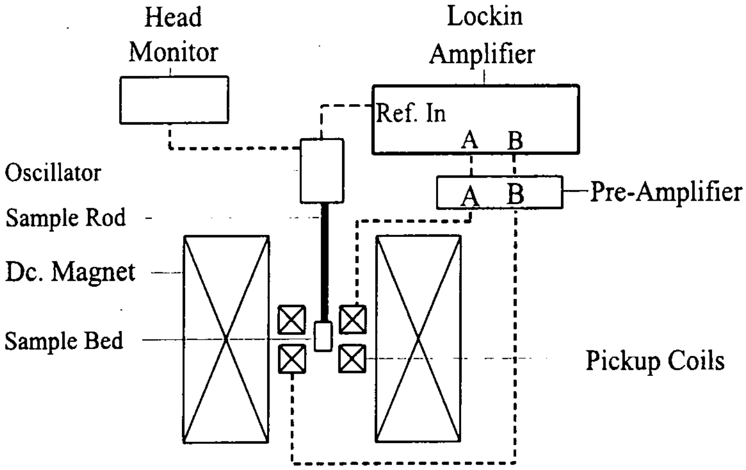

Figure 7.1 **Schematic showing the main components of a VSM system**

The VSM is based on Faraday's Law:

$$E = -A\frac{\delta B}{\delta t} \tag{1}$$

where E is the induced EMF, and A is a constant. The voltage is produced by moving the magnetic moment under study to produce a changing magnetic field.

A schematic of the experimental arrangement is shown in figure 7.1 The sample is vibrated by the oscillator at a fixed amplitude, measured by the head monitor, and a fixed frequency, which is fed to the lockin amplifier. A voltage is induced in the pickup coils, at the frequency of oscillation of the sample, amplified by the preamplifier and measured by the lockin amplifier. This voltage is directly proportional to the magnetic moment of the sample. This can be measured as a function of applied dc field to produce magnetisation curves as discussed in sections 2.4 and 2.5.3.

7.3.2 VSM Development and General Design Considerations

Since the first VSM was developed in the late 1950's the fundamental idea has remained unchanged. The main variations are in the design of the pickup coils used to detect the signal[6][7]. There are a number of other design constraints to consider when constructing a VSM[8][9]. The first to be considered is the space in which the system will operate, usually the bore of a superconducting magnet system. It is essential for the correct operation of a VSM that the pickup coils remain stationary, as any movement will produce spurious results and noisy signals. The pickup coils are therefore normally fastened to the bore of the magnet to prevent movement. Some form of variable temperature insert is then used to allow the sample rod to be positioned in the centre of the pickup coils and the temperature of the sample space varied. Pickup coil designs are varied, usually depending on the space available, the sensitivity required and the size of sample to be measured. To minimise the noise in the system the source of vibration must be uniform, stable and well isolated from the pickup coils and the dc magnet. The sample must oscillate in the pickup coils, centred both radially and axially.

7.4 VSM System in Durham

In this section the VSM system in Durham will be introduced. The original design and construction will be discussed and the sensitivity and limitations presented. Then the modifications made will be explained along with the reasoning behind them. Finally the procedure for operating the VSM will be given including sample mounting and noise reducing procedures.

7.4.1 Original Design

In Durham we have a 15/17T superconducting magnet with a 40 mm bore. A VSM system was required that could operate inside this magnet, and that could be inserted and removed whilst the magnet was cold. A system was designed and commissioned by R. Luscombe with these considerations in mind**[10]**. It was found that due to flux jumping within the 15/17T magnet below 1.5T, a low field insert was required to allow the acquisition of good low field data. The pickup coils were designed following the work of Springford et al**[6]** to have maximum sensitivity with minimum sensitivity to sample positioning. This resulted in coils of inner radius 12.92 mm, outer radius of 15.0 mm, length of 11.02 mm and spacing of 18.1 mm. This gave a 4 mm space in the centre of the coils where the signal was independent of position. The sensitivity of this system was determined to be $0.240\mathrm{Am^2V^{-1}}$. The thermometry consisted of a carbon glass thermometer and a capacitance thermometer in a block at the bottom of the coil set. Two heaters were used to minimise the thermal gradients and improve temperature stability. One was a foil heater around the inside of the pickup coils and the second was a wire wound heater mounted above the pickup coils. This combination of thermometers and heaters gave a temperature accuracy of ± 200 mK in the temperature region of interest for this work, and a temperature stability of better than ± 50 mK.

7.4.2 Problems with Original Design

There were a number of problems with the original system. As discussed in section 7.3.2, it is essential that the pickup coils do not move. With the original system there is no method for fixing the VSM insert with respect to the superconducting magnet. The second problem was that in order to maintain temperature stability and minimise helium consumption, it was necessary to surround the pickup coils and thermometry block in superinsulation. This prevented them from being securely fastened to the steel tube that formed the outside of the VSM insert. This meant that it was possible for the vibration of the sample rod to cause the pickup coils to move at the frequency of measurement, producing noise that the lockin amplifier cannot filter out. The other main problem was that the sensitivity of the coils means that small signals were being produced that were comparable to the noise floor on the lockin amplifier at the measurement frequency. A final problem was that the sample rod and the support for the pickup coils were made from different material. This meant that differential contraction between the two prevented accurate positioning of the sample inside the pickup coils. The results of these problems resulted in noise levels of $1\text{x}10^{-4}\text{Am}^2$ on a nickel sample and $1\text{x}10^{-5}\text{Am}^2$ on a superconductor in high field.

7.5 Probe Modifications

The following three sections give the solutions to the problems of the original design and result in significant improvements in the quality of the data produced.

7.5.1 Secure Mounting for Pickup Coils

In order to overcome the problems of the moving pickup coils, it was found that the VSM insert must be securely fastened within the magnet bore and that the pickup coils must then be securely mounted within the VSM insert. The first was done using a set of "legs" on the outside of the VSM that allowed the fixing of the small dc coil, and hence the rest of the probe to the magnet bore. A cone was made from tufnol and placed on top of the small dc coil. The steel legs with rounded brass "feet" (to avoid damage to the magnet bore) were then screwed down from the magnet neck fitting to wedge the probe firmly into the magnet bore (figure 7.2).

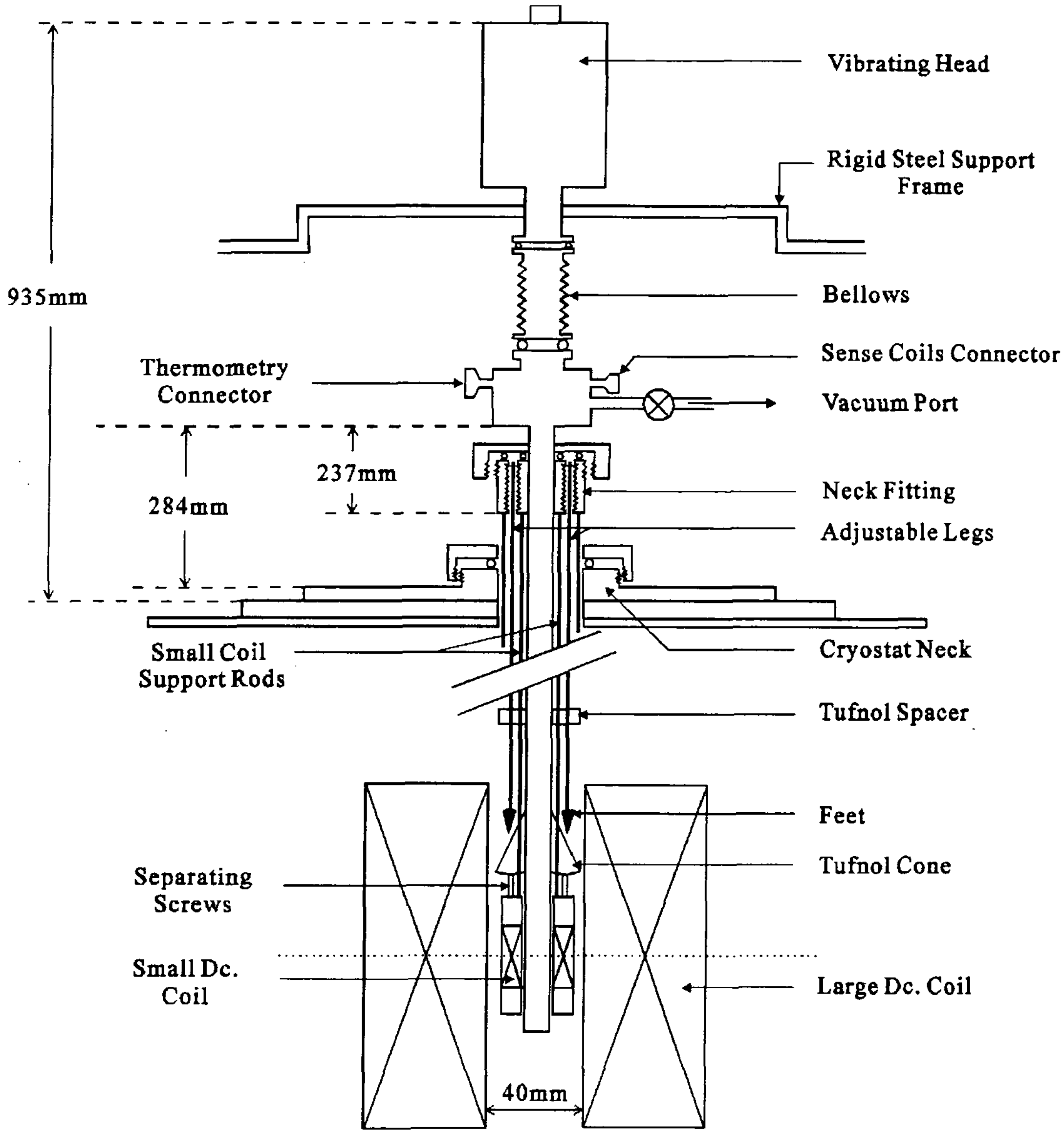

Figure 7.2 Design of legs and feet, to secure the VSM insert within the magnet bore.

Once the low field insert was held fast, this meant that the outer stainless steel tube was also held stable. Thermal consideration meant that it was not possible to remove the superinsulation so instead the system in figure 7.3 was adopted to allow rigid mounting of the pickup coils to the outer stainless steel tube and still allow the superinsulation around the pickup coils and thermometry block.

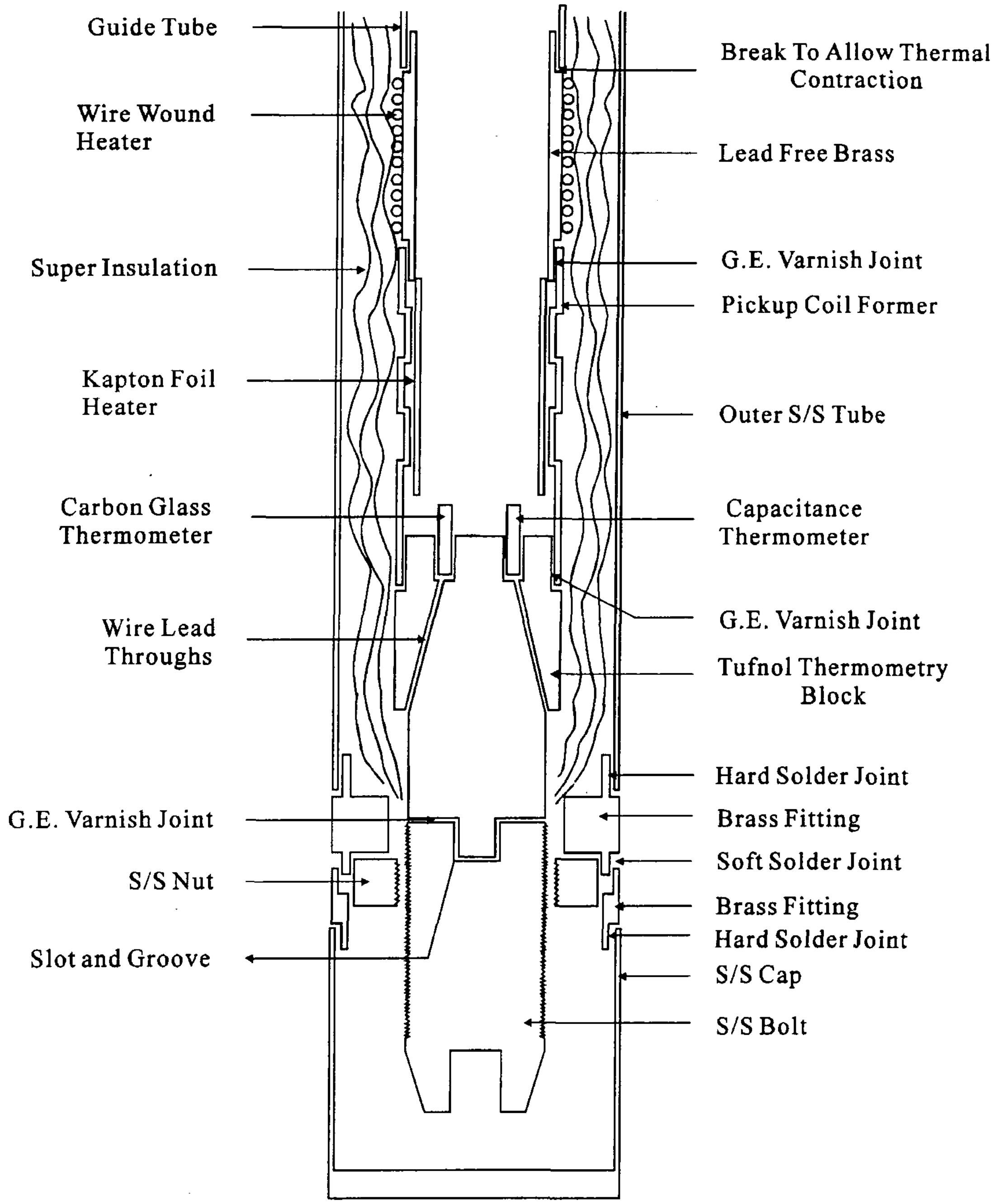

Figure 7.3 Fixing the pickup coils to the bottom of the stainless steel jacket. The thermometry block was extended using a steel bolt which, when the outer stainless steel tube was placed over the pickup coils, protruded through a hole. The thermometry block and pickup coils could then be held firmly in place by a nut. The steel cap is then soft soldered over the end to provide a vacuum seal. The brass fittings were used to aid the soft soldering so as to reduce the heat that reached the thermometry and pickup coils. A break was introduced into the guide tube above the pickup coils to avoid any

problems with differential thermal contraction between the guide tube and the outer stainless steel tube.

7.5.2 Sample and Pickup Coil Positioning

To investigate the problem of differential thermal contraction of the sample rod with respect to the probe and to the magnet, the field centre of the magnet was determined by mounting a field sensitive resistor on to the sample rod.

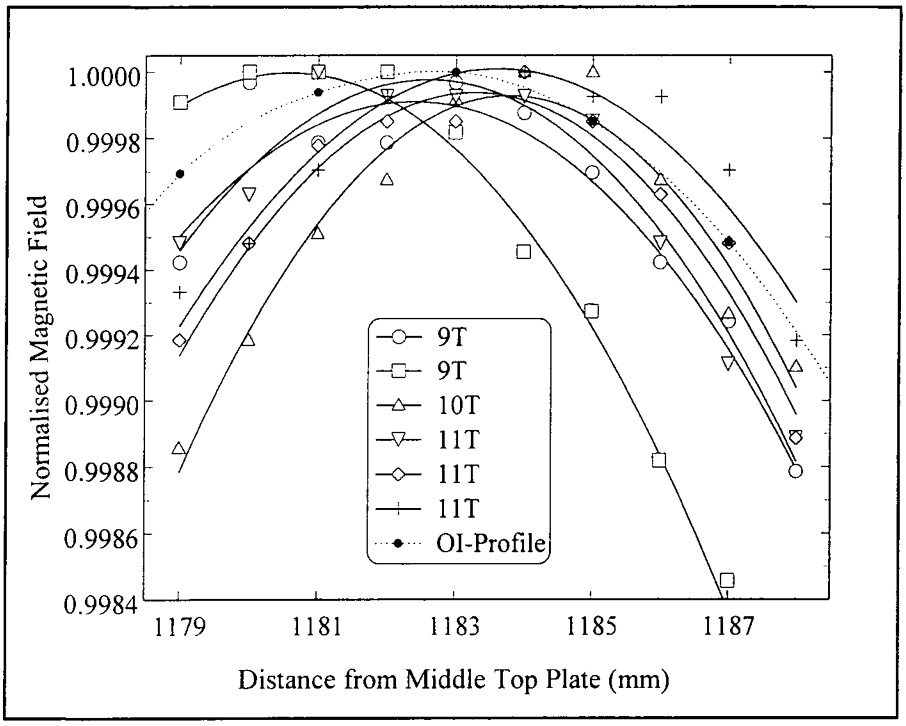

Figure 7.4 Determination of the field profile using an Allen Bradley resistor.

The resulting field profiles are shown in figure 7.4, with the scatter on the data being 2 parts in 10^4. The average position of the peaks measured was taken to be the field centre. The profile supplied by Oxford Instruments for the magnet is also shown in the figure, the dotted line is a smooth curve through the points centred on the average measured field centre at 1183mm.

It can be seen from figure 7.4 that the measured field profile inside the VSM insert is sharper than is provided by the magnet alone. This increased field inhomogeneity becomes important in chapters 8 and 9.

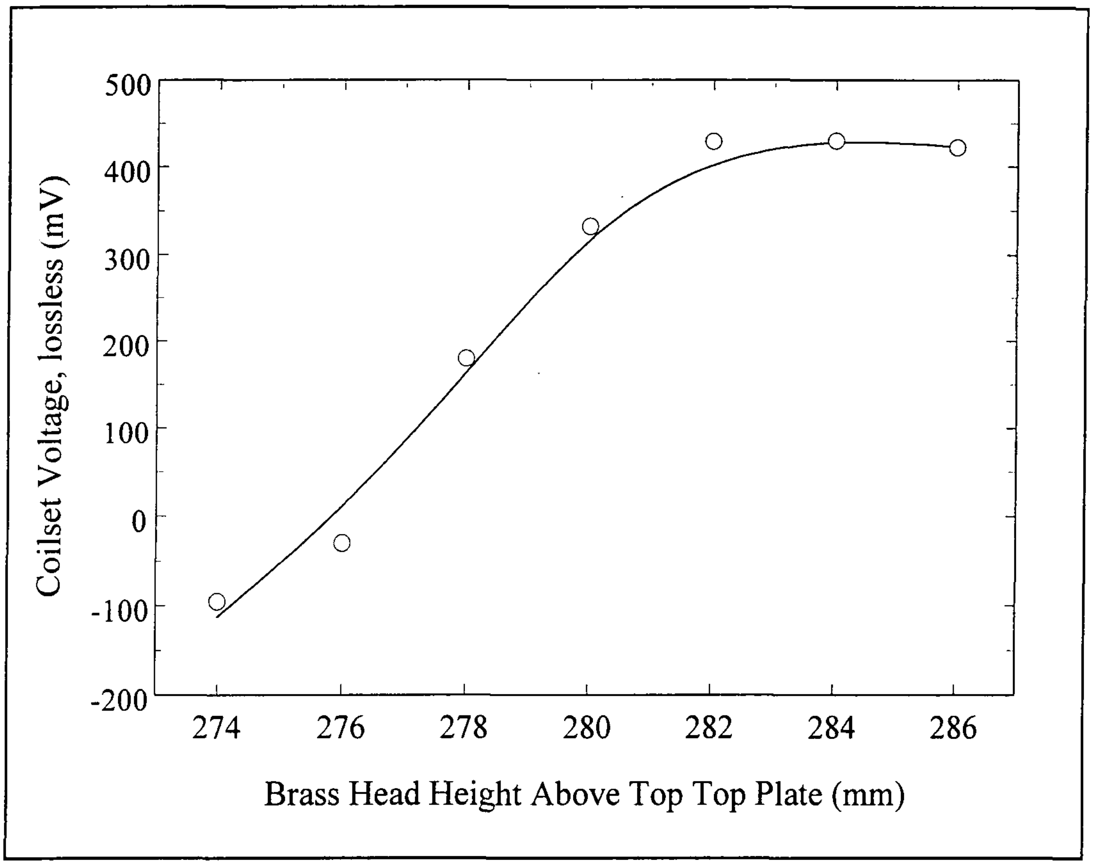

Figure 7.5 **Coilset voltage induced in the pickup coils as a function of distance, allowing the experimental determination of the pickup coil centre.**

Once the centre of the field had been determined, a small superconducting sample was placed on the sample rod, in the field centre and the pickup coils moved to allow the determination of the centre of the pickup coils (figure 7.5).

7.5.3 Use of a Preamplifier

The problem of the sensitivity and the noise floor of the lockin were overcome by introducing a preamplifier into the circuit. With a fixed gain of 100 this gave a better sensitivity, allowing the measurement of smaller magnetic moments without hitting the noise floor on the lockin. The introduction of the amplifier does cause problems for the measurement of large samples, when the lockin amplifier is overloaded. However the amplifier can simply be removed as the signal is large enough for it not to be necessary

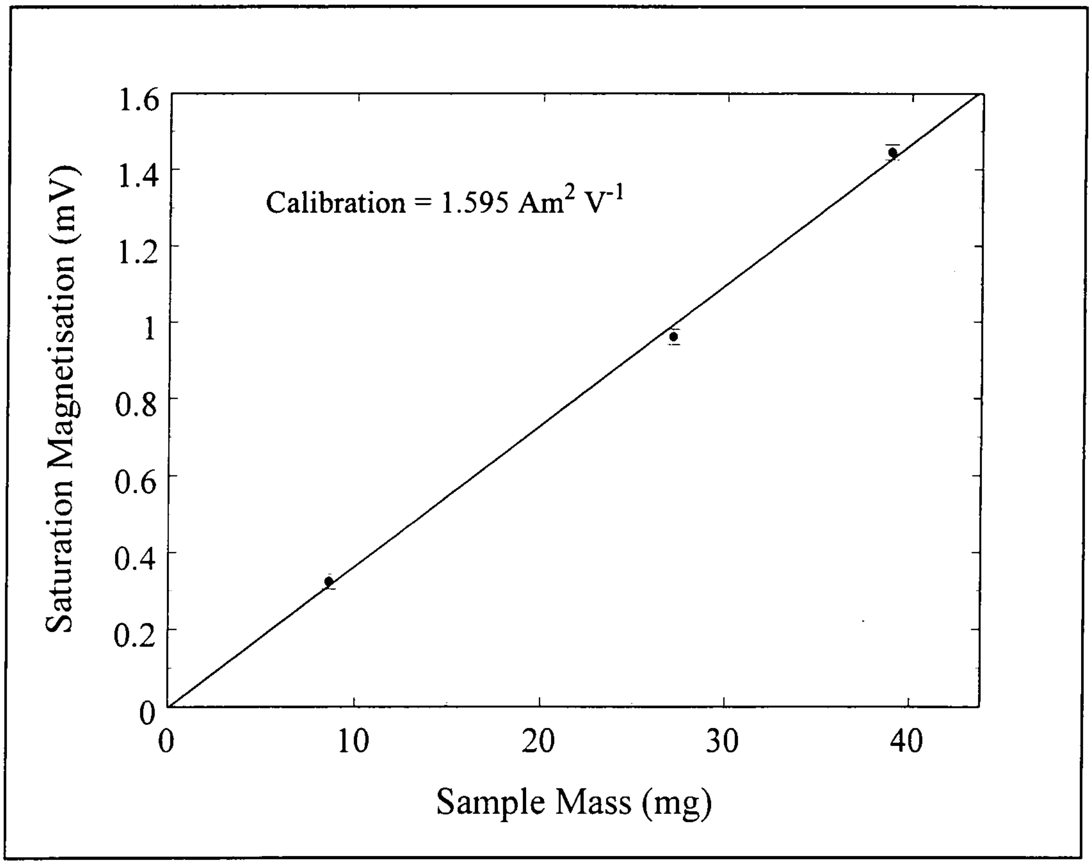

Figure 7.6 **Calibration for the VSM system determined using the saturation magnetisation for three nickel samples.**

The sensitivity was determined using three nickel sample as is shown in figure 7.6. The calibration for the system is $1.595\times10^{-2}\text{Am}^2\text{V}^{-1}$ as determined from a straight line fit through the data points.

7.6 Operating Procedure for the Durham VSM

This section gives a brief overview of the operation of the VSM system in Durham including a measurement schematic, sample mounting techniques and noise reduction procedure.

7.6.1 Experimental Setup

The system should be setup in the magnet as the dimensions in figure 7.2 describe, with the pressure maintained inside the system at 80 Torr of helium gas. The "legs" should be screwed down evenly into the bore of the magnet to hold the low field insert both firm and central.

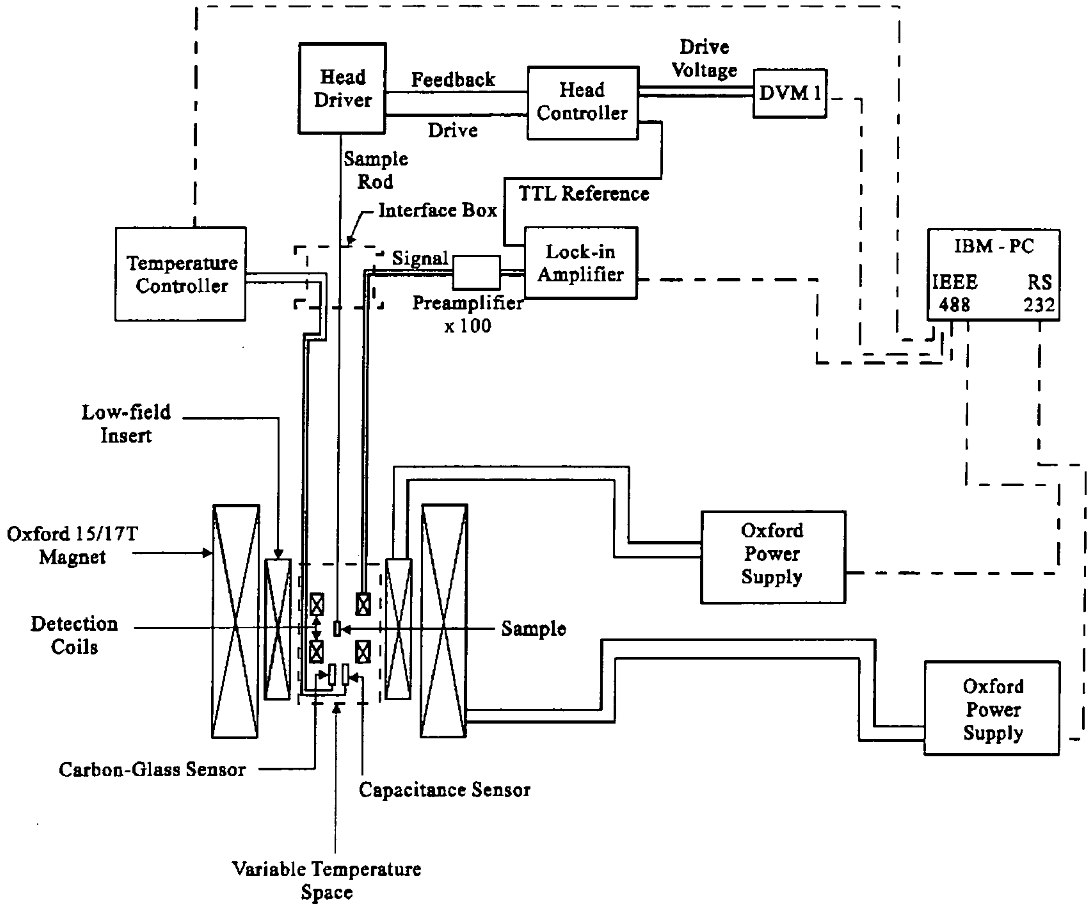

Figure 7.7 **Schematic of the wiring and instrumentation for the VSM system in Durham.**

All the instrumentation should be connected as shown in figure 7.7 and allowed to warm up.

7.6.2 Sample Mounting and Positioning

It is essential for this measurement that the sample does not move with respect to the sample rod. Bulk sample can be mounted directly on to the sample bed, using PTFE tape, which is non-magnetic, within the sensitivity of this system. It was found that wire samples could not be held sufficiently still using PTFE tape. The best way to mount wires is to pot short lengths of the sample in epoxy to form a regular shape with a large flat side. This could then be mounted with PTFE tape as for the bulk samples. The position of the sample on the sample bed should be noted to allow accurate positioning within the pickup coils.

7.6.3 Noise Reduction Procedure

Once the sample is inside the system and the rod is vibrating, the frame should be adjusted to minimise the audible rattling heard within the magnet. This rattling is caused by the sample rod touching the internal guide tube. This rattling is transferred to the pickup coils where it produces vibration and hence voltage noise that the lockin amplifier cannot remove.

7.6.4 Running the System.

The system is computerised using GPIB and RS232 protocols to allow the automated measurement of magnetisation loops for fields up to 15T and for temperatures for 4.2 K up to 30 K. The system can measure fourier components of the signal from 1f to 10f, though the speed of the measurement is reduced when more than one component is measured, to allow for time for the lockin to stabilise every time the frequency is changed.

7.7 Experimental Results

7.7.1 Sample Space Temperature

Once these improvements had been made it was necessary to recalibrate the thermometry in the probe to ensure the correct relation between the sample space temperature and the carbon glass sensor in the thermometry block.

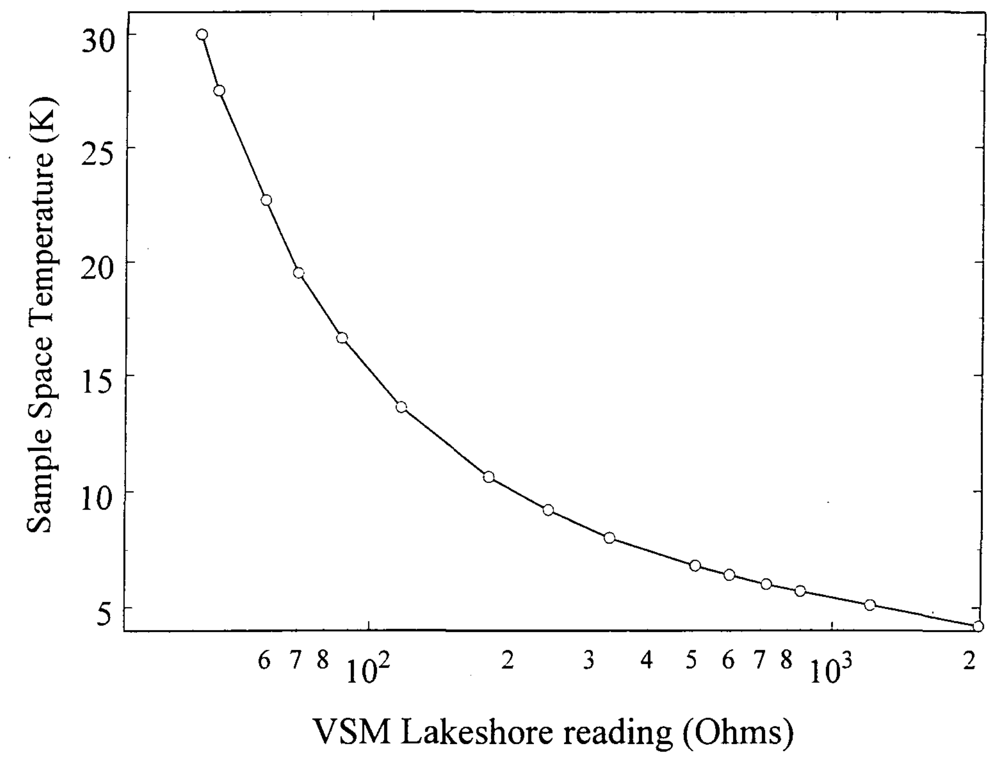

Figure 7.8 **Temperature calibration of sample space against the measured carbon glass resistance using the VSM Lakeshore.**

This was done by mounting an additional carbon glass sensor on to the sample space and performing a static temperature measurement (figure 7.8). The sample temperature is therefore known to better than 0.2 K for temperatures from 4.2K to 30K, with stability of better than ± 50mK.

7.7.2 Driver Sinusoidality

In order to perform the higher frequency measurements required to support the calculations of chapter 8, it was necessary to determine the sinusoidality of the driver vibration.

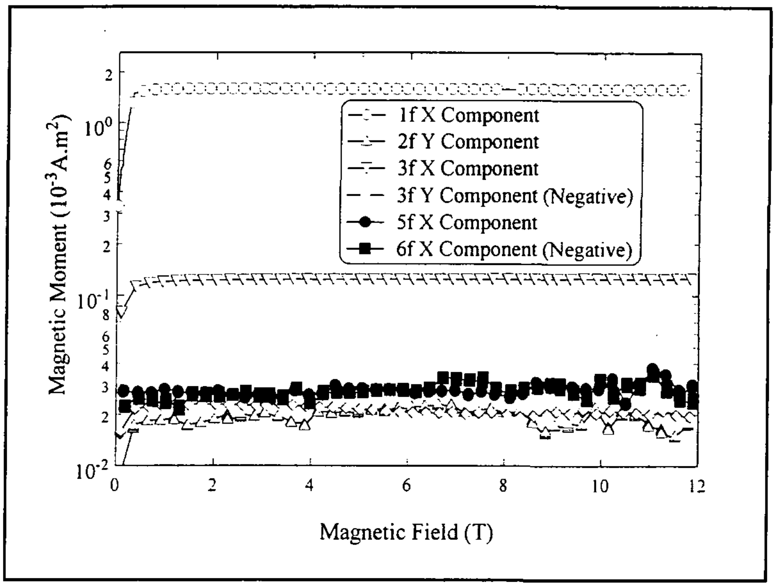

Figure 7.9 **Magnetic moment of a nickel sample for multiples of the driver frequency with large components of the 1f magnetic moment.**

Frequency (Multiples of 1f)	Lossless Voltage Percentage of 1f Lossless Voltage	Loss Voltage Percentage of 1f Lossless Voltage
1f	100	0.0
2f	-0.1	1.2
3f	7.5	1.2
4f	0.12	0.25
5f	1.6	-0.4
6f	1.6	0.2
7f	0.7	0.1
8f	0.1	0.1
9f	0.1	0.03
10f	0.03	0.03

Table 7.1 **The anharmonicity of the driver determined using a nickel sample phased to make the 1f lossless voltage a maximum.**

This was done by measuring integer multiples of the driver frequency up to 10f for a nickel sample. The results of this measurement can be seen in figure 7.9 and are tabulated in table 7.1. There is a significant contribution in the 3f lossless voltage at approximately 7 percent of the 1f lossless voltage. The other voltages have values less than two percent of the 1f lossless voltage. These results means that when measuring the hysteretic region of the magnetisation loop of a superconductor, the higher frequency voltages measured will be hysteretic at the level given by table 7.1.

7.7.3 Noise Level Determination

In order to determine the minimum achievable noise level in this magnet system, the vibration was switched off and the signal in the pickup coils measured as a function of field at each of the frequencies from 1f to 10f, both in the field centre and with the pickup coils 5 cm above the field centre.

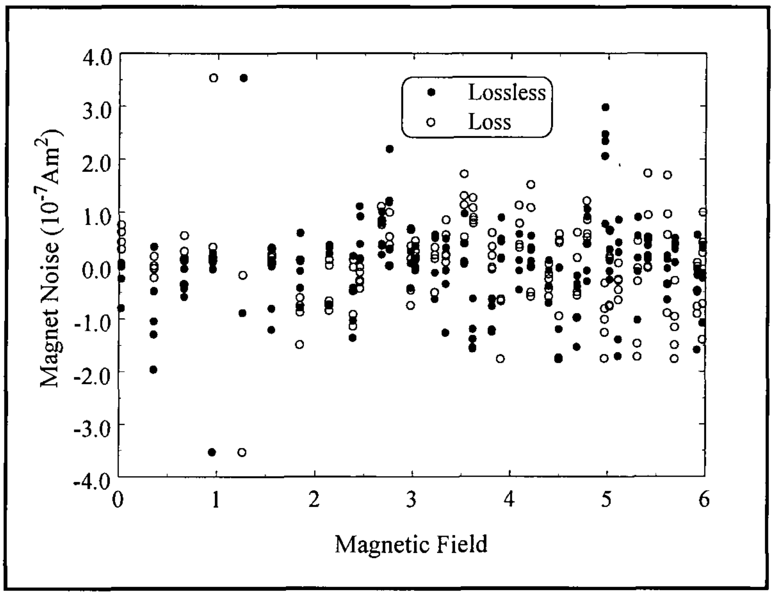

Figure 7.10 The magnet noise in the pickup coils at field centre in the 1f lossless and loss components with no vibration of the sample rod.

Figure 7.10 shows the 1f frequency, lossless and loss components at field centre and figure 7.11 at plus 5 cm with a time constant of 300ms. The results for these and other frequencies are summarised in table 7.2. The noise is always centred about zero.

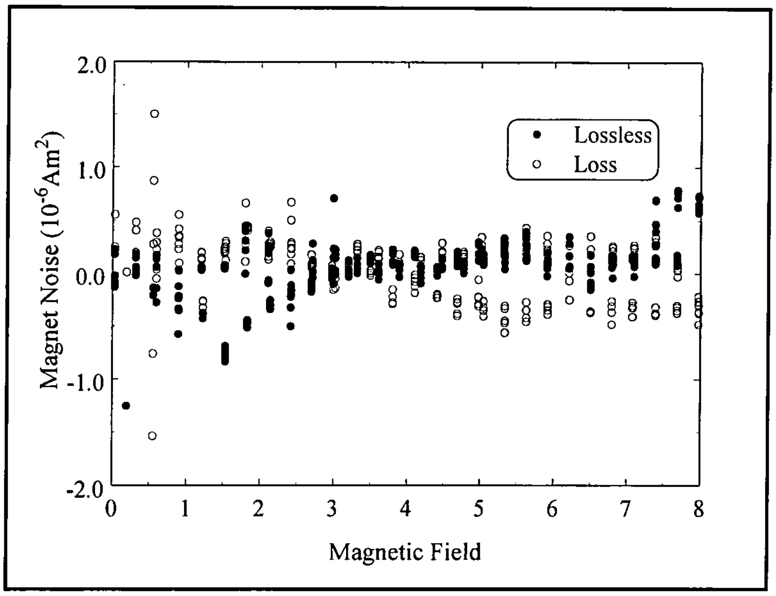

Figure 7.11 **The magnet noise in the pickup coils at plus 5cm in the 1f lossless and loss components with no vibration of the sample rod.**

Harmonic	Magnet Noise Field Centre Am^2	Magnet Noise Plus 5cm Am^2
1	2 x 10^{-7}	7 x 10^{-7}
2	1 x 10^{-7}	2 x 10^{-6}
3	1 x 10^{-7}	2 x 10^{-6}
4	1 x 10^{-7}	1 x 10^{-6}
5	7 x 10^{-8}	1.5 x 10^{-6}
6	7 x 10^{-8}	1 x 10^{-6}
7	5 x 10^{-7}	1 x 10^{-6}
8	5 x 10^{-8}	1 x 10^{-6}
9	5 x 10^{-8}	1 x 10^{-6}
10	5 x 10^{-8}	1.5 x 10^{-6}

Table 7.2 **Peak to peak noise measurement for magnet noise with the pickup coils at field centre and 5 cm above the field centre.**

These noise levels are large compared to commercial available VSM's however the magnet system in Durham is made with jellyroll Nb_3Sn superconducting wire, which is expected to be more noisy than the wire used for magnets in purpose built commercial VSM systems. It can also be seen that the noise is considerably larger in all harmonics when the pickup coils are moved from the field centre. The noise between 0 and 2T is due to flux jumping in the Nb_3Sn sections of the magnet and is avoided by using the low field insert.

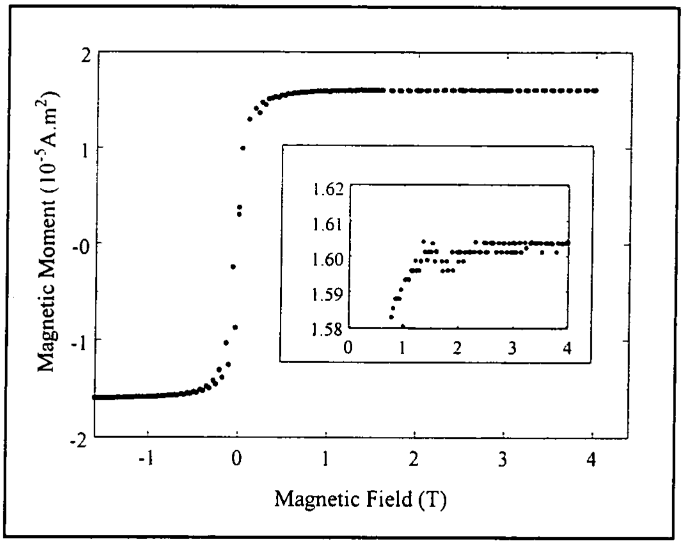

Figure 7.12 **Measurement of a nickel calibration sample giving an indication of the noise level. The inset plot shows the saturation value.**

To demonstrate the noise level on a measurement, a nickel calibration measurement is shown in figure 7.12 where the peak to peak noise level on the saturated magnetic moment can be seen to be ~$2x10^{-7}Am^2$. This compares well with the limiting noise of the magnet.

7.8 Comparison with Commercial Systems

VSM's are commercially available with good sensitivity but are not as flexible as the system developed in Durham. Figure 7.13 shows a comparison between data taken on 3 VSM's, two commercial systems (I.R.C. Cambridge and Birmingham University, taken by Dr Zheng and Dr Hampshire) and the inhouse system developed in Durham. The data from Birmingham was taken with the sample orientated transverse to the applied field and the data was scaled by a factor of 2.8 to account for the geometry.

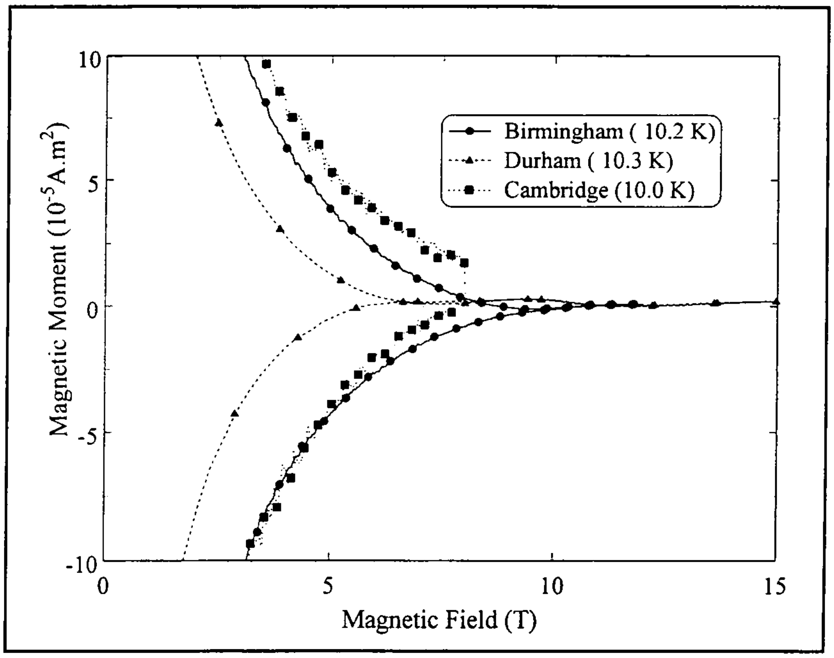

Figure 7.13 **1f lossless magnetic moment for $PbMo_6S_8$ to allow comparison between commercial and in house VSM's**

The data is comparable in noise to the commercial equipment, though the background is not as smooth. By using our system we have access to fields of 15T, higher than those usually available from commercial systems. In addition the magnet does not have to be dedicated for use with the VSM.

7.9 Conclusions

The VSM is an incredibly powerful measurement for characterising superconducting materials. In Durham we possess a system that can operate as an insert in a standard superconducting solenoid magnet with a 40mm cold bore. The sensitivity is $1.595\text{x}10^{-2}Am^2V^{-1}$. Design improvements have decreased the noise level of the system to $2\text{x}10^{-7}Am^2$. This system allows the measurement of magnetic moment in fields up to 15T and temperatures up to 30 K ± 0.2 K with a stability of better than 50 mK. There is the possibility of measuring any integer multiple of the driver frequency, at any position within the magnet bore. This allows the measurement of the Fourier components of the magnetic moment of samples in large field gradients as is required to support the calculations in chapter 8.

7.10 References

[1] Foner S, *IEEE Trans. on Magn.* **17** 3358 1981

[2] A Buyer's Guide to Magnetometer Specifications *Oxford Instruments Technical Bulletins* (1998)

[3] Foner S *Rev. Sci. Inst.* **27** 548 (1956)

[4] Foner S *Rev. Sci. Inst.* **30** 548 (1959)

[5] Foner S *J. Appl. Phys.* **79** 4740 (1996)

[6] Zieba A and Foner S *Rev. Sci. Inst.* **39** 1344 (1982)

[7] Miller L L *Rev. Sci. Inst.* **67** 3201 (1996)

[8] Springford M, Stockton J R and Wampler W R *J. Phys. E* **4** 1036 (1971)

[9] Hoon S R and Willcock S N M *J. Phys. E* **21** 772 (1988)

[10] "Design and Development of a Vibrating Sample Magnetometer for High Magnetic Field Measurements of Superconductors" Luscombe R *MSc Thesis, University of Durham* (1994)

Chapter 8
Calculations for the Measurement of the Magnetic Moment of a Superconducting Sample using a Vibrating Sample Magnetometer

8.1 Introduction to Chapter 8

Magnetic measurement techniques are numerous, one of the most popular being the vibrating sample magnetometer. It is an incredibly powerful tool for characterising magnetic materials[1] and in particular superconductors. It gives information on almost all the critical phenomena that are associated with superconductors including the Ginzburg Landau coherence length, penetration depth and kappa [2]; critical current density[3]; upper and lower critical fields; irreversibility fields and thermal activation energies [4].

In this chapter the measurement of the critical state of superconductors using a vibrating sample magnetometer will be modelled. This modelling will include the effect of field gradient on the sample and the exact positioning of the sample within a pair of counter wound pickup coils to produce a series of predictions as to the voltages measured at multiples of the measurement frequency. The model used is based on Bean's Critical State Model[5] for the calculation of the magnetic moment of the sample and then Mallinson's Principle of Reciprocity[6] to calculate the voltage induced in a set of pickup coils by the magnetic moment of the sample.

Firstly the calculations will be shown for a superconducting cylinder of length l and radius r_m, with a linear J_C vs B relationship, sections 8.2 to 8.6. Once this has been done, results of further calculations will be presented without showing the full mathematical treatment. The mathematics will be extended to include the effect of the positioning of the sample within the pickup coils, section 8.7, and within the dc field profile, section 8.8, including the case of a sample which is perfectly centred within the dc field. A slab shape sample geometry will be considered in section 8.9. A variety of different superconducting samples will then be investigated in section 8.10, using well accepted functional forms for the field dependence of their critical current density. Section 8.11 will provided a summary of the results of the calculations for the different experimental geometries considered. Section 8.12 will include a discussion of the irreversibility field in the literature and the implications of this work considered and the conclusions of this chapter will be discussed in section 8.13. All the calculations presented were performed analytically using Maple V Release 4 on both UNIX and pc platforms.

The irreversibility field, defined as the point at which a magnetisation curve becomes reversible, will be shown to depend on sample geometry and on the homogeneity of the magnet system, and not the point at which the critical current density of the superconductor goes to zero.

8.2 Parameters for the Calculation

In this section all the parameters required for the calculation of the sample magnetic moment will be introduced and explained, with the choice of values justified. All the calculations were performed analytically and the numerical values were substituted in at the end to allow maximum accuracy in the determination of results.

8.2.1 Sample Geometry

The geometry for all the samples is a cylindrical sample of length l and of radius r_m unless otherwise stated. This both simplifies the mathematics and is appropriate for comparison with many experimental results. The length was taken to be 4 mm where numerical values were required and r_m was taken to be 1 mm unless otherwise stated. An additional result is included in section 8.9 where the results were evaluated for a slab geometry. All the samples were orientated with their longest dimension parallel to the applied field.

8.2.2 Critical Current Density Functional Forms

The first calculations shown are all performed using a linear field dependence for the critical current density. This allows for ease of interpretation of the results and any deviation from linear behaviour can be seen. The functional form used for the critical current density J_C was:

$$J_c = \alpha(B_{C2}-B) \quad (1)$$

where B is the applied dc magnetic field, α is a constant, taken to be 5×10^5 $Am^{-2}T^{-1}$ and B_{C2} is the upper critical field taken to be 10 T to mimic the behaviour of NbTi, a well understood, conventional superconductor.

As the focus of the work in the rest of this thesis is on Chevrel phase materials, a Kramer dependence[7]was considered next, as this is found to apply to these and other low temperature superconductors (eg. Nb_3Sn). The functional form chosen was:

$$J_c = \frac{\alpha}{B^{1/2}}(B_{C2}-B)^2 \qquad (2)$$

where B_{C2} is the upper critical field, α is a constant and B is the applied dc field.

Finally, to cover the high temperature superconductors an exponentially decaying critical current density[8] was chosen, which by definition has no irreversibility field as J_C never reaches zero. The functional form is:

$$J_C = \alpha e^{-\frac{B}{\beta}} \qquad (3)$$

where α and β are both constants. These latter functional forms, equations 8.2 and 8.3, are used in section 8.10 to extend the first calculations for the NbTi-like model to a more general set of materials. The broad features seen for the three functional forms chosen will in fact be seen in all superconducting materials.

8.2.3 Definition of the ac Field

The movement of the sample through an inhomogeneous magnetic field means that the applied field varies as the sample moves. For a sample that is positioned so that it does not cross the centre of the dc field profile, the changing field is sinusoidal with period 2π/ω, where ω is the angular frequency of the vibration of the sample, and can be considered as a simple ac field whose amplitude is some fraction of the dc applied field given by:

$$B_{ac} = |\delta B_{Magnet}/\delta x| . \frac{D}{2} \qquad (4)$$

where D is the throw distance, i.e. the peak to peak amplitude of the vibration of the sample, and $\delta B_{Magnet}/\delta x$ is the change in field experienced by the sample as it moves from one extreme of the throw to the other. When the sample is positioned and vibrated such that it crosses the centre of the dc field profile the variation in field is no longer sinusoidal, though it is still periodic, with period $2\pi/\omega$. This special case will be discussed in more detail in section 8.8. For the rest of the calculations, it will be assumed that the sample does not cross the centre of the dc field profile during its vibration. This will allow comparison with the experimental result in chapter 9. The amplitude of the sinusoidal ac field is determined from equation 8.4. In order to emphasise the effect under investigation the ac field was initially taken to be one part in a thousand of the dc field, and to simplify the calculation the field profile was taken as a roof profile, linear decreases either side of a maximum at the field centre. The frequency of vibration was taken as 100Hz as this is typical for VSM systems and is assumed to be quicker than the dc field sweep rate.

8.2.4 Definition of Gamma

For the calculations we define a parameter gamma (γ) which is the ratio of the ac field and the self field produced by the sample and is given by:

$$\gamma = \frac{B_{ac}}{\mu_0 J_c r_m} \qquad (5)$$

where B_{ac} is the effective ac field, as defined in equation 8.4, J_C is the critical current density and r_m is the radius of the sample. Gamma is one when the ac field is equal to the self field of the sample. The mathematics is divided into two regimes. The low field regime is gamma less than 1, and the high field regime is gamma greater than or equal to 1.

8.3 Low Field Regime Calculation

This section covers the low field calculations i.e. gamma < 1. The calculations have been performed using the linear field dependence of critical current density (equation 8.1) with $\alpha = 5\times10^5 \mathrm{Am^{2}T^{-1}}$ and $B_{C2} = 10$ T.

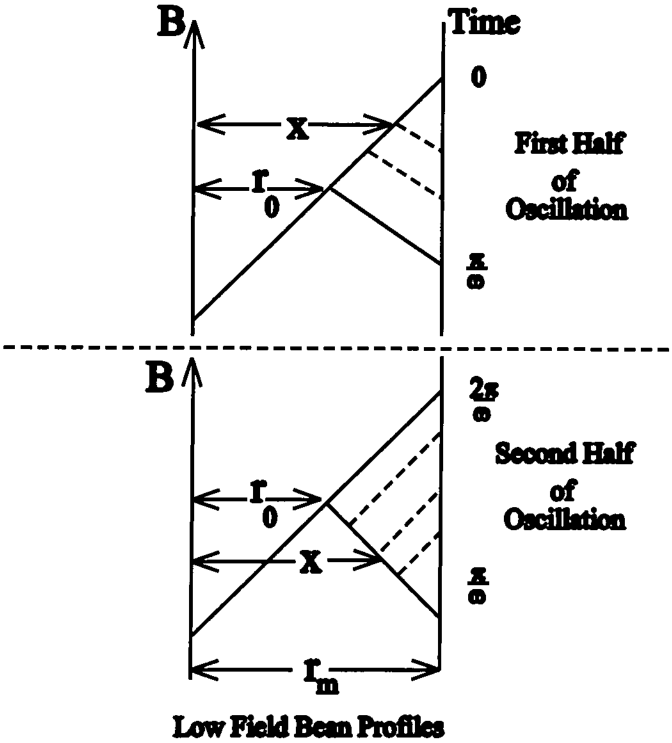

Figure 8.1 Low field Bean profile across a sample of radius r_m for both the first and second halves of the oscillation.

In the low field region we can construct a Bean profile (figure 8.1) considering both the ac and dc components of the applied field. The sample has radius r_m, the point to which the dc field penetrates is r_0 and the point where the ac field gradient changes is x. The sample moves with angular frequency ω and the time is defined equal to zero when the applied field is at its highest value. Hence as the sample moves it sees a decreasing field until a time π/ω, the first half of oscillation, and then an increasing field until a time $2\pi/\omega$, the second half of the oscillation, as it returns to its original position.

8.3.1 First Half of the Oscillation

This is considering the sample moving from the highest dc field to the lowest dc field within the throw distance. From the Bean profile (figure 8.1) it is possible to determine the movement of the turning point in the ac field (x) as a function of time, to be:

$$x = r_m\left(1-\frac{\gamma}{2}\left(1-\cos(\omega t)\right)\right) \tag{6}$$

where r_m is the radius of the sample, γ is as defined in equation 8.5 and ω is the angular frequency of the sample movement. Also from the Bean profile it can be seen that the field gradient within the sample can divided into three sections across the radius of the sample:

$$
\begin{aligned}
0 < r \leq r_0 \qquad & \frac{\delta B}{\delta r} = +\mu_0 J_C \\
r_0 < r \leq x \qquad & \frac{\delta B}{\delta r} = +\mu_0 J_C \\
x < r \leq r_m \qquad & \frac{\delta B}{\delta r} = -\mu_0 J_C
\end{aligned}
\tag{7}
$$

where r_0 is the distance from the centre of the sample to the maximum distance penetrated by the ac field, x is as defined in equation 8.6 and r_m is the radius of the sample. The gradient is positive from $r = 0$ to $r = r_0$ and from $r = r_0$ to $r = x$, and negative from $r = x$ to $r = r_m$, the radius of the sample.

Knowing the field gradients within the sample (equation 8.7) and hence the currents flowing, it is possible to calculate the total magnetic moment of the sample as a sum of the individual current loops (I) over the areas in which they flow (A), hence:

$$
\begin{aligned}
m &= \sum I.A \\
&= \int_0^x J_C \pi r^2 dr.l - \int_x^{r_m} J_C \pi r^2 dr.l \\
&= \left(\frac{J_C \pi l}{3}\right)\left(2x^3 - r_m^3\right)
\end{aligned}
\tag{8}
$$

where l is the length of the sample.

8.3.2 Second Half of the Oscillation

The second half of the motion, i.e. the dc field increasing from lowest value to the highest within the throw distance (figure 8.1) is now considered. The turning point in the ac field is defined by:

$$x = r_m\left(1-\frac{\gamma}{2}(1+\cos(\omega t))\right) \tag{9}$$

The field gradients can be seen from the Bean profile (figure 8.1) and are:

$$\begin{aligned} 0 < r \le r_0 \qquad & \frac{\delta B}{\delta r} = +\mu_0 J_C \\ r_0 < r \le x \qquad & \frac{\delta B}{\delta r} = -\mu_0 J_C \\ x < r \le r_m \qquad & \frac{\delta B}{\delta r} = +\mu_0 J_C \end{aligned} \tag{10}$$

The magnetic moment(m) can be calculated by integrating the smaller loops over the volume of the sample giving:

$$\begin{aligned} m &= \sum IA \\ &= \int_0^{r_0} J_C \pi r^2 dr.l - \int_{r_0}^{x} J_C \pi r^2 dr.l + \int_x^{r_m} J_C \pi r^2 dr.l \\ &= \frac{J_C \pi l}{3}(2r_0^3 - 2x^3 + r_m^3) \end{aligned} \tag{11}$$

where r_0 is the distance over which the dc field penetrates the sample. It can be determined geometrically from the Bean profile (figure 8.1) to be given by:

$$r_0 = r_m(1-\gamma) \tag{12}$$

8.4 Extension to High Fields

Now consider extending the maths from the low field case, section 8.3, to the high field case where the ac field is greater than or equal to the field required to fully penetrate the sample.

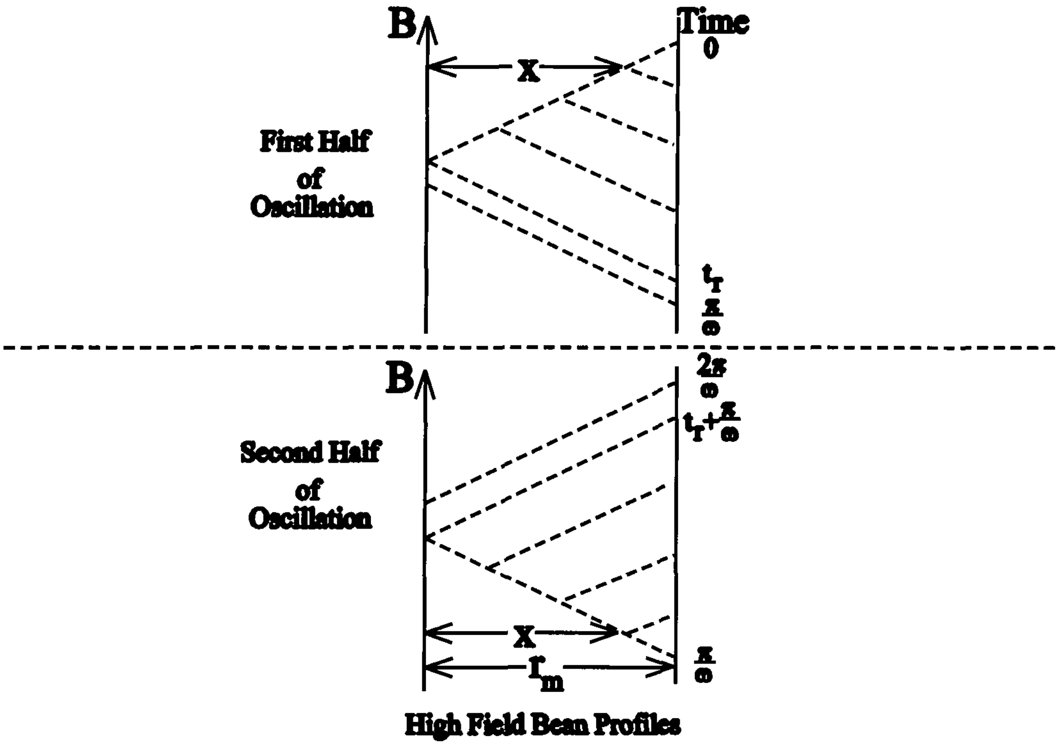

Figure 8.2 High field Bean Profile, with the sample being fully penetrated by the ac field at a time t_r, at which point x = 0. As the dc field increases again, x moves from 0 to r_m, again in a time t_r.

When in the high field regime, the ac field takes a time t_r to fully penetrate the sample, defined by:

$$t_r = \frac{1}{\omega}\arccos\left(1-\frac{2\mu_0 J_c r_m}{B_{ac}}\right) \qquad (13)$$

where ω is the angular frequency of the sample motion, J_C is the critical current density, r_m is the radius of the sample and B_{ac} is the effective ac field as defined in equation 8.4. Hence in the high field regime the motion of the sample can be divided into 4 sections. The first is as the ac field penetrates the sample up until a time t_r, when the sample is fully penetrated. The sample remains this way until the end of its throw at time π/ω. As the sample changes direction the ac field is reversed between time π/ω and time $t_r + \pi/\omega$. The sample remains in this state until time $2\pi/\omega$ when the whole cycle repeats. This is all shown in the Bean profile in figure 8.2.

8.4.1 First Half of the Oscillation

First consider how the turning point of the ac field moves with time, given by:

$$x = r_m\left(1-\frac{\gamma}{2}(1-\cos(\omega t))\right) \ , \ 0 < t \le t_r$$
$$x = 0 \ , \ t_r < t \le \frac{\pi}{\omega} \tag{14}$$

where t_r is as defined in equation 8.13. This is a piecewise definition where once the sample has been fully penetrated, then x is zero from that time (t_r) until the sample changes direction of movement at $t = \pi/\omega$.

The Bean profiles for the high field case only ever have one turning point, at r = x and are given by:

$$0 < r \le x \qquad \frac{\delta B}{\delta r} = +\mu_0 J_C$$
$$x < r \le r_m \qquad \frac{\delta B}{\delta r} = -\mu_0 J_C \tag{15}$$

Again the magnetic moment of the sample can be determined from the turning point in the ac field (equation 8.14) and the field gradients throughout the sample (equation 8.15) to be:

$$m = \sum IA$$
$$= \int_0^x J_C \pi r^2 dr.l - \int_x^{r_m} J_C \pi r^2 dr.l \tag{16}$$
$$= \frac{J_C \pi l}{3}(2x^3 - r_m^3)$$

8.4.2 Second Half of the Oscillation

Similarly for the second half of the oscillation, x is again defined piecewise between π/ω and $2\pi/\omega$ by:

$$x = r_m\left(1-\frac{\gamma}{2}(1+\cos(\omega t))\right) \;,\; \frac{\pi}{\omega} < t \le \left(\frac{\pi}{\omega}+t_r\right)$$

$$x = 0 \;,\; \left(\frac{\pi}{\omega}+t_r\right) < t \le \frac{2\pi}{\omega} \qquad \textbf{(17)}$$

Likewise the field gradients are given by:

$$0 < r \le x \qquad \frac{\delta B}{\delta r} = -\,\mu_0 J_C$$

$$x < r \le r_m \qquad \frac{\delta B}{\delta r} = +\,\mu_0 J_C \qquad \textbf{(18)}$$

The magnetic moment of the sample, for the sample moving into a higher applied field can be determined from equations 8.17 and 8.18 using:

$$m = \sum I.A$$

$$= -\int_0^x J_C \pi r^2 dr.l + \int_x^{r_m} J_C \pi r^2 dr.l \qquad \textbf{(19)}$$

$$= \frac{J_C \pi l}{3}(r_m^3 - 2x^3)$$

The results of sections 8.3 and 8.4, equations 8.6, 8.9, 8.14 and 8.17 can be combined to give the position of the turning point in the ac field throughout the whole range of the motion of the sample for all applied fields, figure 8.3.

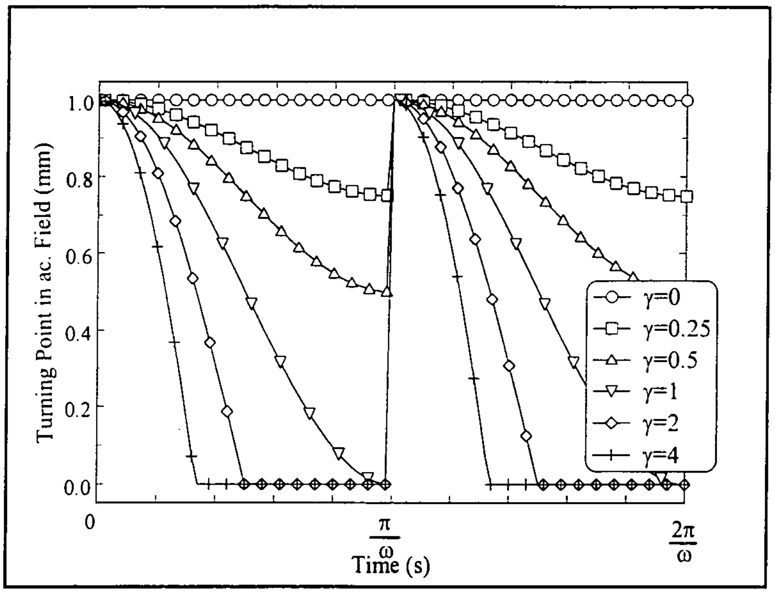

Figure 8.3 **Calculated values of the turning point of the ac field (x) for different values of γ. The sample is fully penetrated at the extremes of the throw distance when γ= 1.**

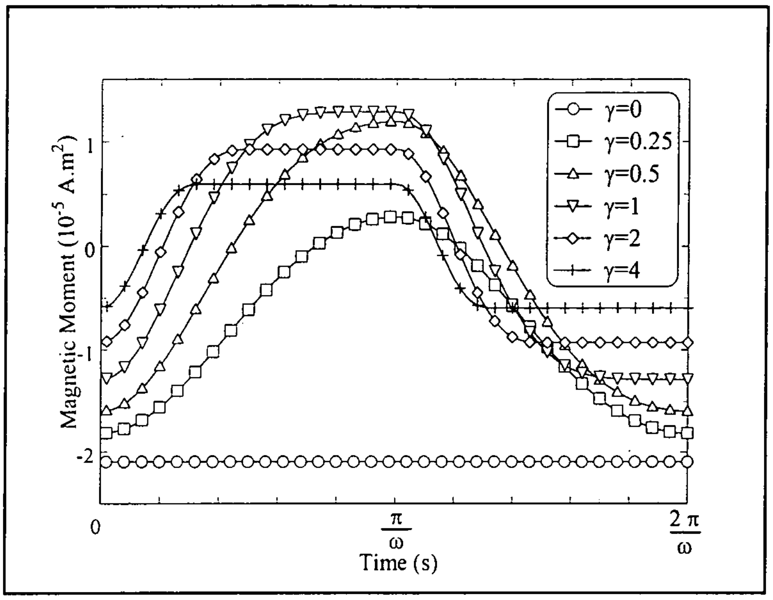

Figure 8.4 **Calculated values of the magnetic moment of the sample for different values of ac field penetration.**

The magnetic moments produced from the previous two sections, equations 8.8, 8.11, 8.16 and 8.19, can also be calculated for the whole field range, as shown in figure 8.4.

With zero ac field ($\gamma = 0$) the magnetic moment is constant throughout the cycle, as is conventionally assumed for all values of dc field. It can be seen that once the ac field is included, even with a small amount of penetration, $\gamma = 0.25$, this signal is quickly distorted.

8.5 Mallinson Theory

To show the affect of the effective ac field, on the superconductor, it is necessary to model a measurement system on which to examine the magnetic moment calculated in sections 8.3 and 8.4.

To do this, Mallinson's Principle of Reciprocity for the voltage induced in a pair of counter wound coils by a moving magnetic moment was used which states that:

$$\Phi = G.b_{COIL}.m \tag{20}$$

where ϕ is the flux inside the coil, G is a geometrical coil constant, m is the magnetic moment inside the pickup coils, and b_{COIL} is the Mallinson field determined from reciprocity arguments.

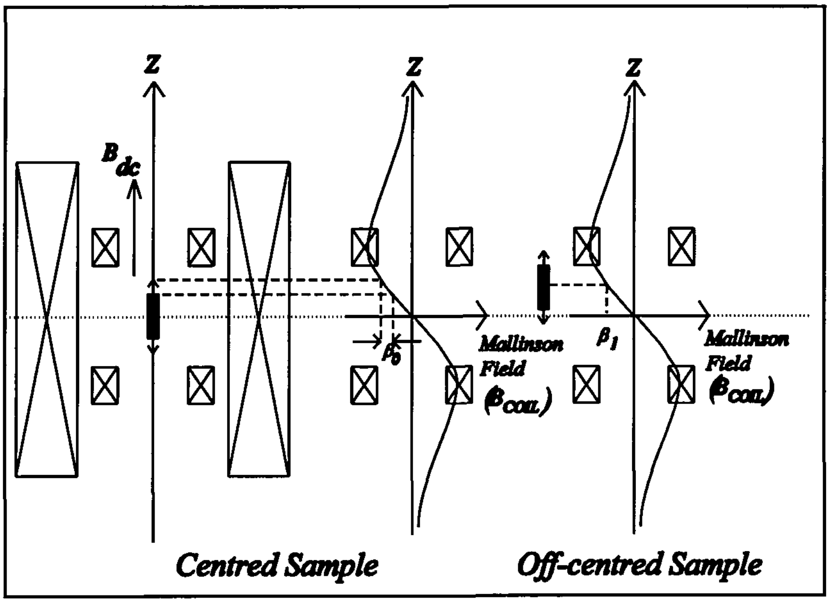

Figure 8.5. The coil geometry and Mallinson Field for the pickup coils used for the calculation.

The Principle of Reciprocity states that the field produced by a current passing through a coil will allow the determination of the sensitivity of the coil to the motion of a magnetic moment within the coil. The Mallinson field profile for the pickup coils is shown in figure 8.5, with the dc field and the sample motion in the z direction, and the Mallinson Field(B_{COIL}) profile for the pickup coils shown. Hence a sample oscillating around the centre of the pickup coils is defined to be equivalent to a Mallinson field given by:

$$b_{COIL} = \beta_0 \cos(\omega t) \qquad \textbf{(21)}$$

where β_0 is a constant. If the sample is not perfectly centred in the pickup coils then an additional term is introduced into equation 8.21 giving:

$$b_{COIL} = \beta_0 \cos(\omega t) + \beta_1 \qquad \textbf{(22)}$$

where β_0 and β_1 are both constants and β_1 is determined by integrating the Mallinson field over the whole sample. For the purpose of the mathematics β_0 will be defined as 1 and β_1 will be taken as 2 as the Mallinson field is linear through the centre of the pickup coils and the ratio of β_0 and β_1 is determined by the ratio of the throw distance and the distance the sample is offcentred by. Equations 8.20 and 8.22 can be combined to give a relation between the flux in the coil and the magnetic moment of the sample as:

$$\Phi = G.\left(\beta_0 \cos(\omega t) + \beta_1\right).m \qquad \textbf{(23)}$$

From this magnetic flux we can calculate the voltage(V) induced in the coil using:

$$V = -\frac{\delta \Phi}{\delta t} = -\frac{\delta}{\delta t}\left[G\left(\beta_0 \cos(\omega t) + \beta_1\right).m\right] \qquad \textbf{(24)}$$

In section 8.6 it will be assumed that the sample is perfectly centred in the pickup coils and hence $\beta_1 = 0$. Section 8.7 will consider the case of $\beta_0 = 0$ and $\beta_1 \neq 0$, i.e. the sample is not perfectly centred. This will allow the features of each case to be clearly distinguished.

In order to analyse the voltage induced in our pickup coils, it is appropriate to use a Fourier deconvolution to describe the distorted sine wave voltage. This will allow comparison between the sine and cosine terms calculated here and the experimental measurements. The Fourier series for the signal V can be produced using the summation of sine and cosine functions as:

$$V = \frac{G'\omega J_c \pi l r_m^3}{3} \sum_{n=1}^{\infty} \left(a_n \cos(n\omega t) + b_n \sin(n\omega t)\right) \qquad \textbf{(25)}$$

where the prefactor $G' = G.\beta_0$ from Mallinson Theory and the remaining prefactors are derived from equations 8.8, 8.11, 8.16, 8.19 and 8.24.

The values for the Fourier coefficients a_n and b_n are given by:

$$a_n = \frac{3}{G'\omega J_c \pi l r_m^3} \frac{\omega}{\pi} \int_0^{\frac{2\pi}{\omega}} V.\cos(n\omega t).dt \qquad \textbf{(26)}$$

$$b_n = \frac{3}{G'\omega J_c \pi l r_m^3} \frac{\omega}{\pi} \int_0^{\frac{2\pi}{\omega}} V.\sin(n\omega t).dt \qquad \textbf{(27)}$$

From the Fourier coefficients, the voltages that would be measured by an idealised lockin amplifier in its two components will be defined as:

$$V(Lossless) = \frac{G'\omega J_c \pi l r_m^3}{3} b_n \sqrt{2} \qquad \textbf{(28)}$$

for the sine components, derived from the b_n's (equation 8.26) and:

$$V(Loss) = \frac{G'\omega J_c \pi l r_m^3}{3} a_n \sqrt{2} \qquad \textbf{(29)}$$

for the cosine components, derived from the a_n's (equation 8.27).

8.6 Calculation of Voltage Due to Inhomogeneity in the dc Field

In this section the voltage induced in the sense coils will be determined for a sample perfectly positioned in the centre of the sense coils, i.e. $\beta_1 = 0$ and the Fourier components calculated.

8.6.1 Total Voltage Induced in the Pickup Coils

From equation 8.24, if the sample is centred, the voltage induced in the pickup coils can be determined using:

$$V = \frac{\delta\Phi}{\delta t} = G'\left(\omega.m.\sin(\omega t) - \cos(\omega t).\frac{\delta m}{\delta t}\right) \qquad (30)$$

These voltages are displayed in figure 8.6.

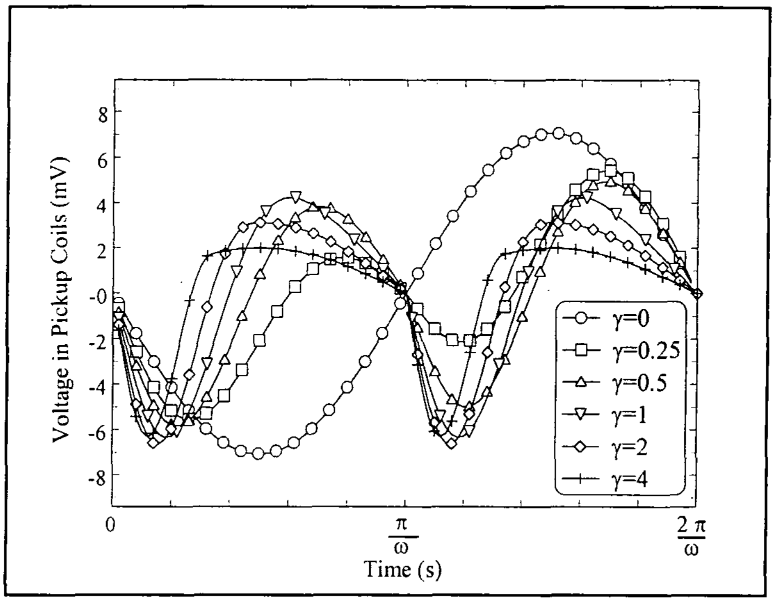

Figures 8.6 Calculated voltage waveform in the pickup coils for various values of γ.

Clearly this wave can be seen to be non-sinusoidal for all non-zero values of γ. It is this distortion that means the 1f signal conventionally measured when using a VSM no longer represents the magnetic moment or the critical current density of the sample. Hence a more sophisticated measurement is required to determine the actual magnetic moment and critical current density.

8.6.2 Calculation of Fourier Coefficients

To quantify the distortion in figure 8.6, the Fourier coefficients (a_n and b_n) been evaluated for magnetic fields from 0 to B_{C2} for the NbTi-like superconductor, using the functional form for J_C in equation 8.1 with $\alpha=5\times10^5 Am^{-2}T^{-1}$ and B_{C2} = 10T.

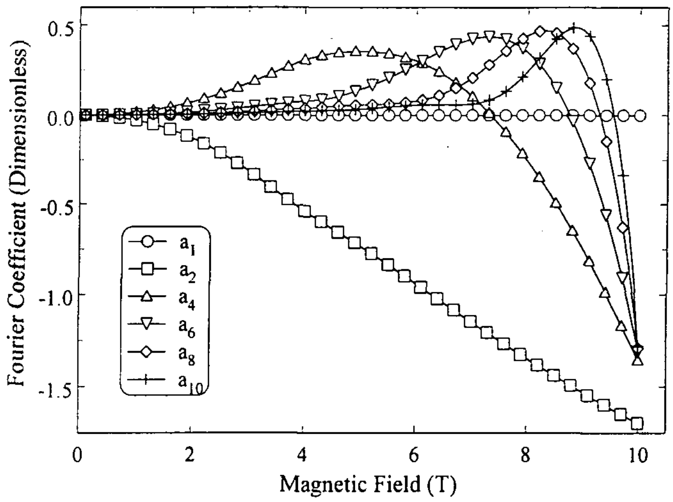

Figures 8.7 **Calculated values of the Fourier coefficient a_n as a function of dc field. All the odd coefficients are zero.**

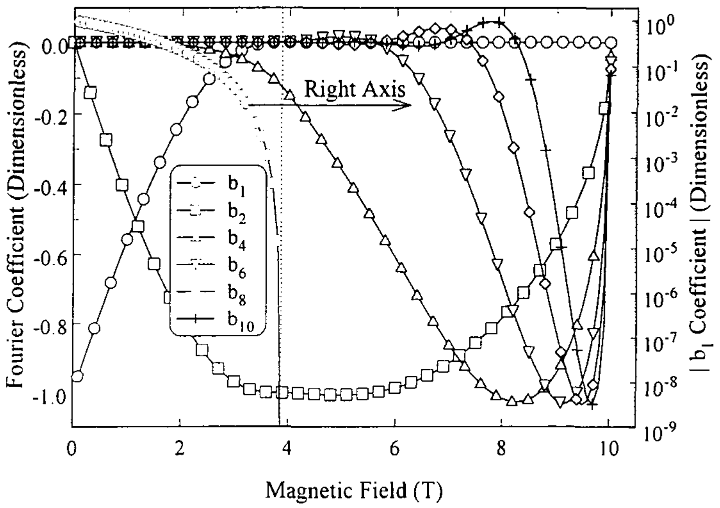

Figures 8.8 **Calculated values of Fourier coefficient b_n as a function of dc field. All the odd coefficients except b_1 are zero.**

The a_n coefficients, that is the coefficients for the cosine terms are shown in figure 8.7, with the odd coefficients all being zero. Figure 8.8 shows the b_n coefficients, that is the sine terms, again for the NbTi-like superconductor from 0 to B_{C2}. The b_1 coefficient represents the traditionally measured component and can be seen to drop to zero on the linear scale (left) and its magnitude seen to fall to zero on the log scale (right). The dotted line indicates $\gamma = 1$.

8.6.3 Lossless and Loss Voltages

The 1f lossless voltage is that which is traditionally measured using a vibrating sample magnetometer and a lockin amplifier on 1f, the driver frequency. Clearly from the results of the calculations shown in figure 8.9, it can be seen that this does not represent the magnetic moment, or the screening currents present in the sample, as it drops to zero at a field well below the field at which the critical current density goes to zero.

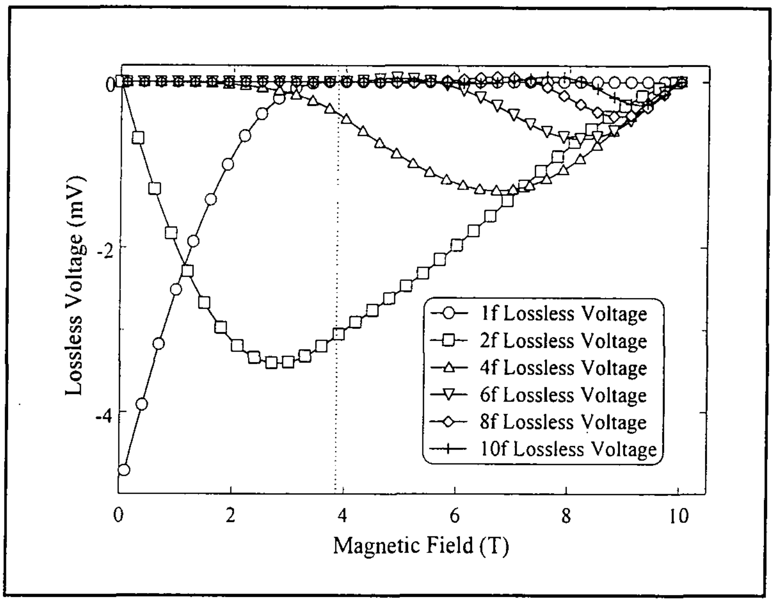

Figures 8.9 Calculated values for the lossless voltages as a function of dc field. All voltages except 1f are zero and all even voltages go to zero at B_{C2} i.e. 10 T. The dotted line indicates $\gamma = 1$.

This 1f lossless voltage does in fact go to zero at gamma = 1, the point at which the ac field fully penetrates the sample. The higher frequency odd lossless voltages are all zero, and the even frequency voltages all go through a minimum at negative values before going to zero at the upper critical field.

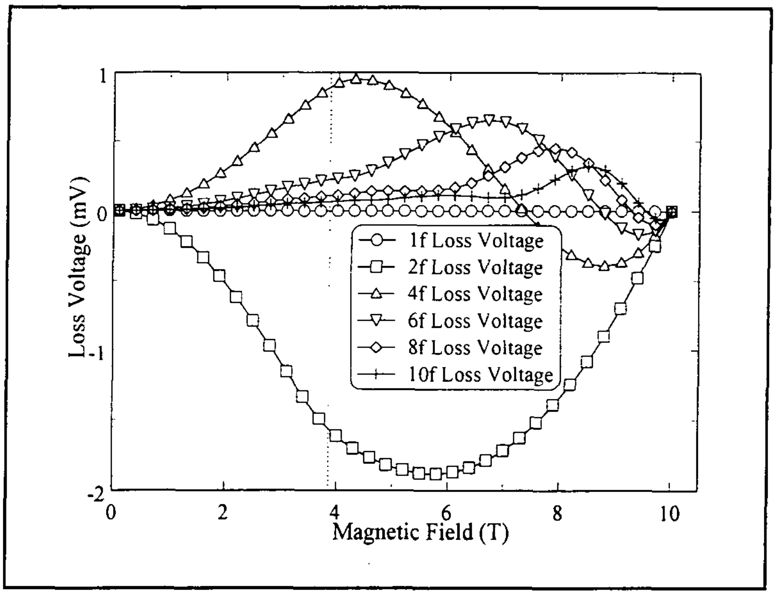

Figures 8.10 Calculated values of the loss voltages as a function of dc field. The dotted line indicates $\gamma = 1$.

The 1f loss voltage is zero, as would be expected from an idealised VSM measurement where γ=0. The even voltages for the loss are all non-zero, quantifying the distortion seen in figure 8.6. and all go to zero at the upper critical field when $J_C = 0$. The odd loss voltages are all zero.

8.6.4 Summary of ac Field Effect for Low Critical Current Density NbTi-like Sample

This section has considered a NbTi-like sample moving within an inhomogeneous magnetic field, without crossing the centre of the dc field profile, and perfectly centred in the pickup coils. The magnetic moment and the voltages that would be observed on an idealised lockin amplifier have been calculated. It has been shown that the lossless voltage at the driver frequency, as is traditionally measured for a VSM measurement, no longer represents the total magnetic moment, and hence critical current density of the sample. An irreversibility field is introduced into this component at the point when then the ac field is equal to the sample self field. By measuring the other voltages at higher frequencies it is possible to find the point at which the critical current density actually goes to zero. The calculations shown have been for an increasing dc field sweep. The 1f lossless voltages are calculated to be hysteretic on the reversal of the direction of the dc field sweep, symmetric about m = 0. The decreasing field results have been omitted from the figures for clarity. All other voltages were reversible on the changing of the dc field sweep direction.

8.7 Calculation of the Voltage Due to the Sample Not Perfectly Centred in the Pickup Coil

This section will calculate the voltages produced when the sample is not perfectly centred inside the pickup coils. In terms of equation 8.22, this means $\beta_0 = 0$ and $\beta_1 \neq 0$, allowing just the terms produced by the offcentring to be seen. The value for β_1 will be taken as 2 since the Mallinson field is linear through the centre of the pickup coils and therefore the ratio of β_0 and β_1 is determined by the ratio of the throw distance and the distance the sample is offcentred by. This should give an approximate order of magnitude estimate to allow the comparison of the two terms.

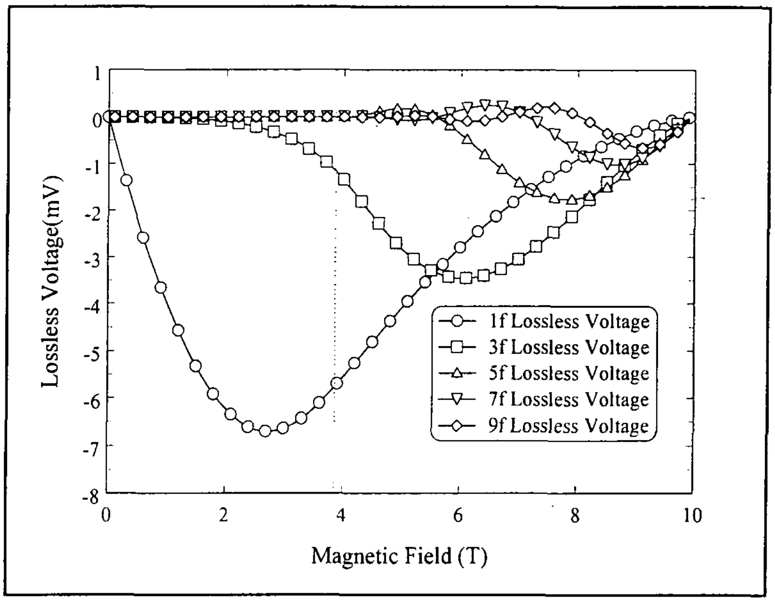

Figure 8.11 **Lossless voltages calculated for the β_1 component of the offcentring term for the NbTi-like sample.**

The lossless and loss voltages were calculated for the NbTi-like sample and are shown in figures 8.11 and 8.12.

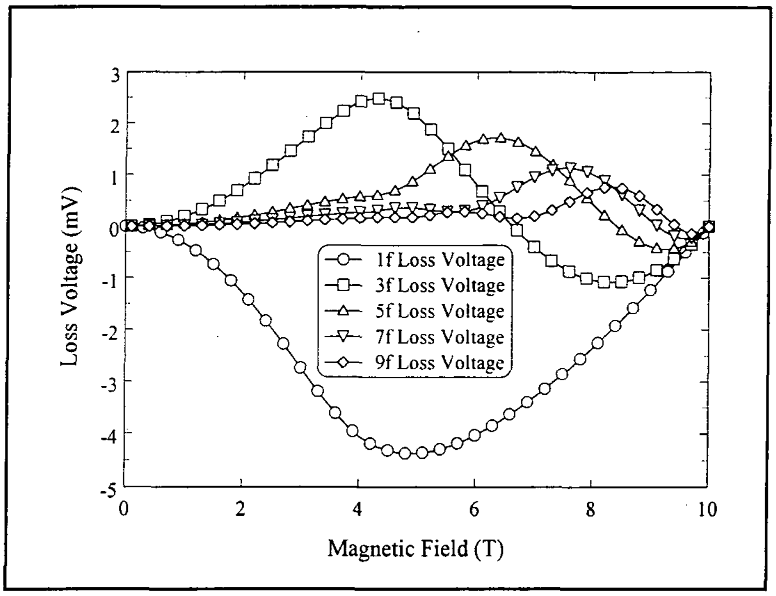

Figure 8.12 **Loss voltages calculated for the β_1 component of the offcentring correction for the NbTi like sample.**

All the even voltages are zero and the odd voltages are non-zero. All voltages were reversible on the reversal of the field sweep direction and all the voltages become zero at the upper critical field, when the critical current density becomes zero.

8.8 Calculation of the Voltages for a Sample Oscillating Symmetrically about the Centre of the dc Field

This section considers the effect of the sample lying across the turning point in the dc field on the Bean profiles within the sample and hence on the measured magnetic moment of the sample. Firstly the principles behind this special case will be outlined, and then the results of the calculation presented. These results will then be compared to those for a similar sample which does not cross the turning point in the dc field.

8.8.1 Centre Field Calculation

Other calculations in this chapter assume that the dc field profile produces a constant amplitude sinusoidal ac field for the moving sample. This is not the case if the sample oscillates about the centre of the dc field profile.

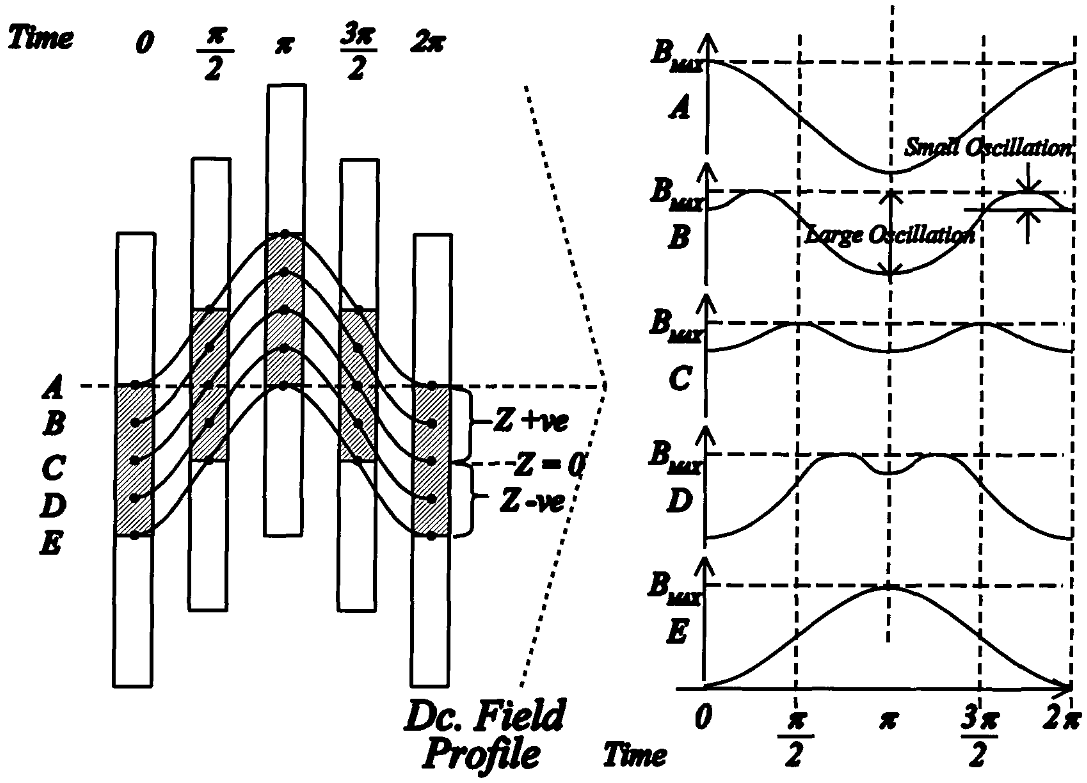

Figure 8.13 The effective ac field experienced by a sample positioned in the centre of the dc field, as the sample moves from time t = 0 to t = 2π/ω. Effective ac field plots on the right are for points within the sample marked A to E.

In figure 8.13 the sample is positioned so as to oscillate symmetrically about the centre of the dc field profile. The plots on the right hand side of figure 8.13 show how the dc field changes at five points across the sample with time. These changing dc fields can no longer be considered to be simple ac fields as the amplitude of the variation is not constant. These variations are still periodic with period 2π and will be referred to as non-sinusoidal ac fields.

The sample can be divided into four distinct regions using the coordinate Z which is taken to be zero at the centre of the sample. The first region of the sample is that above point A. This part of the sample never crosses the centre of the field profile, hence the effective ac field is sinusoidal.

The region between points A and E is that which is swept out by the turning point in the dc field as the sample moves from one extreme of its throw to the other. This central region can itself be divided into two section, A to C in which Z is positive and C to E in which Z is negative. The final region is that below point E, which never crosses the centre of the dc field profile and hence experiences a sinusoidal ac field equal and opposite to that for the region above point A.

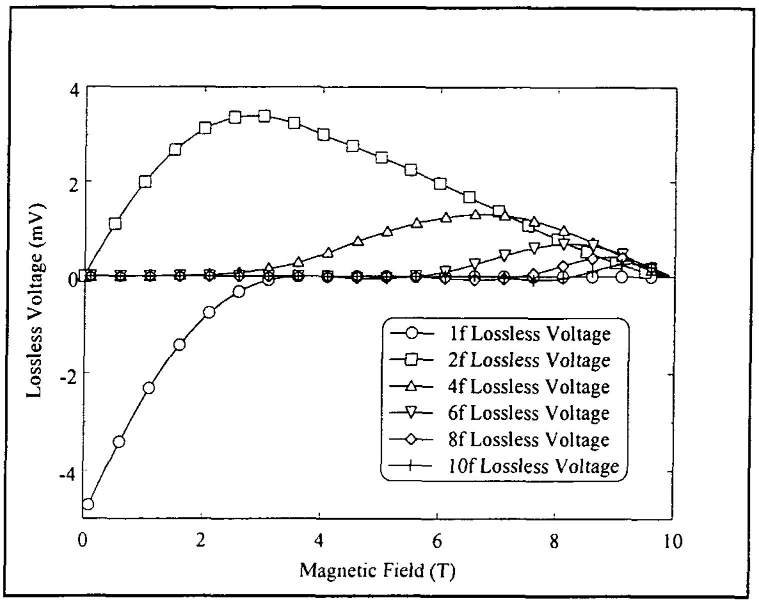

Figure 8.14 Lossless voltages calculated for the region of the sample that does not pass through a turning point in the dc field and is in a negative field gradient.

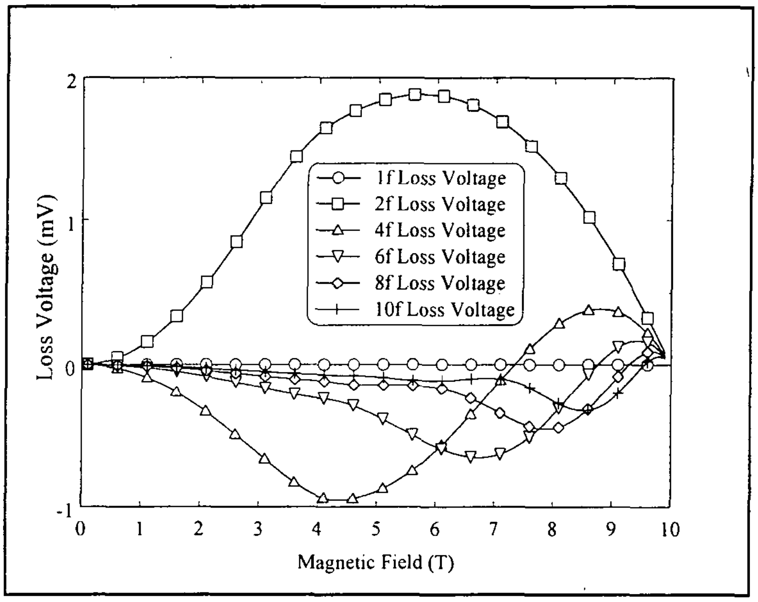

Figure 8.15 Loss voltages calculated for the region of the sample that does not pass through a turning point in the dc field and is in a negative field gradient.

The two outer regions produce equal and opposite magnetic moments from the effect of the sinusoidal ac field, but the same magnetic moments from the dc field effect. This can be seen by comparing figures 8.14 and 8.15 which were calculated for a negative field gradient with figures 8.9 and 8.10 which were calculated for a positive field gradient. This means that for a sample oscillating symmetrically about the centre of the dc field, the only contribution to the voltages measured at frequencies higher than 1f will come from the section of the sample swept out by the turning point in the dc field.

The voltages that would be produced by this centre section of the sample are calculated below. Consider a sample such that its length is equal to the throw distance, the region of the sample between points A and E in figure 8.13, taken in this case to be 1mm. The physical principles behind the maths are the same as for the sample that does not cross the turning point in the dc field except the definition of the nonsinusoidal ac field is more complicated. The variation in the applied field can be considered as two sections, a small oscillation in field and a large oscillation (figure 8.13), the relative sizes of each depending on the dc field and Z, the position within the sample.

For the sample that does not cross the turning point in the dc field, the mathematics could be divided into two regions for magnetic field, the high field region in which the ac field fully penetrated the sample and the low field region when it did not. For the sample which crosses the field centre, three regions must be used to define the field regimes since the ac field is no longer sinusoidal.

The first region is that in which neither the small oscillation or the large oscillation in dc field fully reverse the Bean profile for any point within the sample and is when $\gamma<1$. The first time the Bean profile is reversed occurs when $\gamma=1$, and then the profile is reversed only for the points on the sample that see the biggest large field oscillations, i.e. points A and E. As the large field oscillation gets bigger, more regions of the sample have their Bean profiles reversed by it. Hence the calculation must be divided as a function of Z such that for positive values of Z:

$$\begin{aligned} Z &\le \frac{D}{\gamma} - \frac{D}{2} \quad \textit{No Profile Reversed By Either Oscillation} \\ Z &> \frac{D}{\gamma} - \frac{D}{2} \quad \textit{Profile Reversed By Only Large Oscillation} \end{aligned} \tag{31}$$

and for negative values of Z:

$$\begin{aligned} &Z \geq \frac{D}{2} - \frac{D}{\gamma} \ \textit{No Profile Reversed By Either Oscillation} \\ &Z < \frac{D}{2} - \frac{D}{\gamma} \ \textit{Profile Reversed ByOnly Large Oscillation} \end{aligned} \qquad \textbf{(32)}$$

where D is the throw distance, Z is the position on the sample and γ is as defined in equation 8.4. As the ac fields increases, i.e.γ increases, the volume of the sample in which the large oscillation reverses the Bean profile, increases.

At γ=2 the ac field has increased such that the small field oscillation is sufficient to reverse the Bean profile for the points on the sample that see the biggest small field oscillation. The sample can again be divided into two regions as a function of Z such that for positive Z:

$$\begin{aligned} &Z > \frac{D}{2}\left(1 - \frac{2}{\gamma}\right) \ \textit{Only Large Oscillation Reverses the Profile} \\ &Z < \frac{D}{2}\left(1 - \frac{2}{\gamma}\right) \ \textit{Both Large plus Small Oscillations Reverse the Profile} \end{aligned} \qquad \textbf{(33)}$$

and for negative Z:

$$\begin{aligned} &Z < \frac{D}{2}\left(\frac{2}{\gamma} - 1\right) \ \textit{Only Large Oscillation Reverses the Profile} \\ &Z < \frac{D}{2}\left(\frac{2}{\gamma} - 1\right) \ \textit{Both Large plus Small Oscillations Reverse the Profile} \end{aligned} \qquad \textbf{(34)}$$

As the oscillations increase in size the amount of the sample in which both oscillations reverse the field profile gets bigger.

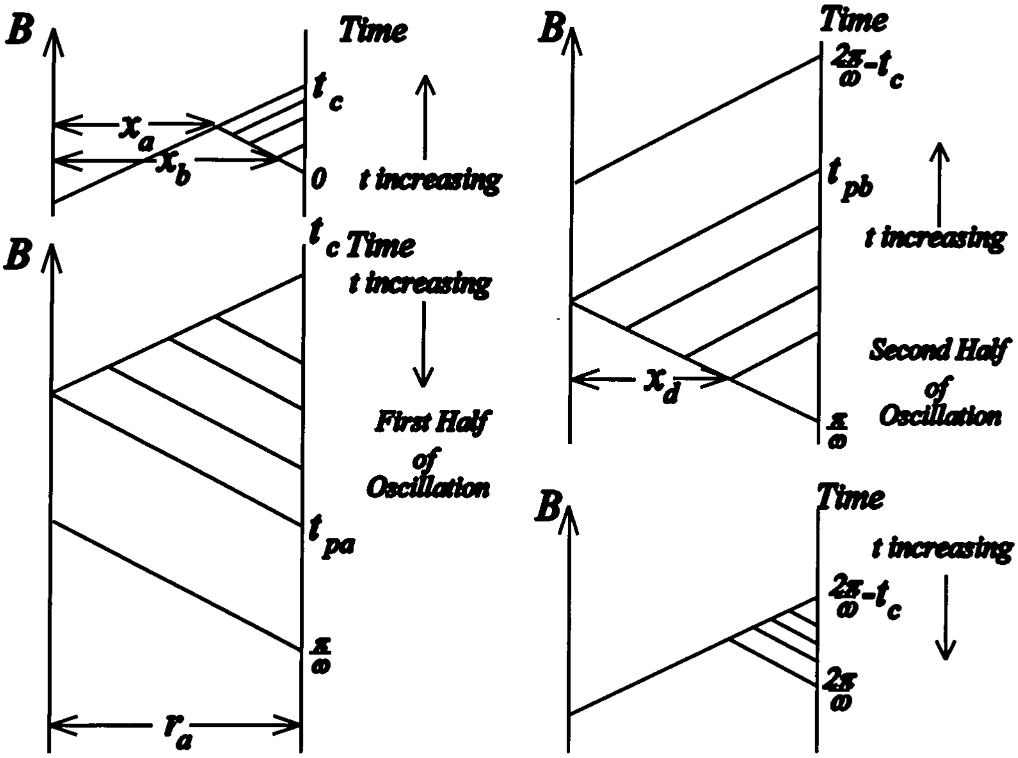

Figure 8.16 An example of the Bean profile for Z positive in the intermediate field region.

An example of the Bean profile for positive Z, in the intermediate field region is shown in figure 8.16, where t_c is the time at which this point of the sample crosses the field centre, t_{pa} and t_{pb} are the times at which the field profile is completely reversed by the large ac field loop. Similar Bean profiles can be constructed for each point on the sample in each of the field regimes using the definitions in equations 8.31 to 8.33. The magnetic moments can then be calculated as a function of Z which can then be integrated for Z positive and Z negative and the results combined to give the total magnetic moment of the sample. Once the moment has been calculated, a voltage and its Fourier components can be calculated in the same way as for the sinusoidal ac field case. Firstly the calculations were performed for the sample perfectly positioned within the coil set, i.e. $\beta_1 = 0$ for a NbTi like sample with $\alpha=5\text{x}10^5\text{Am}^{-2}\text{T}^{-1}$ and $B_{C2} = 10\text{T}$.

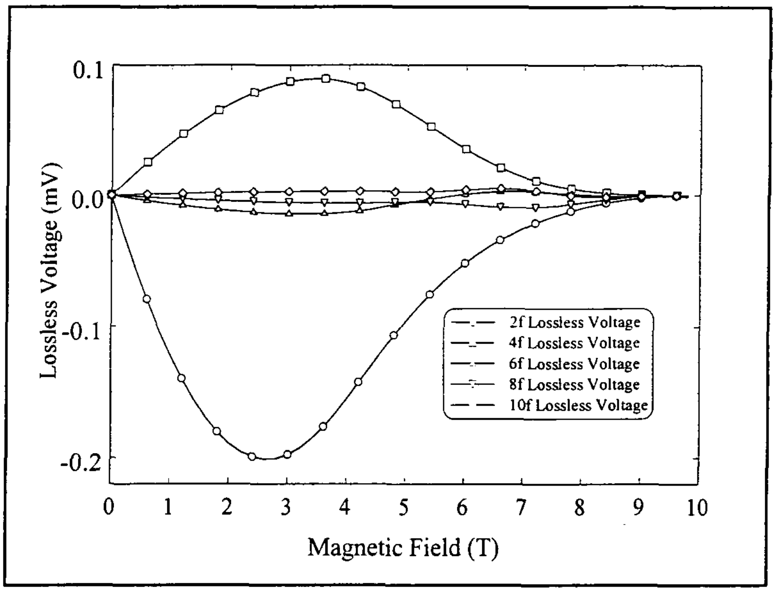

Figure 8.17 Calculated values for the even lossless voltages for the positive Z section of the sample that crosses the field centre, perfectly positioned within the coil set, which sums to zero with the negative Z voltages.

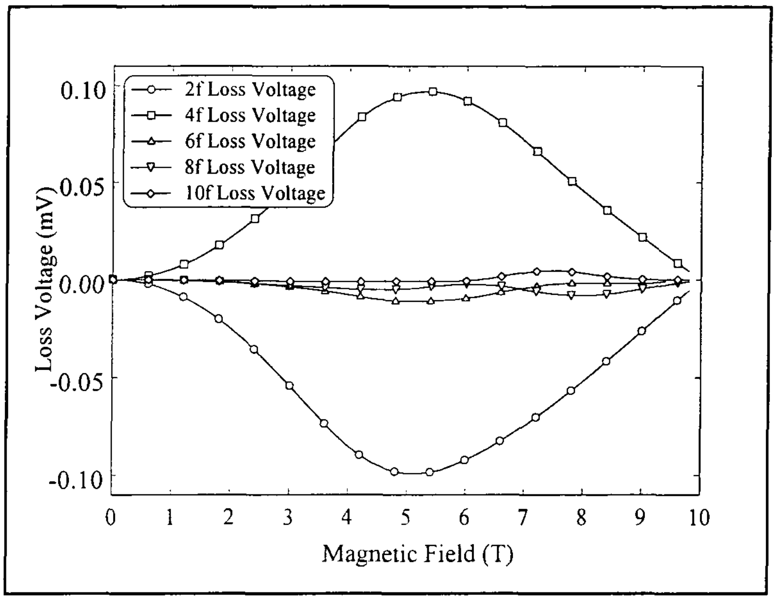

Figure 8.18 Calculated values for the even loss voltages for the positive Z section of the sample that crosses the field centre, perfectly positioned within the coil set, which sums to zero with the negative Z voltages.

The even lossless and loss voltages for the positive Z half of the sample are shown in figures 8.19 and 8.20.

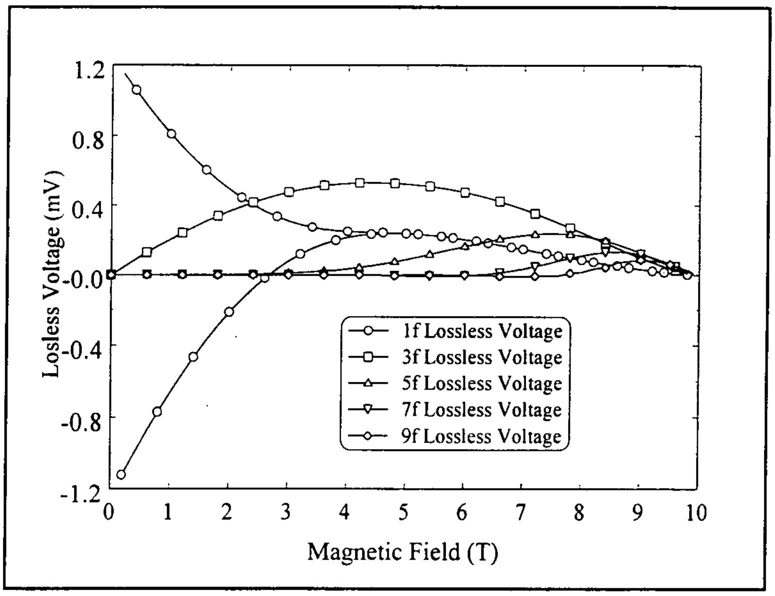

Figure 8.19 **Calculated values for the odd lossless voltages for the section of the sample that crosses the field centre, perfectly positioned within the coil set.**

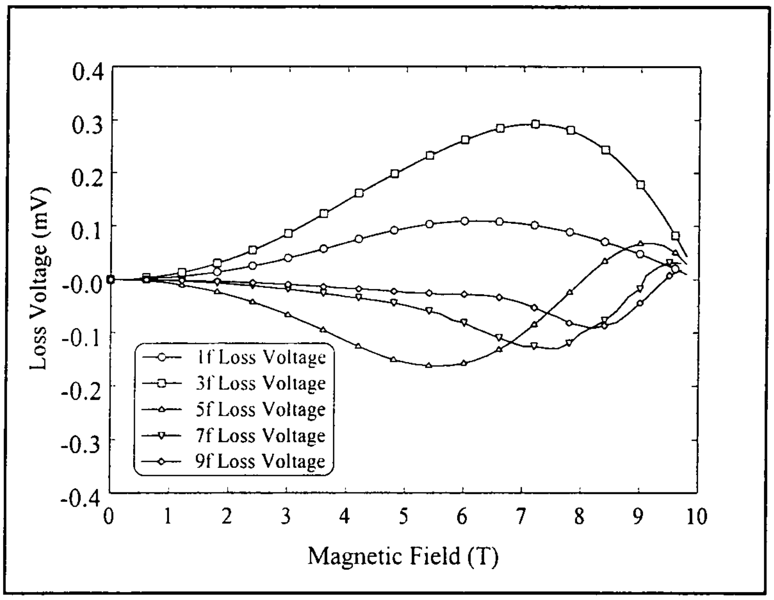

Figure 8.20 **Calculated values for the odd loss voltages for the section of the sample that crosses the field centre, perfectly positioned within the coil set.**

It was found that the Z positive and Z negative sections of the sample produced equal and opposite even voltages and equal odd voltages. Hence when the total signal for the two halves of the sample was calculated, only voltages at odd multiples of the driver frequency were non zero. The odd lossless and loss voltages for the whole sample are shown in figures 8.19 and 8.20. The calculations were repeated for decreasing applied field, with hysteresis found only in the 1f lossless voltage, shown in figure 8.19. The total voltage measured at the driver frequency can be seen to contain both a positive reversible component and an irreversible component. The irreversibility remains above $\gamma=1$, as the sample is not fully penetrated throughout its entire volume.

In contrast to the results from the sample which does not cross the centre of the field profile, figures 8.9 and 8.10, in figures 8.17 and 8.18, a reversible component was found in the 1f lossless voltage and the voltages at even multiples of the driver frequency are zero and the odd multiples are none zero. The lossless voltages go through a positive maximum before falling to zero at B_{C2}. The loss voltages 1f and 3f both go through a positive maximum while the 5f, 7f and 9f go through a negative minimum, then a positive maximum, with all voltages falling to zero at B_{C2}.

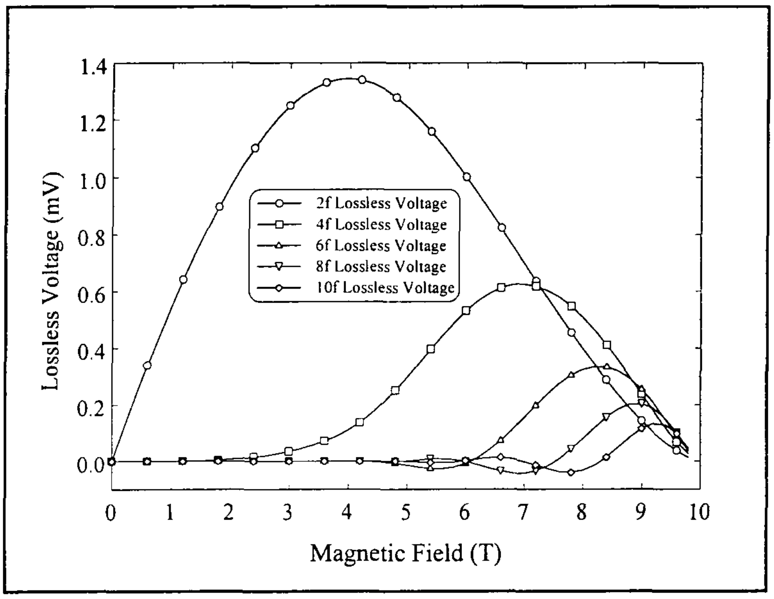

Figure 8.21 Calculated values for the even lossless voltages for the section of the NbTi like sample that crosses the field centre, imperfectly positioned within the coil set.

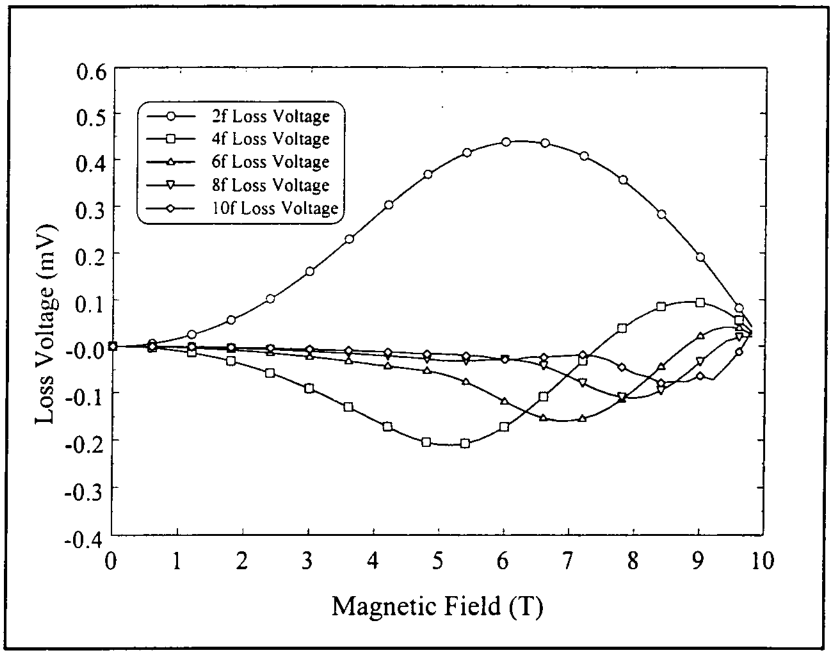

Figure 8.22 Calculated values for the even loss voltages for the section of the NbTi like sample that crosses the field centre, imperfectly positioned within the coil set.

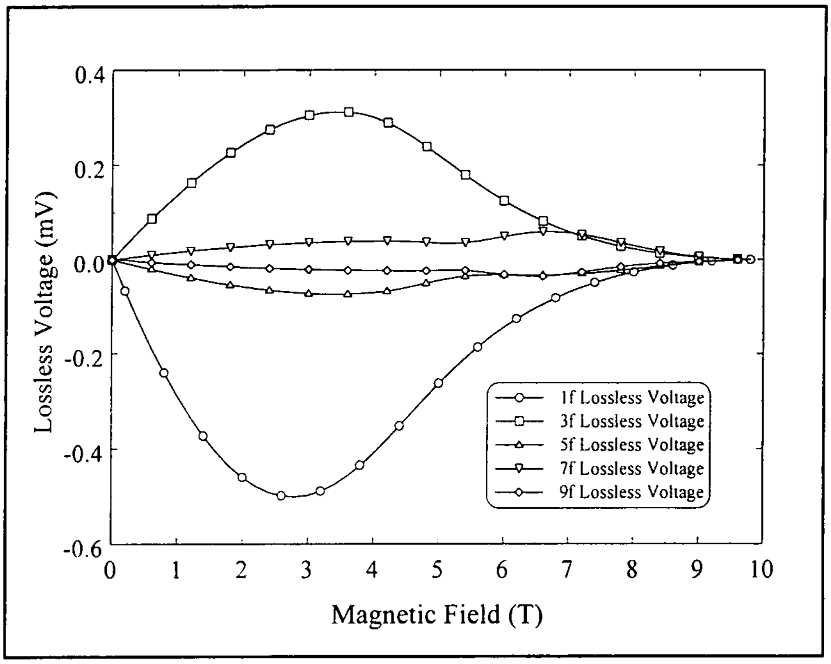

Figure 8.23 Calculated values for the odd lossless voltages for the section of the NbTi like sample that crosses the field centre, imperfectly positioned within the coil set.

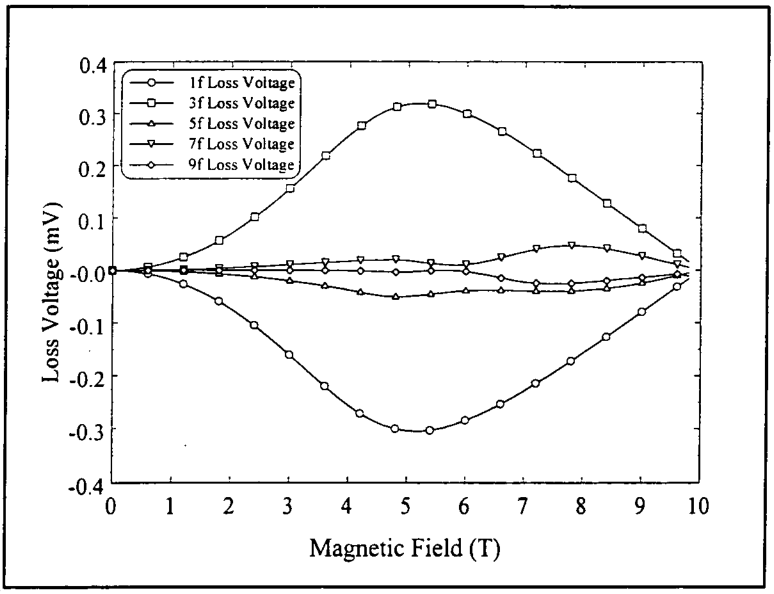

Figure 8.24 Calculated values for the odd loss voltages for the section of the NbTi like sample that crosses the field centre, imperfectly positioned within the coil set.

Now considering a sample imperfectly centred using $\beta_0 = 0$ and $\beta_1 = 2$, again for the NbTi like sample, the lossless and loss voltages were calculated. The even voltages for the whole sample and shown in figures 8.21 and 8.22 while the odd voltages for the positive Z section of the sample are shown in figures 8.23 and 8.24. It was found that the odd voltages were equal and opposite in the two halves of the sample and hence summed to zero. The even voltages however were the same for the two halves of the sample and hence had a non zero sum. In contrast to the results for a sample which does not cross the centre of the dc field, c.f. figures 8.11 and 8.12, the voltages calculated for odd multiples of the driver frequency, including 1f are all zero and the even multiples are all non zero.

8.8.2 Comparison of a Sample Crossing the dc Field Centre and a Sample Not Crossing the dc field Centre

In this section a comparison will be made between the results for a sample that crosses the field centre and one that does not. This will be performed for a NbTi like sample where the upper critical fields, B_{C2}, will be varied to model a change in temperature for the sample.

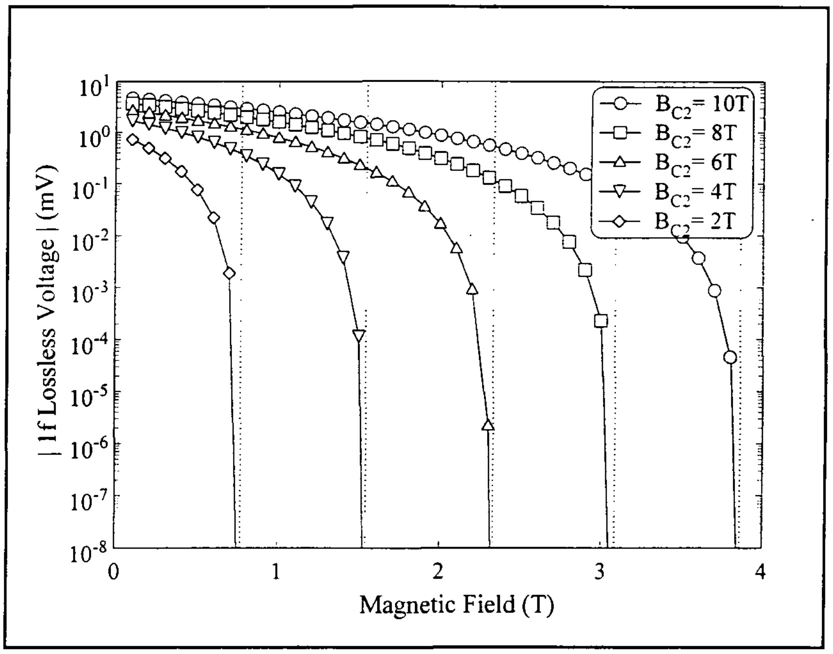

Figure 8.25 Magnitudes of the 1f lossless voltage for various upper critical fields in a NbTi-like superconductor with a constant ac field along its length. The dotted lines indicate $\gamma = 1$

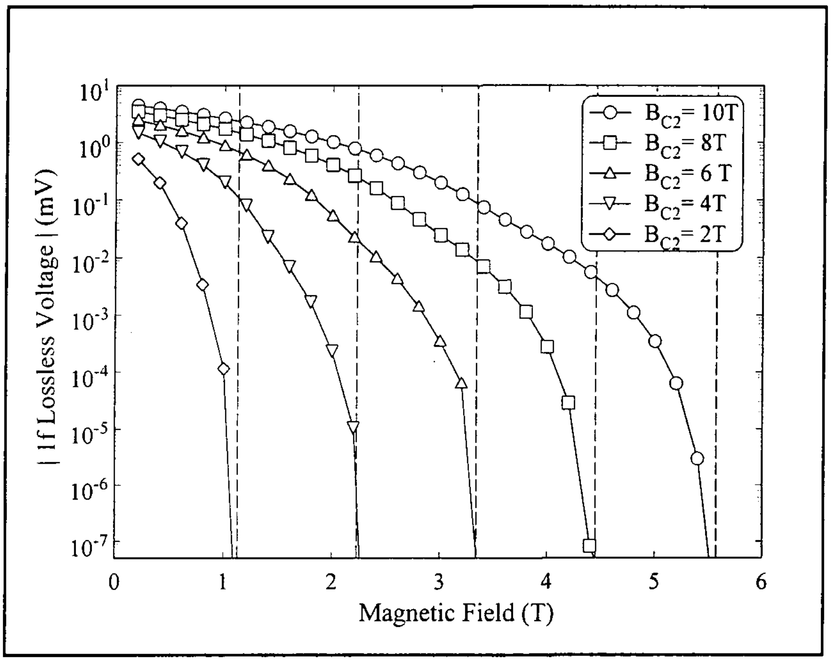

Figure 8.26 Magnitudes of the 1f lossless voltage for various upper critical fields in a NbTi-like superconductor when positioned across the turning point in the dc field. The dashed lines indicate $\gamma = 2$.

Equation 8.1 has been used with $\alpha=5\times10^5\text{Am}^{-2}\text{T}^{-1}$ and the results shown in figure 8.25. It can be seen that all the 1f lossless voltages fall to zero at $\gamma = 1$, at fields of less than half the upper critical field at which the critical current density goes to zero. The variation in upper critical field has also been examined for a sample that oscillates symmetrically about the centre of the dc field and is perfectly centred in the coil set. It can be seen from figure 8.22 that the magnitude of the 1f lossless signal falls to zero at $\gamma = 2$ if the sample crosses the turning point in the dc field, compared to $\gamma = 1$ if the sample does not.

8.8.3 Implications of Centre Field Special Case

The case of the sample that crosses the centre of the dc field profile is actually the one most relevant for most VSM measurements. This section has shown that for a sample oscillating symmetrically about the centre of the dc field, perfectly centred in the pickup coils, voltages are measured at odd multiples of the driver frequency. If the sample is imperfectly positioned in the pickup coils but still oscillates symmetrically about the centre of the dc field profile then voltages at even multiples of the driver frequency are also measured.

It should be noted that the symmetry of the sample about the centre of the dc field was critical for the conclusions above, as it is the symmetry that causes the even and odd components to disappear for the pickup coil centred and offcentred geometries respectively. This symmetry is difficult to achieve experimentally and hence a complicated combination of both odd and even voltages is expected for a sample which crosses the centre of the dc field profile. Cases not considered explicitly in this thesis are asymmetric samples and those which are smaller than the throw distance. These samples will also produce both odd and even voltages for which it will not be possible to separate their sources.

8.9 Calculation For a Slab Geometry

All other calculations in this chapter have been performed for a cylindrical sample geometry. In this section the mathematics for a sample with a slab geometry will be outlined and results of the calculations presented.

8.9.1 Definition of the Sample Geometry

The slab will be taken to have dimensions a mm × b mm × l mm where l is the sample length and l > a > b. The sample is orientated with its long axis parallel to the magnetic field.

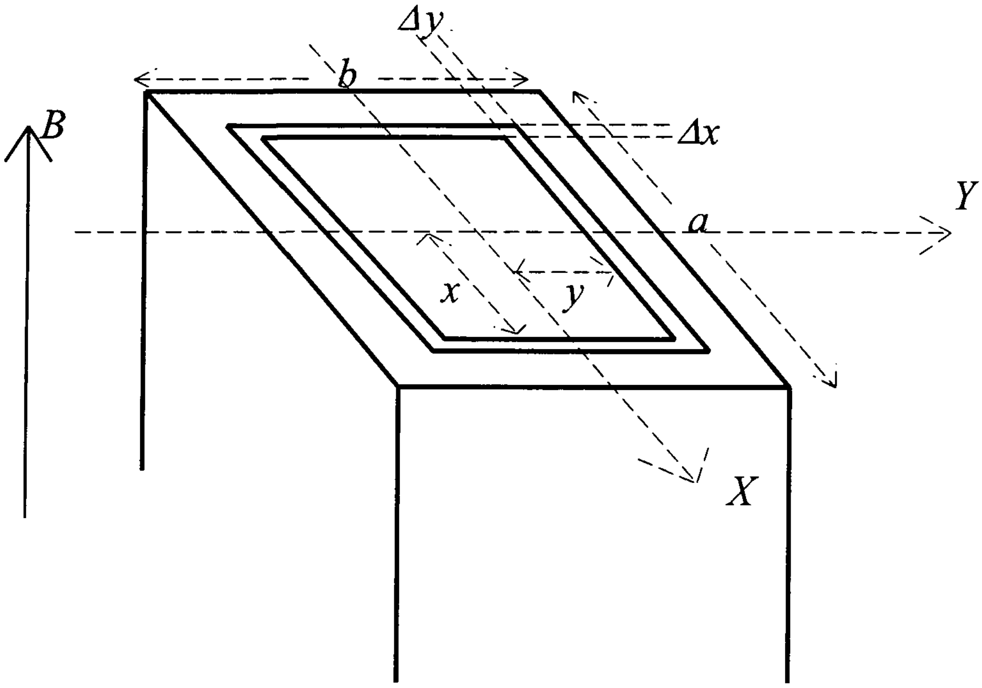

Figure 8.27 Sample geometry for the slab calculation.

The geometry is shown in figure 8.27 where it can be seen that the field penetration depth is the same from all the surfaces of the sample, and therefore once the ac field fully penetrates the smallest cross section, the sample will be fully penetrated throughout its volume. As a consequence of the penetration being the same from all surfaces it is only necessary to consider one of the radial dimensions of the slab. The two dimensions can related such that:

$$y = x - \frac{a}{2} + \frac{b}{2} \qquad (35)$$

where x and y are the distances from the centre of the sample to the point to which the ac field penetrates in the X and Y direction, and a and b are the dimensions of the sample perpendicular to the magnetic field in the X and Y directions respectively. The magnetic moment of an element of the sample around the slab can be determined using:

$$dm = J_c.dx.l.2x.2y. \tag{36}$$

Combining equations 8.35 and 8.36 allows the determination of an magnetic moment element dm using just the X coordinate. This element is given by:

$$dm = A.I = 4J_c.l.x\left(x-\frac{a}{2}+\frac{b}{2}\right)dx \tag{37}$$

The mathematics for the slab is similar to that for the cylinder. The parameter gamma must be redefined as the ratio of the distance the field penetrates into the sample in the x direction divided by half the smallest sample dimension. Gamma for the slab sample geometry is defined as:

$$\gamma = \frac{2.B_{ac}}{\mu_o J_C b} \tag{38}$$

The problem is now one dimensional and can be solved in a similar way to the cylindrical geometry.

8.9.2 Calculation for the Slab Shaped Sample

The voltage induced in a set of pickup coils can be determined and the Fourier voltages be calculated in the same way as for the cylinder. The results of these calculations as shown in figure 8.28 and 8.29 for both the lossless and the loss voltages and are for a NbTi like sample as described in equation 8.1 with $\alpha=5\text{x}10^5\text{Am}^{-2}\text{T}^{-1}$ and $B_{C2}=10\text{T}$, for a sample with a constant field gradient across its length that is perfectly centred in the coil set.

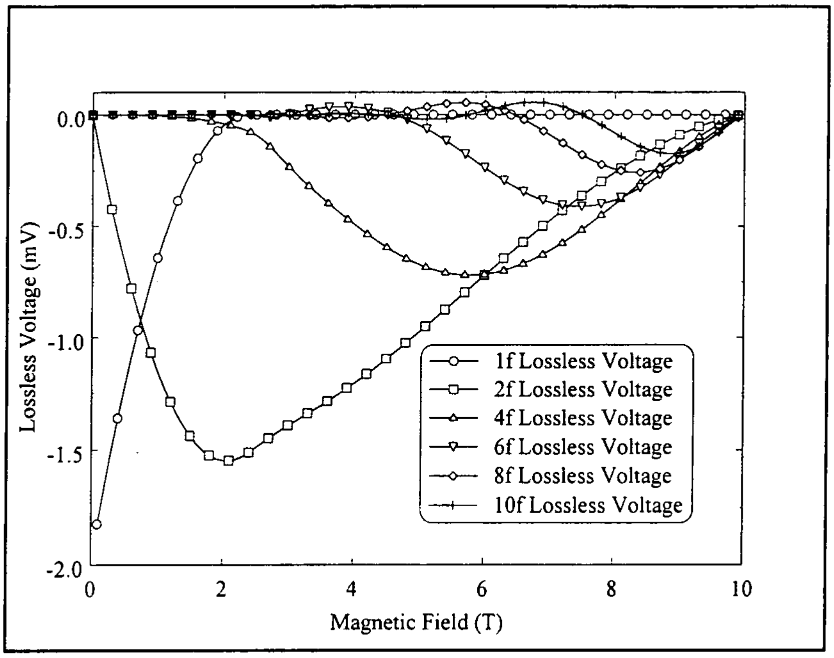

Figure 8.28 Lossless voltages calculated for a NbTi-like sample with a slab geometry, out of dc field centre, centred in the coil set.

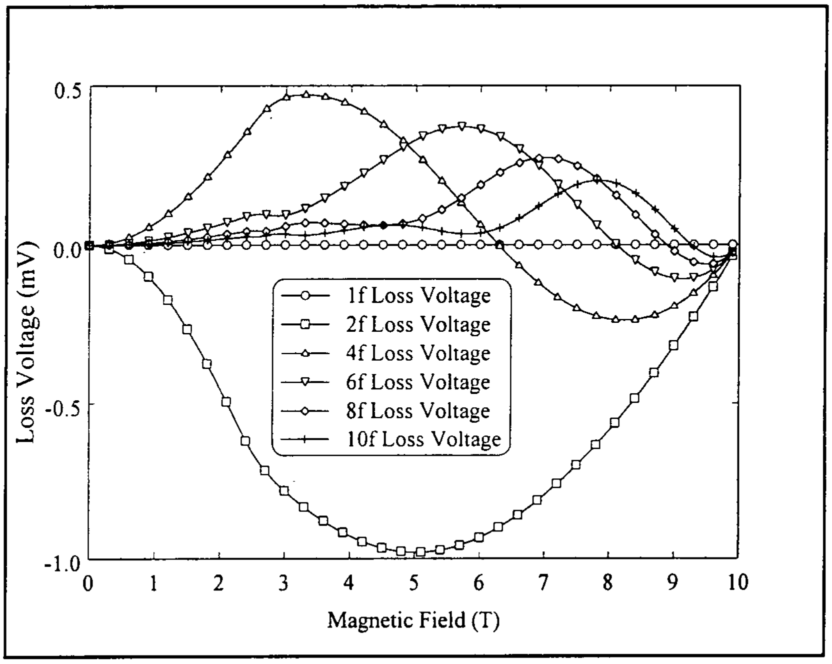

Figure 8.29 Loss voltages calculated for a NbTi-like sample with a slab geometry out of dc field centre, centred in the coil set.

8.10 Varying the Field Dependence of J_C, Sample Dimensions and Field Inhomogeneity

So far most of the calculations have been performed for a NbTi-like sample (equation 8.1) with values for $\alpha=5\times10^5\text{Am}^{-2}\text{T}^{-1}$ and $B_{C2} = 10\text{T}$. In the following sections, the field dependence of J_C, sample dimensions and applied field inhomogeneity will be varied to show that this work has significant consequences in the measurement of critical current density and irreversibility field in general, and that the calculations shown so far were not a special case. In each case a constant field gradient will be assumed across the sample length as this is the appropriate calculation for the results in Chapter 9 where the sample is positioned outside the field centre of the magnet.

8.10.1 Low Critical Current Density NbTi-like Sample

Consider variations in the value of the field gradient, effectively the homogeneity of the magnet. This is done for the NbTi-like sample with $\alpha = 5\times10^5\text{Am}^{-2}\text{T}^{-1}$ and $B_{C2} = 10$ T. The field gradient is varied from a perfect magnet i.e. $B_{ac} = 0$, to a poor homogeneity magnet, $B_{ac} = B / 100$ where B is the applied field.

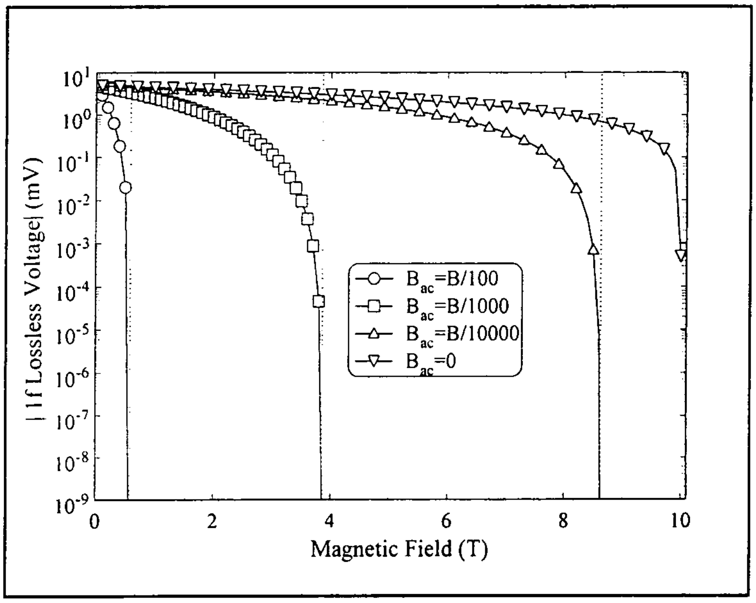

Figure 8.30 **Magnitudes of the 1f lossless voltage for various field homogeneities, showing the effect of B_{ac} on the measurement of critical current density and irreversibility fields.**

The zero ac field case represents the actual magnetic moment of the sample, and therefore allows the determination of the actual critical current density, going to zero at B_{C2}. For all non-zero field gradients the 1f lossless voltage goes to zero at gamma = 1, indicated by the dotted lines. This shows that the irreversibility field is not when the current density of the sample goes to zero, but is the point at which the ac field fully penetrates the sample. It can also be seen that the value of the 1f lossless voltage that is measured deviates significantly from that produced in the ideal case for the actual magnetic moment, at all fields greater than two thirds of the irreversibility field for all field gradients shown and hence any critical current densities calculated from the measured magnetic moment will be incorrect by more than a factor two, when at fields greater than two thirds of the upper critical field, even for the best case of field gradient calculated.

8.10.2 High Critical Current Density NbTi-like Sample

The next change was to increase the current density of the NbTi-like sample by setting $\alpha=5\times10^7 Am^{-2}T^{-1}$. This has the effect of moving the point at which gamma = 1 to much higher fields as the sample self field is much higher.

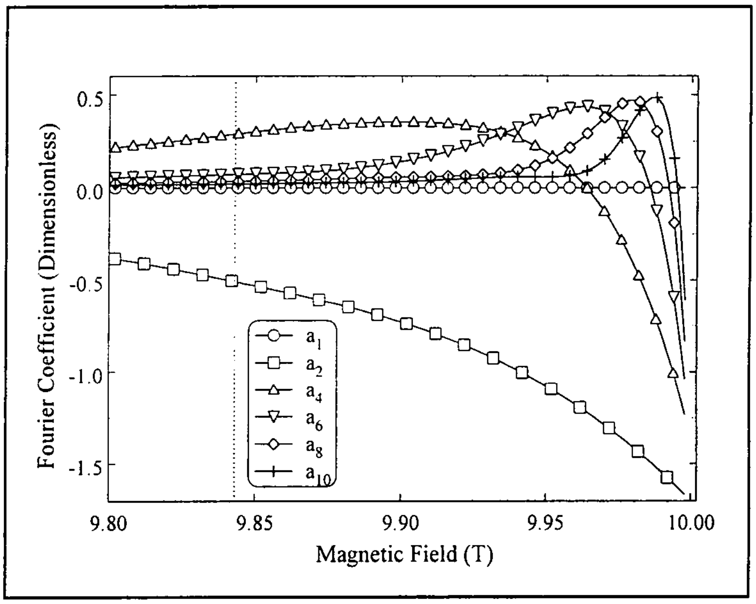

Figure 8.31 **Calculated values for the cosine Fourier coefficient a_n as a function of dc field.**

Figures 8.31 and 8.32 show the calculated Fourier coefficients in the high field region.

Again in both sine and cosine terms the odd Fourier coefficients are zero except for 1f and have a similar structure (i.e. the number of turning points and relative magnitudes of the peaks) to the lower J_C NbTi-like sample.

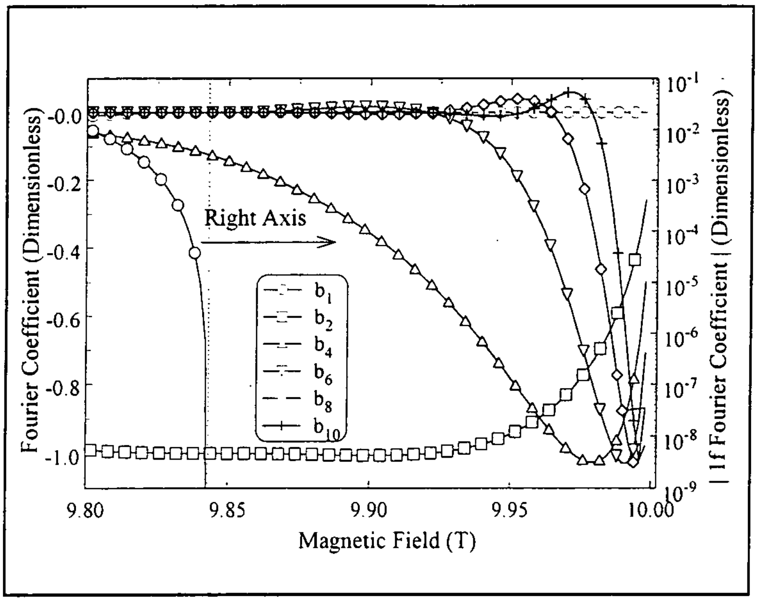

Figure 8.32 Calculated values for the sine Fourier coefficient b_n as a function of dc field. The magnitude of b_1 can be seen to go to zero on the log axis(right).

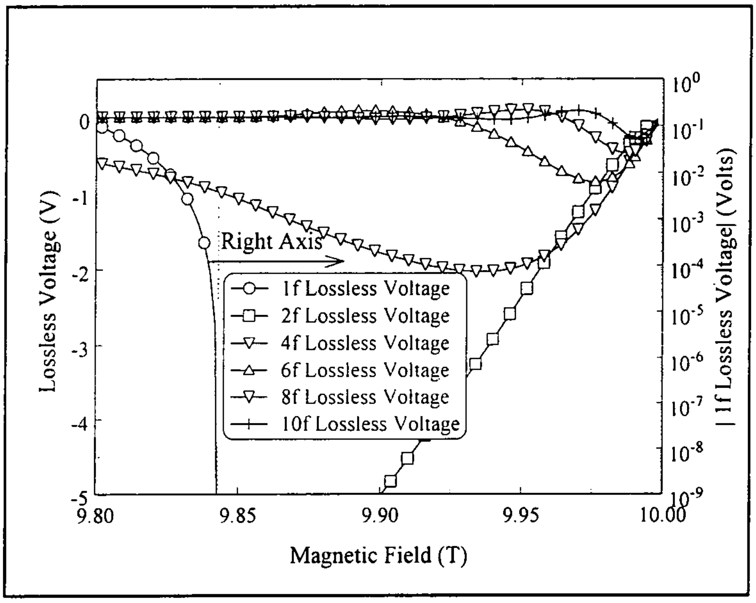

Figure 8.33 Calculated values for the lossless voltages as a function of dc field for the higher J_C sample.

These Fourier coefficients can be used to calculate the lossless and loss voltages as would be measured on an idealised lockin and are shown in figures 8.33 and 8.34.

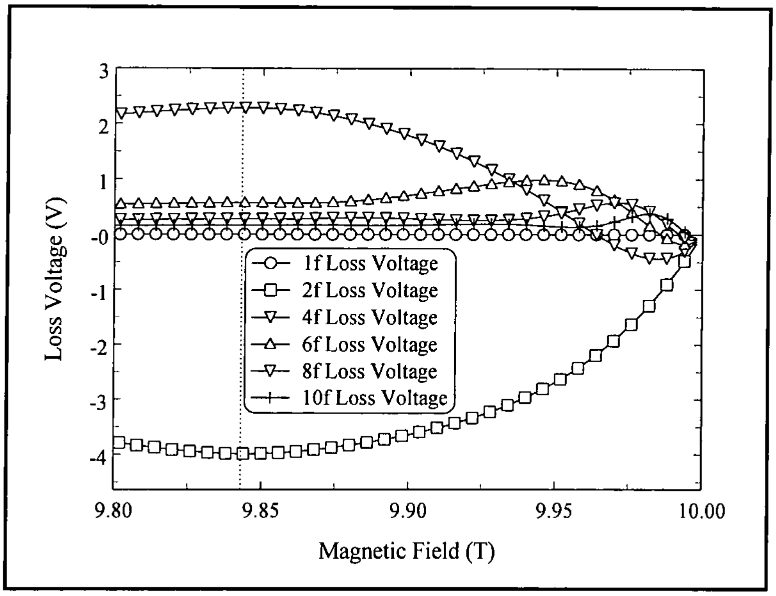

Figure 8.34 **Calculated values for the loss voltages as a function of dc field for the higher J_C sample.**

Again the 1f lossless voltage falls to zero below the upper critical field for the sample. The structures of all the voltages are similar to those of the low J_C sample.

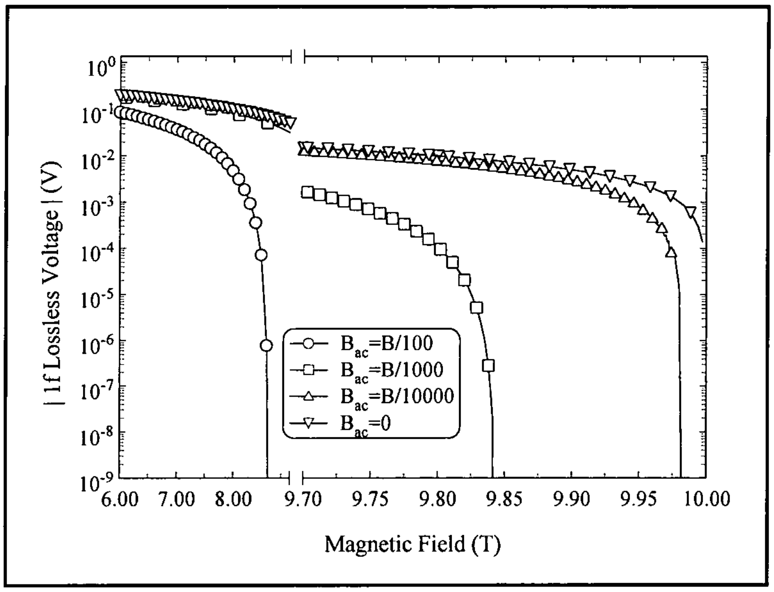

Figure 8.35 **Effect of varying field gradient for the high J_C sample showing that the field gradient always produces changes in irreversibility field and in measured Jc.**

For this sample the effect of varying the field gradient was considered across the same field homogeneity range as in figure 8.30. The results are shown in figure 8.35, the axis break allowing the whole range to be seen clearly. It can be seen that the irreversibility field is moved for even the best case of field gradient.

The final parameter to be varied is the sample radius as this is involved in determining the sample self field. It is also varied considerably in experimental measurements found in the literature, with sample radii commonly varying from a few tens of microns[9] to approximately 1 millimetre [2].

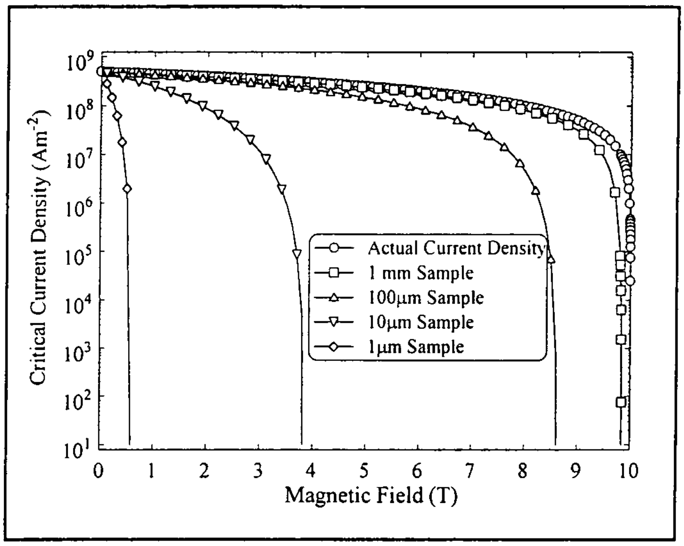

Figure 8.36 The variation in measured critical current density, calculated from the hysteresis in the 1f lossless voltage for samples with radii from 1mm to 1μm.

The results of these calculations are shown in figure 8.36, where the critical current density was determined from the magnetic moment measurement using the Bean Model. The irreversibility field is affected by the sample radius as is the measured critical current density. For samples of radius less than 100μm, the irreversibility field is reduced by at least 1T and the measured critical current density is lower by a factor 2 than the actual critical current density for all fields greater than half the upper critical field for this choice of critical current density and field inhomogeneity (one part in one thousand). This implies that the irreversibility field and the critical current density of samples of differing radii cannot be compared using only the 1f lossless component if the ac field is within one order of magnitude of the sample self field.

8.10.3 Kramer Critical Current Density

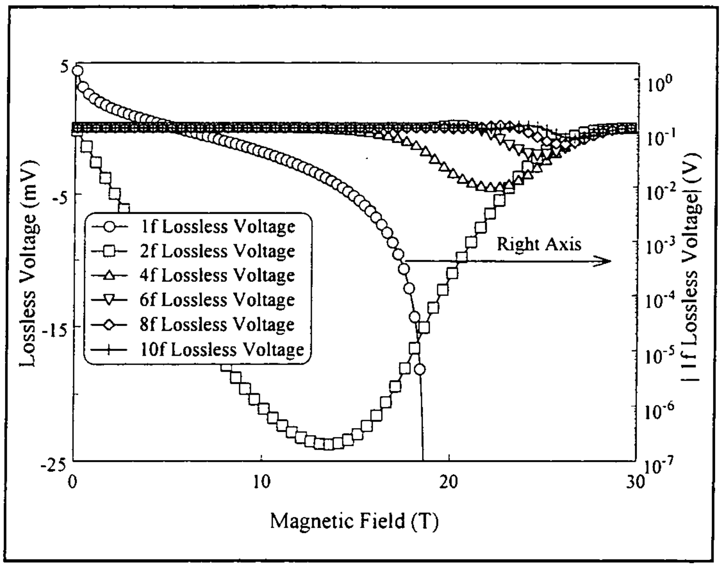

Figure 8.37 **Lossless voltages for a Kramer field dependence of critical current density for a sample that does not cross the centre of the dc field profile and is perfectly positioned within the coil set.**

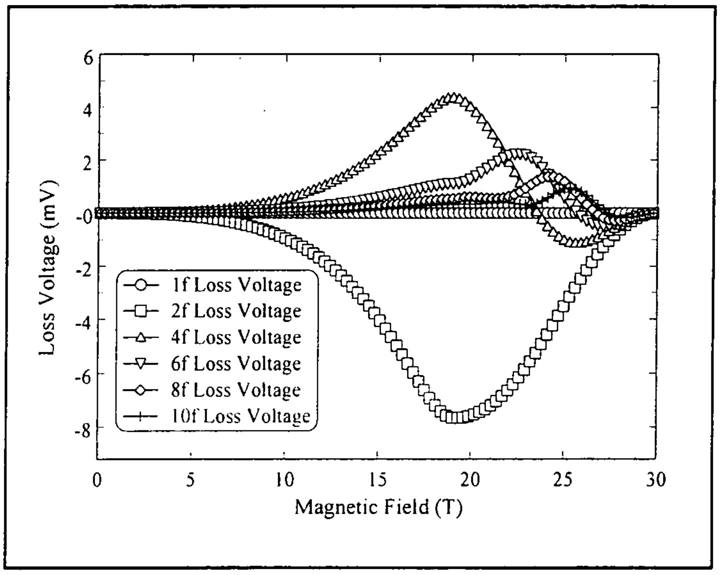

Figure 8.38 **Loss voltages for a Kramer field dependence of critical current for a sample that does not cross the centre of the dc field profile and is perfectly positioned within the coil set.**

This section considers a Kramer model for the critical current density, as is found to be applicable to Chevrel phase superconductors. Equation 8.2 describes the functional form of J_C where $\alpha = 5\times10^5 \mathrm{Am^{-2}T^{-3/2}}$ and $B_{C2} = 30$ T. First the calculations were performed for a sample that does not cross the centre of the dc field profile and that is perfectly positioned within the coil set. Figure 8.37 and 8.38 show the calculated lossless voltages and loss voltages respectively, all having similar structure to the NbTi-like sample, with the odd voltages all being zero except for the 1f lossless which goes to zero at $\gamma = 1$.

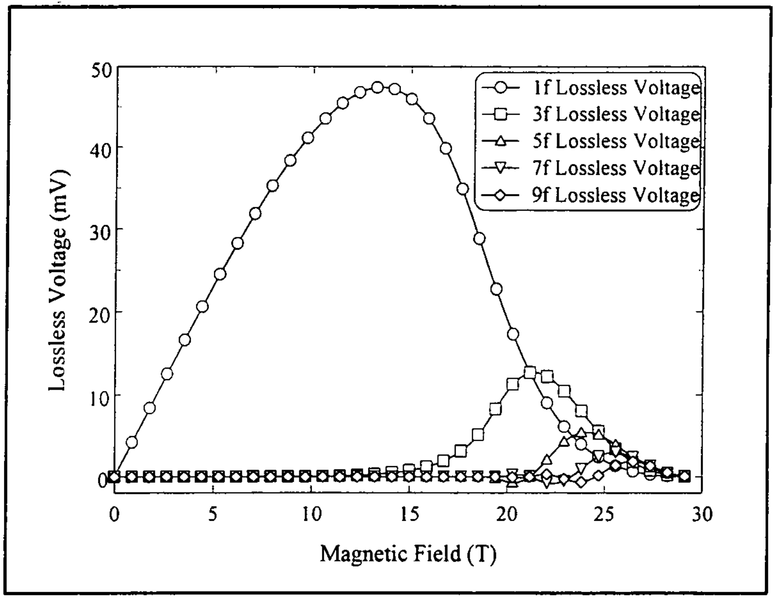

Figure 8.39 Lossless voltages calculated for the β_1 components of the offcentring term for a Kramer critical current density.

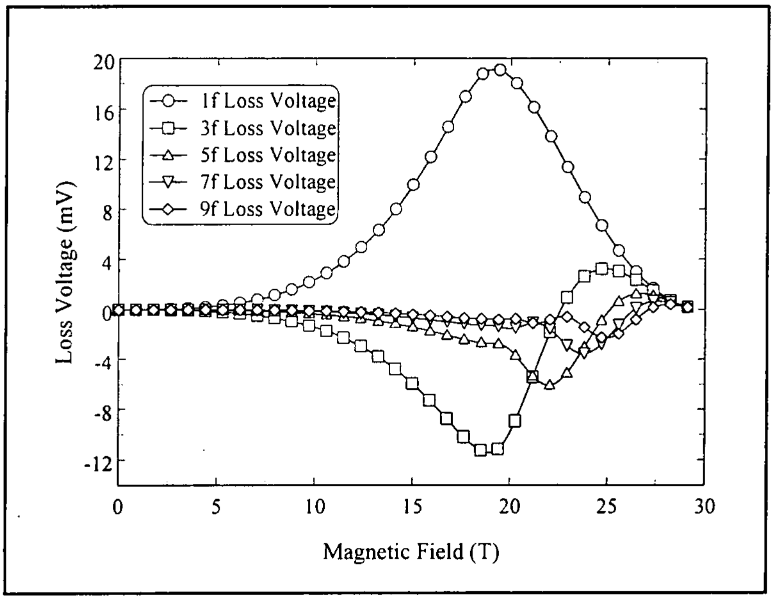

Figure 8.40 Loss voltages calculated for the β_1 components of the offcentring term for a Kramer critical current density.

Next the calculations were repeated to determined the voltages produced by the mispositioning of the sample within the pickup coils, i.e. β_0=0 and β_1=-2, the sign of β_1 being arbitrary and chosen to compare with a sample above the centre of the pickup coils, the results are shown in figures 8.39 and 8.40.

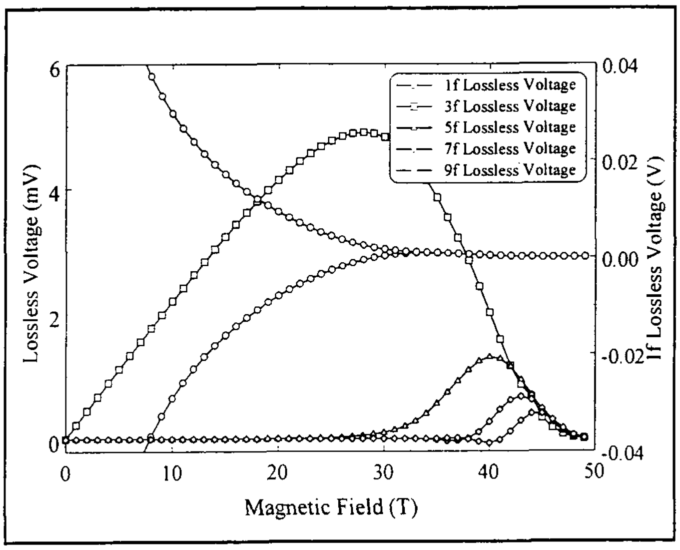

Figure 8.41 Calculated values for the lossless voltages for the section of the Kramer sample that crosses the field centre, perfectly positioned within the coil set.

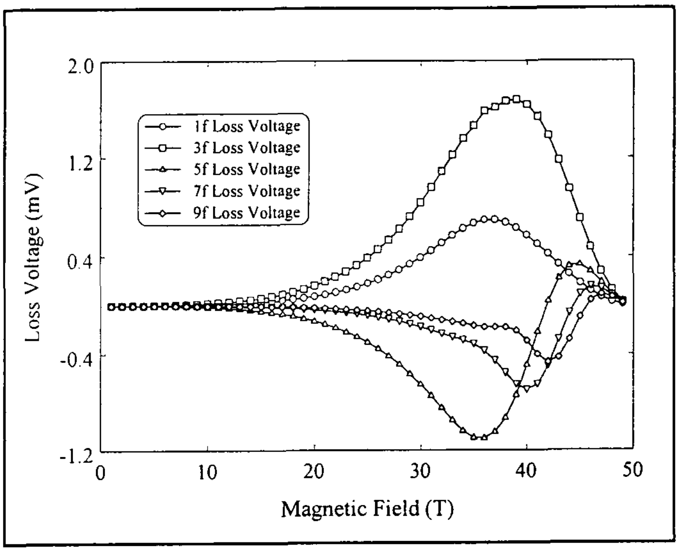

Figure 8.42 Calculated values for the loss voltages for the section of the Kramer sample that crosses the field centre, perfectly positioned within the coil set.

In figure 8.45, the values of B_{C2} were taken from 50 T to 10 T. All the 1f lossless voltages falls to zero at $\gamma = 1$, indicated by the dotted line. Hence the measured critical current density falls to zero at fields less than two thirds of where the actual critical current density becomes zero. Figure 8.46 shows the effect of varying the field homogeneity. The deviation from the actual magnetic moment, described by the $B_{ac} = 0$ case is clear from both the movement of the irreversibility field and the measured magnetic moment at fields greater than two thirds of the irreversibility field.

8.10.4 High T_C Superconductor Critical Current Density

Finally for this section a model for high temperature superconductivity is used as is described in equation 8.3 with $\alpha = 5 \times 10^8 \mathrm{Am}^{-2}$.

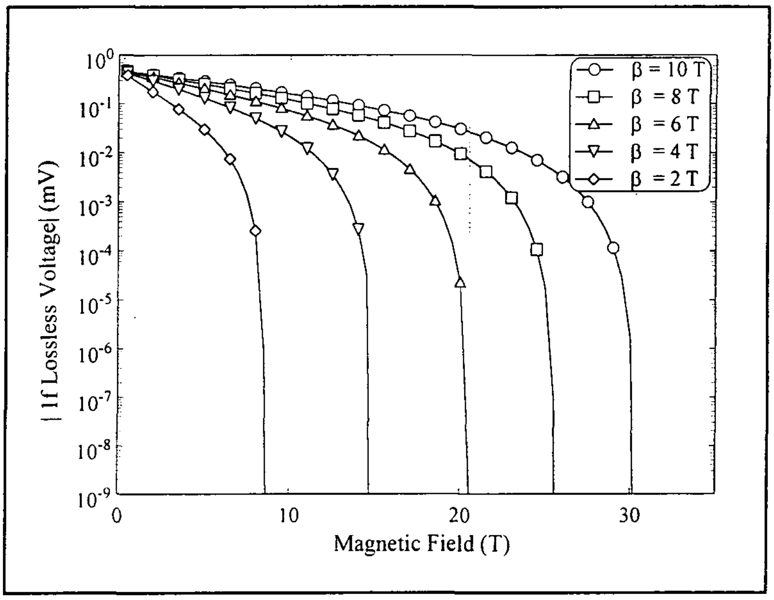

Figure 8.47 The magnitude of the 1f lossless voltage for a high temperature superconductor.

The special feature of this model is that with an exponentially decaying current density there is no irreversibility field as the current density never reaches zero. The affect of the field inhomogeneity is to introduce an irreversibility field at the point at which $\gamma = 1$. Figure 8.47 shows this for different values of β, all of which fall to zero at $\gamma = 1$ indicated by the dotted line, when in fact the actual magnetic moment never reaches zero for any finite value of B or β.

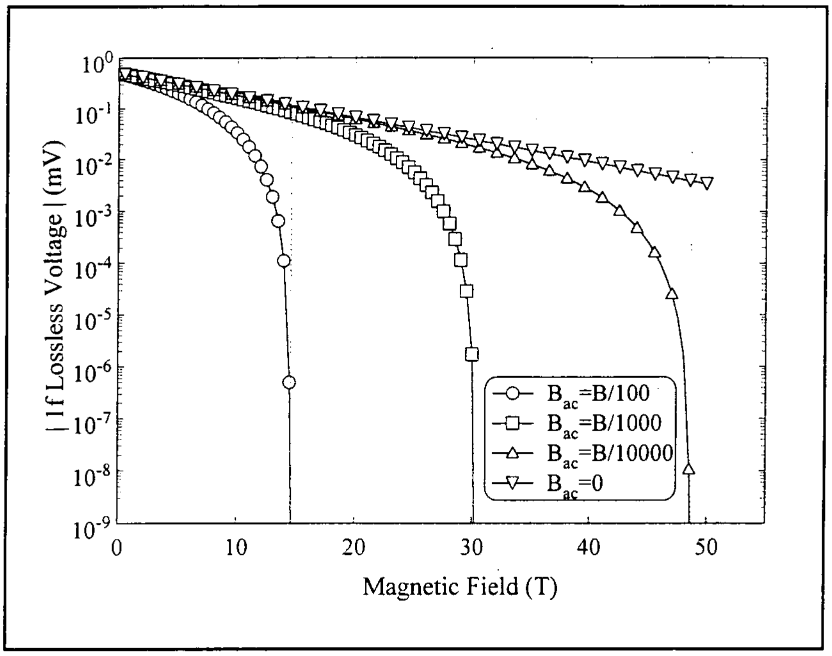

Figure 8.48 The magnitude of the 1f lossless voltage for various values of field inhomogeneity for a HTS like material. The perfectly homogenous magnet represented by $B_{ac} = 0$ has no irreversibility field.

Figure 8.48 shows clearly the effect of field inhomogeneity, with the actual magnetic moment being represented by $B_{ac} = 0$ and having no irreversibility field and the irreversibility field being introduced purely as an outcome of the ac field penetrating the sample. The measured magnetic moment for this sample is again significantly different from the actual magnetic moment, for any field greater than two thirds of the irreversibility field.

8.11 Summary of Predicted Voltages

In a idealised VSM measurement, the Bean profile through the superconductor produces a 1f lossless voltage proportional to the critical current density of the sample. By including the affect of the inhomogeneous dc field found in all real VSM systems, we have demonstrated that in fact this 1f lossless voltage does not represent the total magnetic moment of the sample. The effect of the inhomogeneous field is to reduce the size of the voltage at the driver frequency, hence changing the measured critical current density and irreversibility field.

Experimental Geometry	Even Multiples of the Driver Frequency	Odd Multiples of the Driver Frequency
Crossing dc Field Centre, Pickup Coil Centred Term	✗*	✓
Crossing dc Field Centre, Pickup Coil Offcentred Term	✓	✗*
Not Crossing dc Field Centre, Pickup Coil Centred Term	✓	✗
Not Crossing dc Field Centre, Pickup Coil Offcentred Term	✗	✓

* Present for (small) non symmetric sample

Table 8.1 Harmonics produced for the four experimental geometries considered. N.B. a 1f lossless magnetic moment is seen for all geometries.

It also produces reversible lossless and loss voltages at multiples of the driver frequency, the nature of which depends on the experimental geometry as shown in table 8.1.If the sample is perfectly positioned with the coil set and moves symmetrically about the turning point in the dc field, reversible voltages will be measured at the driver frequency and odd multiples of it in addition to the irreversible lossless voltage at the driver frequency. If the sample is not perfectly positioned within the pickup coils but still oscillates symmetrically about the turning point in the dc field then the odd voltages measured will be unchanged and additional voltages at even multiples of the driver frequency will be observed. If the sample is not moving symmetrically about the centre of the dc field then some combination of odd and even voltages will be measured, making analysis difficult. If the sample is vibrated so that no part of it crosses the centre of the dc field profile and is perfectly centred within the pickup coils then an irreversible lossless voltage will be measured at the driver frequency and reversible lossless and loss voltages at only even multiples of it. If the sample is not perfectly positioned within the pickup coils then reversible lossless and loss voltages will be measured at odd multiples of the driver frequency in addition to the even voltages. This allows the separation of the two effects experimentally to determine the relative contributions of each of the new effects under consideration for a sample that does not cross the centre of the dc field profile.

8.12 Discussion

The magnetic phase diagram for superconductors has been the subject of investigation since it was found by Muller et al**[10]** that the field cooled and zero field cooled magnetisation of La_2CuO_{4-y}:Ba were reversible close to the upper critical field before becoming hysteretic at lower fields. The field above which the magnetisation curve was reversible became know as the Irreversibility Field and a debate then ensued as to the nature of the superconductivity in this reversible region. It was postulated that as the superconductor crossed into the reversible region, the state of the flux line lattice changed from being a solid to another state, a consensus on the nature of this other state has yet to be reached, but one popular theory is that the lattice melts and becomes a liquid. As the name suggests the fluxons in a flux liquid can move though the material and are unpinned, which in turn implies that the critical current density is zero, i.e. a lossless supercurrent cannot flow. The "melting" of the flux line lattice can be mapped out on the magnetic phase diagram for a superconductor and numerous theories have been developed to try to explain this so called "melting line" e.g. Density Functional Theory**[11]**. Alternatives to "melting" include Anderson-Kim Flux creep**[12]** and Giant Flux Creep**[13]**, all of which are discussed in chapter three. Many measurements have been performed using various techniques, some of which are described in chapter three, one of which was the vibration sample magnetometer, to try to determine which, if any, of these theories were correct. The understanding of this phenomena is crucial as it places a limit of the possible application of high temperature superconductors.

The reversible region of the magnetisation curve was also of interest as in this region when there is no pinning, the fundamental properties of the superconducting state can be investigated. In particular the penetration depth, coherence length and hence kappa.

could all be derived from the reversible region of the magnetisation curve.

The calculations presented in this chapter have shown that when measuring a magnetisation curve using a vibrating sample magnetometer, the irreversibility field, defined as the point at which the magnetisation curve becomes reversible is not the point at which the critical current density of the sample becomes zero, but is instead the point at which the effective ac field produced by the sample moving in an inhomogeneous field fully penetrates the sample throughout its volume. Hence for a vibrating sample magnetometer, sample self field and field inhomogeneity are the two parameters that determine when the magnetisation curve becomes reversible. Voltages at multiples of the driver frequency are measured, their properties depending on the exact experimental arrangement, and the positioning of the sample with respect to the dc field and the pickup coils. The size of these voltages is also dependent on the critical current density of the sample, hence in order to measure the field at which the critical current densities becomes zero, using a VSM, it is necessary to measure higher multiples of the driver frequency as these become zero when the critical current density becomes zero.

In addition to the problem with the irreversible part of the magnetisation curve, the reversible part of the magnetisation curve, measured at the driver frequency, which has previously been attributed solely to the reversible superconducting properties of the sample, has been shown to be dependent also on the positioning of the sample within the pickup coils and the dc field.

In light of these results, previous information derived from magnetisation curves measured using a vibrating sample magnetometer in the literature must be re-examined to determine whether the effects presented here were the determining factors in the conclusions reached or whether the corrections are small enough to be neglected. This is true for both the irreversible region of the magnetisation curve, i.e. critical current density and irreversibility field; and the reversible region i.e. Ginzburg Landau parameters of penetration depth, coherence length and hence kappa. Each will now be considered in turn.

For the irreversible region, both the sample dimensions and the field inhomogeneity will be considered as these are the determining factors in accessing the validity of measurements of critical current density and irreversibility field made using a VSM.

Firstly consider the effects of variation in sample geometry. Samples of small dimensions will necessarily have small self fields and therefore be penetrated by much smaller ac fields. In particular consider the technique in which samples are ground into powder to distinguish between inter- and intragranular critical current densities**[14][15]**. The comparison of J_C and B_{IRR} before and after grinding is only valid if the self field of the sample in both cases is more than an order of magnitude larger than the ac field. Furthermore the comparison of any two samples with differing dimensions must be examined to ensure the results were comparable e.g. the comparison of monofilamentary and multifilamentary wires can only be done if the self field of the individual filaments for both wire types is at least an order of magnitude higher than the ac field, otherwise the critical current density determined from the magnetisation loop will be incorrect. This is difficult to do in the literature as samples are compared, with no sample dimensions given **[16]**.

Secondly, the field inhomogeneity of the magnet system used has also been shown to be a determining factor for the value of the measured critical current density and irreversibility field. It is possible to estimate the minimum critical current density that can be measured on a VSM system of a given homogeneity using equations 8.4 and 8.5. Typical values for the field inhomogeneity in commercial systems are 1 part in 10^3 over 10mm, which for a 5mm sample oscillating about the field centre with a typical throw distance of 1mm, gives an effective ac field of approximately 0.4mT for a dc field of 10T using equation 8.4 and as explained in more detail in section 9.22. For the effect of the ac field on the measurement to be small $\gamma<0.1$, and hence for a sample of radius 1mm:

$$J_c > \frac{B_{ac}}{\gamma \cdot \mu_0 r_m}$$

$$J_c > \frac{4\times10^{-4}}{0.1.\mu_0.1\times10^{-3}} > 4\times10^{6} Am^{-2} \tag{39}$$

Field inhomogeneity is rarely considered in the literature, making comparison between results obtain by different groups difficult, particularly when non commercial measurement systems are used[17] as then the magnet could be of any homogeneity. Also consider the practise, when using high field facilities, of taking low field data on a standard laboratory system, and then combining this with data from the high field system, where the field inhomogeneities will almost certainly be different[18]. Considering the reversible part of the magnetisation curve, positioning of the sample within the pickup coils and the dc field has been shown to produce reversible voltages at the driver frequency in both the lossless and loss components. Therefore it is essential that in order to determine the genuine reversible region of the magnetisation curve, higher harmonics are measured. Once these harmonics fall to zero, the critical current density is zero and hence any reversible properties measured are due solely to the reversible properties of the superconductor. It should be noted that other methods of measurement of magnetisation curves have found both irreversible and reversible regions, and that by these techniques the onset of the reversible region is when the critical current density becomes zero. It is not suggested here that the reversible region is purely an artefact of the measurement of magnetic moment, however it has been shown that the point at which the magnetisation curve become reversible, when measured using a vibrating sample magnetometer is not the point at which the critical current density becomes zero, nor is the reversible region purely determined by the reversible superconducting properties of the sample. The size of both these corrections is dependent on sample geometry, field inhomogeneity and sample positioning, and hence none of these features of the magnetisation curve can be considered characteristic of the material being measured when using a VSM.

8.13 Conclusion

The effect of inhomogeneity in the applied dc magnetic field and the positioning of the sample within the pickup coils and the dc field for a VSM measurement of magnetic moment has been determined. The magnetic moment of a sample has been determined using the critical state model and from this, the voltage induced in the pickup coils has been calculated and Fourier deconvoluted. It was found that when the effective ac field penetrates the sample throughout its volume, the magnetisation loop becomes reversible at the driver frequency. Hence the irreversibility field, the point at which the magnetisation loop becomes reversible, is not the point at which the critical current density goes to zero. This implies that B_{IRR} is dependent on sample geometry, field inhomogeneity and the geometry of the sample and pickup coils relative to the centre of the dc field profile. It therefore cannot be considered a characteristic property of the material alone. The field at which the critical current density goes to zero can be determined from a measurement of the higher harmonics, as these become zero when the critical current density is zero. It was also found that if the sample was not perfectly centred within the pickup coils or the sample crossed the centre of the dc field profile, reversible voltages at odd multiples of the driver frequency, including the driver frequency itself would be measured. In order to measure the genuine reversible properties of the superconducting sample it is necessary to measure the harmonics of the 1f as when these become zero, the critical current density is zero and hence the magnetic moment measured can be considered to represent only the reversible superconducting properties of the sample (i.e. independent of J_C). In the light of this, previous work on irreversibility fields, critical current densities, and the reversible magnetisation, measured using a VSM must be re-examined to ensure that the effects calculated in this chapter can be neglected.

8.14 References

[1] Review of magnetometery, Foner S *IEEE Trans. Mag.* **17** 3358 (1981)

[2] Zheng D N, Ramsbottom H D and Hampshire D P *Phys. Rev. B* **52** (17) 12931 (1995)

[3] Bean C P *Rev. Mod. Phys.* **36** 31 (1964)

[4] Perkins G K, Cohen L F, Zhukov A D and Caplin A D *Phys. Rev. B* **51** (12) 8513 (1995)

[5] Bean C P *Rev. Mod. Phys.* **36** 31 (1964)

[6] Mallinson J *J. Appl. Phys.* **37** 2514 (1966)

[7] Kramer E J *J. Appl. Phys.* **44** 1360 (1972)

[8] Osamura K, Nonaka S, Matsui M, Oku T, Ochiai S and Hampshire D P *J. Appl. Phys.* **79** 7877 (1996)

[9] Cohen L F, Totty J T, Perkins G K, Doyle R A and Kadowaki K *Supercon. Sci. Technol.* **10** 195 (1997)

[10] Muller K A, Takashige M and Bednorz J G *Phys. Rev. Let.* **58** 1143 (1987)

[11] Ramakrishman T V and Youssouff M *Phys. Rev. B* **19** 2775 (1979)

[12] Anderson P W and Kim Y B, *Rev. Mod. Phys.* **36** 39 (1964)

[13] Yeshurun Y and Malozemoff A P, *Phys. Rev. Let.* **60** 2202 (1988)

[14] Dhalle M, Cuthbert M, Johnston M D, Everett J, Flukiger R, Dou S X, Goldacker W, Beales T and Caplin A D *Supercon. Sci. Technol.* **10** 21 (1997)

[15] Sekula S T, Brynestad J, Christen D K, Thompson J R and Kim Y C *IEEE Trans. Mag.* **25** 2266 (1989)

[16] Zhukov A A, Kupfer H, Perkins G, Cohen L F, Caplin A D, Klestov S A, Claus H, Voronkova V I, Wolf T and Wuhl H *Phys. Rev. B* **51** (18) 12704 (1995)

[17] Schlenker C, Liu C J, Buder R, Schubert J and Stritzker B *Physica C* **180** 148 (1991)

[18] Han G C, Awaji S, Watanabe K, Kobayashi N, Kimura K and Hashimoto M *Physica C* **262** 292 (1996)

Chapter 9
Vibrating Sample Magnetometer Measurements of Superconductors in Inhomogeneous Magnetic Fields

9.1 Introduction to Chapter 9

In this chapter experimental support for the predictions of Chapter 8 is presented. All the data in this chapter has been taken on the VSM system described in chapter 7. The experimental detail will be discussed in section 9.2. In order to compare directly the calculations with the experimental results it is necessary to account properly for the anharmonicity of the driver, explained in section 9.3, and the phase angle correction for the different measurement frequencies explained in section 9.4. These corrections will then be applied to the data, an example of which is shown in section 9.5, with the raw data and corrected results being shown. After this point all results will only be shown after the corrections have been performed. The remainder of this chapter will contain the results of a series of measurements designed to investigate the predictions of the calculations in chapter 8. Samples were chosen to allow comparison with the calculation for the NbTi like sample and the Kramer sample used in chapter 8, and were multifilamentary NbTi wire and the Chevrel phase superconductors PMS and SMS, discussed in chapters 4 and 5 respectively. It is however important to note that the agreement for both the size and position of the features predicted in chapter 8 depends on the ratio of the sample self field to the effective ac field at any particular field. Hence if the critical current density of the sample is not exactly the same as that of the model sample, then the position and the magnitude of the features will change. It is also expected that the positions of the features relative to the irreversibility field will also change for different ac fields, dependent on the field dependence of the sample's critical current density.

For the measurements performed above T_C, the backgrounds were found to be dominated by the noise level, centred about zero. The non zero backgrounds introduced in this section for both the SMS sample measured at 8.4K and the PMS sample measured at 10.4K are intended as guides to the eye. They are determined primarily using the measurements at 6.8K and 6.7K for SMS and PMS respectively where the critical current densities of the samples are higher and hence the ac field effect features occur at higher fields. This means that in the lower field regions, the non zero harmonic magnetic moments that are not due to the ac field effects can be estimated from the low temperature measurements and any deviations from these can be seen in the higher temperature measurements.

The effect of the positioning of the sample within the pickup coils will be considered in section 9.6, by comparing a sample in the pickup coil centre with one raised above the pickup coil centre and one below the pickup coil centre. The sample positioned above the pickup coil centre is a NbTi wire sample and, as discussed in section 9.9, is limited by the size of the signal produced by the sample. It still however shows features at the driver frequency and odd multiples of it, as predicted by the mathematics in section 8.7. In order to improve the signal to noise ratio, a PMS sample was measured 4mm below the centre of the pickup coils, with the pickup coils positioned 5cm above the centre of the dc field profile. This measurement contains signals at both odd and even multiples of the driver frequency, as the sample is both in a large field gradient and out of the centre of the pickup coils. The magnetic moments measured at the odd multiples of the driver frequency agree well with those predicted by the mathematics in section 8.10.3, as do the 2f magnetic moments, however the 4f magnetic moments are dominated by the noise. In section 9.7 harmonic measurements will be presented for a sample of $SnMo_6S_8$, at two temperatures, in three different field gradients. This sample is the largest of the three samples measured and therefore has the best signal to noise ratio. The measurement at +5cm are in good agreement with the calculations of section 8.10.3 in both 2f, 4f and 6f, though for the 6f magnetic moments measured are comparable with the noise level. The other field positions show most of the expected maxima and minima, however the backgrounds become more important. For the field centre case, good agreement is not expected due to the importance of the exact positioning of the sample as explained in section 8.8. The 3f, 5f and 7f magnetic moments contain non zero backgrounds, attributed to the anharmonicity of the driver and which makes the distinguishing of the maxima and minimax more difficult, however they are broadly consistent with the calculations of section 8.10.3. The measured critical current density, determined from the hysteresis in the 1f lossless component will also be presented for this sample at three temperatures and three field gradients. Section 9.8 will contain harmonic data for $PbMo_6S_8$ for two temperatures and two field positions. Again good agreement is found for the +5cm measurement at both temperatures, allowing for the non zero backgrounds introduced in some of the measurements, while the field centre measurement appears to be dominated by the difficulties discussed in section 8.8 where the exact sample positioning was found to be crucial. Finally in this section, the measured critical current density, determined from the hysteresis in the 1f lossless component will be presented for this sample at three temperatures and two field gradients Section 9.9 will contain harmonic data for NbTi multifilamentary wire, in two field gradients at 4.2K.The small size of the signal produced by this sample meant that harmonic measurements at temperatures above 4.2K were below the sensitivity of the instrument The measured critical current density will also be presented for three temperatures in two field gradients. The results and their implications will be discussed in section 9.10 and the conclusions of this chapter will be discussed in section 9.11.

9.2 Experimental Detail

The experiments described in this chapter were all performed using the VSM system in Durham as described in chapter 7, inserted inside an Oxford Instruments 15/17T superconducting solenoid magnet.

9.2.1 VSM Insert Positioning

In order to vary to field inhomogeneity in which the sample vibrated, the VSM insert was raised above the centre of the dc field by 2cm and 5cm. For the measurement at +2cm the small dc coil was also raised 2 cm but for the +5cm position it was kept central in the dc field. This was to prevent the small dc coil protruding from the top of the 15/17T magnet as this would prevent the VSM insert from being held rigid within the bore of the magnet.

9.2.2 Ac. Field Determination

The magnet used for these measurements was specified as having a homogeneity of 1 part in 1000 over a 10mm dsv.

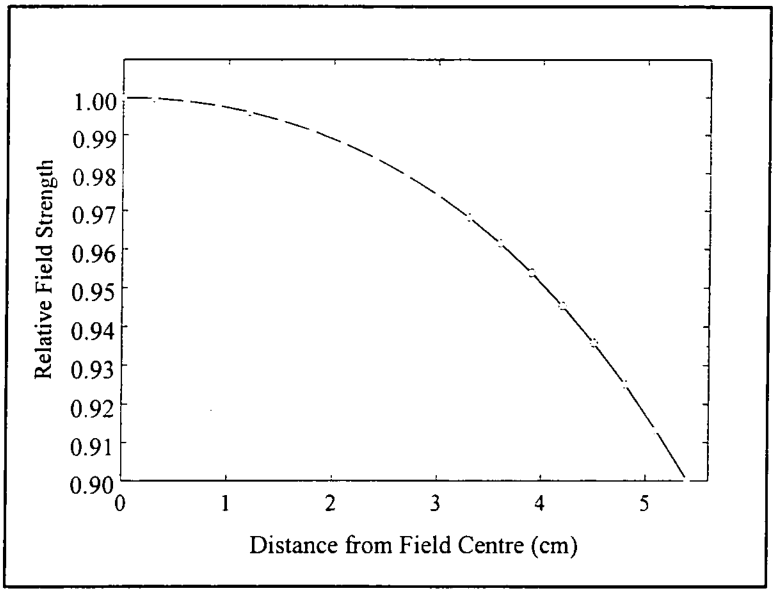

Figure 9.1 **Dc. field profile for the 15/17T magnet allowing the determination of the effective ac field.**

The field profile is shown in figure 9.1 and it can be seen that the value of the dc field changed by less than 10% even at +5cm and no correction has been made for this in the data presented, except in the critical current density figures. For the calculations in chapter 8, the field profile was take to be a roof profile, with a constant slope on either side of the maximum at the field centre. This can clearly be seen not to be the case for the actual field profile, but is a good approximation away from the centre of the field. The field profile in figure 9.1 was differentiated, allowing the field inhomogeneity for the three measurement positions to be determined. For the sample positioned across the centre of the dc profile this definition becomes more complicated, however as is shown in section 8.8, the net effect is certainly non zero, no matter how well the sample is positioned. Consider a 5mm sample oscillating about the dc field centre, with a throw distance of 1mm. This leaves a 2mm section of the sample on either side of the section of the sample swept out by the dc field centre. Both of these sections can be considered to oscillate about a position 1.5mm from the centre of the dc field profile and so it is at this point that the field gradient will be used to calculate the effective ac field for the field centred sample. Hence for this work the field gradients determined from the profile in figure 9.1 are:

- Field Centre = B x 8.0×10^{-4}T.cm^{-1}
- Plus 2cm = B x 1.1×10^{-2}T.cm^{-1}
- Plus 5cm = B x 4.0×10^{-2}T.cm^{-1}

where B is the dc field. This allows the determination of the effective ac magnetic fields, using equation 8.4, applied to the sample which for a throw distance of 0.8mm for the Durham VSM system are:

- Field Centre = B.3.2×10^{-5}T
- Plus 2cm = B.4.4×10^{-4}T
- Plus 5cm = B.1.6×10^{-3}T

9.2.3 Measurement Procedure

The VSM system was inserted in the 15/17T magnet and the noise level reduce to an acceptable level. The temperature was then set manually using a Lakeshore temperature controller, controlling on a capacitance thermometer, which is insensitive to magnetic field. The dc field was swept at 0.09 T.min^{-1} and 5 points were taken of both X and Y channels of the lockin for each of the harmonics, then the harmonic was increased, allowing time for the lockin to stabilise after each change of frequency before the next set of points was recorded. Measuring the harmonics in this manner instead of sweeping the field and measuring one harmonic on each field sweep reduces the possibility of instrumental or temperature drift affecting the results.

9.3 Anharmonicity Correction

As explained in Chapter 7, the vibration of the driver is not perfectly sinusoidal. This complicates the comparison between the calculated voltages and the measured voltages in two ways. Firstly, as shown by the nickel measurement in section 7.7.2, a percentage of the signal measured as the 1f lossless magnetic moment is also measured in the higher harmonics. In order to correct for this, the values in table 7.1 have been used to correct the higher frequency voltages by subtracting the percentage of the 1f lossless that is due to the driver anharmonicity using:

$$\begin{aligned} Corrected(\ nf\ )_X &= Measured(\ nf\ )_X - Anharmonic\%(\ 1f\ )_X \\ Corrected(\ nf\ )_Y &= Measured(\ nf\ )_Y - Anharmonic\%(\ 1f\ )_X \end{aligned} \qquad \textbf{(1)}$$

where the Anharmonic% is as given in table 7.1 and the Measured(nf)$_X$ and Measured(nf)$_Y$ are the lockin X and Y values at the nth multiple of the driver frequency. The other problem caused by the anharmonicity of the driver is that it is no longer the case that a simple sinusoidal ac field is being applied to the superconductor by its movement in the inhomogeneous dc field. Due to the driver anharmonicity there is also an effective ac field in 3f, the calculations for which have not been covered in this work, and no correction will be made for this effect.

9.4 Phase Angle Correction

As explained in chapter 7, the sample is vibrated by the vibration head in an almost sinusoidal manner. This frequency of vibration is fed to the lockin amplifier which then measures the signal produced from the pickup coils at this frequency, or an integer multiple of it. When a sample is measured, the phase angle is taken so as to make the signal produced from Ni a positive sine wave, and the signal for a superconductor below T_c and in the Meissner state a negative sine wave. The cosine wave in both cases is by definition equal to zero

9.4.1 First Harmonic Measurements

The rotation required to give the correct signals for nickel and superconductor was obtained as follows. The lockin amplifier was autophased on the signal, which by definition makes the sine coefficient a maximum and a positive value and hence zeros the cosine value. For Ni, this was ideal, however for a superconductor a negative coefficient was required and hence a 180 degree rotation was introduced. The autophase on a superconductor gave a phase angle ϕ, of approximately 92 degrees. Then the lockin phase was rotated by 180 degrees to give a negative signal. Hence the initial phase angle for the reference on the lockin was ϕ - 180 = -88 degrees.

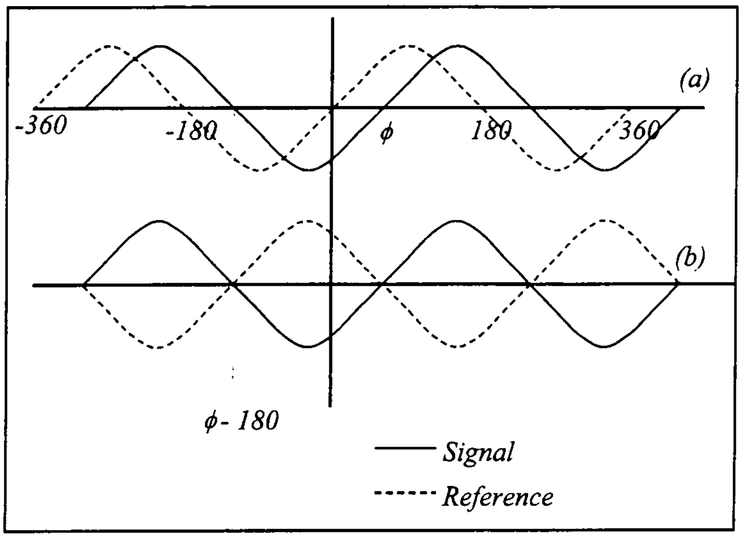

Figure 9.2 **The phase relation between the 1f lossless signal and the 1f lossless reference where ϕ is the 1f phase angle.**

This is represented in figure 9.2, with the initial relation between signal and reference being shown in trace (a) and the relation after adjustment being shown in trace (b).

9.4.2 Higher Harmonic Measurements

First consider the measurement of the voltage at twice the measurement frequency.

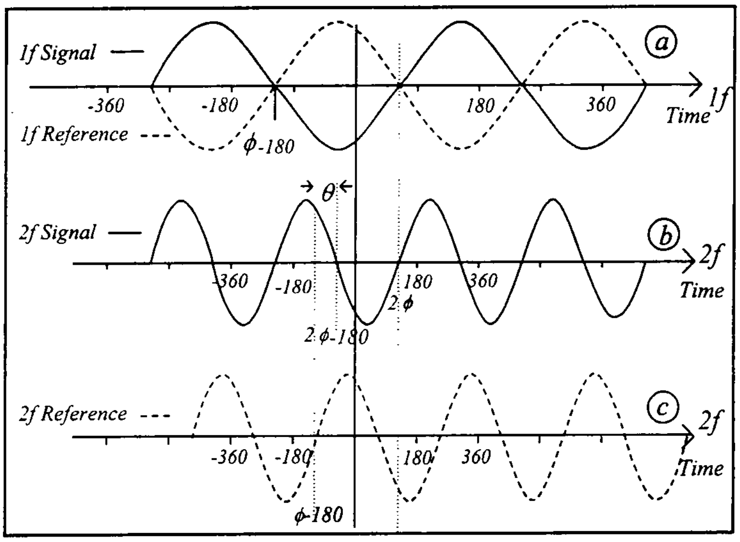

Figure 9.3 **Phase relation between the 1f and the 2f lossless signal and reference, showing the phase shift(θ) required to compare the data and experiment for a 1f phase angle of ϕ.**

The signal at 2f will be in phase with the signal in 1f as shown in figure 9.3 traces a and b, i.e. the signal will be shifted by an angle ϕ in 1f and hence shifted by an angle 2ϕ in 2f. In order to compare the measured values with the mathematics, it is necessary to determine the lossless and loss voltages at each frequency from the X and Y measured values. The reference signal will have a phase such that the phase shift with respect to the origin is ϕ- 180 in 2 f as shown in figure 9.3 trace (c). The combination of these two phase shifts leads to a difference in phase between the lockin sine reference and the sine component of the signal, preventing the voltages measured on the lockin being compared directly with the lossless and loss voltages predicted by the calculations. A phase shift (θ) is required to make the signal and reference in antiphase as is the case in 1f, allowing comparison with the calculations.

From figure 9.3, this phase shift required to relate the X and Y measured voltages to the lossless and loss voltages can be seen to be for the 2f voltage:

$$\left(2\omega t+(180-2\phi)\right) - \left(2\omega t+(180-\phi)\right) = -\phi \qquad \textbf{(2)}$$

and can be generalised for the n f voltage to:

$$\theta = (180-n\phi) - (180-\phi) = (1-n)\phi \qquad \textbf{(3)}$$

where n is an integer and ϕ is the initial autophase angle in 1f for the sample. To allow the comparison of calculated and measured fourier components the data will be rotated through θ as follows.

A signal measured as (X,Y) can be transformed into a signal (X',Y') when the two coordinate axes are related by a simple rotation through an angle θ using:

$$R=\sqrt{X^2+Y^2} \qquad \textbf{(4)}$$

and:

$$\tan(\psi)=\frac{Y}{X} \qquad \textbf{(5)}$$

where X and Y are the measured values on the lockin amplifier. This is shown schematically in figure 9.4.

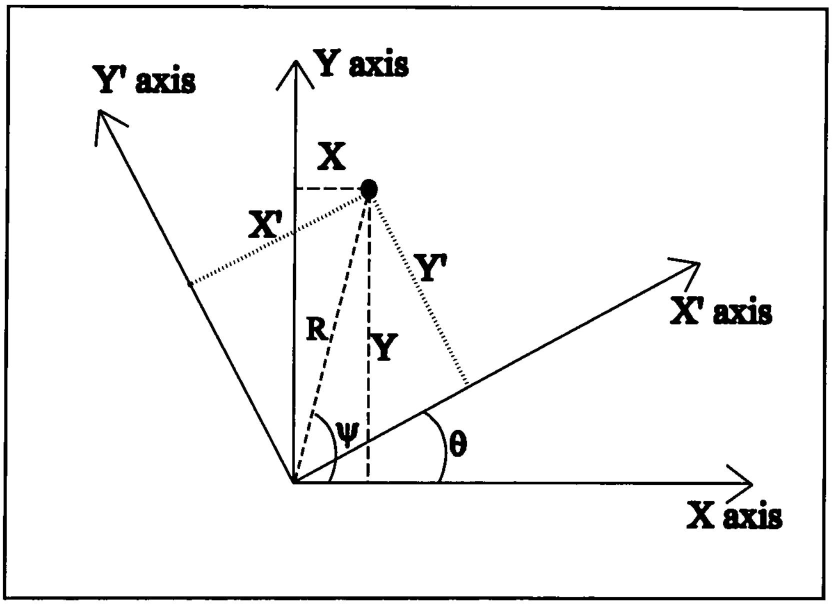

Figure 9.4 The rotation applied to two coordinate axes for a rotation of angle θ.

From R and ψ it is then possible to calculate values for X' using:

$$X'=R\cos(\psi-\theta) \tag{6}$$

and Y' using:

$$Y'=R\sin(\psi-\theta) \tag{7}$$

9.5 Conversions to Allow Comparison Between the Calculations and the Experimental Results

In this section the conversions of the data to allow comparison with the mathematics will be demonstrated on one of the data sets. The data will be presented firstly as raw data and then the corrected data will be presented. The sample is $SnMo_6S_8$ measured 5cm outside the centre of the dc field at a temperature of 8.4K. As SMS is thought to be a grain boundary pinning material, it is appropriate to compare these measurements with the Kramer sample calculations in section 8.10.3.

9.5.1 Raw Data

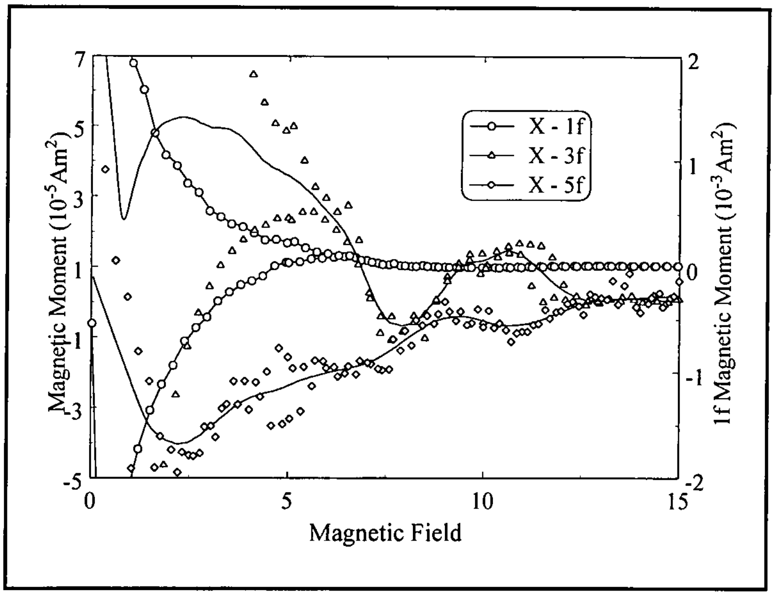

Figure 9.5 **Voltages measured in the X component at odd multiples of the driver frequency.**

Figure 9.5 shows the voltages measured in X on the lockin amplifier at odd multiples of the driver frequency to 5f. The 1f voltage is shown on the right hand axis and the other two are shown on the left hand axis.

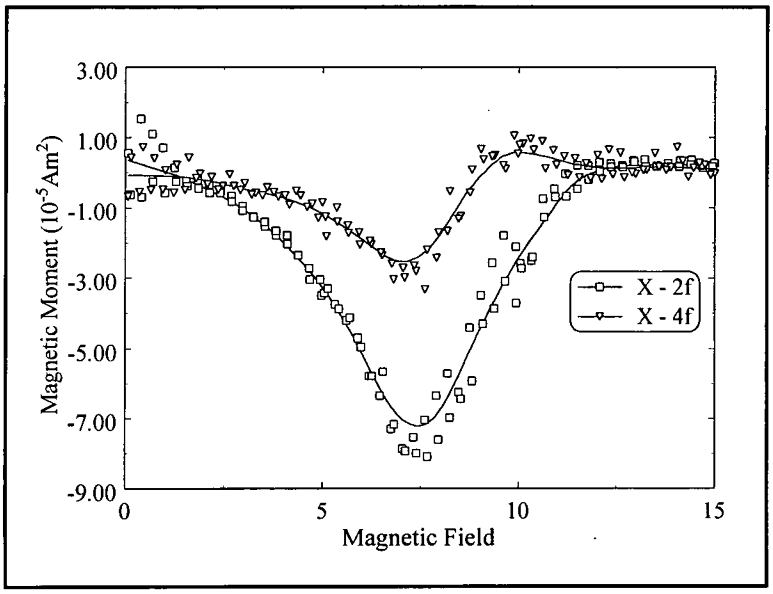

Figure 9.6 **Voltages measured in the X component at even multiples of the driver frequency.**

For the even multiples of the driver frequency, it can be seen that the hysteresis and background are small compared to the odd voltages as expected due to the small anharmonicity corrections in the even voltages.

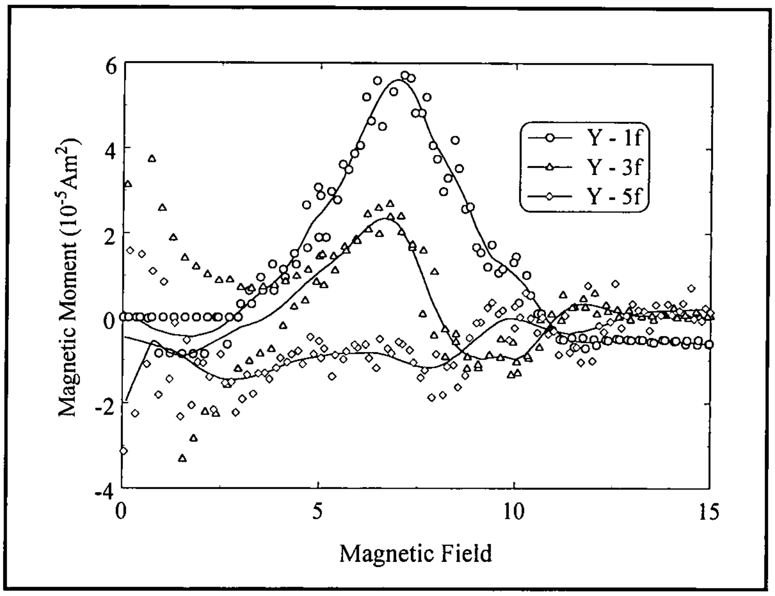

Figure 9.7 **Voltages measured in the Y component at odd multiples of the driver frequency.**

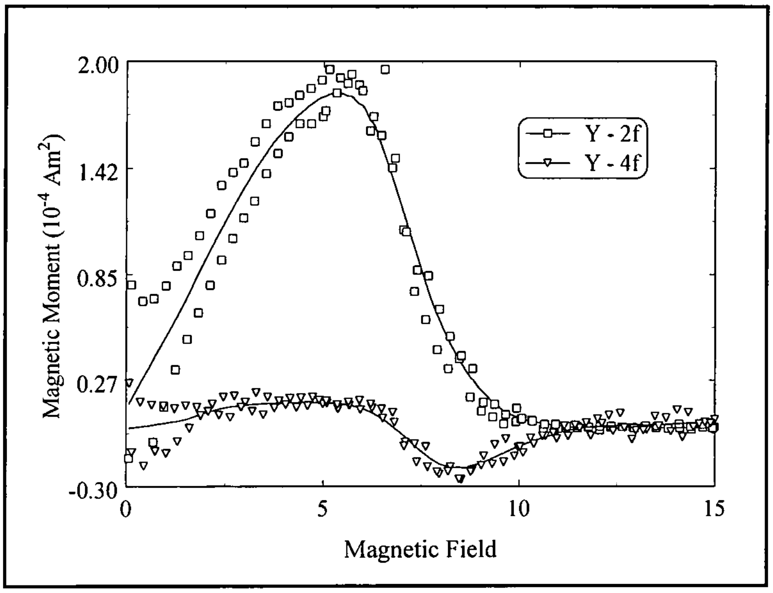

Figure 9.8 **Voltages measured in the Y component at even multiples of the driver frequency.**

Similarly for the Y voltages we can measure both the odd and even voltages, as shown in figures 9.7 and 9.8. Again hysteresis can be seen due to the anharmonicity of the driver. The spread on the data points is indicative of the noise on the measurements and in the corrected figures an error bar will be included to show this.

9.5.2 Conversion of Data to Lossless and Loss

It is now possible to correct for the anharmonicity of the driver and the phase angle allowing the comparison of the data with the mathematics. Firstly the correction was performed to account for the anharmonicity of the driver as described in section 9.3. A smooth reversible curve was fit through the 1f lossless data, removing the hysteresis. This was then subtracted, at the correct level determined from the nickel measurement, from a smooth reversible curve through the higher frequency data. In this way the hysteresis was removed from the higher harmonics as this is attributed entirely to the anharmonicity of the driver.

Once the data had been corrected for the anharmonicity, the conversions described in section 9.4 were performed, making the X and Y lockin amplifier voltages into lossless and loss voltages which in turn were converted to magnetic moments and can be compared directly with the calculations.

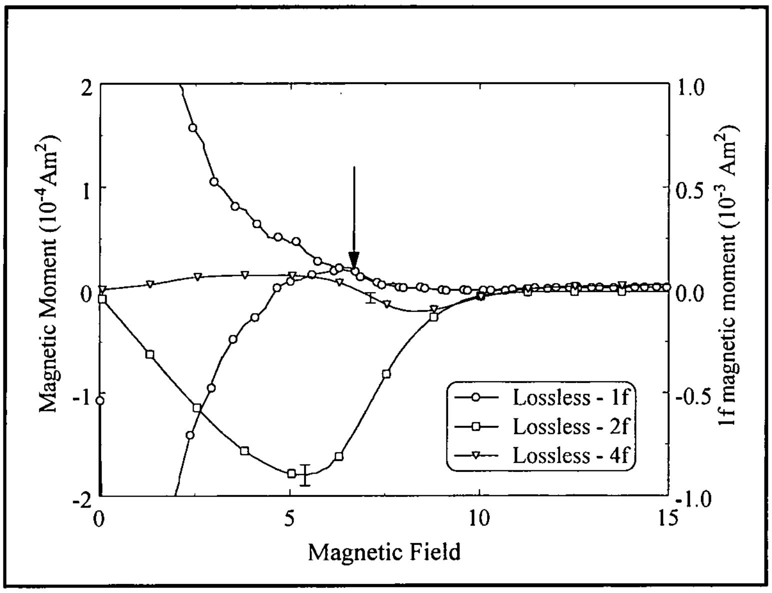

Figure 9.9 **Lossless 1f and even magnetic moments converted from X and Y for comparison with the calculations. The arrow indicates B_{IRR}.**

Figure 9.9 shows the 1f lossless magnetic moment with an irreversibility field at 6.7T. The ratio of the fields at which the 2f and 4f lossless magnetic moment peaks relative to B_{IRR} is given by 0.8 : 1.2 : 1. This can be compared to the calculated values shown in figure 8.37 where the ratio of peak field positions to B_{IRR} is 0.7 : 1.2 : 1. The ratio of the magnitudes of the minima for the 2f and 4f lossless magnetic moments in figure 9.9 is 7 : 1 compared to 5.5 : 1 for the calculated 2f and 4f lossless peaks in figure 8.37.

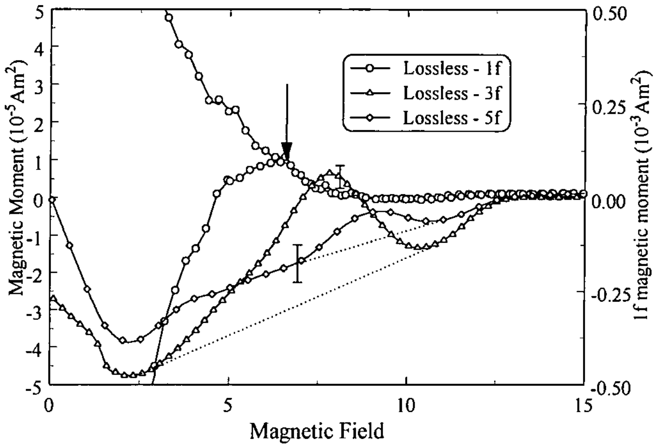

Figure 9.10 Lossless odd magnetic moments converted from X and Y for comparison with the calculated, the arrow indicates B_{IRR}.

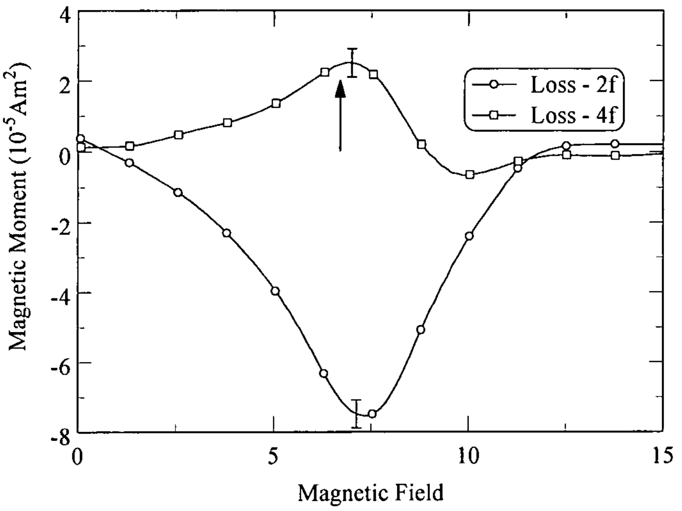

Figure 9.11 Loss even magnetic moments converted from X and Y for comparison with the calculations.

Figure 9.10 shows the odd lossless magnetic moments. The backgrounds have been taken as the dotted lines. The ratio of the field positions of the peaks in the 1f reversible voltage, 3f and 5f to B_{IRR} are in a ratio 0.8 : 1.2 : 1:4 : 1, which can be directly compared with figure 8.39 where the ratios are 0.7 : 1.1 : 1.3 : 1. The ratio of the relative magnitudes of the peaks in the 1f, 3f and 5f lossless magnetic moments is 1 : 0.4 : 0.2, compared to figure 8.39 where the ratio is 1 : 0.25 : 0.1 for the calculated 1f, 3f and 5f lossless peaks. Now looking at the even loss magnetic moments shown in figure 9.11. The ratio of the magnitude of the 2f loss minimum, the 4f loss maximum and the 4f loss minimum is 1 : 0.3 : 0.09 compared to the equivalent calculated values shown in figure 8.38 of 1 : 0.6 : 0.1. The ratio of the fields at which the 2f loss minimum, the 4f loss maximum and the 4f loss minimum occur relative to the irreversibility field are 1.1 : 1.05 : 1.5 : 1, compared to the calculations in figure 8.38 where the equivalent ratio is 1.05 : 1.02 : 1.4 : 1.

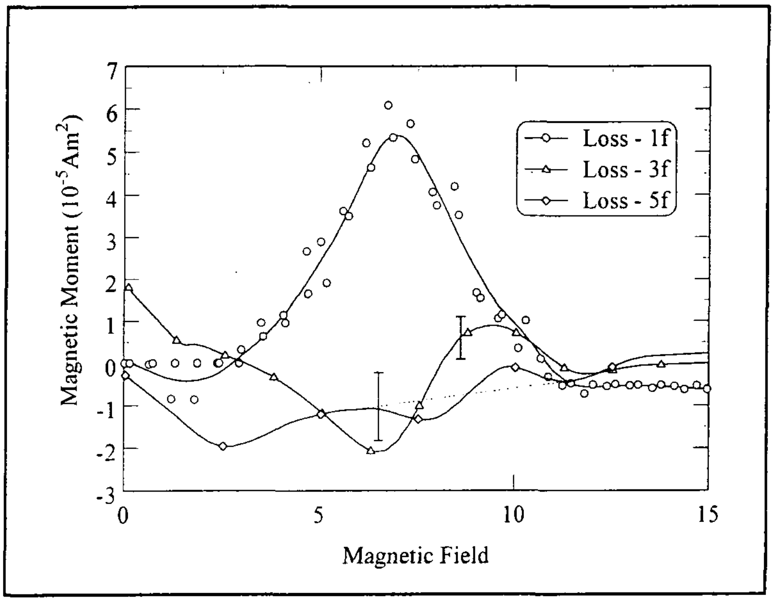

Figure 9.12 **Loss odd magnetic moments converted from X and Y for comparison with the calculations.**

Finally looking at the odd loss magnetic moments shown in figure 9.12. The ratio of the magnitude of the 1f loss maximum, the 3f loss minimum, the 3f loss maximum, the 5f loss minimum and the 5f loss maximum is 1 : 0.3 : 0.1 : 0.01 : 0.01 compared to the equivalent in figure 8.40 of 1 : 0.6 : 0.2 : 0.3 : 0.05. The ratio of the fields at which the 1f loss maximum, the 3f loss minimum, the 3f loss maximum, the 5f loss minimum and the 5f loss maximum occur relative to the irreversibility field are 1.05 : 0.95 : 1.4 : 1.2 : 1.5 : 1, compared to the calculations in figure 8.40 where the equivalent ratio is 1.01 : 1.01 : 1.4 : 1.2 : 1.4 : 1.

In summary, good correlation can be seen for all magnetic moments both in relative heights and field positions relative to B_{IRR}, compared with the calculations. The odd lossless magnetic moments appear to have a non zero background, indicated by the dotted line. A possible explanation could be the anharmonicity of the driver which has a significant component in 3f and 5f. It is suggested that the 3f ac field could produce a voltage at 3f due to the sample not being positioned perfectly in the pickup coils in the same manner as the 1f ac field produces a 1f reversable voltage, c.f. figure 8.39. It should also be noted here that the sign of the odd reversable magnetic moments is determined by the positioning of the sample with respect to the centre of the pickup coils and so can take either sign. Allowing for the background, the calculations and the data are consistent in both 3f and 5f lossless and loss magnetic moments. Hence all the features predicted by the calculations can be seen in the experimental results, allowing for the 3f ac field produced at the 7% level, c.f. table 7.1, by the anharmonicity of the driver that has not been accurately corrected for. The remaining data in this chapter will be presented in its corrected form to allow direct comparison with the calculations.

9.6 Sample Centring Within the Coil Set

In order to determine the effect of sample off-centring within the pickup coils two samples were measured. Firstly a NbTi wire sample was measured in the centre of the pickup coils and 5mm above the centre of the pickup coils, with the pickup coils in the centre of the dc field. Then a PMS sample was measured 4mm below the centre of the pickup coils, with the pickup coils positioned 5cm above the centre of the dc field. Each will now be considered in turn.

9.6.1 NbTi Wire Sample

The magnetic moment of the sample was measured for 1f to 10f and from -1.6 T to 8.0 T at 8.0 K ± 0.2 K. The results are shown in figure 9.13 to 9.17, with the noise level indicated on the figures. Data is not shown for the any higher frequencies than 4f as the signals were below the noise level of the experiment. These data have been corrected as described in sections 9.2 to 9.5 for the driver anharmonicity and the phase angle.

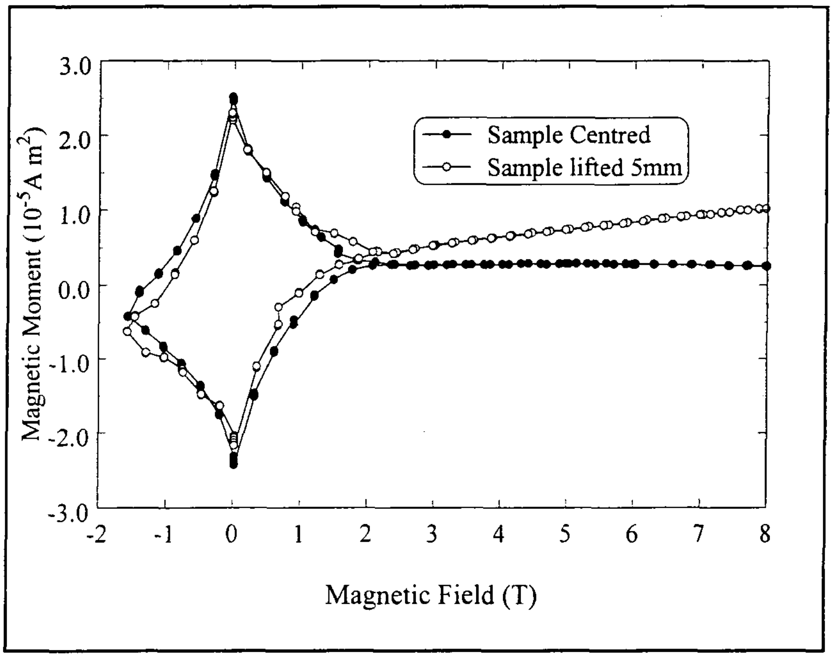

Figure 9.13 **1f lossless magnetic moment of NbTi wire at 8.0 K, for two sample positions.**

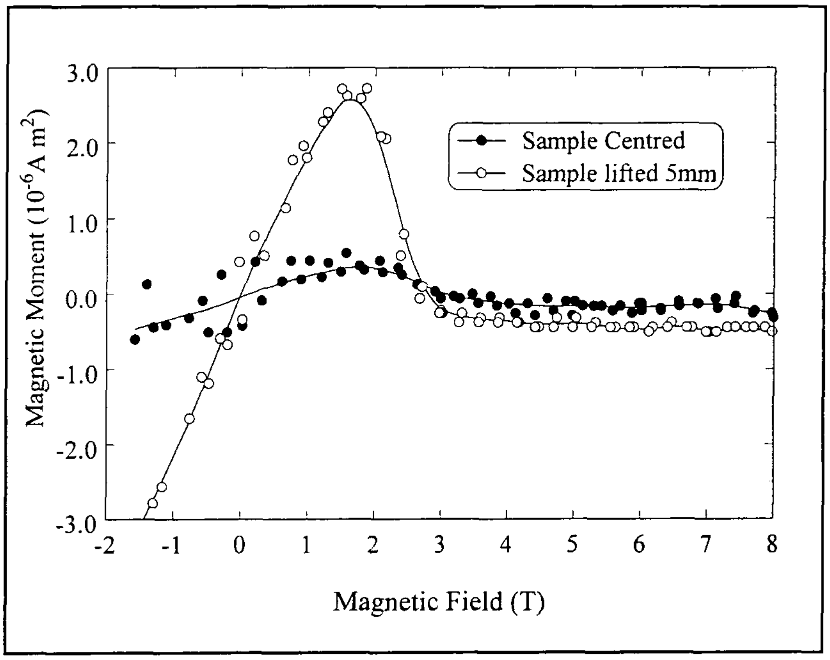

Figure 9.14 **1f loss magnetic moment of NbTi wire at 8.0 K, for two sample positions.**

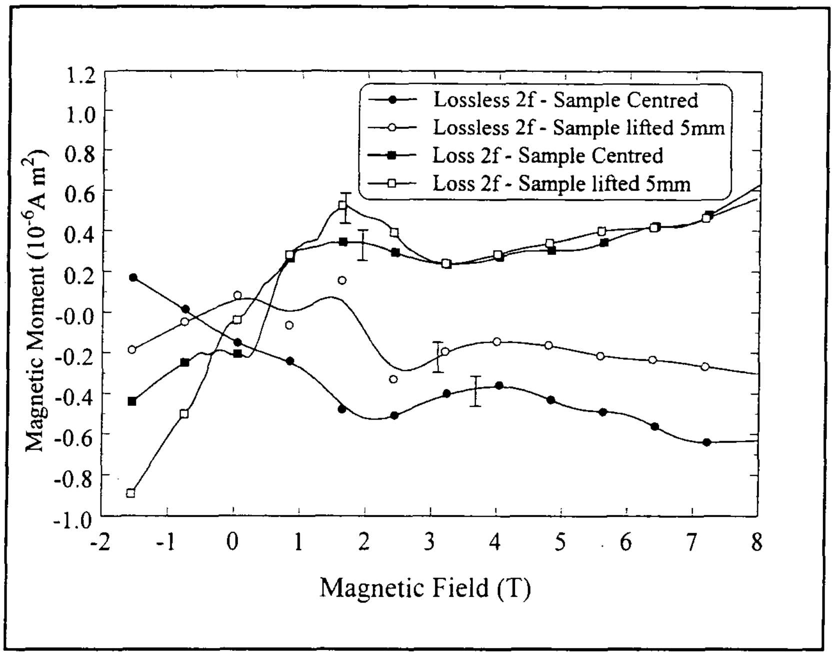

Figure 9.15 **2f measurement of NbTi wires at 8.0 K.**

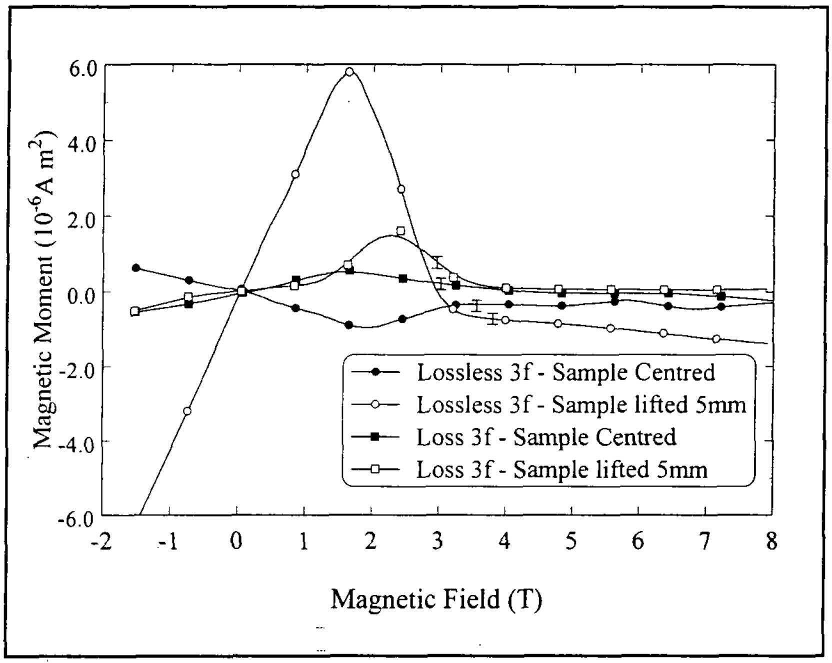

Figure 9.16 **3f measurement of NbTi wires at 8.0 K, showing the effect of positioning the sample.**

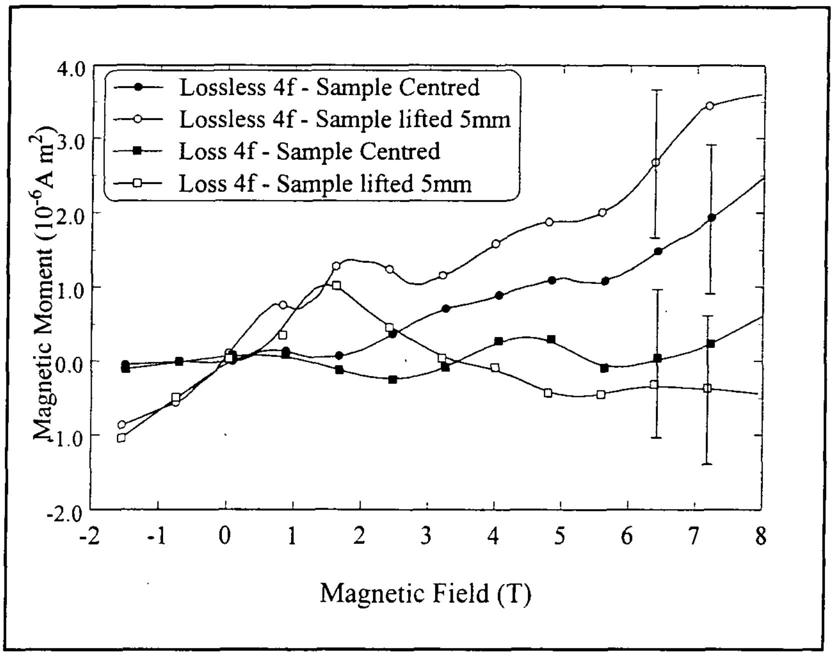

Figure 9.17 4f measurement of NbTi wires at 8.0 K.

From figure 9.13 it can be seen that the 1f lossless magnetic moment has similar hysteresis for both positions in the pickup coils, and hence any critical current densities derived from the magnetisation curve will be approximately the same. The normal state background does change considerably, attributed to the change in position of the sample rod. The loss magnetic moments shown in figure 9.14 both have a reversible peak, which increases in magnitude as the sample is moved out of the pickup coils. The peak occurs at a field of $0.8B_{IRR}$ which can be compared to that calculated for a NbTi sample mispositioned in the pickup coils as shown in figure 8.12 which occurs at $1.2B_{IRR}$. Figure 9.15 shows the 2f lossless and loss components which are expected to be unaffected by the movement of the sample within the pickup coils. Any features in the 2f magnetic moments should be small as the sample is centred in the dc field and hence the ac fields are small. No features can be seen above the noise level. The lossless 3f magnetic moments shown in figure 9.16 shows a peak for the sample out of the pickup coils, though at a field below the irreversibility field, as compared to that predicted by the calculations and shown in figure 8.11 which indicates a peak at approximately twice B_{IRR}. The 3f loss magnetic moment in figure 9.16 is also changed by the movement of the sample out of the centre of the pickup coils, though the oscillation predicted by the calculations and shown in figure 8.12 is not present. The final figure of this set, figure

8.17 shows the 4f lossless and loss magnetic moments which show no change with sample position as expected.

In summary it can be seen that sample off centring gives reversible signals in the odd multiples of the driver frequency while the even multiples are not changed significantly within the experimental error on the measurement, as predicted by the calculations. The ac field in this experimental arrangement was small and hence the features expected in each of the harmonics were small. In order to see more clearly the effect of sample positioning, this experiment was repeated on a PMS sample in a large field gradient.

9.6.2 PMS Sample

This sample was measured with the pickup coils positioned 5cm above the centre of the dc field, hence introducing a large field gradient. The sample was positioned 4mm below the centre of the pickup coils and measurements were performed from 1f to 10f at 10.4K in fields up to 15T. The noise level is dominant above 5f so only the lower frequencies will be shown. As PMS is thought to be a grain boundary pinning material, it is appropriate to compare these measurements with the Kramer sample in section 8.10.3.

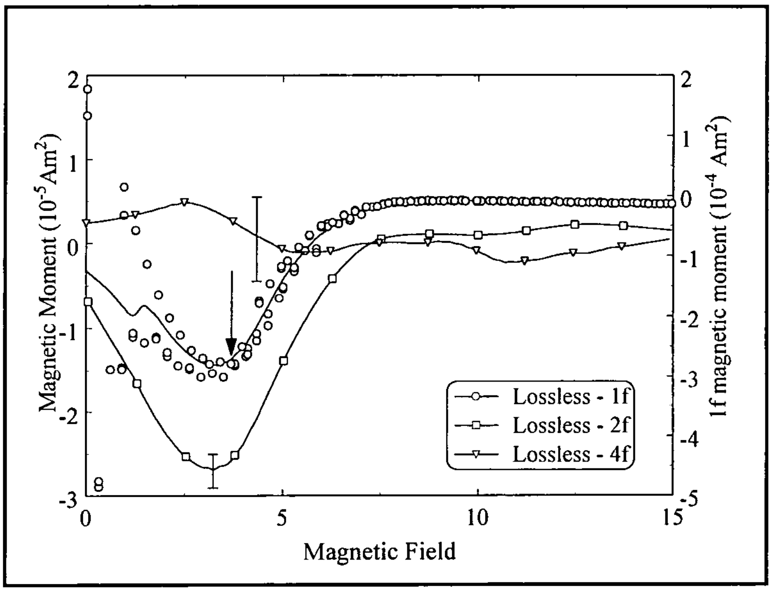

Figure 9.18 Lossless 1f and even magnetic moments for comparison with the calculations. The arrow indicates B_{IRR}.

Figure 9.18 shows the 1f lossless magnetic moment with an irreversibility field at 3.7T. A large negative reversable signal can also be seen on top of the irreversibility. Note that the negative minimum is found for a sample below the pickup coil centre, where a positive maximum was shown in the previous section for the NbTi sample above the pickup coil centre. The ratio of the field at which the 2f lossless magnetic moment peaks relative to B_{IRR} is 0.8 : 1. This can be compared to the calculated values shown in figure 8.37 where the ratio of peak field positions to B_{IRR} is 0.7 : 1. The 4f magnetic moment is dominated by noise.

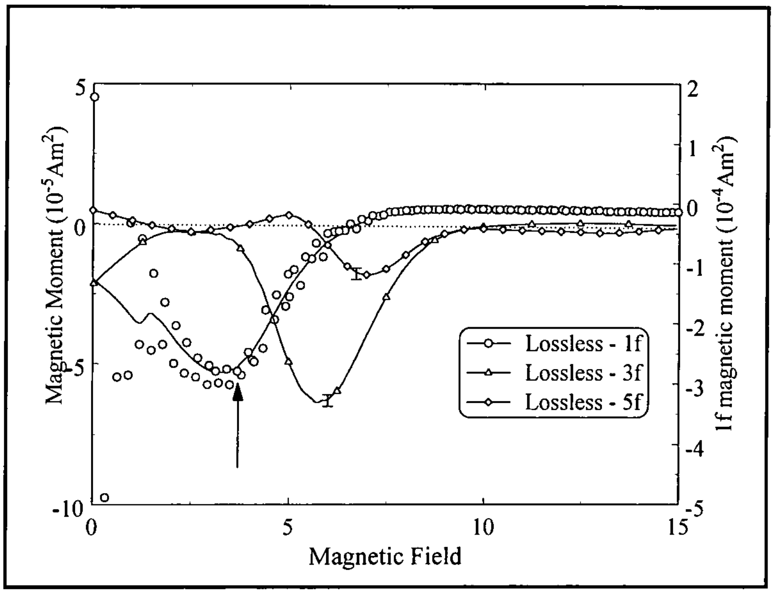

Figure 9.19 **Lossless odd magnetic moments for comparison with the calculations, the arrow indicates B_{IRR}.**

Figure 9.19 shows the odd lossless magnetic moments. The background has been taken as the dotted line. The field positions of the peaks in the 1f reversible voltage, 3f and 5f to B_{IRR} are in a ratio 0.8 : 1.5 : 1.9 : 1, which can be directly compared with figure 8.39 where the ratios are 0.7 : 1.1 : 1.3 : 1. The ratio of the relative magnitudes of the peaks in the 1f, 3f and 5f lossless magnetic moments is 1 : 0.3 : 0.1, compared to figure 8.39 where the ratio is 1 : 0.25 : 0.1 for the calculated 1f, 3f and 5f lossless peaks.

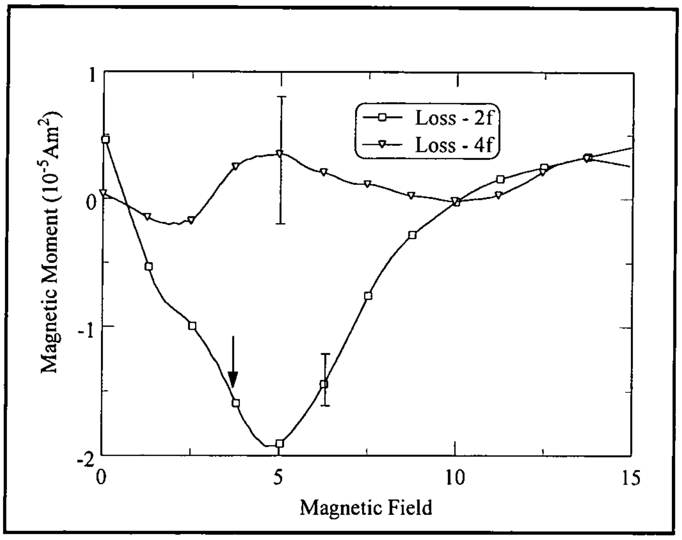

Figure 9.20 **Loss even magnetic moments converted from X and Y for comparison with the calculations, the arrow indicates B_{IRR}.**

Looking at the even loss magnetic moments shown in figure 9.20. The ratio of the magnitude of the 2f loss minimum, to the 2f lossless minimum in figure 9.18 is 0.7 : 1 which compares with the ratio predicted by the calculations of the 2f loss minimum shown in figure 8.38 and the 2f lossless minimum in figure 8.37 of 0.4 : 1. The ratio of the fields at which the 2f loss minimum occurs relative to the irreversibility field is 1.3 : 1, compared to the calculations in figure 8.38 where the equivalent ratio is 1.05 : 1.

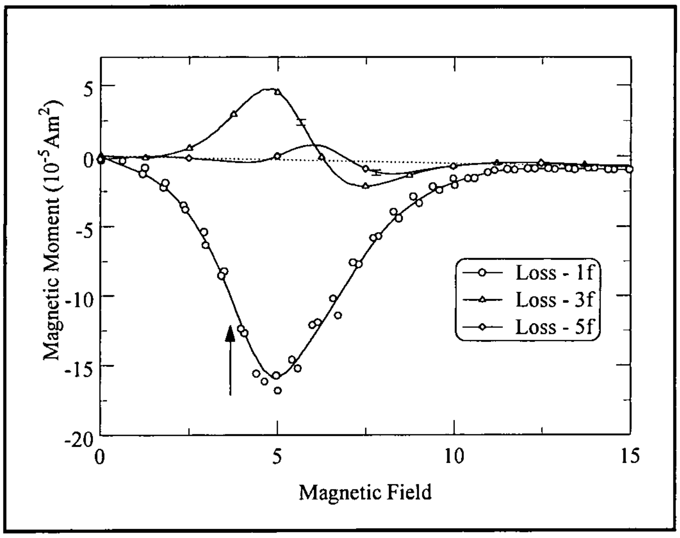

Figure 9.21 **Loss odd magnetic moments converted from X and Y for comparison with the calculations.**

Finally looking at the odd loss magnetic moments shown in figure 9.12. The ratio of the magnitude of the 1f loss minimum, the 3f loss maximum, the 3f loss minimum, the 5f loss maximum and the 5f loss minimum is 1 : 0.3 : 0.12 : 0.04 : 0.03 compared to the equivalent in figure 8.40 of 1 : 0.6 : 0.2 : 0.3 : 0.05. The ratio of the fields at which the 1f loss minimum, the 3f loss maximum, the 3f loss minimum, the 5f loss maximum and the 5f loss minimum occur relative to the irreversibility field are 1.3 : 1.3 : 2 : 1.6 : 2.2 : 1, compared to the calculations in figure 8.38 where the equivalent ratio is 1.01 : 1.01 : 1.4 : 1.2 : 1.4 : 1.

9.6.3 Summary of Samples Offcentred in the Pickup Coils

The results of this section show that moving the sample out of the centre of the pickup coils introduces reversible components at odd multiples of the driver frequency. The form of these components, relative to the 1f loss voltage is given by the calculations in section 8.7. The sign of the 1f loss peak is determined by the whether the sample is above or below the pickup coil centre. As shown in the previous two sections, a sample above the pickup coil centre produces a positive reversable component in the 1f loss peak c.f. NbTi sample, and a sample below the centre of the pickup coils produces a negative 1f loss peak, c.f. PMS sample.

9.7 Tin Molybdenum Sulphide

In this section the results will be presented for a sample of tin molybdenum sulphide (SMS), the same sample as used in chapter 5. The sample dimensions are 5.55mm x 2.45mm x 1.88mm, and it was oriented with the long dimension parallel to the applied field. Three temperatures were measured, 4.2K, 6.8K and 8.4K in fields up to 15T with the sample and pickup coils positioned at the dc field centre, 2cm above field centre and 5cm above field centre. Each frequency measured will now be presented for the three ac fields, in both the lossless and loss components, allowing the trends with increasing ac field to be seen. Again it is appropriate to compare these measurements with the Kramer sample in section 8.10.3, however the exact shape and position of the features will depend on the field dependence of the critical current density. In SMS this field dependence is know to contain the peak effect, as discussed in chapter 5 which is not included in the Kramer model in the calculations for section 8.10.3. Background measurements above T_C were not performed for this sample however it was found for the other samples discussed in this chapter that the normal state backgrounds were smaller than the noise on the measurement except in the 1f lossless component where the background was primarily due to the sample rod. Hence any backgrounds introduced in this section are not measured, but inferred and are intended as guides to the eye.

9.7.1 SMS Measured at 8.4K

The features predicted in section 8.10.3 for the Kramer dependence of the critical current density on field are expected to be seen, with the size of the features increasing with increasing ac field. The irreversibility field is also expect to be reduced by increasing ac field.

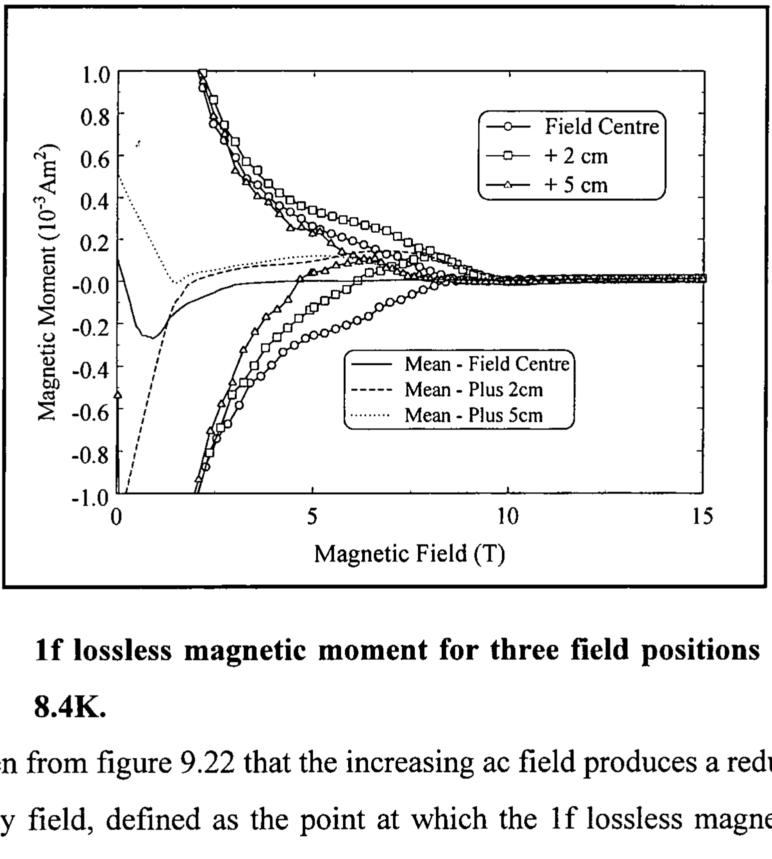

Figure 9.22 1f lossless magnetic moment for three field positions for SMS at 8.4K.

It can be seen from figure 9.22 that the increasing ac field produces a reduction in the irreversibility field, defined as the point at which the 1f lossless magnetic moment becomes reversible. This can be compared with that predicted by the calculations in chapter 8, where in figure 8.46 the irreversibility field for a Kramer critical current density is decreased by increasing ac field. It can also be seen in figure 9.22 that a positive reversible component is introduced, indicating that the sample is positioned above the pickup coil centre. The sign of this reversible contribution should be consistent through the remaining odd multiples of the driver frequency presented for this sample. Also note the increase in noise level with increasing field gradient. This is expected as any movement of the pickup coils will results in a large voltage being produced if they are in a large field gradient. Finally in figure 9.22 it can be seen that all three measurements agree at low field, as in this region the correction for the ac field is small as the self field of the sample is relatively large, compared to the effective ac magnetic field.

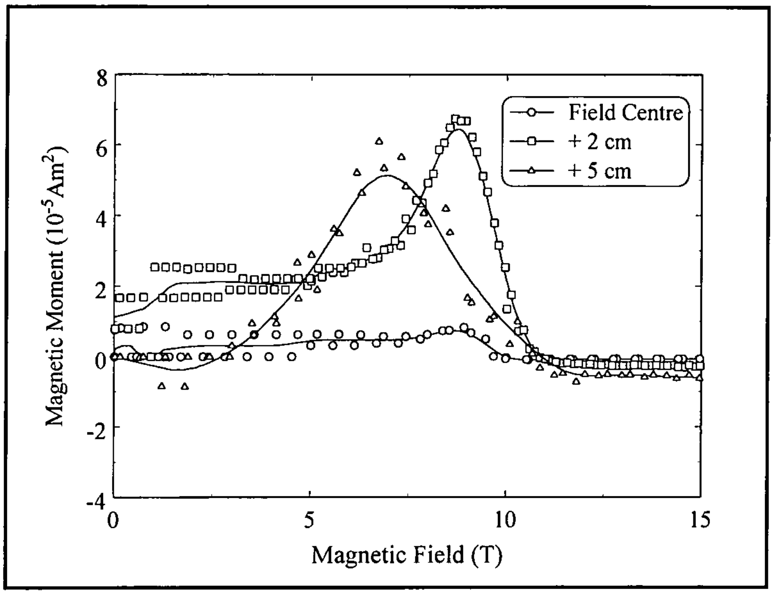

Figure 9.23 1f loss magnetic moment for three field positions for SMS at 8.4K.

In figure 9.23, positive reversible peaks can be seen in the 1f loss magnetic moment for all field positions. This is consistent with the positive peaks shown in the 1f lossless magnetic moment in figure 9.22 and with that predicted by the calculations, shown in figure 8.40. The ratios of the reversible 1f lossless peaks, shown by the lines, to the 1f loss peaks, for the +2cm and +5cm are 1 : 0.5 and 1 : 0.4, which compares to the ratio of the calculated values in figures 8.39 and 8.40 of 1 : 0.4. The position at which the loss peak occurs in figure 9.2.3 is $1.1B_{IRR}$ for the +5cm and the +2cm measurements and $0.95B_{IRR}$ for the field centre measurement. This compares with the calculated value, shown in figures 8.37 where the irreversibility field is 18.7T and figure 8.40 which shows the 1f loss peak occurring at $1.02B_{IRR}$. The field centre and +2cm magnetic moments in figure 9.23 go to zero at approximately the same field, 11T and the +5cm magnetic moment goes to zero at approximately 12T in figure 9.23 which is equal to an applied field of approximately 11T after correction for the positioning. By comparison with figure 8.40 this is therefore the point at which the critical current density becomes zero. This is significantly higher than the irreversibility field defined from the close up of the 1f lossless magnetic moment which occurs in figure 9.22 between approximately 6 and 9T, depending on the field inhomogeneity. The onset of the susceptibility transition for this sample is estimated to be 11T±0.2T at 8.4K±0.2K from figure 5.6. The digitisation in figure 8.23 is due to the resolution of the lockin amplifier measuring the large 1f lossless voltage and the small 1f loss voltage simultaneously.

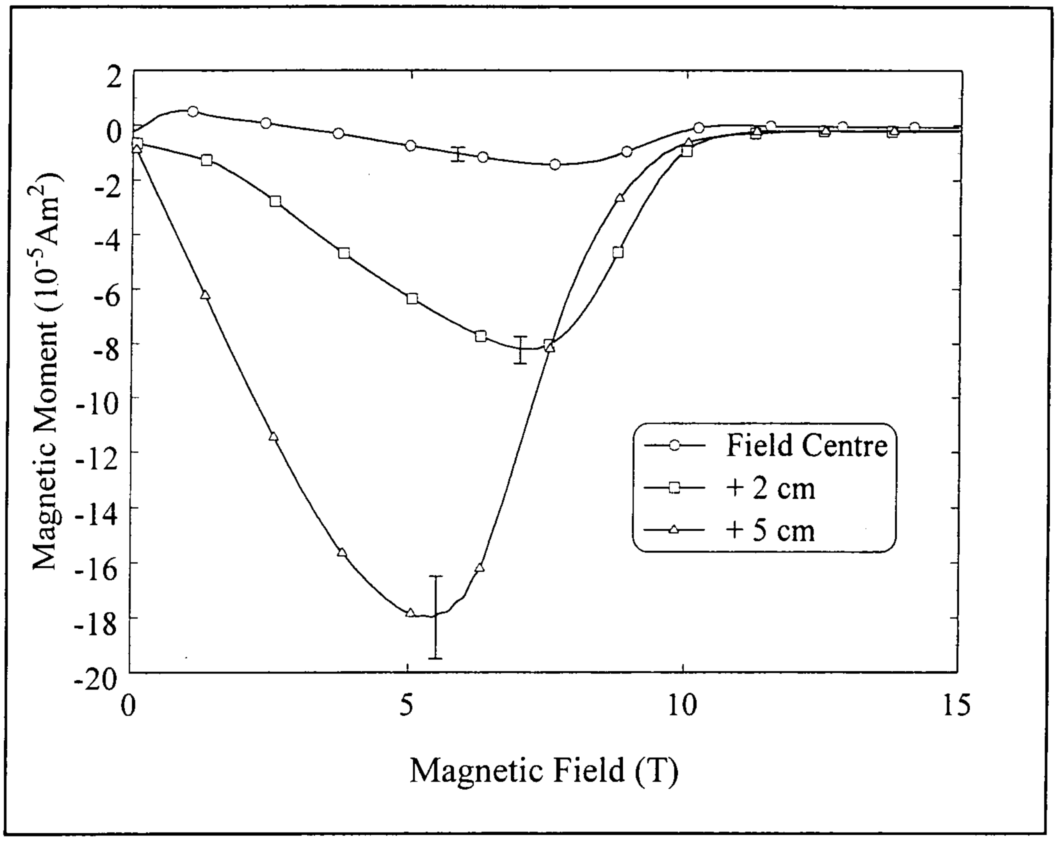

Figure 9.24 2f lossless magnetic moment for three field positions.

Figures 9.24 and 9.25 show the magnetic moments measured at 2f, and in each case the size of the peak increases with increasing ac field. The position in field is moved to lower field for both the lossless and the loss magnetic moments. For the lossless magnetic moment in figure 9.24 the peaks are at $0.85B_{IRR}$, $0.9B_{IRR}$ and $0.85B_{IRR}$ for the

+5cm,+2cm and field centre respectively. These can be compared to the result of the calculations for the 2f lossless magnetic moment shown in figure 8.37 which has a peak at $0.7B_{IRR}$.

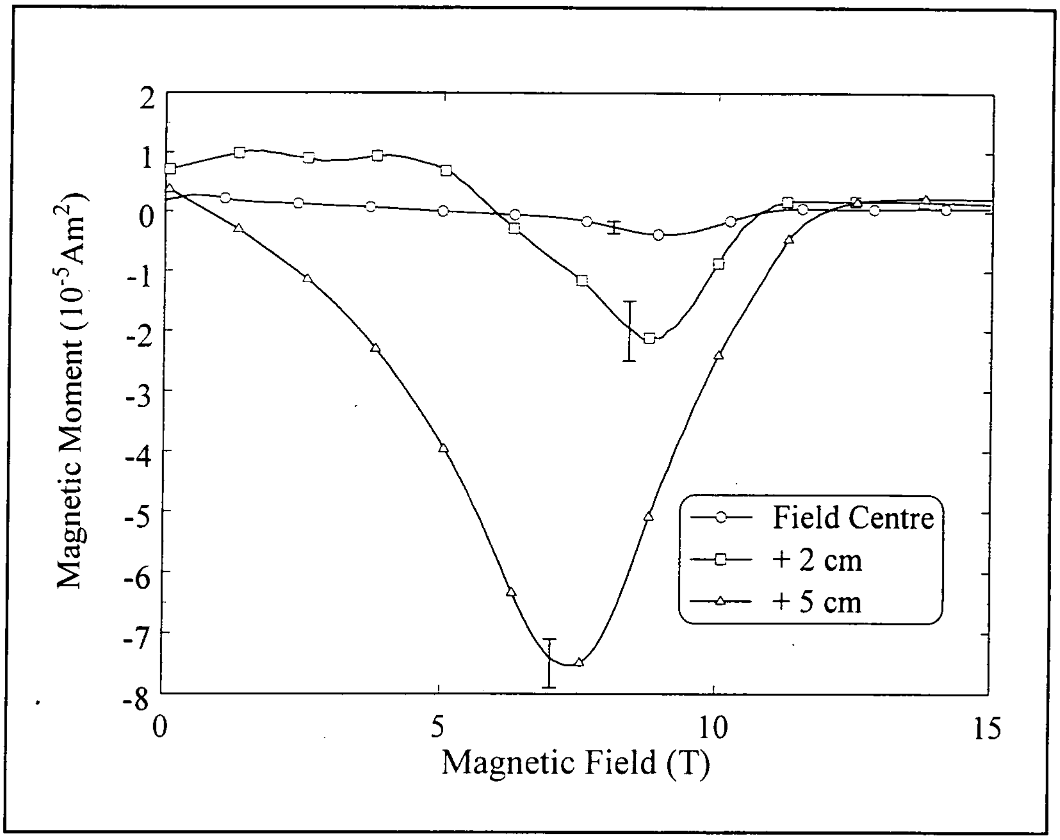

Figure 9.25 2f loss magnetic moment for three field positions.

Similarly for the 2f loss magnetic moments in figure 9.25 the fields at which the peaks occurs are $1.2B_{IRR}$, $1.1B_{IRR}$, $1.0B_{IRR}$ for the +5cm, +2cm and field centre cases respectively. This can be compared to figure 8.38 where the calculated loss peak occurs at $1.05B_{IRR}$. The relative heights of the 2f lossless and loss peaks shown in figures 9.24 and 9.25 can be compared, with the ratio of 2f lossless to 2f loss being 2.4 : 1, 4.1 : 1 and 3 : 1 for the +5cm, +2cm and field centre measurements. This is compared to the calculated ratio, determined from figure 8.37 and 8.38 of 3.1 : 1. Again note that the magnetic moments for each of the field positions in both figures 9.24 and 9.25 go to zero at an applied field of 11T (the +5cm measurement goes to zero at 12T in the figure which, allowing for the approximate 10% error in the value of dc field is an 11T applied field).

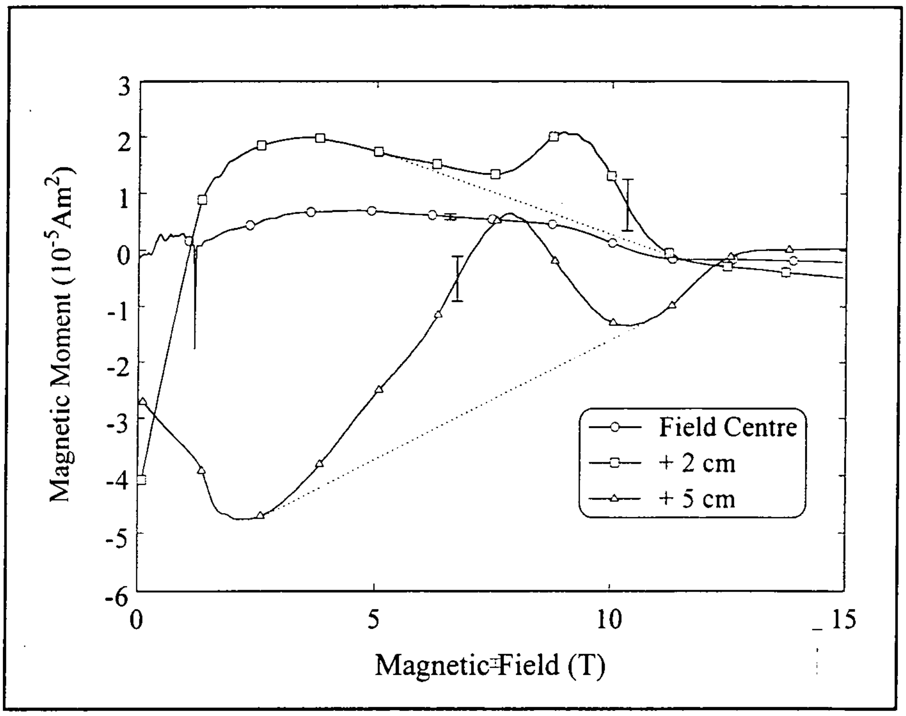

Figure 9.26 3f lossless magnetic moment for three field positions.

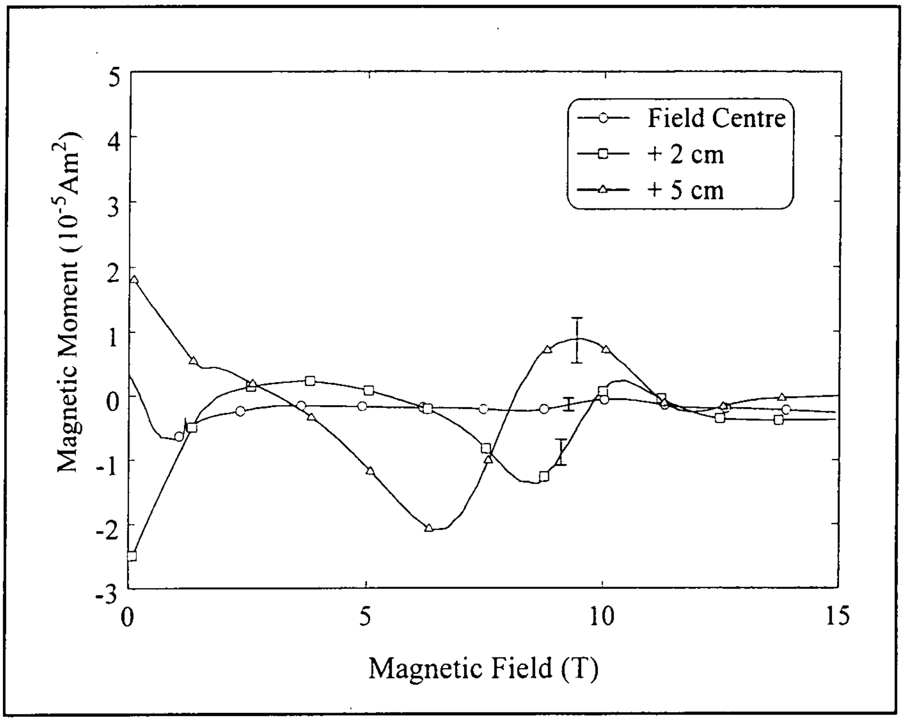

Figure 9.27 3f loss magnetic moment for three field positions.

Figures 9.26 and 9.27 show the measurements of the 3f lossless and loss magnetic moments. As discussed in sections 7.7.2, 8.7, and 9.6, there are two significant factors affecting the 3f measurement. Firstly the anharmonicity of the driver has a 7%

component in the 3f lossless component, which as well as introducing a 3f ac field, not included in the calculations, also means that 7% of the 1f signal is measured at 3f. The second effect has been corrected for as described in section 9.6 however there still appears to be a non zero background in the lossless magnetic moment at this frequency, indicated by dotted line. Allowing for this background, the relative heights of the 3f lossless peaks in figure 9.26, compared to the 1f loss peaks in figure 9.23 are in the ratio 0.6 : 1 and 0.3 : 1 for the +5cm and +2cm measurement respectively. This is compared with the calculated ratio derived from figure 8.39 and figure 8.40 of 0.7 : 1. The positions of the 3f lossless peaks in field for the + 5cm and +2cm are $1.2B_{IRR}$ and $1.1B_{IRR}$ respectively. Similarly the fields at which the 3f loss maxima and minima occur, shown in figure 9.27 are $1.0B_{IRR}$ and $1.5B_{IRR}$ for the +5cm and $1.0B_{IRR}$ and $1.1B_{IRR}$ for the +2cm respectively. This can be compared to those predicted by the calculations and shown in figures 8.39 and 8.40 which show that the 3f lossless peak occurs at $0.7B_{IRR}$ and the 3f loss minimum and maximum occur at $1.05B_{IRR}$ and $1.3B_{IRR}$ respectively. The 3f lossless and loss signals show no features in the field centre case as expected from knowing the ratio of the 1f loss and 3f loss peak heights plus the height of the 1f loss peak. Note that both the +2cm and +5cm 3f lossless and loss magnetic moment all go to zero at approximately 11T.

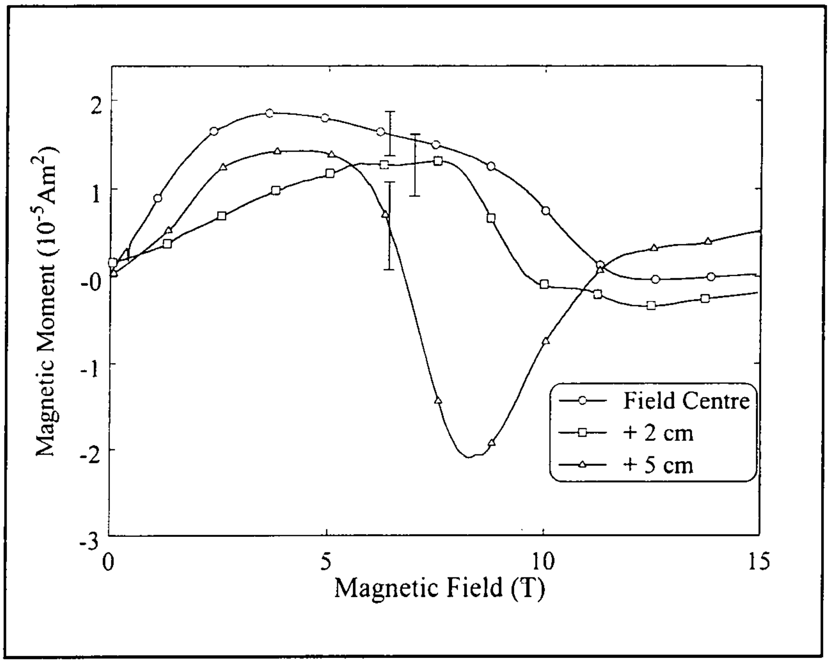

Figure 9.28 4f lossless magnetic moment for three field positions.

Figure 9.28 shows the 4f lossless magnetic moments for the three field positions measured. Each of the field positions show a positive increase at low field, which is not predicted in the calculations. This feature dominates for the field centre and +2cm measurements, however the +5cm measurement has a negative minimum at $1.3B_{IRR}$, in the ratio of 0.1 : 1 with the 2f lossless signal shown in figure 9.24. This compares to the results of the calculations shown in figure 8.37 where the 4f lossless peak occurs at $1.2B_{IRR}$ and the calculated ratio for the magnitude of the 4f lossless peak to the 2f lossless peak is 0.2 : 1. Using these ratios and the size of the 2f lossless peak at the field centre and + 2cm it can be determined that the size of the features expect in the 4f lossless measurements at field centre and +2cm are below the noise level and so are not seen.

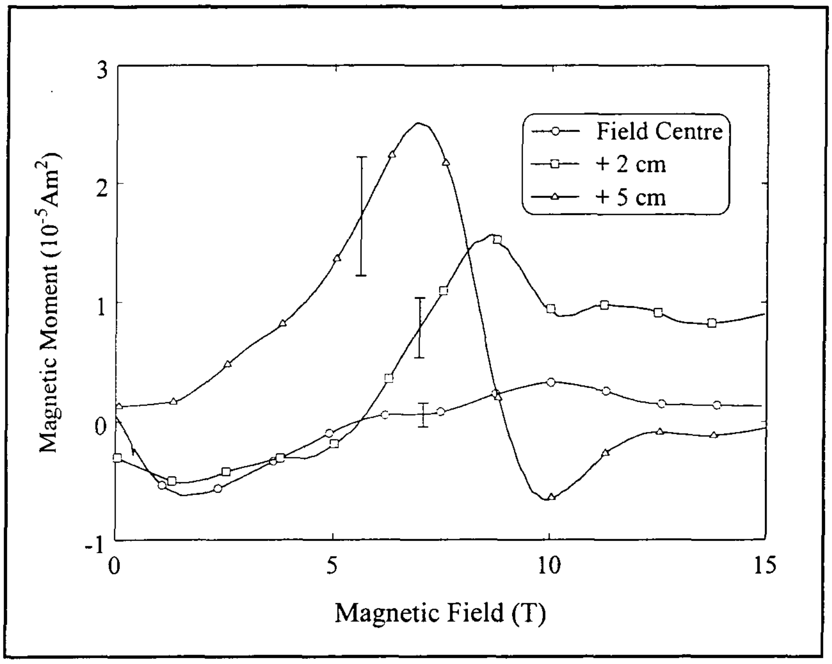

Figure 9.29 4f loss magnetic moment for three field positions.

Figure 9.29 shows the 4f loss magnetic moment with the only clear signal being the +5cm data again. The maximum and minimum occur at $1.1B_{IRR}$ and $1.6B_{IRR}$ respectively and are in the ratio of 0.3 : 1 and 0.1 : 1 with the magnitude of the 2f loss peak shown in figure 9.25. The ratio between the magnitude of the maximum and the minimum in the +5cm loss magnetic moment is 3.6 : 1. These values can be compared to the calculated values shown in figure 8.38 where the 4f maximum and minimum occur at $1.0B_{IRR}$ and $1.4B_{IRR}$ respectively and the heights of the maximum and minimum are in the ratio of 0.6 : 1 and 0.15 : 1 with the magnitude of the 2f loss. The ratio of the magnitudes of the 4f loss maximum and the minimum shown in figure 8.38 is 3.9 : 1.

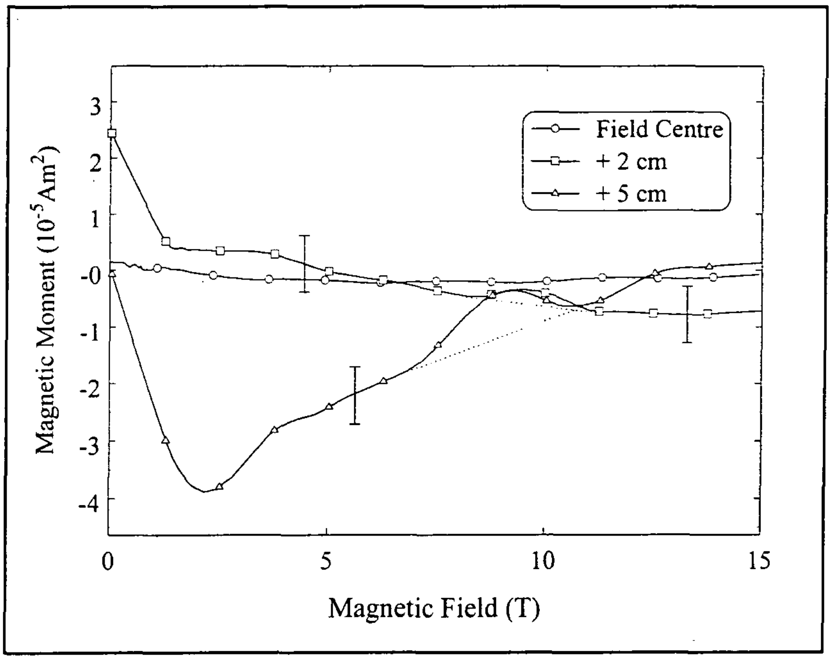

Figure 9.30 5f lossless magnetic moment for three field positions.

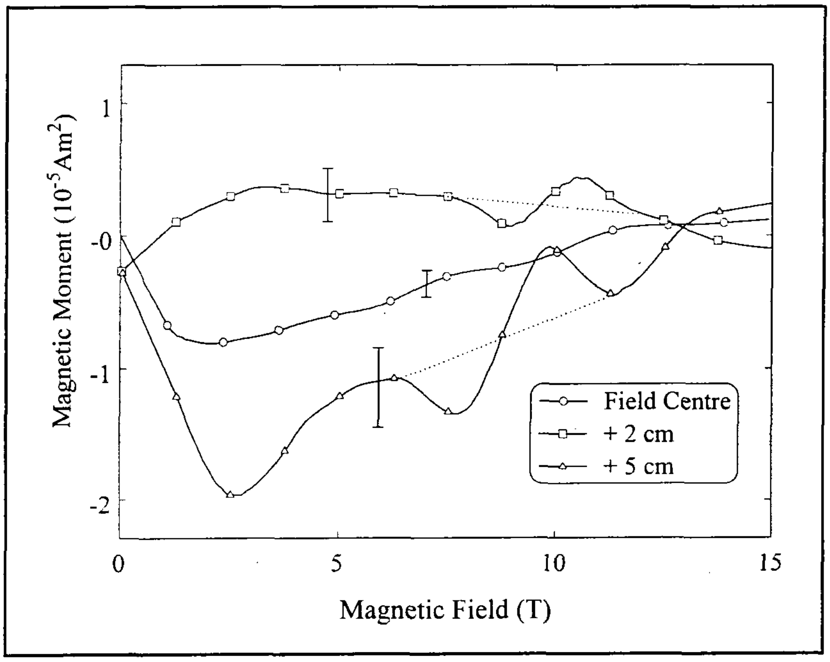

Figure 9.31 5f loss magnetic moment for three field positions.

Figure 9.30 shows the 5f lossless magnetic moment. In a similar manner to the 3f lossless measurement shown in figure 9.26 a non zero background is measured for the +5cm data. This again can be attributed to the anharmonicity of the driver which is 1.6%

of the 1f, as shown in table 7.1. The background is taken on the dotted line as shown giving the ratio of the amplitude of the 5f lossless peak to that of the 1f loss peak in figure 9.23 is 0.16 : 1 and to the 3f lossless peak shown in figure 9.26 is 0.3 : 1. The 5f lossless peak occurs at 1.5B_{IRR}. This compares to the results of the calculations shown in figures 8.39 and 8.40 which give the ratio of the height of the 5f lossless peak relative to the 1f loss peak as 0.3 : 1 and relative to the 3f lossless peak as 0.4 : 1. The calculated peak in the 5f lossless occurs at 1.3B_{IRR}. The ratios obtained from the +5cm data and the calculations imply that any peaks that are present in the 5f lossless magnetic moment for the +2cm and field centre cases would be smaller than the noise level on the measurement. However in the smooth curve fit through the +2cm measurement a peak can be seen in the 5f lossless magnetic moment at 1.2B_{IRR} with an amplitude in the ration 0.13 : 1 to the 3f lossless peak at +2cm which compares with the calculated values from figure 8.39 of a peak at 1.3B_{IRR} and a height ratio of 0.4 : 1 between the 5f lossless peak and the 3f lossless peak.

The 5f loss data shown in figure 9.31 also requires a non zero background to obtain agreement with the calculations, the background is indicated by the dotted lines. It is noted here that the backgrounds are negative in the +5cm 3f lossless, 5f lossless and 5f loss, and positive in the +2cm 3f lossless, 5f lossless and 5f loss and it is in these components that the driver anharmonicity is the largest.

Allowing for the backgrounds, the magnitudes of the 5f loss maximum and minimum are in the ratio of 0.2 : 1 and 0.4 : 1 with the 3f loss maximum and minimum for the +5cm measurement and in the ratio of 0.2 : 1 and 0.3 : 1 with the 3f loss maximum and minimum for the +2cm measurement. This can be compared to the same ratio derived from figure 8.40 which gives 0.5 : 1 for both the maximum and minimum in the 5f loss signal. The fields at which the maximum and minimum occur for the +5cm loss measurements are 1.2B_{IRR} and 1.6B_{IRR} respectively and 1.1B_{IRR} and 1.3B_{IRR} for the +2cm measurement. The calculated values, shown in figure 8.40 are 1.2B_{IRR} and 1.5B_{IRR} for the maximum and minimum in the 5f loss.

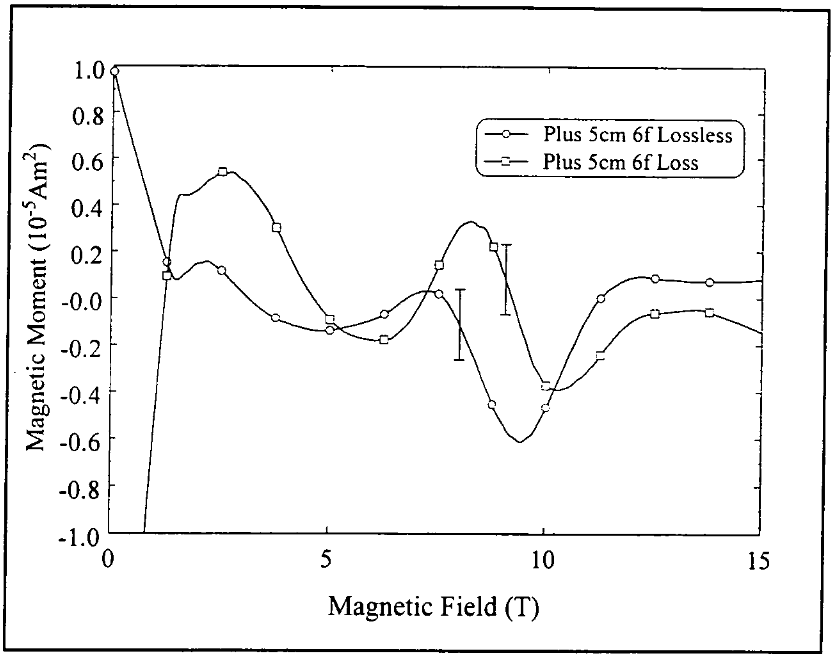

Figure 9.32 6f Magnetic moment for SMS at 8.4K and positioned at plus 5cm.

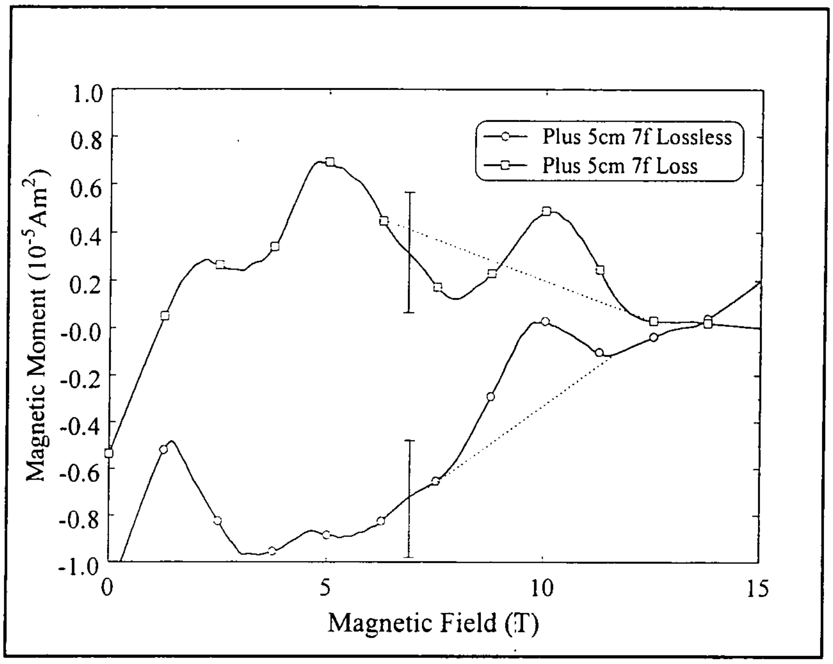

Figure 9.33 7f magnetic moment for SMS at 8.4K and positioned at plus 5cm.

The +5cm measurement gives the best signal to noise ratio for these measurements and allows both the 6f and 7f magnetic moment to be seen. Figure 9.32 shows both the lossless and the loss components of magnetic moment. The 6f lossless magnetic moment has a minimum at 1.5B$_{IRR}$ and the amplitude is in the ratio 0.3 : 1 with the magnitude of the minimum in the 4f lossless magnetic moment. The results of the calculations shown in figure 8.37 give the 6f lossless minimum occurring at $1.3B_{IRR}$, with the magnitude of the minimum being in the ratio of 0.4 : 1 with the 4f lossless minimum. The 6f loss magnetic moment, also in figure 9.32 has a maximum at $1.3B_{IRR}$ and a minimum at $1.6B_{IRR}$. The magnitudes of the maximum and minimum are approximately equal and are in the ratio 0.04 : 1 with the magnitude of the 2f loss minimum in figure 9.25. These values can be compared to those calculated and shown in figure 8.38 where the maximum and minimum in the 6f loss are at $1.2B_{IRR}$ and $1.5B_{IRR}$ and the magnitudes of the maximum and minimum are in the ratios 0.3 : 1 and 0.15 : 1 with the magnitude of the 2f loss.

Figure 9.33 shows the measurement of the 7f lossless and loss magnetic moment at +5cm, with the smooth line showing features at the positions expected from the mathematics. Again a non zero background is required, as is the case for the other odd multiples of the driver frequency. The peak in the 7f lossless magnetic moment occurs at $1.6B_{IRR}$ and the minimum and maximum in the 7f loss magnetic moment occur at $1.3B_{IRR}$ and $1.6B_{IRR}$ respectively. These values compare to those in figures 8.39 and 8.40 where the calculated 7f lossless maximum occurs at $1.4B_{IRR}$ and the 7f loss minimum and maximum occur at $1.3B_{IRR}$ and $1.5B_{IRR}$ respectively. The magnitude of the 7f lossless magnetic moment is in the ratio 0.1 : 1 with the 3f maximum in figure 9.26 and the 7f loss minimum and maximum are approximately the same magnitude and are half the size of the minimum and maximum in the 5f loss magnetic moment shown in figure 9.31. The calculated value for the magnitude of the peak in the 7f lossless magnetic moment shown in figure 8.39 is one quarter of the magnitude of the 3f lossless maximum. The calculated 7f loss minimum shown in figure 8.40 is three fifths of the minimum in the 5f loss calculation and the 7f loss maximum, also in figure 8.40 is approximately eighty percent of the magnitude of the 5f loss maximum.

In summary the features found in the experimental results are consistent with those predicted by the calculations. The measurements at higher frequencies than 7f show no features above the noise level. The non zero background in the odd multiples of the driver frequency is attributed to the anharmonicity of the driver.

9.7.2 SMS Measured at 6.8K

The measurements in this section were performed in an identical manner to those in the previous section, with the temperature at 6.8 K.

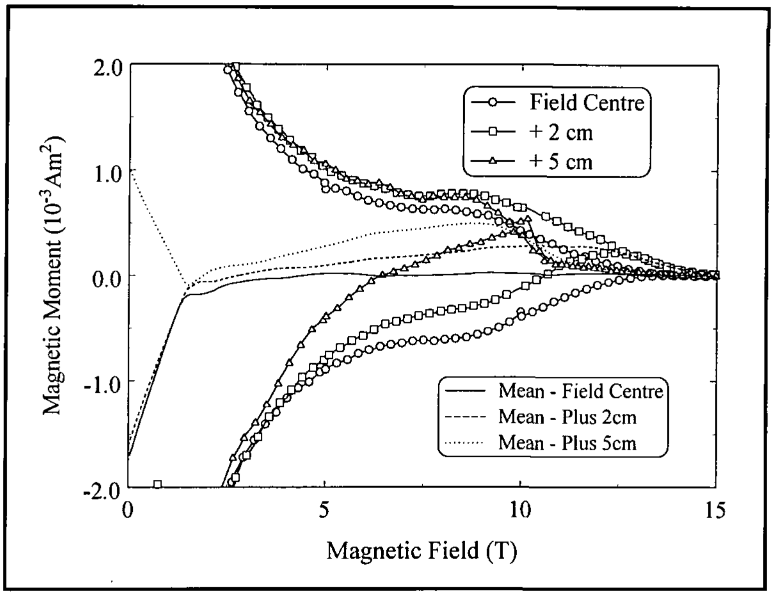

Figure 9.34 1f lossless magnetic moment for three field positions.

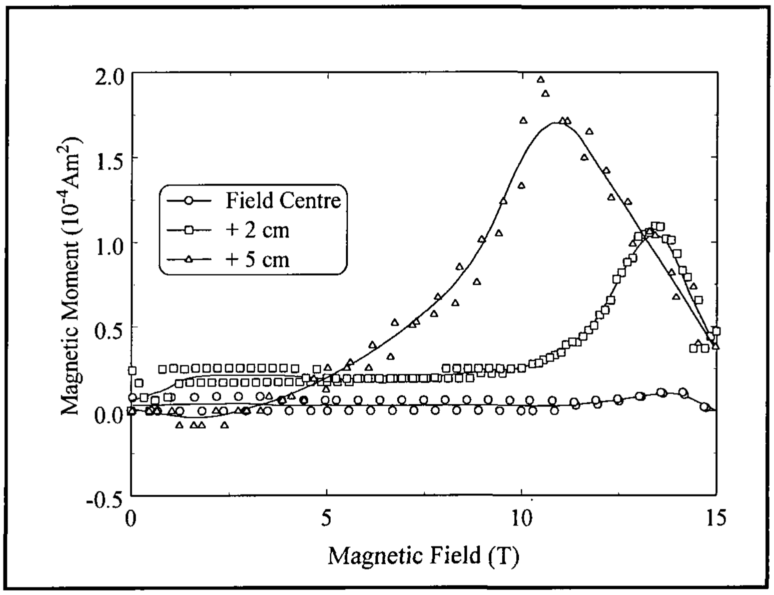

Figure 9.35 1f loss magnetic moment for three field positions.

The 1f lossless components in figure 9.34 show a movement in the close up(B_{IRR}) of the MH loop to lower fields with the increase in ac field. The irreversibility fields are 10.6T, 12.7T and 14.4T for the +5cm, +2cm and field centre measurements respectively. In both the +2cm and +5cm measurements, positive reversible components are also introduced, shown by the lines, determined by fitting a curve through the increasing and decreasing field sections of the curve. The increase in ac field increases the noise level on the traces, as expected and all three of the traces overlay at low dc field where the sample self field is much larger than the effective ac field for all the positions measured. The hysteresis in the 1f lossless exhibits the Peak effect as is explained in chapter 5. Now looking at figure 9.35, positive peaks can be seen for all the field positions with the amplitude increasing with increasing ac field. The peaks occur at 1.0 B_{IRR}, 1.05 B_{IRR} and 1.0 B_{IRR} for the +5cm, +2cm and field centre measurements respectively. The height of the peaks in the reversible 1f lossless magnetic moment for the +5cm and +2cm are in the ratios 2.9 : 1 and 2.7 : 1 with the peaks in the 1f loss magnetic moment. The calculated value for the same ratio is 2.5 : 1, determined form figures 8.39 and 8.40, with the calculated 1f loss peak occurring at $1.02B_{IRR}$. Similarly to figure 9.23 the digitisation is caused by the lockin amplifier measuring the large 1f lossless magnetic moment and the smaller 1f loss magnetic moment simultaneously.

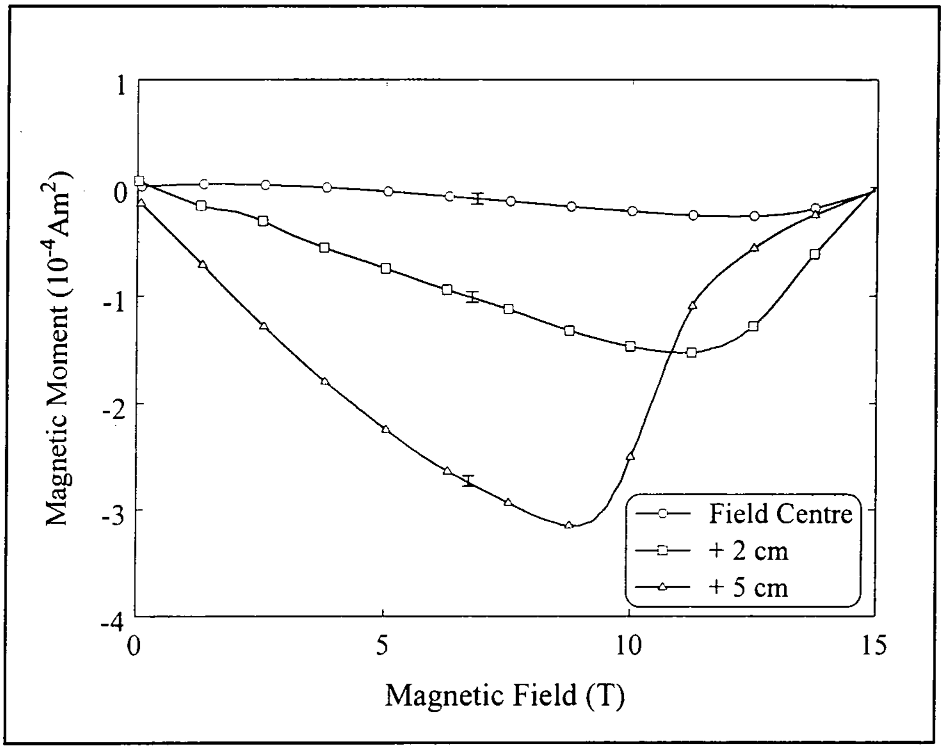

Figure 9.36 2f lossless magnetic moment for three field positions.

Figure 9.36 shows the 2f lossless magnetic moments, all going through a negative minimum. The fields at which the minima occur are $0.8B_{IRR}$, $0.9B_{IRR}$ and $0.95B_{IRR}$ for the +5cm, +2cm and field centre measurements respectively. The calculated position of the 2f lossless minimum is shown in figure 8.37 and is at $0.7B_{IRR}$.

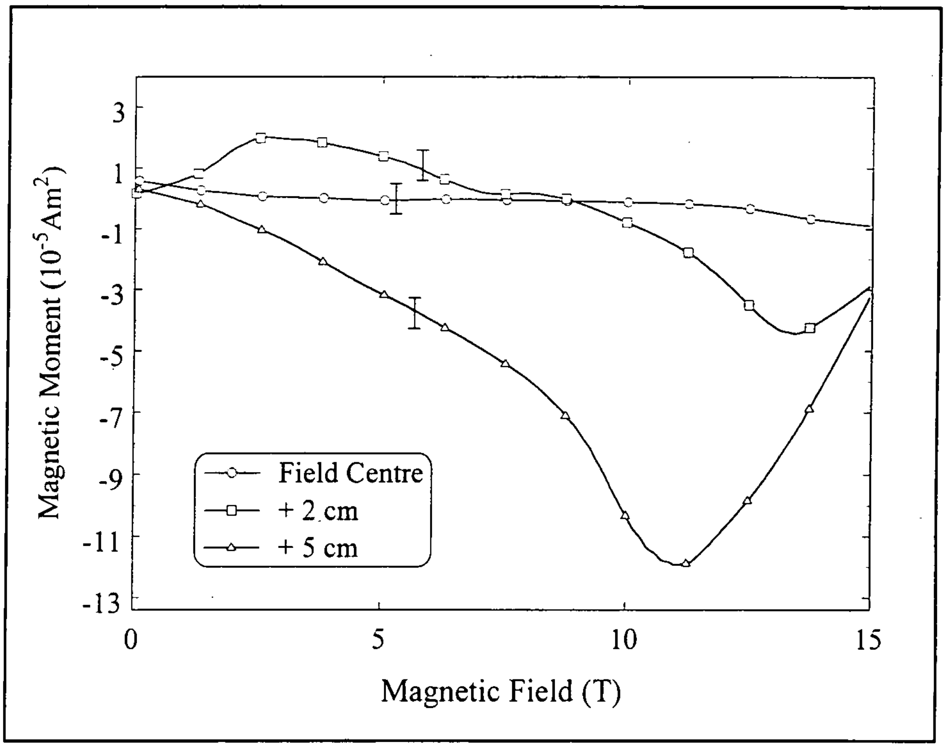

Figure 9.37 2f loss magnetic moment for three field positions.

The results in figure 9.37 show the 2f loss magnetic moment, with the minima occurring at $1.05B_{IRR}$ for both the +5cm and the +2cm measurements. No peak can be seen in the field centre measurement which is as expected, B_{IRR} = 14.4T implies that the peak should occur at over 15T, the limit of these measurements. The calculated position of the 2f loss peak is shown in figure 8.38 and is $1.05B_{IRR}$. The ratio of the magnitudes of the 2f loss peaks to the magnitude of the 2f lossless peaks, shown in figures 9.37 and 9.36 respectively, are 0.4 : 1 for both the +5cm and the +2cm measurements. No peak is measured for the 2f loss field centre magnetic moment. This ratio can be determined for the calculated values from the data in figures 8.37 and 8.38, giving 0.3 : 1 for the ratio of the magnitudes minima from the 2f loss and the 2f lossless calculations.

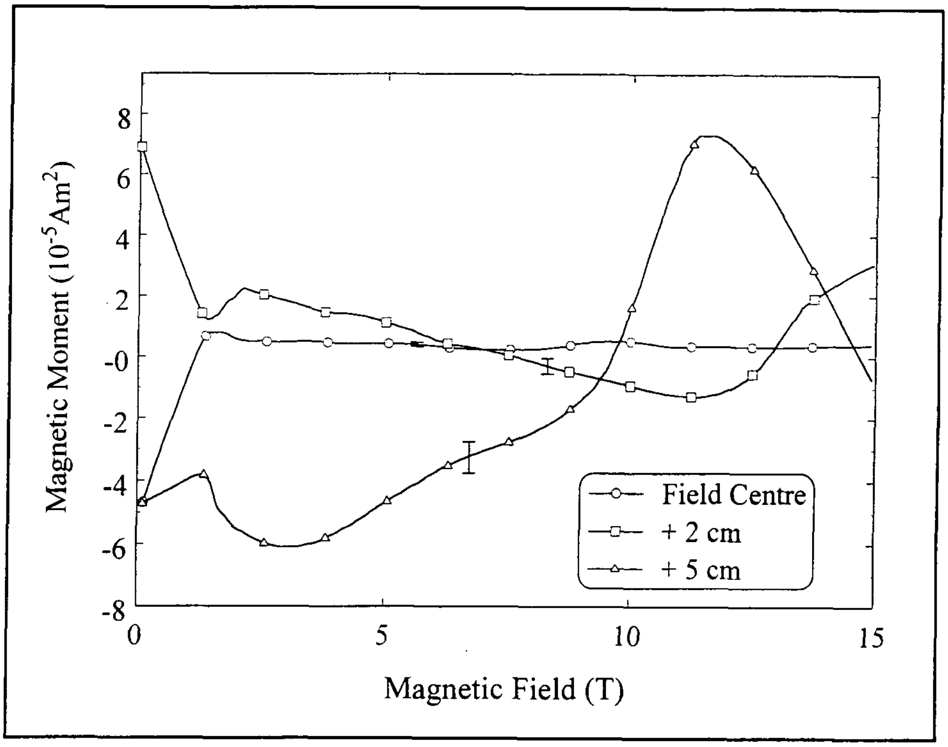

Figure 9.38 3f lossless magnetic moment for three field positions.

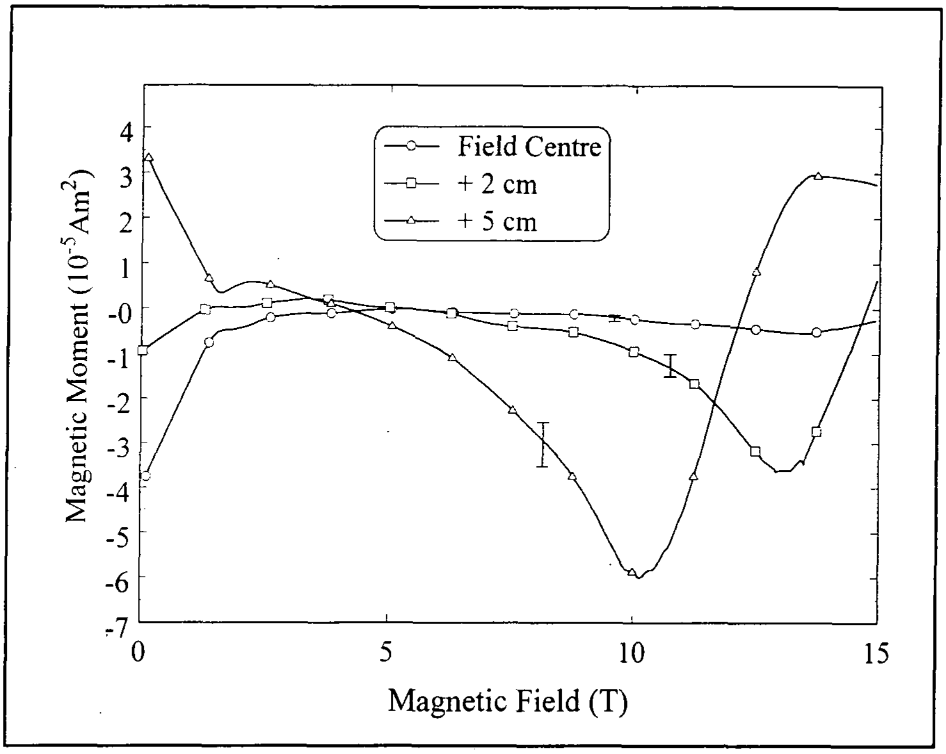

Figure 9.39 3f loss magnetic moment for three field positions.

The 3f lossless magnetic moments are shown in figure 9.38. The field centre measurement shows no features, as expected from the amplitude of the 1f loss maximum. The +2cm and +5cm both have non zero backgrounds, attributable to the anharmonicity of the driver. The only feature that can be quantified is in the +5cm measurement where a maximum is found at $1.1B_{IRR}$. The amplitude of this maximum relative to the peak in the +5cm 1f loss magnetic moment shown in figure 9.35 is 0.4 : 1. The calculations of the 3f lossless magnetic moment are shown in figure 8.39 where it can be seen that the peak occurs at $1.15B_{IRR}$, with the ratio of its magnitude to that of the 1f loss peak shown in figure 8.40 being 0.7 : 1. The +2cm measurement shows a positive increase above 12T which is consistent with the positive increase of the 3f lossless magnetic moment in the calculations. The peak in the 3f lossless measurement is expected between $1.15B_{IRR}$ from the calculation and $1.2B_{IRR}$ from the higher temperature measurement. For the +2cm measurement this means the peak should occur between 9T and 15.2T. As the maximum field used for this measurement is 15T, it is possible that this feature will not be seen.

The 3f loss magnetic moment shown in figure 9.39 shows no clear features for the field centre case as expected. The +2cm 3f loss magnetic moment has a minimum at $1.0B_{IRR}$, with a maximum expected above the maximum field of the measurement. The +5cm 3f loss magnetic moment has a minimum and a maximum at $0.95B_{IRR}$ and $1.1B_{IRR}$. The mathematics predicts that the minimum and maximum will occur at $1.05B_{IRR}$ and $1.3B_{IRR}$ respectively, as shown in figure 8.40. The ratio of the magnitudes of the minimum and maximum seen in the +5cm 3f loss magnetic moment, figure 9.39, to the magnitude of the 1f loss peak in figure 9.35 is 0.35 : 1 and 0.2 : 1. This is compared to that calculated and shown in figure 8.40 where the ratios of the 1f loss peak to the 3f minimum and maximum are 0.6 : 1 and 0.15 : 1 respectively.

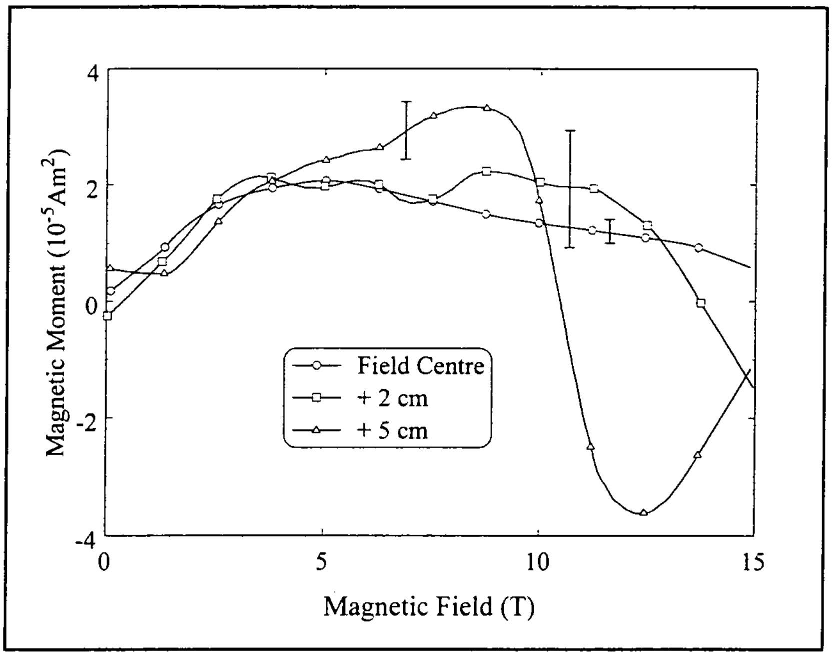

Figure 9.40 4f lossless magnetic moment for three field positions.

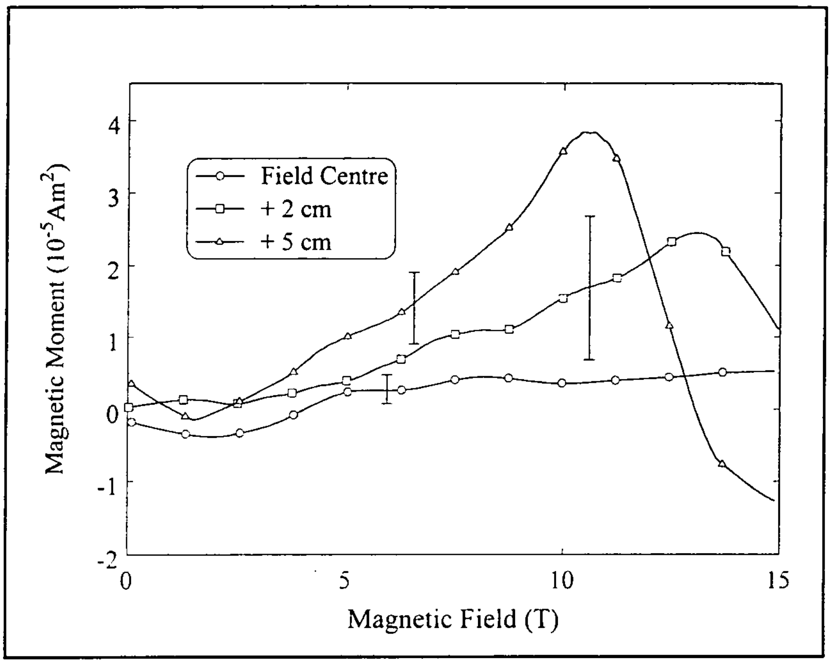

Figure 9.41 4f loss magnetic moment for three field positions.

The 4f lossless magnetic moment shown in figure 9.40, similarly to that shown in figure 9.28 shows a positive increase from zero field that is not predicted by the mathematics. Allowing for this the +5cm shows a negative minimum at $1.2B_{IRR}$ and has a magnitude in the ratio of 0.1 : 1 with the minimum in the 2f lossless magnetic moment. This can be compared with the results in figure 9.37 where the 4f lossless voltage has a minimum at 1.2B_{IRR} and has a magnitude in the ratio 0.2 : 1 with the 2f lossless minimum. The irreversibility field for the +2cm measurement is 12.7T which means that the minimum in the 4f lossless is expected at 15.2T, above the maximum field of this measurement, however a negative decrease is seen approaching 15T.

From figure 9.41 it can be seen that the 4f loss magnetic moment contains a maximum at 1.0B_{IRR} for both the +5cm and +2cm measurement. The magnitudes of these peaks are in the ratios of 0.3 : 1 and 0.6 : 1 with the magnitudes of the minima in the +5cm and +2cm 2f loss magnetic moment shown in figure 9.37. The calculations for the 4f loss magnetic moment shown in figure 8.38 predict that the maximum should occur at 1.0B_{IRR} and have a magnitude in the ratio of 0.6 : 1 with the magnitude of the 2f loss minimum. The calculations also predict a minimum in the 4f loss magnetic moment at 1.4B_{IRR} which is above the maximum field of the measurement for the field centre and +2cm positions and equal to 14.5T for the +5cm measurement. The data in figure 9.41 also shows a decrease in the slope, suggesting a minimum, however a higher measurement field would be required to see this. No signal is expected in the field centre case as the ratio with the 2f loss minimum implies that the peak is below the sensitivity of the measurement.

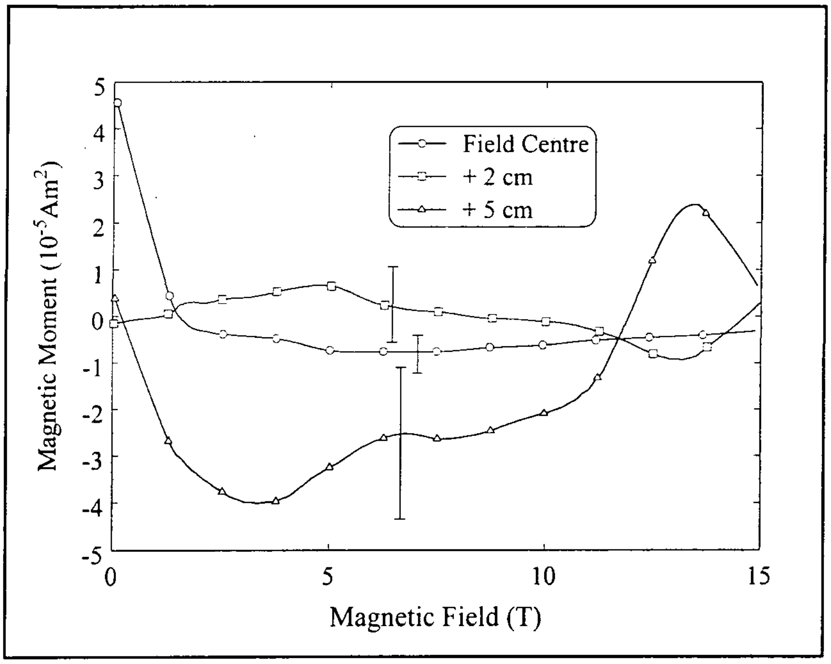

Figure 9.42 5f lossless magnetic moment for three field positions.

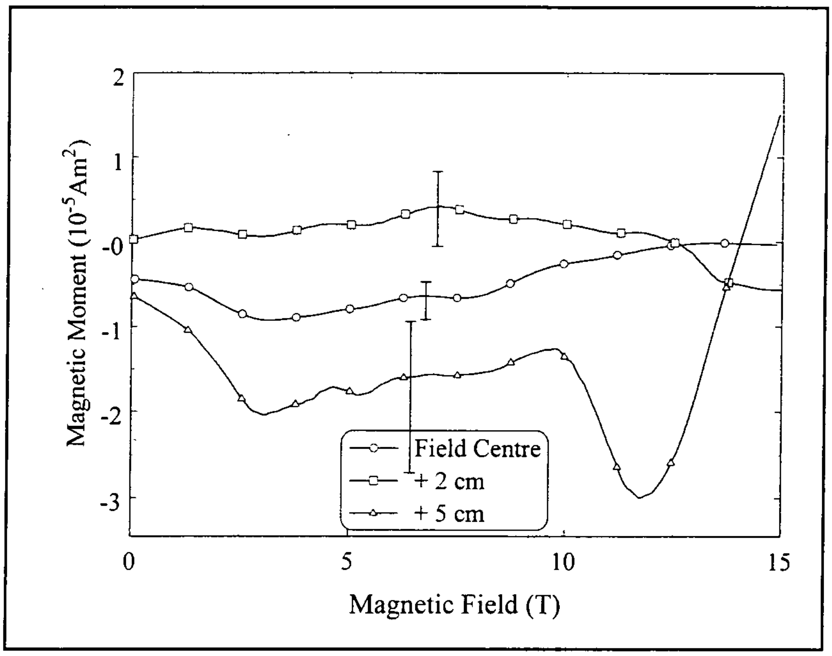

Figure 9.43 5f loss magnetic moment for three field positions.

The results of the calculations shown in figure 8.39 and the higher temperature measurement in section 9.7.1 suggest that the peak in the 5f lossless magnetic moment should occur at between $1.3B_{IRR}$ and $1.5B_{IRR}$, meaning that a maximum is expected only in the +5cm measurement as the others occur at field greater than 15T. The maximum in the +5cm 5f lossless magnetic moment occurs at $1.3B_{IRR}$ and is in the ratio of 0.3 : 1 with the maximum in the 3f lossless magnetic moment shown in figure 9.38.

Similarly for the 5f loss magnetic moment the minimum and maximum are expected at fields of approximately $1.2B_{IRR}$ and $1.5B_{IRR}$ respectively, derived from the higher temperature results in section 9.7.1 and the results of the calculations shown in figure 8.40. Hence the only feature seen is a minimum in the 5f loss magnetic moment at +5cm. This occurs at $1.1B_{IRR}$ and is in the ratio 0.5 : 1 with the magnitude of the minimum in the +5cm 3f loss magnetic moment shown in figure 9.39. This compares to the calculated values shown in figure 8.40 which has a minimum in the 5f loss at $1.2B_{IRR}$ and a magnitude in the ratio of 0.5 : 1 with the magnitude of the minimum in the 3f loss magnetic moment.

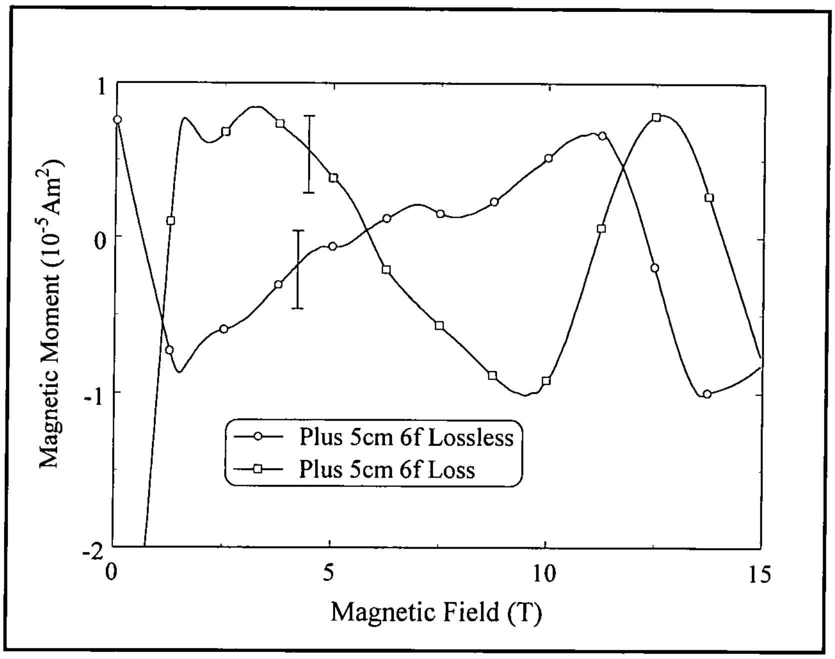

Figure 9.44 6f magnetic moment for SMS at 6.8K and positioned at plus 5cm.

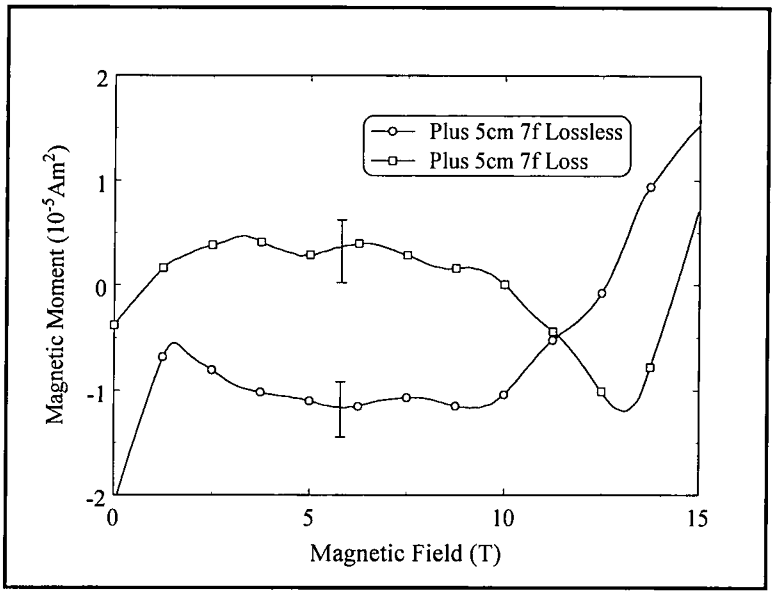

Figure 9.45 7f magnetic moment for SMS at 6.8K and positioned at plus 5cm.

Just as with the measurement on SMS at 6.8K, it was possible to observe features in both the 6f and 7f magnetic moments in the plus 5cm measurements. The results are shown in figures 9.44 and 9.45.

Firstly considering the 6f lossless magnetic moment, this contains a minimum occurring at $1.3B_{IRR}$ with a magnitude of one third of the 4f lossless minimum. This compares to the calculated values in figure 8.37 in which the minimum occurs at $1.3B_{IRR}$ and has a magnitude of 0.45 times the 4f lossless minimum. The 6f loss magnetic moment in figure 9.44 has a maximum at $1.2B_{IRR}$ with an amplitude of one fifth of the 4f loss maximum. The calculations, shown in figure 8.38 predict a maximum at $1.2B_{IRR}$ with an amplitude of half the 4f loss maximum.

Finally the 7f magnetic moments shown in figure 9.45 have only one quantifiable feature in the loss magnetic moment which is a minimum at $1.2B_{IRR}$ and a magnitude of two fifth the 5f loss minimum. The calculated values shown in figure 8.40 predict a minimum at $1.3B_{IRR}$ with an amplitude of half that of the 5f loss minimum. The 7f lossless magnetic moment is expected, via the results of the calculations shown in figure 8.39 and the higher temperature measurement in section 9.7.1, to contain a maximum between $1.4B_{IRR}$ and $1.6B_{IRR}$ which for the +5cm measurement is 14.5T to 17T. The results in figure 9.45 show an increasing 7f magnetic moment which could be expected to give a maximum in the correct range.

In summary all the features predict by the mathematics that occur below the maximum field of the measurement and above the sensitivity of the experiment are observed and are in approximately the correct ratios in both size and field position.

9.7.3 Critical Current Density Measurements

From the hysteresis in the 1f loss magnetic moment it is possible to determine the critical current density using the equation:

$$J_C = \frac{2\Delta M}{Volume.Thickness\left(1-\dfrac{Thickness}{3.Width}\right)} \qquad \textbf{(8)}$$

This has been done for the two data sets already presented plus one taken at 4.2K for the same three field positions.

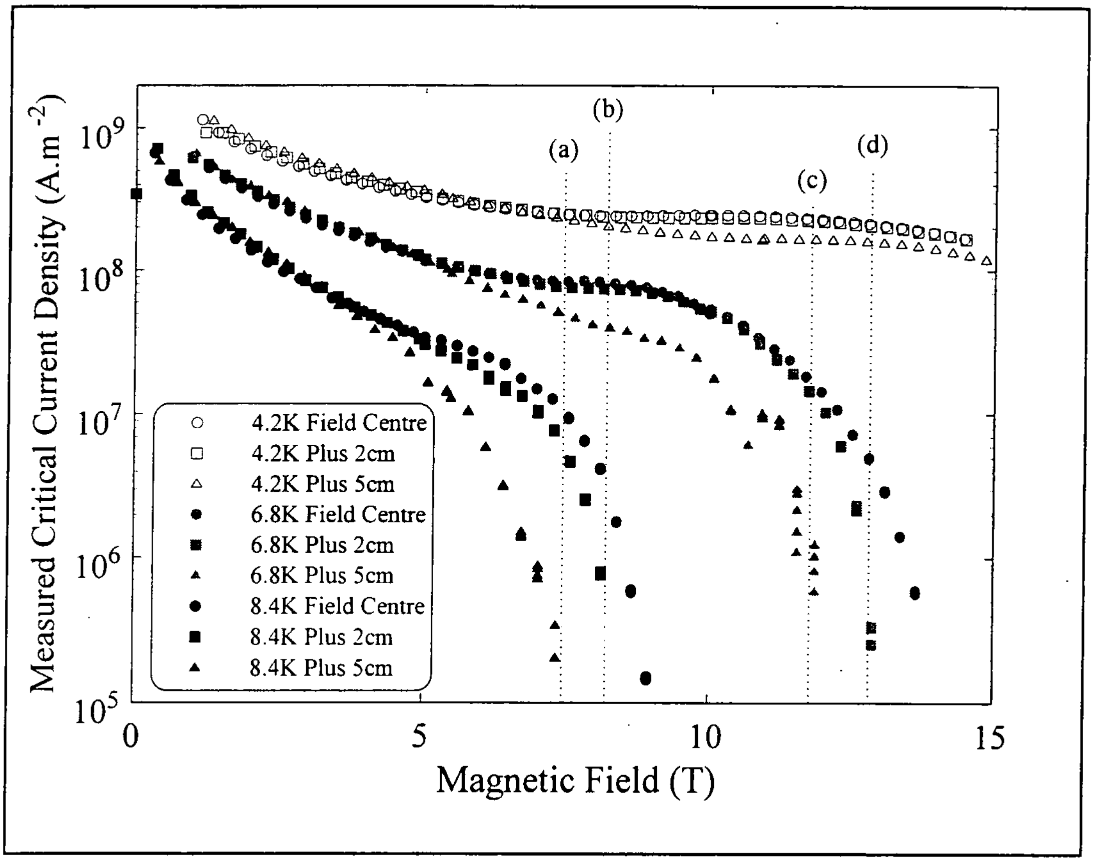

Figure 9.46 **Critical current density for the SMS sample calculated from the hysteresis of the 1f lossless voltage. Lines (a) to (d) represent $\gamma=1$ for the 8.4K +5cm, 8.4K +2cm, 6.8K +5cm and 6.8K +2cm measurements respectively.**

As can be seen from figure 9.46, the measurements agree at low fields where the sample self field is much larger than the ac field. The increase in the ac field reduces the irreversibility field and also decreases the critical current density at fields below the irreversibility field. The dotted lines on the figure indicate $\gamma=1$ calculated using equation 8.5 and using the field centre critical current density as the actual current density. This will hold true until the field centre critical current density reduces enough for the sample self field to be comparable with the ac field.

9.7.4 Summary of the results on SMS

The SMS sample has been measured at three temperatures in three effective ac fields. All the features predicted by the calculations up to 7f have been observed and are of the correct order in both field position relative to the irreversibility field and relative magnitudes of the peaks. Both the irreversibility field and the critical current density have been found to be dependent on the magnitude of the effective ac field and therefore cannot be considered as purely properties of the sample. The backgrounds in some of the odd multiples of the driver frequency we attribute to the anharmonicity of the driver and the positive increasing background in the 4f measurement is yet unexplained by the calculations. Further work on the effect of the 3f ac field is necessary to explain these features.

9.8 Lead Molybdenum Sulphide

The sample measured in this section is lead molybdenum sulphide, and is the stoichiometric $Pb_1Mo_6S_8$ sample measured in chapter four. The sample dimensions are 4.9mm x 3.0mm x 0.74mm, and again it was orientated with the long axis parallel to the applied field. Four temperatures were measured, 4.2K, 6.7K, 10.4K and a background measurement above T_C. This sample was measured at two field positions, field centre and +5cm. The measurements of each of the magnetic moments at multiples of the driver frequency will be presented and discussed in turn for the 10.4K and 6.7K measurements, then the critical current density derived from the hysteresis in the 1f lossless magnetic moment will be presented for the three temperatures below T_C studied. The pinning mechanism in PMS is thought to be grain boundary pinning and hence a Kramer critical current density as described in section 8.10.3 is appropriate to compare the calculations with the experimental results. The background measurements showed no signal in the harmonics of the driver frequency and hence any backgrounds shown are a guide to the eye.

9.8.1 PMS Measured at 10.4K

Measurements were taken at 10.4K, in dc fields up to 15T and the magnetic moments measured to 10f. No signals can be seen above the noise level above 5f and so only these figures will be presented.

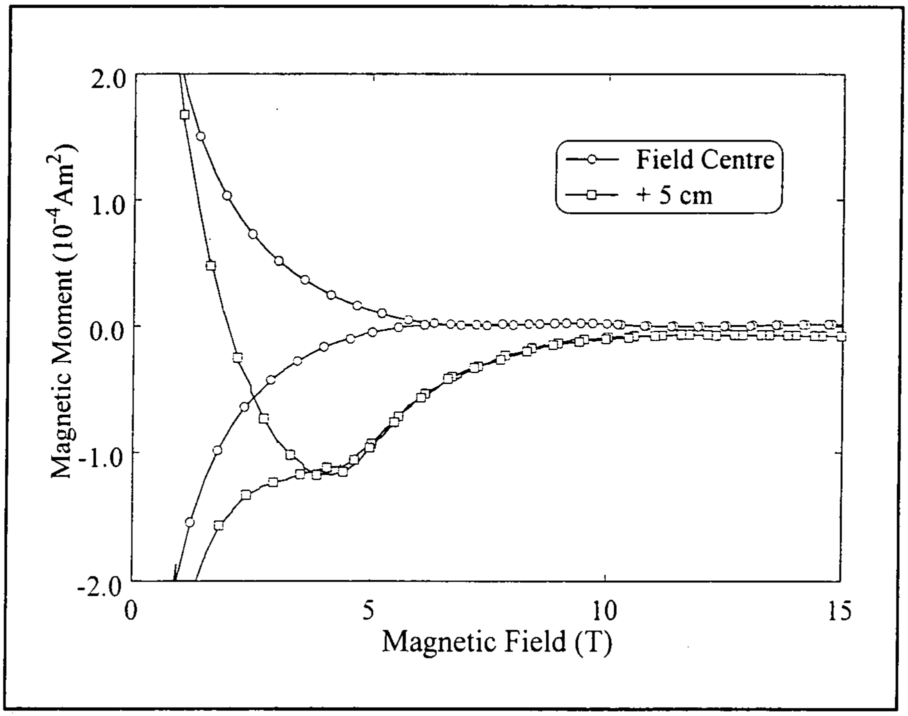

Figure 9.47 1f lossless magnetic moment for two field positions.

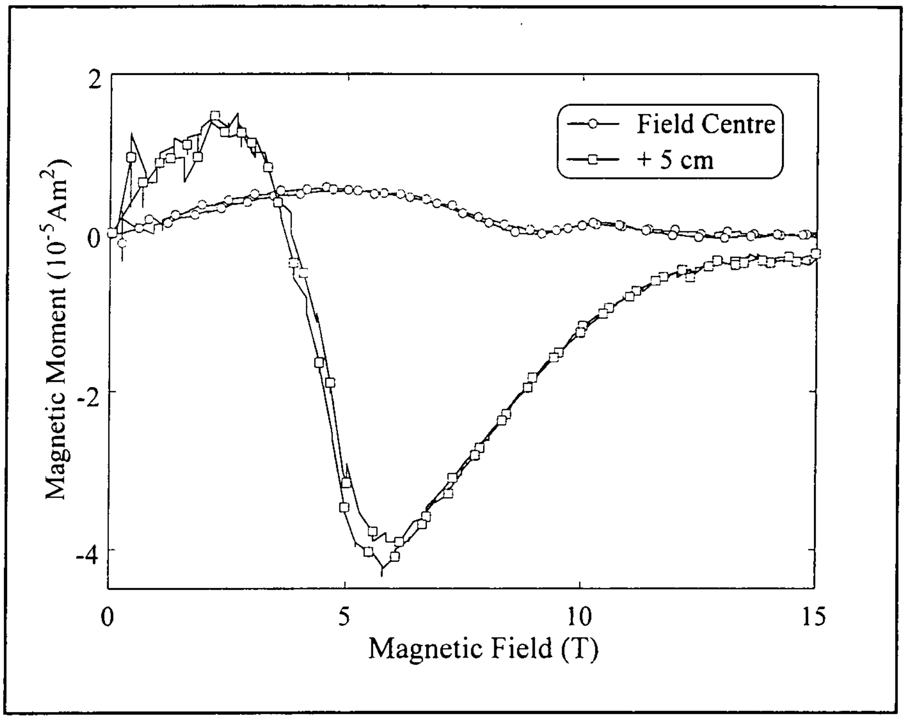

Figure 9.48 1f loss magnetic moment for two field positions.

The 1f lossless magnetic moment in figure 9.47 shows a large change in B_{IRR} with the increase in ac field. There is also a large negative reversible component introduced for the sample at +5cm, suggesting the sample is positioned below the centre of the pickup coils. The irreversibility fields are at 4.2T and 6.7T for the +5cm and the field centre measurements respectively. At low fields the hysteresis from both of the field positions is similar as the sample self field is large with respect to the effective ac field.

Figure 9.48 shows the 1f loss magnetic moments, with no features being visible in the field centre data. The +5cm 1f loss magnetic moment has a clear minimum at $1.4B_{IRR}$ with its magnitude in the ratio of 0.35 : 1 with the magnitude of the reversible component of the 1f lossless magnetic moment. The calculated value for the peak in the 1f loss magnetic moment is $1.02B_{IRR}$ as shown in figure 8.40 and the ratio of the magnitude of the 1f loss minimum to magnitude of the 1f lossless minimum is 0.4 : 1, derived from figures 8.39 and 8.40. The 1f loss magnetic moment falls to zero at approximately 12.5T which by comparison with figure 8.40 suggests that the critical current density falls to zero at approximately 12.5T. The onset of the susceptibility measurement for the $Pb_1Mo_6S_8$ sample shown in figure 4.12 occurs at 12T±0.2T for a temperature of 10.4K±0.1K.

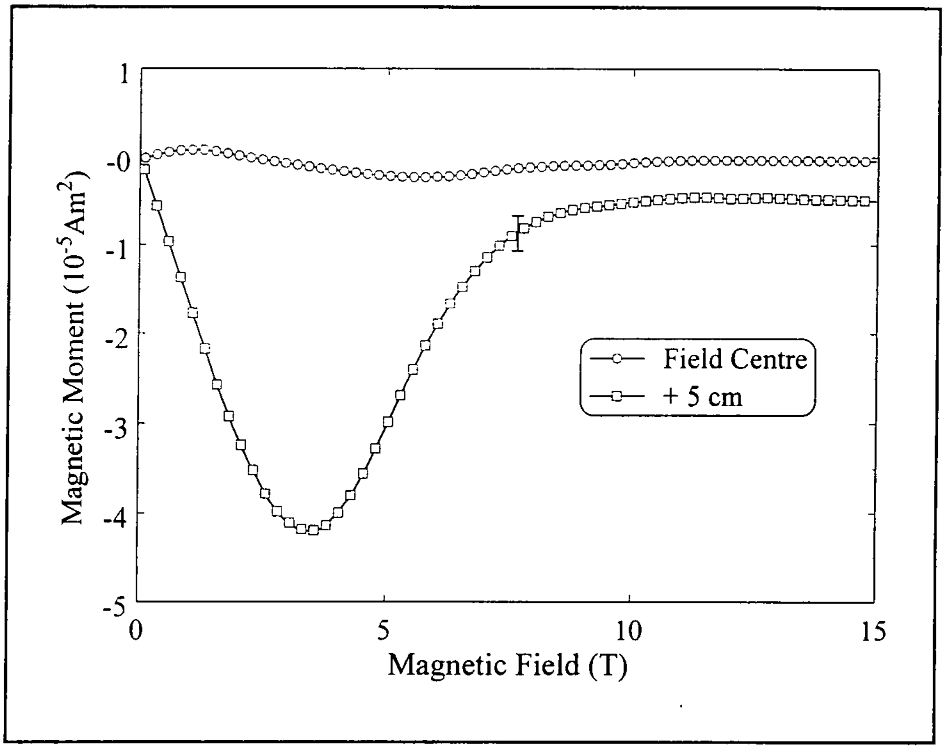

Figure 9.49 2f lossless magnetic moment for two field positions.

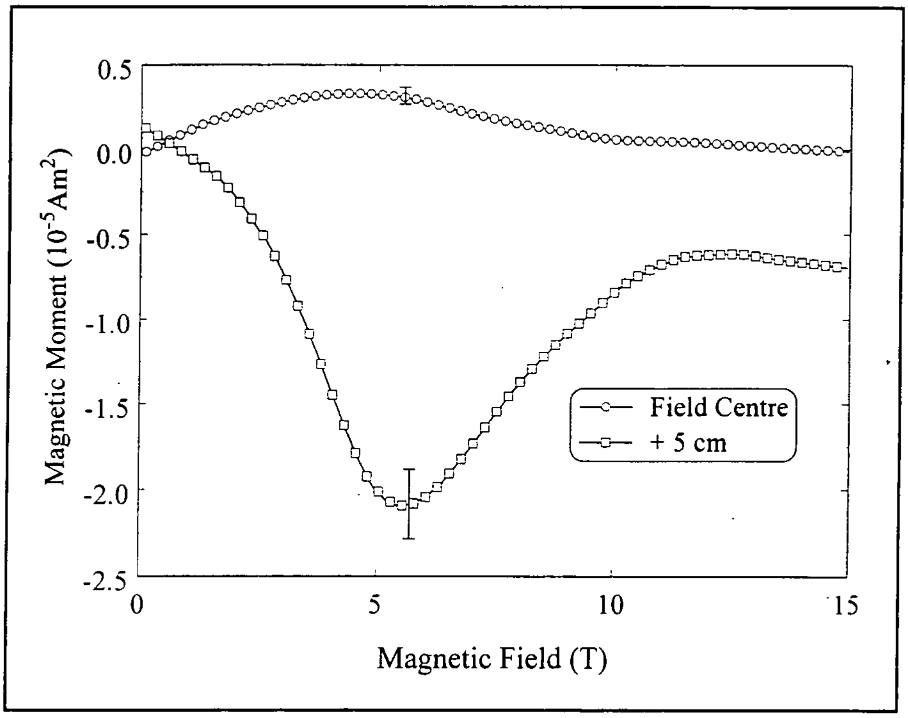

Figure 9.50 2f loss magnetic moment for two field positions.

Figure 9.49 shows a clear negative minimum in the 2f lossless magnetic moment in the +5cm case and a small negative minimum can be seen in the field centre case. The minima occur at $0.9B_{IRR}$ and $0.85B_{IRR}$ for the +5cm and field centre measurements respectively. This compares to the calculated minimum shown in figure 8.37 which shows a minimum in the 2f lossless at $0.7B_{IRR}$. The 2f loss magnetic moment shown in figure 9.50 shows a clear negative minimum for the +5cm case, occurring at $1.3B_{IRR}$, the ratio between the magnitudes of the 2f lossless minimum and the 2f loss minimum being 2 : 1. These compare to the calculated values shown in figures 8.37 and 8.38 where the 2f loss minimum occurs at $1.03B_{IRR}$ and the ratio of the magnitudes of the 2f lossless and loss minima is 3.1 : 1. The 2f loss magnetic moment for the field centre sample is small and shows a positive magnetic moment. This case is covered by mathematics for the sample crossing the field centre which is however difficult to do as it was shown in section 8.8 that the voltages measured are dependent on the exact positioning and symmetry of the sample. The 2f lossless and loss magnetic moments can both be seen to go to backgrounds at approximately 12T for the +5cm measurement.

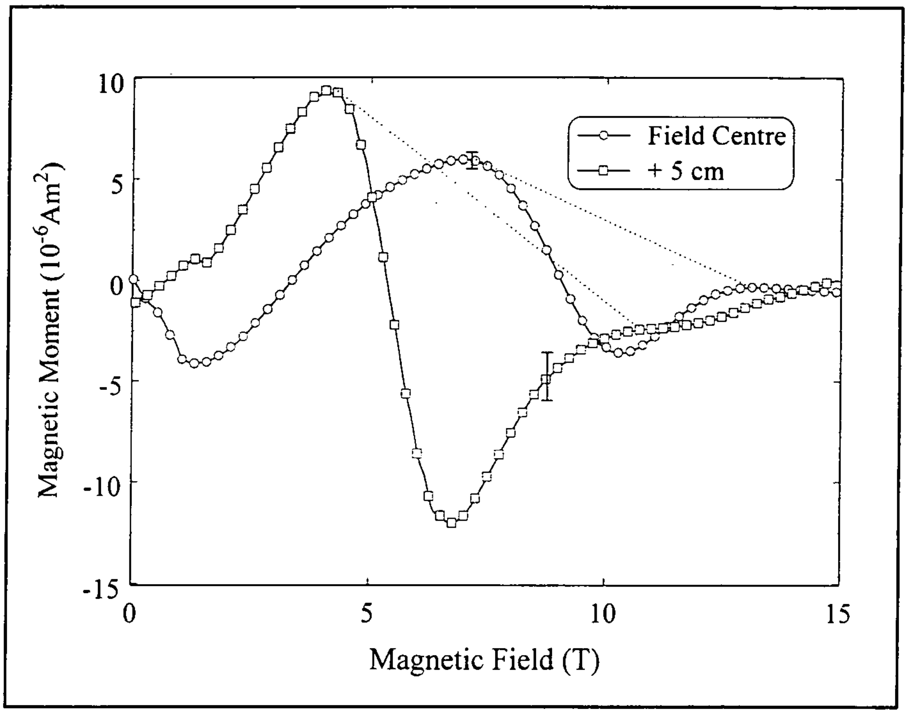

Figure 9.51 3f lossless magnetic moment for two field positions.

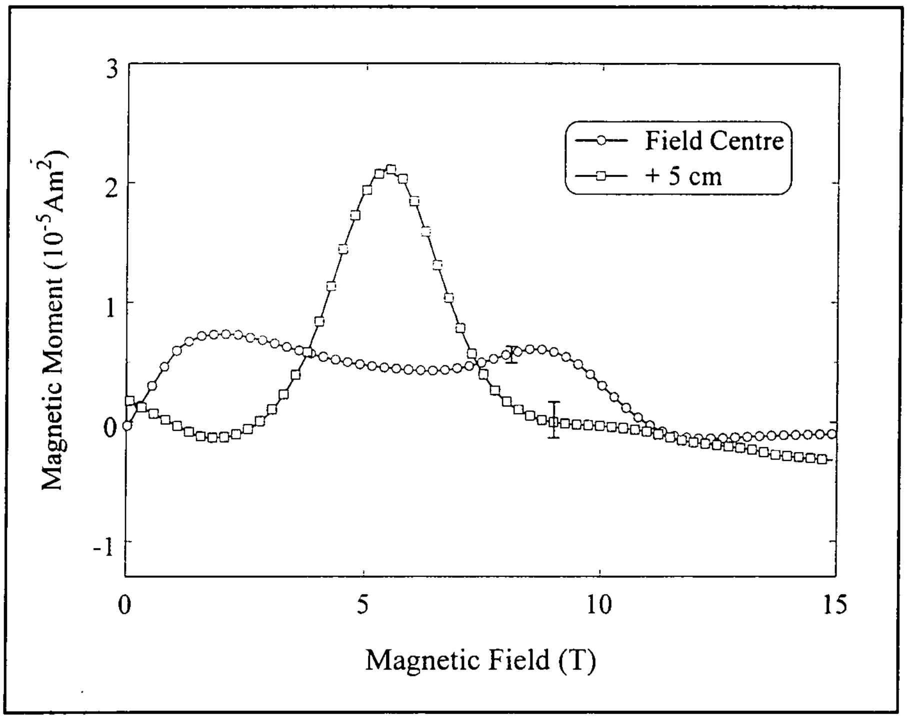

Figure 9.52 3f loss magnetic moment for two field positions.

As explained in section 9.3, the 3f lossless magnetic moment is strongly affected by the anharmonicity of the driver. It is possible to include backgrounds, similar in structure to those seen in the 3f lossless measurements in figure 9.26 for SMS. These backgrounds, shown by the dotted lines, give negative minima in both the field centre and +5cm measurements at 1.6B$_{IRR}$. The calculations predict a minimum in the 3f lossless magnetic moment at 1.15B$_{IRR}$, shown in figure 8.39. If the backgrounds shown by the dotted lines were subtracted this would lower the position of the minima in field, improving the agreement with the calculated values. The magnitudes of the minimum in the +5cm 3f lossless measurement can be compared to the 1f loss shown in figure 9.48 and can be seen to be in the ratio 0.4 : 1. This can be compared to the calculated value for the ratio of the magnitude of the 3f lossless peak to the 1f loss peak which is shown in figures 8.39 and 8.40 and is 0.7 : 1. Figure 9.52 shows the results for the 3f loss measurement and again the features predicted by the mathematics are not seen in the field centre case, though could be explained using a combination of the solutions for a sample crossing the field centre and accounting for the anharmonicity of the driver. The +5cm shows a clear maximum at 1.3B$_{IRR}$ which is comparable with that calculated for the 3f loss maximum shown in figure 8.40 which occurs at 1.02B$_{IRR}$. The expected minimum is not seen, and should be visible above the noise level. This suggests a background for the +5cm data that is similar in form to the field centre data.

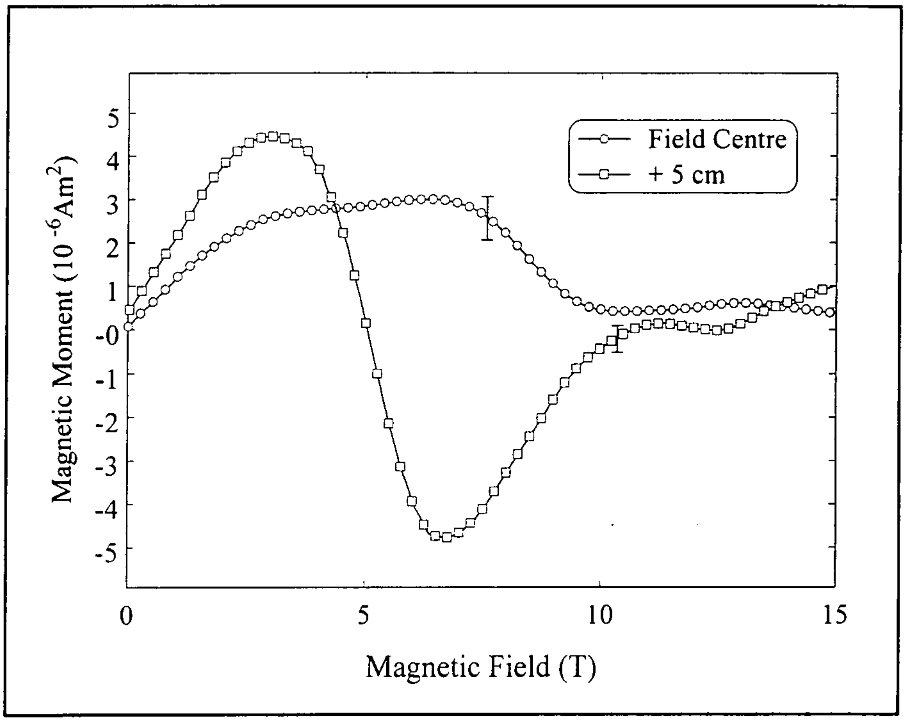

Figure 9.53 4f lossless magnetic moment for two field positions.

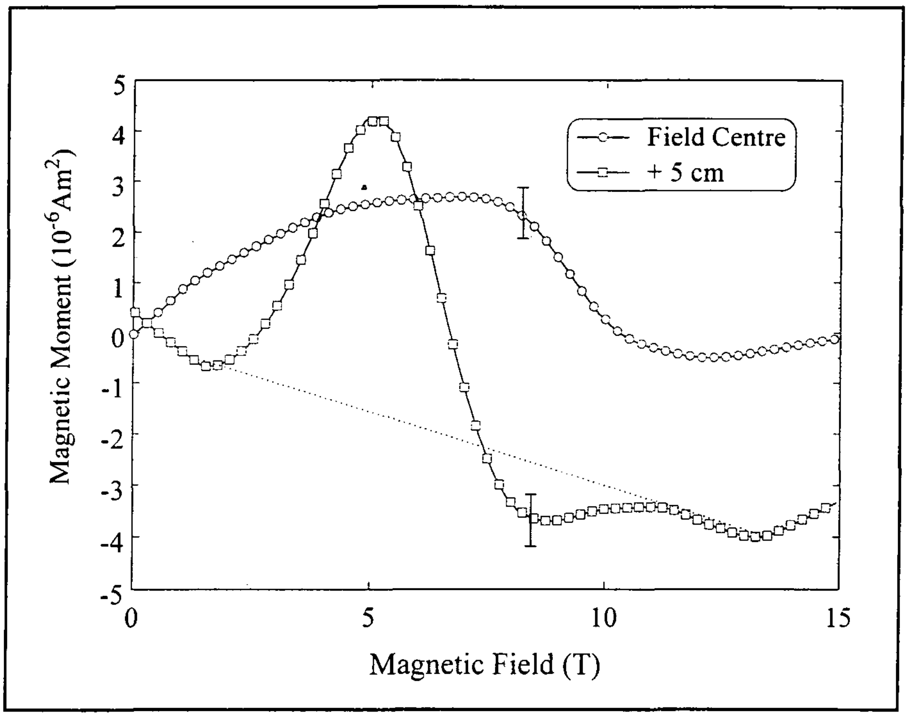

Figure 9.54 4f loss magnetic moment for two field positions.

The 4f lossless magnetic moment in figure 9.53 shows a positive increasing value with increasing field for both the field centre and the +5cm measurements as is also seen for the SMS sample in figures 9.28 and 9.40. For the field centre measurement this feature dominates however for the +5cm measurement a minimum can be seen at $1.6B_{IRR}$ which has a magnitude in the ratio of 0.2 : 1 with the magnitude of the minimum in the 2f lossless magnetic moment at +5cm, shown in figure 9.49. The calculated values for the 4f lossless magnetic moment, shown in figure 8.37 have a minimum at $1.2B_{IRR}$ and the magnitude of the minimum is in the ratio 0.2 : 1 with the magnitude of the minimum in the calculated 2f lossless magnetic moment.

For the 4f loss magnetic moment in figure 9.54, the unexplained positive background dominates for the field centre case. For the +5cm measurement, in order for the features predicted in the calculation to be present, it is necessary to take a background as indicated by the dotted line. The maximum and minimum occur at $1.2B_{IRR}$ and $2.0B_{IRR}$ which compares to the values calculate in the mathematics and shown in figure 8.38 where the maximum and minimum occur at $1.0B_{IRR}$ and $1.4B_{IRR}$ respectively. The ratios of the magnitudes of the maximum and minimum in the 4f loss +5cm measurement, in figure 9.54 with the minimum in the 2f loss measurement in figure 9.50 is 0.2 : 1 and

0.1 : 1. The compares to the ratios predicted by the mathematics, shown in figure 8.38 of 0.6 : 1 and 0.15 : 1.

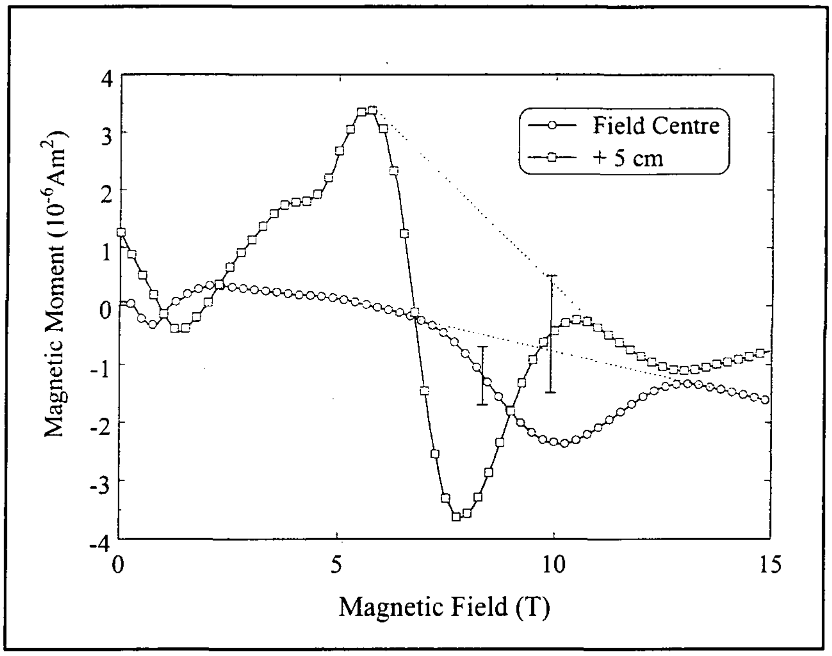

Figure 9.55 5f lossless magnetic moment for two field positions

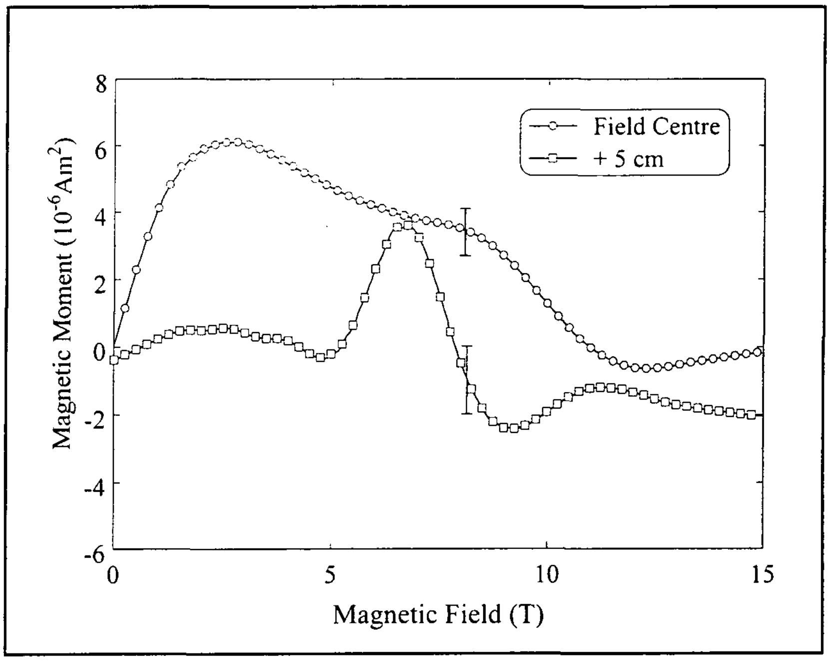

Figure 9.56 5f loss magnetic moment for two field positions

Similarly to the previous odd harmonics a non zero background must be defined in figure 9.55 to show the 5f lossless magnetic moment with the features predicted by the calculations in both the field centre and +5cm measurements. Minima occur in each at

$1.9B_{IRR}$ and $1.5B_{IRR}$ for the +5cm and field centre measurements respectively, in comparison to that calculated for the 5f lossless minimum show in figure 8.39 which occurs at $1.3B_{IRR}$. Allowing for the backgrounds, the magnitudes of the minima in the 5f lossless, in ratio with the 3f lossless minima for both the +5cm and field centre measurements shown in 9.51 are 0.4 : 1. This compares to the calculated ratio derived from figure 8.39 where the ratio of the same two components is 0.4 : 1.

The behaviour of the 5f loss magnetic moment in the field centre, figure 9.56 is attributed to the results predicted by the field centre calculations plus the driver anharmonicity. For the +5cm measurement 5f loss magnetic moment, also figure 9.56 the oscillation predicted by the calculations, shown in figure 8.40, is seen with measured maximum and minimum occurring at $1.6B_{IRR}$ and $2.2B_{IRR}$, compared to the calculated maximum and minimum in figure 8.40 at $1.2B_{IRR}$ and $1.4B_{IRR}$. The ratios of the magnitudes of the maximum with respect to the 3f loss maximum determined experimentally and shown in figure 9.52 is 0.24 : 1 and calculated in figure 8.40 is 0.5 : 1. The ratio of the minimum in the +5cm 5f loss cannot be taken with the +5cm 3f loss minimum as no clear minimum is seen in the 3f loss, figure 9.52, however the ratio can be taken with the 3f lossless minimum for the +5cm measurement shown in figure 9.51 and is 0.15 : 1, compared to the calculated value for the same ratio, determined from figures 8.39 and 8.40 to be 0.3 : 1.

In summary, the signals measured on this sample are approximately an order of magnitude lower than those measured on the SMS sample and so the backgrounds become more important. The field centre cases have been compared to the calculations for a sample not crossing the field centre and have not shown good agreement. It was shown in chapter 8 that the case where the sample crosses the field centre is sensitive to the exact positioning of the sample and hence no meaningful comparison can be made with experimental results. The measurements at +5cm are broadly consistent with the calculations in section 8.10.3, allowing for non zero backgrounds in the odd multiples of the driver frequency, which we attribute to the anharmonicity of the driver.

9.8.2 PMS Measured at 6.7K

In this section the measurements at 6.7K will be discussed and up to 5f and 15T. There are no significant features on the field centre measurements, with the exception of the 1f lossless magnetic moment so these will not be discussed further but are included for completeness.

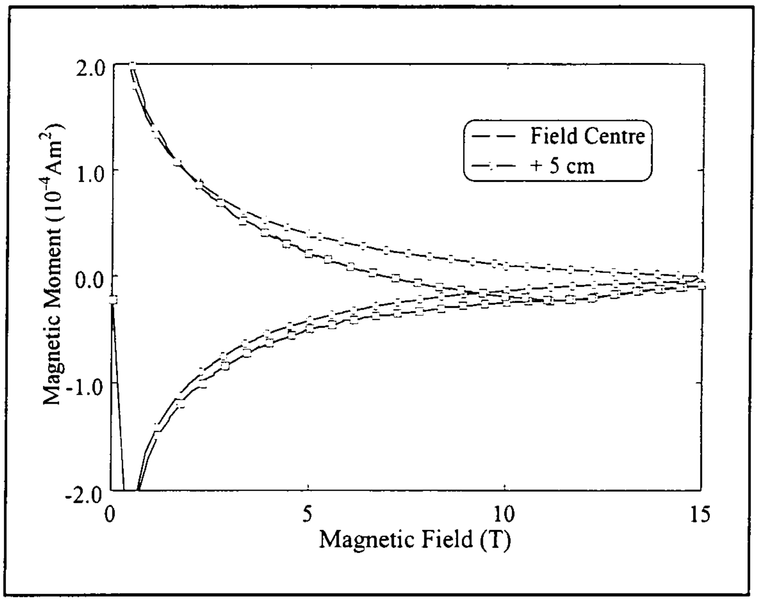

Figure 9.57 1f lossless magnetic moment for two field positions.

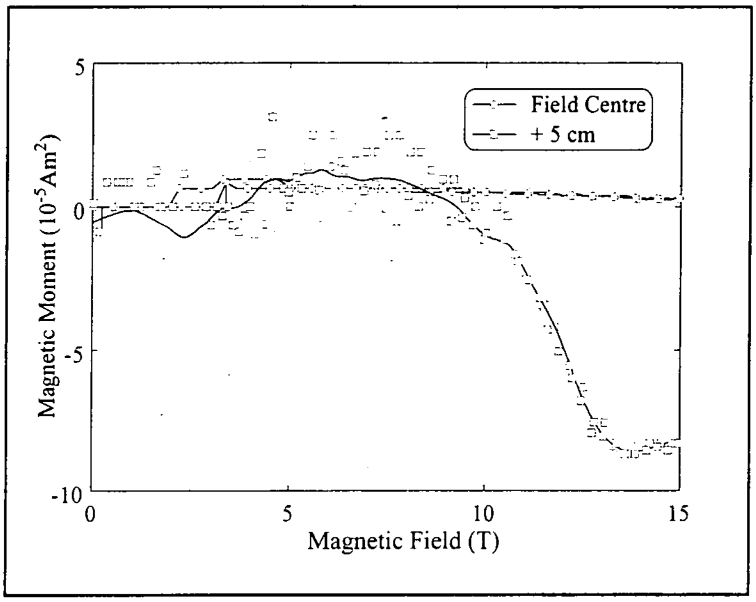

Figure 9.58 1f loss magnetic moment for two field positions.

In the field centre case there is no irreversibility field in this sample as can be seen from figure 9.57. For the +5cm measurement an irreversibility field is introduced at 11.3T where the 1f lossless magnetic moment becomes reversible. The measurements at both field positions can be seen to be in good agreement at low fields where the sample self field is greater than the effective ac field. A negative reversible component is introduced into the 1f lossless magnetic moment at +5cm, indicative of the sample being positioned below the centre of the pickup coils. The 1f loss magnetic moment for the +5cm measurement shown in figure 9.58 shows a negative minimum at $1.2B_{IRR}$ which can be compared to that shown in figure 8.40 where the calculated minimum occurs at $1.02B_{IRR}$.

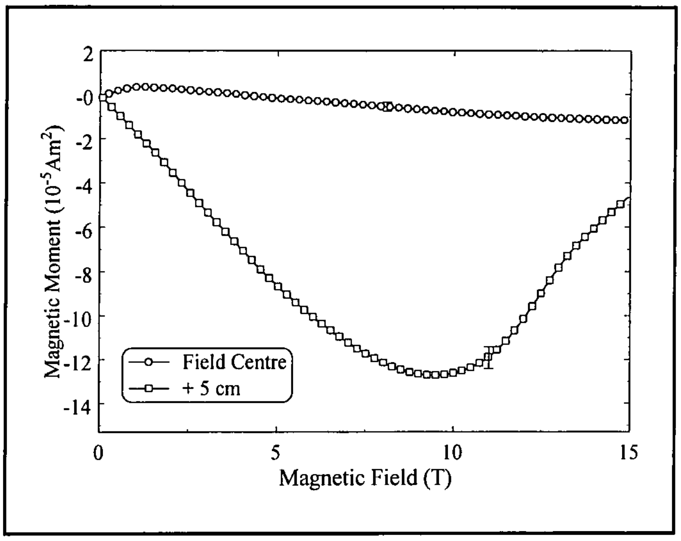

Figure 9.59 2f lossless magnetic moment for two field positions

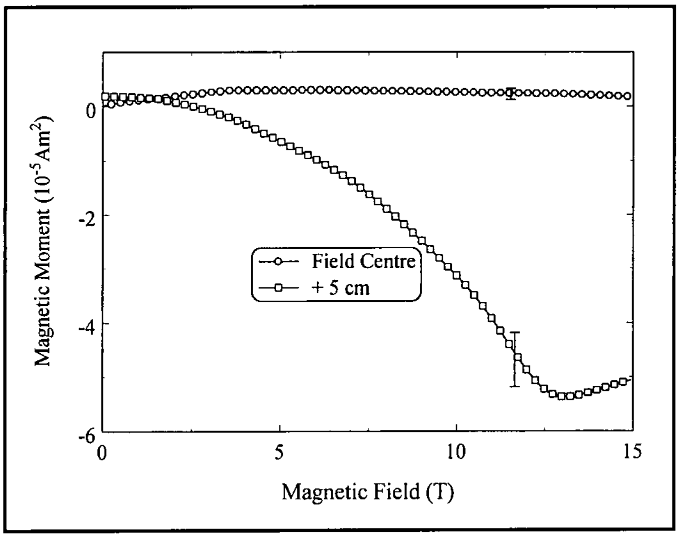

Figure 9.60 2f loss magnetic moment for two field positions

The +5cm measurement of the 2f lossless and loss magnetic moments shows a negative minimum in each at $0.85B_{IRR}$ and $1.15B_{IRR}$ for the lossless and loss respectively shown in figures 9.59 and 9.60. The calculated positions of the 2f lossless and loss minima, from figures 8.37 and 8.38, occur at $0.7B_{IRR}$ and $1.03B_{IRR}$. The magnitudes of the 2f lossless and 2f loss minima for the +5cm measurement are the same to ±5% and can be compared to that predicted by the calculations where the ratio of the magnitudes of the minima in the 2f lossless to the 2f loss is 3.1 : 1.

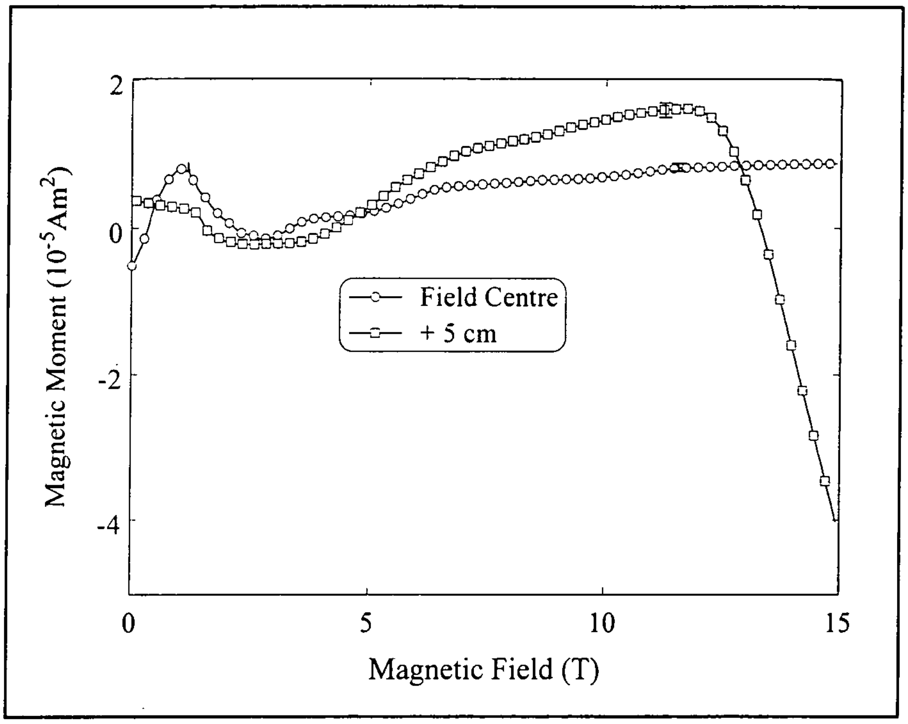

Figure 9.61 3f lossless magnetic moment for two field positions

The 3f lossless magnetic moment shown in figure 9.61 shows a negative decrease approaching 15T, suggesting a minimum above the maximum field of the measurement which would be $>1.3B_{IRR}$. The minimum is expected, from the results of the calculations shown in figure 8.39 at $1.15B_{IRR}$ which for this sample is 13T

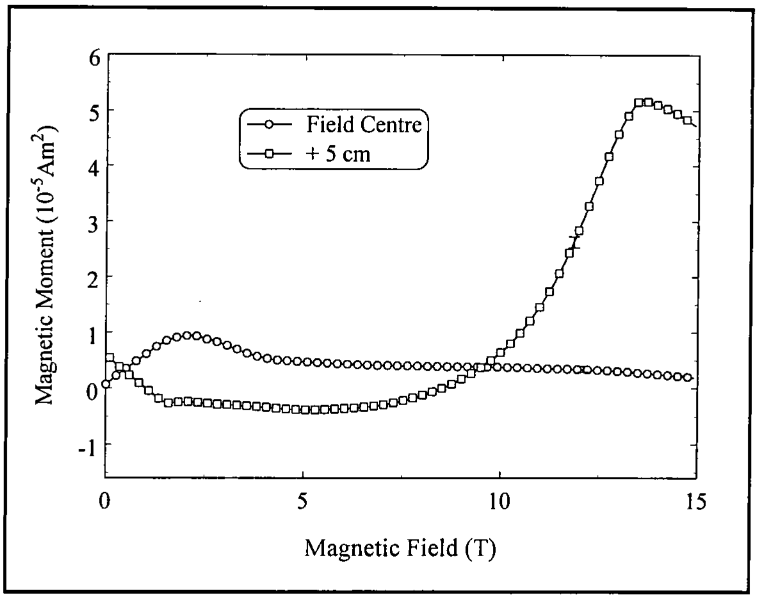

Figure 9.62 3f loss magnetic moment for two field positions

The 3f loss magnetic moment in figure 9.62 shows a maximum at $1.2B_{IRR}$, with the expected oscillation and minimum being above the maximum field of the measurement. The ratio of the magnitude of the 1f loss minimum to the magnitude of the 3f loss maximum is 0.6 : 1. The calculated position for the maximum in the 3f loss, shown in figure 8.40 is at $1.02B_{IRR}$ and the ratio of the magnitude the 3f loss maximum and the 1f loss minimum is 0.6 : 1.

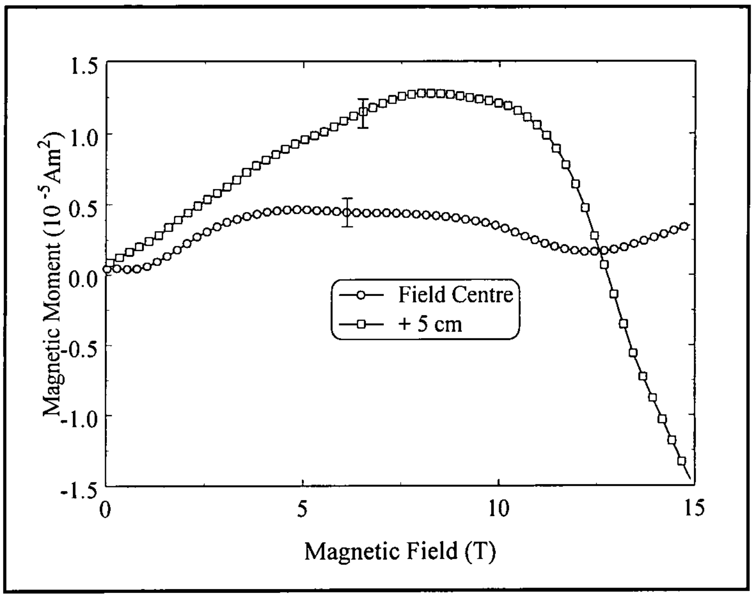

Figure 9.63 4f lossless magnetic moment for two field positions

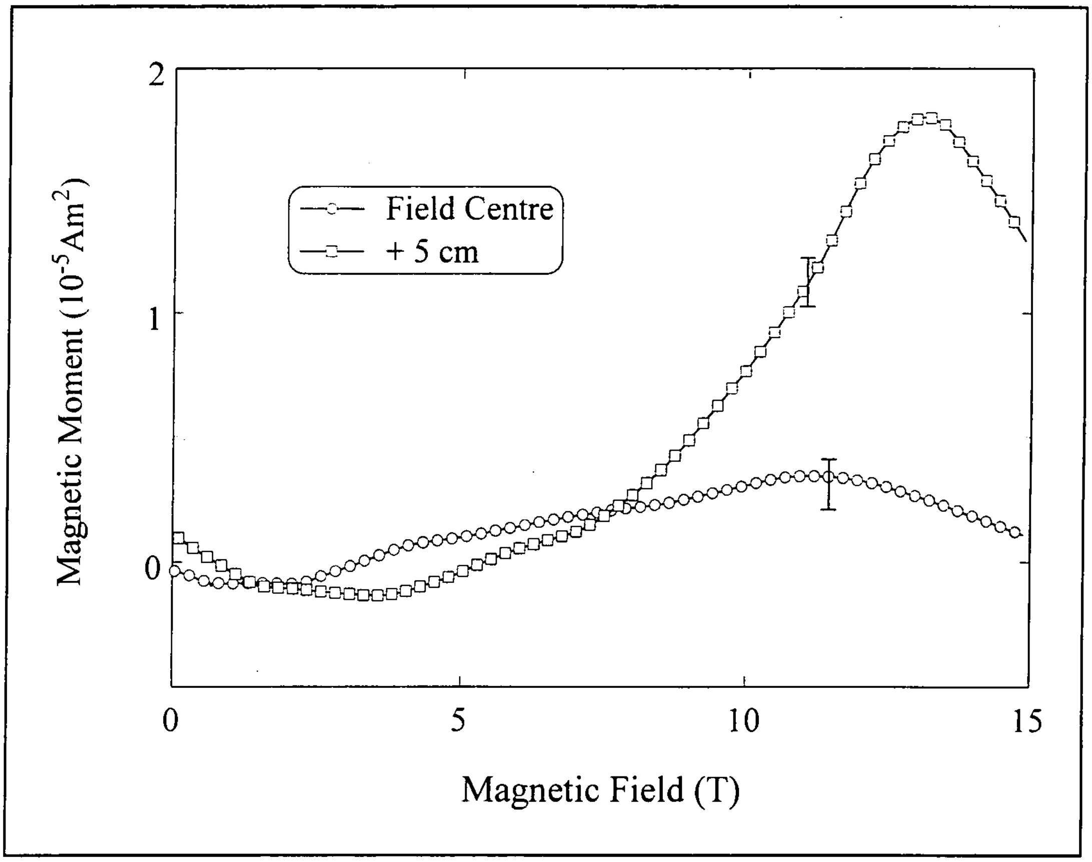

Figure 9.64 4f loss magnetic moment for two field positions

Again similar to the previous 4f measurements a positive increasing background is seen in the +5cm measurement. A minimum is expected, from the results of the calculations shown in figure 8.37, in this component at $1.2B_{IRR}$ which is 13.5T. The sharp negative decrease seen in the 4f lossless measurement in figure 9.63 at high field suggests that the minimum will occur at over 15T which is $>1.3B_{IRR}$. The 4f loss magnetic moment in figure 9.64 has a maximum at $1.2B_{IRR}$ which has a magnitude in the ratio of 0.3 : 1 with the magnitude of the minimum in the 2f loss +5cm magnetic moment shown in figure 9.52. The calculations shown in figure 8.38 give the maximum in the 4f loss magnetic moment occurring at $1.0B_{IRR}$ and having a magnitude in the ratio of 0.6 : 1 with the magnitude of the minimum in the 2f loss magnetic moment.

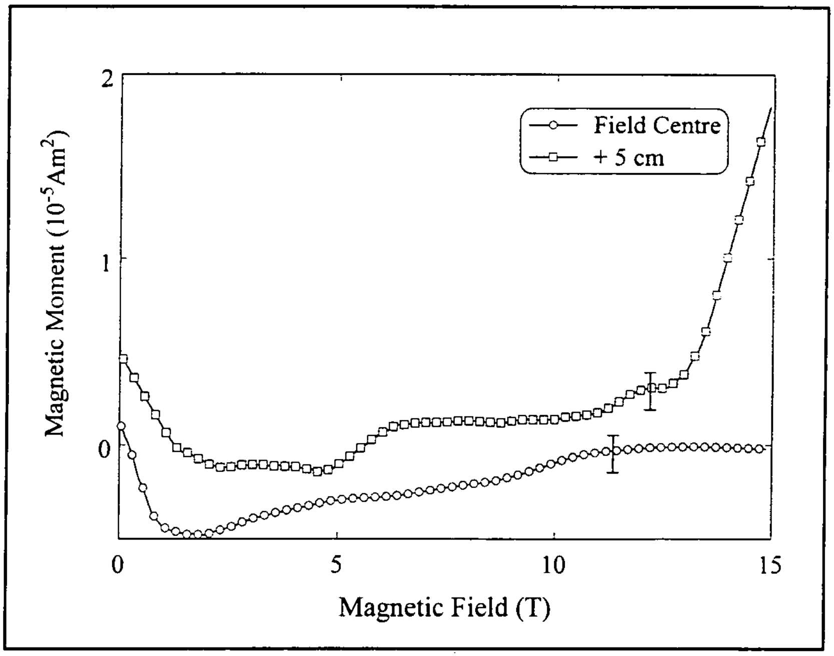

Figure 9.65 5f lossless magnetic moment for three field positions

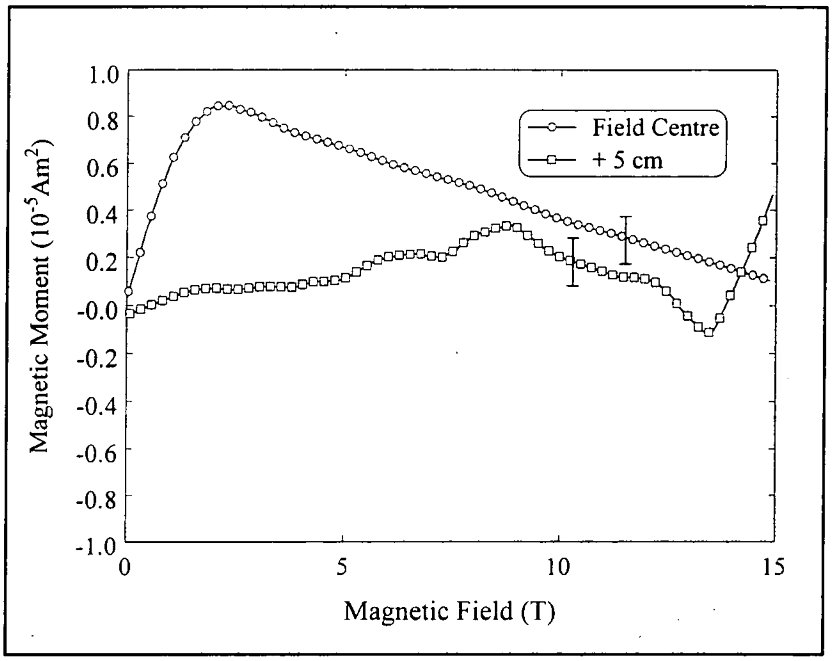

Figure 9.66 5f loss magnetic moment for three field positions

The calculations of the 5f lossless magnetic moment predict a minimum at $1.3B_{IRR}$, shown in figure 8.39, which for this sample is 14.7T. The measurement of the 5f lossless magnetic moment, shown in figure 9.65 shows a positive increase approaching 15T which cannot easily be explained away. The 5f loss magnetic moment in figure 9.66 is not consistent with that predicted by the mathematics as a small negative minimum is observed before the signal increases positively to the maximum field of the measurement. The calculations for the 5f loss shown in figure 8.40 predict a positive maximum at 1.2B_{IRR}, followed by a negative minimum at 1.5 B_{IRR}.

To summarise the results presented in this section, the features predicted by the mathematics have been seen in the +5cm magnetic moment from 1f to 4f. The 5f measured magnetic moments are not consistent with the calculations. These features are not seen in the higher temperature measurements on this sample nor in the measurements presented in section 9.7.

9.8.3 Critical Current Density Measurements

The critical current density has been calculated from the hysteresis in the 1f lossless magnetic moment for the three temperatures measured below T_C using equation 9.8, and is shown in figure 9.67.

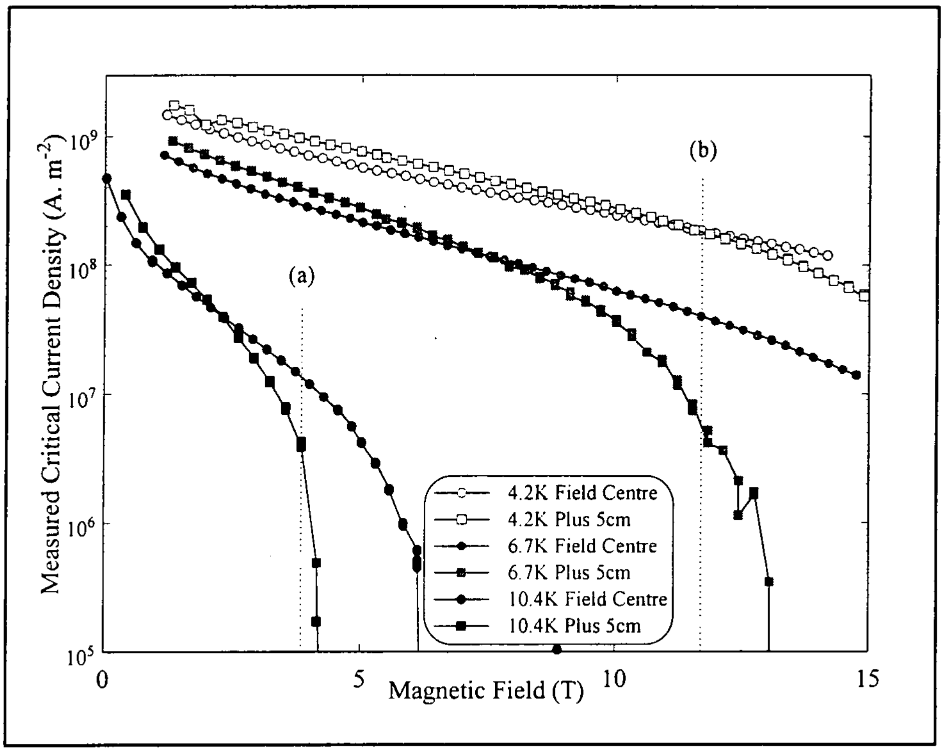

Figure 9.67 Critical current density for PMS sample calculated from the hysteresis of the 1f lossless voltage. Lines (a) and (b) represent γ=1 for 10.4K +5cm and 6.7K +5cm respectively.

Reasonable agreement can be seen between both field positions when the sample self field is large with respect to the effective ac field, i.e. at low applied field. The irreversibility field is reduced by the increase in effective ac field with the critical current density approaching zero at approximately $\gamma=1$, calculated from equation 8.5 assuming the centre field measured critical current density is a good approximation to the actual critical current density.

9.9 Multifilamentary Niobium Titanium Wires

NbTi multifilamentary wires were measured, mounted as described in section 7.6.2 having first removed the copper matrix using concentrated nitric acid. The wire contained 54 filaments, each of 28μm diameter, and a 6.1 cm length in total was used. The sample was orientated with the length of the wires parallel to the field. Once the copper had been removed it was however difficult to maintain alignment the filaments while potting them in the stycast epoxy. This means some distribution in the alignment of the filaments parallel to the applied field existed during the measurement. The signal produced by this sample was small, meaning that the noise and the backgrounds on the measurement become significant. The sample was measured at 3 temperatures below T_C, 4.2K, 6.8K and 8.0K, plus a background measurement in the normal state at both the field centre and +5cm. In the temperatures greater than 4.2K no features could be seen in the harmonics of the driver frequency above the noise level, and so these will not be presented. The appropriate calculations to compare the results in this section are in sections 8.6, 8.7 and 8.8 where the behaviour of a NbTi like sample is modelled. The backgrounds measured above T_C in the harmonics of the driver frequency were dominated by the noise which was symmetric about m=0.

9.9.1 NbTi Measured at 4.2K

With the sample positioned at both the field centre and +5cm, magnetic moments were measured up to 10 times the driver frequency in fields up to 15T.

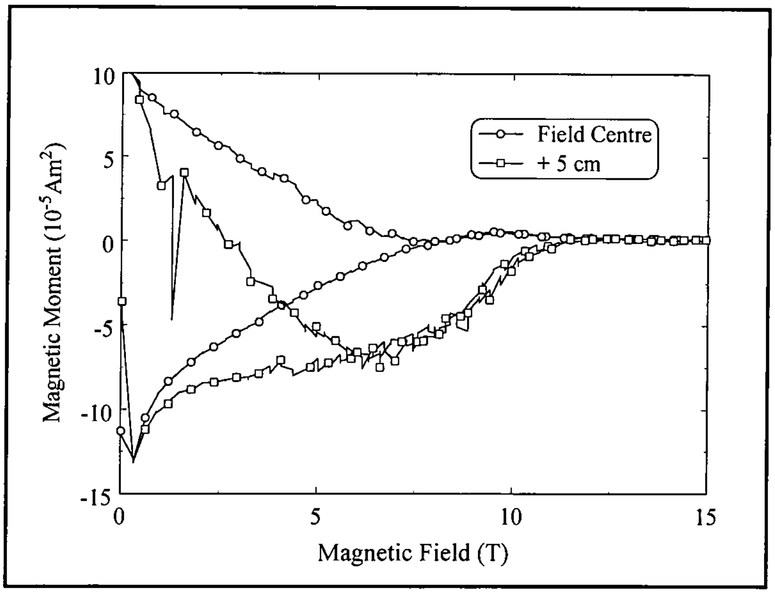

Figure 9.68 1f lossless magnetic moment for two field positions

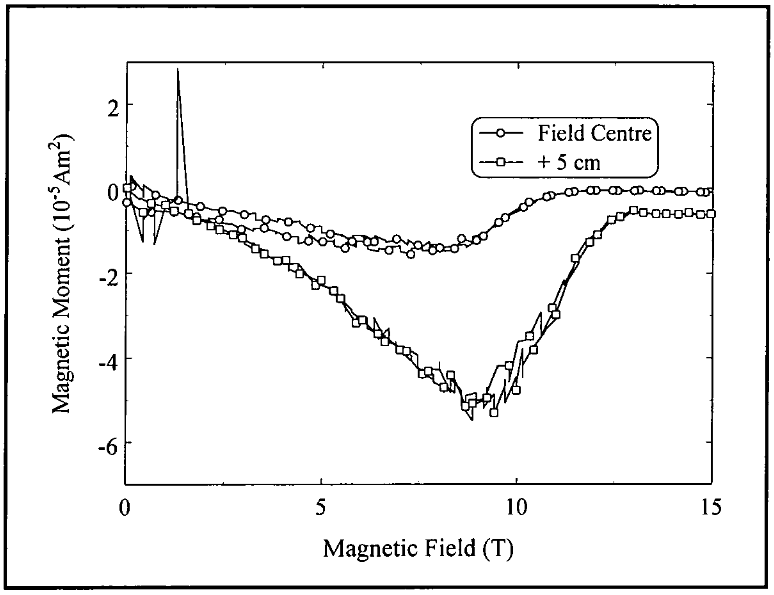

Figure 9.69 1f loss magnetic moment for two field positions

Figure 9.68 shows the 1f lossless magnetic moments for the samples measured at +5cm and field centre. The size of the hysteresis can be seen to be the same at low fields where the sample self field is large relative to the effective ac field for both sample positions. The irreversibility field for the sample positioned at +5cm is 6.0T and for the field centred sample is 8.0T. A negative reversible component can also be seen for both the field centre and the +5cm sample. Figure 9.69 shows the 1f loss measurements which also shows a negative reversible component for both the field centre and the +5cm sample. The minima in the 1f loss magnetic moment measurements occur at 1.0B_{IRR} and 1.5B_{IRR} for the field centre and +5cm measurements respectively. The calculated values for the minimum in the 1f loss magnetic moment for a NbTi like sample is shown in figure 8.12 and occurs at 1.25B_{IRR}.

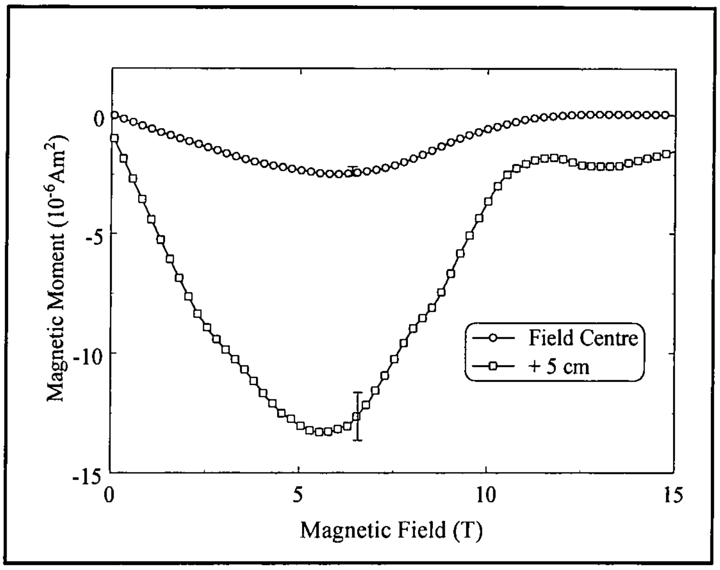

Figure 9.70 2f lossless magnetic moment for two field positions.

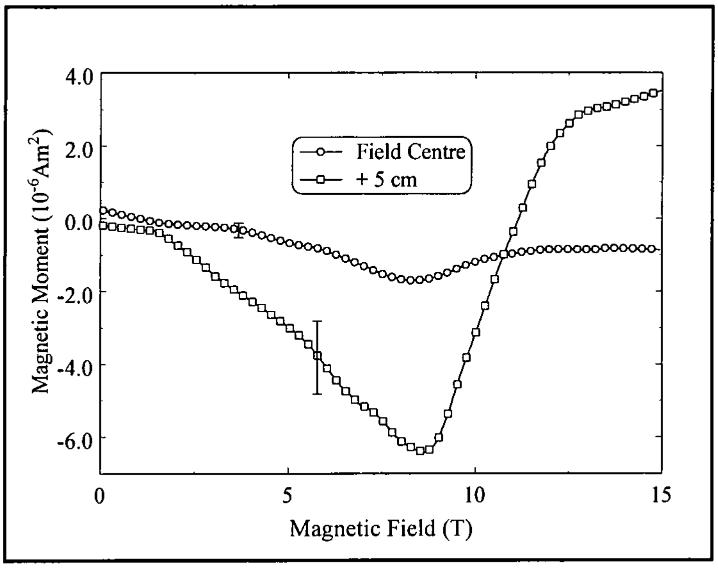

Figure 9.71 2f loss magnetic moment for two field positions.

The 2f lossless magnetic moment shown in figure 9.70 shows negative minima in both field centre and +5cm measurements occurring at 0.7B_{IRR} and 0.9B_{IRR} respectively, compared to the calculated minimum for the 2f lossless magnetic moment that is shown in figure 8.9 and occurs at $0.7B_{IRR}$. Figure 9.71 shows the 2f loss magnetic moment which again shows negative minima in both the field centre and +5cm measurements at $1.05B_{IRR}$ and $1.4B_{IRR}$ respectively. This compares with the calculated values of the 2f loss magnetic moment shown in figure 8.10, where the minimum occurs at $1.5B_{IRR}$. The relative magnitudes of the 2f lossless and 2f loss minima in figures 9.70 and 9.71 are in the ratio of 1.5 : 1 and 2.1 : 1 for the field centre and +5cm measurements respectively, which can be compared to the ratio of the calculated values, figures 8.9 and 8.10, of 1.8 : 1.

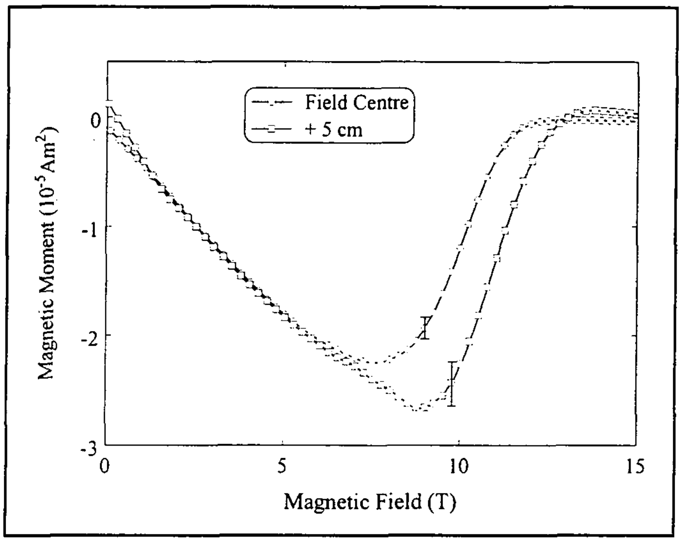

Figure 9.72 3f lossless magnetic moment for two field positions.

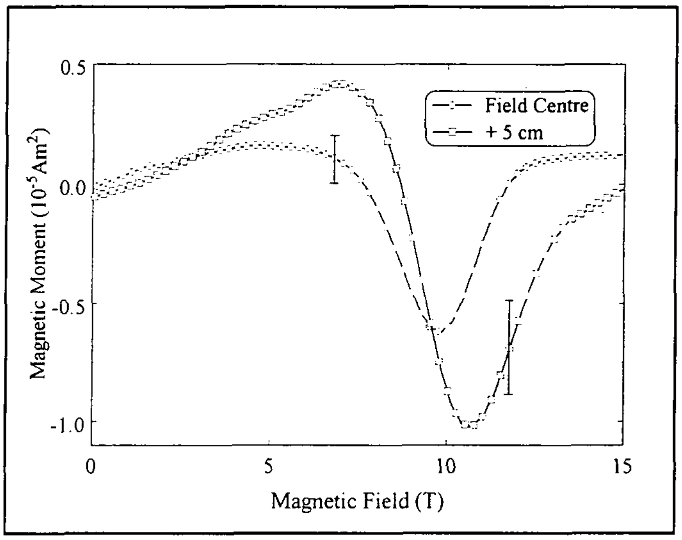

Figure 9.73 3f loss magnetic moment for two field positions.

The measured 3f lossless magnetic moments for the field centre and +5cm are shown in figure 9.72 and can be seen to be similar for both field positions. The minima occur at $0.95B_{IRR}$ and $1.5B_{IRR}$ for the field centre and +5cm measurements respectively. This is in comparison with the calculated values shown in figure 8.11 where the minimum occurs at $1.6B_{IRR}$. The ratios of the magnitudes of the 3f lossless minima with 1f loss minima, shown in figure 9.69 are 0.5 : 1 and 2.1 : 1 for the +5cm and field centre measurements respectively. This is compared to the calculated ratio shown in figure 8.11 which is 0.5 : 1. The 3f loss magnetic moment is shown in figure 9.73 and again the signals from the field centre and the +5cm are of comparable magnitude. The maximum and minimum occur at $0.6B_{IRR}$ and $1.2B_{IRR}$ for the field centre measurement and at $1.2B_{IRR}$ and $1.8B_{IRR}$ for the +5cm measurement. The calculated fields at which the maximum and minimum occur in the 3f loss component are shown in figure 8.12 and are $1.1B_{IRR}$ and $2.2B_{IRR}$. The magnitudes calculated for the maximum and minimum in the 3f loss are also shown in figure 8.12 and are in the ratio 0.6 : 1 and 0.25 : 1 respectively. The experimentally measured ratios of the magnitudes of the maxima and minima in the 3f loss, in figure 9.73, with the 1f loss shown in figure 9.69 are 0.15 : 1 and 0.12 : 1 for the field centre measurement and 0.1 : 1 and 0.2 : 1 for the +5cm measurement.

In summary the NbTi sample at +5cm contained all the features predicted by the mathematics up to 3f. The sample in field centre also contained some of the features predicted, suggesting that the sample in field centre was also subject to an ac field comparable to the self field of the sample.

9.9.2 Critical Current Density Measurements

The critical current density was determined from the magnitude of the hysteresis in the 1f lossless magnetic moment. The equation:

$$J_C = \frac{\Delta m}{r_f \times V_f \times N_f} \qquad \textbf{(9)}$$

where r_f, and V_f are the radius and volume of a single filament and N_f is the total number of filaments in the wire.

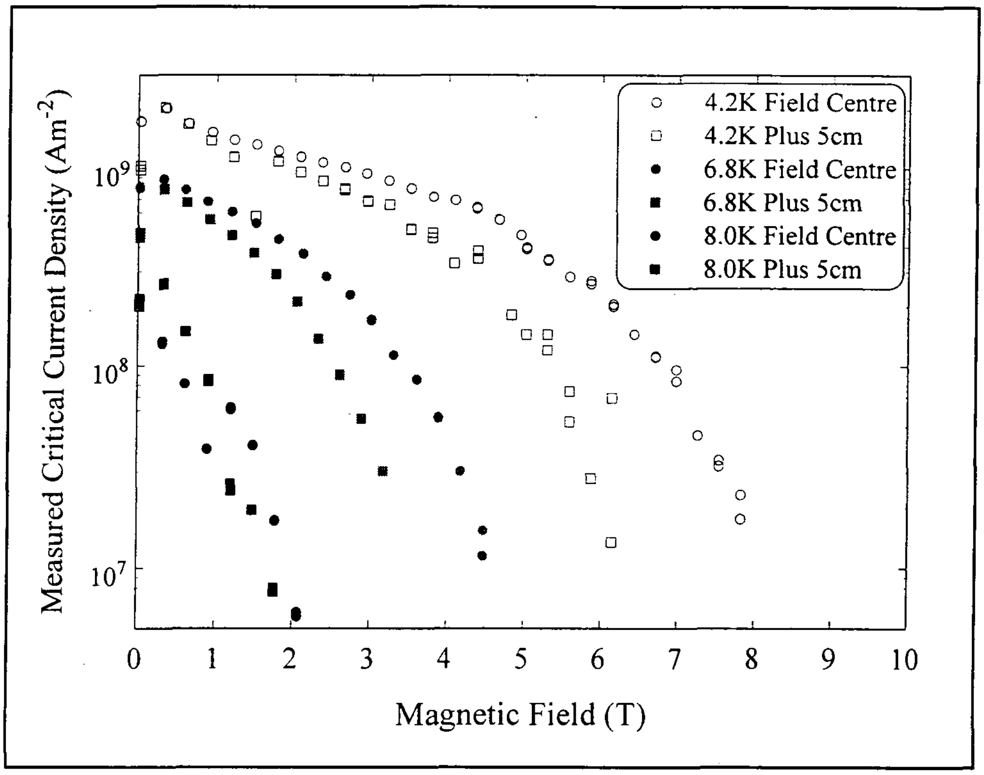

Figure 9.74 Critical current density for NbTi wire sample calculated from the hysteresis of the 1f lossless voltage.

The critical current density of the wire measured by transport measurement is 2.6x10^{9}A.m^{-2} at 4.2K and 5T. The sample used for the VSM measurement has had the stabilizing copper removed and the filaments potted in stycast. The filaments are therefore not well connected to each other and are no longer thermally stabilized with copper. The currents flowing in the wire in the magnetisation measurement also flow in a different direction to the transport currents measured which may also contribute to the reduced value of the measured critical current density as the wires are thought to be anisotropic. The calculation of the self field of the sample for the estimated critical current density of 8x10^{8}A.m^{-2} intermediate between the magnetisation and the transport measurement suggests that at 5T the sample self field, given by:

$$B_{sample} = \mu_0 J_c r = 4.\pi.\times 10^{-7} \times (8\times 10^8) \times (14\times 10^{-6}) = 14mT \qquad \textbf{(10)}$$

This can be compared to the effective ac field from the magnet which is calculated as described in section 9.2 at 5T for the field centre measurement is approximately equal to 0.15mT. This suggests that $\gamma \approx 0.01$ and hence the sample should be unaffected by the ac field. It appears however that the sample is affected by the ac field as the magnetic moments measured at multiples of the driver frequency are non zero. The sample used is thin filament wire, 28μm diameter, with the stabilizing copper removed and the filaments potted in stycast. The filaments are therefore not well connected to each other and are no longer thermally stabilized with copper. The measured critical current density and irreversibility field can be clearly seen to be decreased by the increase in effective ac field. A $\gamma=1$ line cannot be included in these figures as the actual critical current density as a function of field is not know.

9.10 Discussion

The discussion will be divided into two sections. Firstly the results presented in this chapter will be summarised and compared to the predictions of chapter 8. Secondly the implications of this work on the measurement of magnetic moments of superconductors using a VSM will be considered.

9.10.1 Overview of Results

The calculations presented in chapter 8 predicted that measuring the magnetic moment of a superconductor using a VSM was not simply a matter of measuring the magnetic moment at the driver frequency. The irreversibility field and measured critical current density were predicted to be dependent on the field inhomogeneity in which the sample moved and voltages were predicted at both odd and even multiples of the driver frequency. For a sample not crossing the centre of the dc field profile, the voltages at even multiples of the driver frequency were dependent on the size of the field inhomogeneity(β_0 term) and the voltages at odd multiples of the driver frequency were caused by the positioning of the sample within the pickup coils(β_1 term). For a sample that did cross the centre of the dc field profile the calculations predicted that the exact positioning of the sample was critical and that for any real experimental arrangement the β_0 term produced both odd and even multiples of the driver frequency as did the β_1 term. The aim of this chapter was to provide experimental support for each of the conclusions of chapter 8 and so each will now be discussed in turn.

Both critical current density and irreversibility field have been shown to be dependent on the effective ac magnetic field experienced by the sample, as shown in figures 9.46, 9.67 and 9.74 where SMS, PMS, and NbTi were measured in various field gradients at various temperatures. The predictions of the calculations is that for the sample not crossing the field centre, the magnetisation curve will become reversible(B_{IRR}) when $\gamma=1$, which is indicated on the each of the figures and good agreement is found between the calculations and the experimental results.

In order to investigate the nature of the odd harmonics, measurements were performed with the sample positioned both above and below the centre of the pickup coils. These results are shown in section 9.6 for a PMS sample and a NbTi sample. The PMS sample is the most compelling, with the signal to noise ratio being large and the expected features clearly seen up to 5f, showing excellent agreement with the results of the calculations in section 8.10.3. The NbTi sample also shows features at odd multiples of the driver frequency being amplified by moving the sample out of the pickup coil centre. Note that these two samples are positioned at opposite sides of the pickup coil centre and as predicted by the calculations shown in section 8.7 and 8.10.3 have features with opposite signs.

The calculations go on to predict magnetic moments measured at even multiples of the driver frequency, the magnitude and position of the features being determined by the critical current density of the sample and the effective ac field experience by the sample as it moves. The strongest experimental support for this is found in section 9.7 where for the SMS the agreement between the measured magnetic moments at +5cm and the calculated predictions of section 8.10.3 is compelling. In addition the PMS and NbTi samples in sections 9.8 and 9.9 also show good agreement with the calculations in the 2f magnetic moment for the +5cm measurement. The signal is smaller for these samples and the 4f measurement has a non zero background which makes the features predicted more difficult to distinguish however the general form can still be seen. The field centre measurement for each of the samples shows non zero magnetic moments above the irreversibility field for all the samples measured. The form of these signals was shown in section 8.8 to be very difficult to predict due to the dependence on the exact positioning of the sample, however their existence above B_{IRR} suggests that the critical current density is non zero.

Hence strong experimental support has been found for the predictions of chapter 8, implying that the features discussed in both chapters 8 and 9 has serious implications for the measurement of magnetic moment of superconductors using a VSM.

9.10.2 Implications for the Use of a VSM System

When using a VSM to characterise superconducting materials, it is essential to understand the effects discussed in chapters 8 and 9 and to determine whether they are significant. In order to do this, the field homogeneity of the magnet and the throw distance of the VSM must be know for the effective ac magnetic field to be determined. Once this has been calculated using equation 8.4, it is necessary to determine the self field of the sample. In order to do this the critical current density must be measured, or known, and then the parameter γ can be determined. As a first order approximation, $\gamma=0.1$ leads to an error of 25% in the measured critical current density, the exact nature depending on the field dependence of the critical current density. By definition however when a sample is measured, the self field goes to zero at the irreversibility field, as the measured critical current density goes to zero. In order to determine whether this is actually the point at which the critical current density goes to zero it is necessary to measure the harmonics of the driver frequency. These harmonics fall to zero when the critical current density falls to zero, independently of when the 1f lossless magnetic moment becomes reversible.

When measuring the harmonics of the driver frequency it is necessary to understand the definition of the phase angle, as described in section 9.4, plus it is also important to measure the sinusoidality of the VSM driver unit. This can be done either by using a nickel sample, as described in section 7.7.2, or by comparing the signals in the harmonic measurements of a superconductor with the 1f lossless magnetic moment at low field, where the ac field is small. The ratios of the magnetic moments in the harmonics to the 1f lossless magnetic moment will be field dependent if the ac field effect is significant. Two possible experiments can be performed to determine the limiting factor for the measurement of the close up in the MH loop. Firstly moving the sample from the centre of the pickup coils increases the size of the Mallinson field (β_1 term) and hence the size of the magnetic moment measured at odd multiples of the driver frequency. It may then be possible to measure magnetic moments in 3f which are non zero above the close up of the 1f lossless magnetic moment which indicates that the close up(B_{IRR}) is not the point at which the critical current density falls to zero. If nothing is seen in the 3f magnetic moment, both the sample and the pickup coils can be moved into a large field gradient to increase the effective ac magnetic field. If the sample is then also moved out of the centre of the pickup coils, magnetic moments in both 2f and 3f can be measured. The irreversibility field will necessarily be moved to lower field, however the point at which the 2f and 3f magnetic moments becomes zero is the point at which the critical current density becomes zero. This field can be compared to the point at which the 1f lossless magnetic moment becomes reversible for the field centred sample and if the two agree then the field centred sample is not significantly affected by the ac magnetic field, and the irreversibility field is a good approximation to the point at which the critical current density falls to zero.

9.11 Summary

The vibrating sample magnetometer described in chapter 7 has been used to measure the magnetic moment of three superconductors at temperatures between 4.2K and $T>T_C$, at fields up to 15T, measuring at multiples of the driver frequency up to 10f. The measurements were performed on the SMS sample described in chapter 5, the stoichiometric PMS sample described in chapter 4 and some commercial multifilamentary NbTi wire. The measured magnetic moments were corrected for the anharmonicity of the driver and then converted into the lossless and loss magnetic moments to allow direct comparison with the calculations in chapter 8. The results support the calculations presented in chapter 8. Hence it is essential that the work in the literature be reexamined to investigate whether the issues raised in this chapter and chapter 8 were the dominate causes of the features observed. We have suggested an experimental method which allows the origin of the irreversibility field to be investigated to determine whether it is a good approximation to the point at which the critical current density falls to zero.

Chapter 10
Conclusion

10.1 Introduction

In this chapter a summary of this thesis will be given and its conclusions outlined. Each of the chapters will be considered in turn, highlighting the important results and the implications of these on the wider community. Finally some suggestions for further work will be given.

10.2 Thesis Summary

After an introduction to superconductivity and a review of the literature relevant for this work, this thesis can be considered in two sections. The first concentrates on Chevrel phase superconductors, and in particular lead molybdenum sulphide(PMS) and tin molybdenum sulphide(SMS). Chapter 4 investigates the variation in superconducting properties with changes in stoichiometry for hot isostatically pressed PMS. The samples were all of high quality, with the stoichiometric sample found to be single phase by x-ray powder diffraction. The trends seen with changing stoichiometry were weak, and did not result in samples being significantly better or worse than state of the art bulk samples, even at the extremes of the compositions investigated.

Chapter 5 moves on to investigate the pinning in SMS and in particular the peak effect which is found in this material. A sample of SMS was fabricated using a hot isostatic press, and characterised electromagnetically. The high and low field pinning mechanisms were separated and each was found to obey a scaling law of the form proposed by Kramer, where the scaling held as a function of temperature in the field regime in which each of the mechanisms was appropriate. This is the first time the peak effect in SMS has been scaled in both field regions with a physically meaningful functional form. A better understanding of the peak effect may lead to the increase in critical current density that is required to make Chevrel phase materials into practical materials for the production of static dc fields above 30T.

With this goal in mind, magnetic pinning and the coexistence of superconductivity and magnetism were the subjects of chapter 6. The Chevrel phase crystal structure allows magnetic ions to be introduced into the lattice without destroying the superconductivity. Samples were fabricated by Dr D N Zheng and characterised by the author. The presence of the magnetic ions was found to significantly improve both $B_{C2}(0)$ and dB_{C2}/dT while reducing T_C and J_C. The 35% doped sample has the highest recorded $B_{C2}(0)$ and dB_{C2}/dT in the literature for any SMS based sample. The microstructural properties were degraded by the introduction of europium, with the sintering of the sample worsening with increasing doping. This could be the cause of the reduction in J_C, and hence with the correct heat treatment, high B_{C2} values could be obtained without the decrease in J_C, again making Chevrel phase materials useful high field materials.

The second section of this thesis concentrates on high field dc magnetisation measurements using a vibrating sample magnetometer. Chapter 7 describes the design improvements made to the existing system in Durham that both improved the sensitivity and reduced the noise level. This system allows automated dc magnetisation measurements to be made as a function of field and temperature from 4.2K to 30K, in fields up to 15T in a 40mm bore superconducting solenoid magnet. The system also allowed the measurement of multiples of the driver frequency up to 10f, in different field inhomogeneities, by allowing the movement of the pickup coils and sample with respect to the centre of the dc field profile.

The VSM measurement of the magnetic moment of a superconductor is considered in chapter 8. Traditionally, only the effect of the dc applied field on the superconductor is considered, however in all real VSM measurements the superconductor also experiences an effective ac magnetic field due to its motion in an inhomogeneous magnetic field. The effect of this ac field is included into the Bean profiles and the voltage induced in the pickup coils calculated. This voltage is then Fourier deconvoluted into the lossless and loss components that would be measured on an idealised lockin amplifier at the driver frequency and its harmonics up to 10f. There are two main cases to consider for these calculations, the sample oscillating so that it never crosses the centre of the dc field and the sample oscillating symmetrically about the centre of the dc field, each of which must be considered for the sample perfectly positioned in the centre of the pickup coils and for a sample offcentred with respect to the centre of the pickup coils. The results of these calculation shows that the 1f lossless magnetic moment cannot be considered to represent the critical current density of the sample if the effective ac field is within one order of magnitude of the sample self field. It was also found that the point at which the 1f lossless hysteresis loop becomes reversible is not the point at which the critical current density falls to zero but is the point at which the ac field fully penetrates the sample throughout its volume. Hence the irreversibility field is dependent on the sample dimensions, the homogeneity of the magnet used to apply the dc field, the critical current density and the experimental geometry of the sample and pickup coils relative to the dc field centre. It cannot therefore be considered as a property of the superconductor alone. One further implication of this work is that the reversible 1f lossless magnetisation cannot be assumed to be due entirely to the reversible properties of the superconductor, as the critical current density is not necessarily zero. Measurement of magnetic moment at harmonics of the driver frequency are non zero while the critical current density is non zero, and hence allow the determination of the point at which the critical current density falls to zero.

In order to support the calculations of chapter 8, the VSM system in chapter 7 was used to measure the magnetic moment of the stoichiometric PMS sample described in chapter 4, the SMS sample described in chapter 5 and a sample made from commercial multifilamentary NbTi wires, in fields up to 15T from 4.2K to above T_C and at multiples of the driver frequency up to 10f. The results of the measurement were consistent with the calculations presented in chapter 8 for almost all cases. The anharmonicity of the driver is only accounted for to first order, meaning that the measurements at 3f and 5f need additional backgrounds including for agreement with the calculations. It was found, as predicted by the calculations that both the measured critical current density and the irreversibility field were dependent on the field inhomogeneity in which the sample was measured. The implications of chapters 8 and 9 is that previous results from VSM measurements presented in the literature must be reviewed in light of these findings to ensure that the conclusions drawn from them are genuine properties of the samples and that the effects described in these two chapters can be neglected to first order.

10.2 Suggestions for Future Work

In the materials side of this thesis, there are two areas in which this work could be extended. The pinning analysis performed on the peak effect in chapter 5 has shown that the Kramer functional form can be used to describe the pinning in both of the field regimes. The high T_C superconductors have also been seen to exhibit the peak effect or fishtail effect as it is also known. The extension of this pinning analysis into high T_C materials may give a better understanding of the fundamental mechanisms behind the pinning and hence provide a route for increasing the high field pinning in this class of materials.

Secondly, the fabrication of Chevrel phase superconductors doped with magnetic ions is an extremely interesting and exciting field of research, as it offers the opportunity to investigate both the fundamental coexistence of superconductivity and magnetism plus it appears to offer the possibility of improving the properties of the Chevrel phase material to make them commercially important materials. The doping of europium in to SMS has shown great potential by improving both B_{C2} and dB_{C2}/dT. The degradation in J_C attributed to the reduced sintering of the samples, may be overcome by changing the heat treatment, and or the doping level to optimise the critical current densities and critical fields.

For the measurement of the irreversibility field and the critical current density, this work suggests that magnetic field homogeneity and experimental geometry are critical in order to gain a good approximation to the actual properties of the superconductor under investigation using a VSM, measuring only the 1f lossless magnetic moment. By measuring the harmonics of the driver frequency it may be possible to determine the critical current density at fields above the point at which the 1f lossless magnetic moment becomes reversible, allowing the production of a genuine field dependence of the critical current density and hence the determination of the magnetic phase diagram, which may or may not include a field below the upper critical field at which the critical current density falls to zero.

The basis of these calculations is the changes in the Bean profiles caused by the movement of the sample in an inhomogeneous magnetic field. In the case of a VSM this produces an ac magnetic field. For a SQUID magnetometer the sample is also often moved from one coil to another. This movement will also change the Bean profile and may result in similar consequences to those predicted for a VSM also being applicable to a SQUID measurement. Further work is required to consider how the movement of the sample will affect the measured magnetic moment when using a SQUID magnetometer.

Appendix 1

Conferences Attended

CRIM '98	Oxford Instruments, Abingdon	Poster Presentation	1998
EUCAS '97	Eindhoven, Holland	Poster Presentation	1997
CMMP '96	York	Poster Presentation	1996
CMMP '95	Liverpool	Poster Presentation	1995

Courses Attended

Java for Beginners	Durham University ITS	1998
C for Beginners	Durham University ITS	1998
CRAC Course	Birmingham University	1997
Red Cross First Aid at Work	Durham University	1996
Workshop Techniques Course	Durham University	1996
IRC Winter School in Superconductivity	Cambridge University	1996
Low Temperature Techniques Course	Birmingham University	1995

Publications

"An Investigation of the Peak Effect in the Chevrel Phase Superconductor Tin Molybdenum Sulphide" Daniel I J, Zheng D N and Hampshire D P *Inst. Phys. Conf. Ser.* **158** 1169 (1997)

Asyst Programs Written

These programs control the experiments on which the majority of the data presented in this thesis was taken.

Resistivity Program

Field control and capacitance thermometer included into original program hence allowing the simultaneous measurement of ac. resistivity and ac. susceptibility as a function of temperature and magnetic field.

Program Files

- devices.pro
- ressus.var
- ressus1.ijd
- ressus2.ijd
- ressus3.ijd
- ressus4.ijd
- ressusgo.ijd

VSM Programs

VSM variable temperature programs:- Temperature control and IEEE small coil control included into original program, allowing the automated measurement of magnetisation loops at different temperatures for fields up to 15T

Program Files

- drive.com
- drive.ovl
- devices.pro
- vsmtemp.ijd
- vsmtemp.var
- tempcont.var
- tempcont.ijd
- pooltemp.ijd
- setup.ijd
- stuff.ijd
- stuff2.ijd

VSM Multiple Harmonic Measurement Program:- Allowing measurement of voltages at multiples of the driver frequency up to 10f at a fixed temperature for fields up to 15T.

Program Files

- harm.com
- harm.ovl
- devices.pro
- vsmharm.ijd
- vsmharm.var
- harmcont.var
- harmcont.ijd
- setuphrm.ijd
- poolharm.ijd
- stufhrm.ijd
- stufhrm2.ijd

Additional Programs

Program to calculate critical current density from the magnetisation data for a slab shaped sample measured at different temperatures for a given sample size.

Program Files

- dong.com
- dong.ovl
- Jccalc.ijd
- Jccalc.var

Program to remove the empty values in the harmonic measurement data files.

Program Files

- dong.com
- dong.ovl
- qwikb.ijd
- qwikharm.var

Maple Programs Written

The maple programs written to allow the calculation of the results presented in chapter 8 are listed below. These programs are written for the NbTi-like sample but allow the substitution of the functional form for the critical current density at the beginning of the program allowing the results for the other samples to be simply calculated. The programs run in Maple V Rel 4.

Sample not crossing the field centre

Basic NbTi Sample

lia-a-vs-B1 - calculates Loss voltages

lia-B-vs-B1- calculates Lossless voltages

Offcentred in Pickup Coils -(β_1 Term)

lia-A-vs-constant- calculates Loss voltages

lia-B-vs-constant- calculates Lossless voltages

Decreasing Field

dec-b-lia-a-calculates Loss voltages

dec-b-lia-b-calculates Lossless voltages

Negative Field Gradient

lia-A-neg-dbdt-calculates Loss voltages

lia-B-neg-dbdt-calculates Lossless voltages

Slab Sample geometry

slab-Lia-A-calculates Loss voltages

slab-Lia-B-calculates Lossless voltages

Sample crossing the field centre

Negative Z - Pickup Coil Centred

working-cent-b-cent-coil-nbti-an-neg-z- calculates Loss voltages

working-cent-b-cent-coil-nbti-bn-neg-z- calculates Lossless voltages

Negative Z - Offcentred in Pickup Coils

working-cent-b-offcent-coil-nbti-an-neg-z- calculates Loss voltages

working-cent-b-offcent-coil-nbti-bn-neg-z- calculates Lossless voltages

Positive Z - Pickup Coil Centred

working-cent-b-cent-coil-nbti-an-pos-z- calculates Loss voltages

working-cent-b-cent-coil-nbti-bn-pos-z- calculates Lossless voltages

Positive Z - Pickup Coil Centred - Decreasing Field

working-dec-b-cent-b-cent-coil-nbti-an-pos-z- calculates Loss voltages

working-dec-b-cent-b-cent-coil-nbti-bn-pos-z- calculates Lossless voltages

Negative Z - Offcentred in Pickup Coils

working-cent-b-offcent-coil-nbti-an-pos-z- calculates Loss voltages

working-cent-b-offcent-coil-nbti-bn-pos-z- calculates Lossless voltages

Appendix 2

Development of an Ac. Calorimetry System

Ian J Daniel

C.A.S.E. Award Student, Durham University

Nestor Patrikios

System and Software Engineer, Measurement Systems Group

August to October 1997

Abstract

Ac. calorimetry allows for a continuous measurement of heat capacity, giving better resolution and comparable absolute values to those obtainable using a relaxation technique. The focus of this work was to use the present commercial relaxation method heat capacity probe, produced by Oxford Instruments, as the basis for a new ac. calorimeter. The aim was to produce a system able to measure the superconducting transition of an YBCO single crystal. The superconducting transition was measured first in tin, to demonstrate the low temperature operation of the system and then in YBCO, to demonstrate the high temperature operation of the system.

At 4 K it was not possible to find a suitable measurement frequency. However at 90 K measurements were made and the superconducting transition in YBCO was clearly visible. The absolute value of the heat capacity was disappointing but the resolution of the measurement was 0.07 %. This represents an improvement over the relaxation measurement of more than a factor of 10. A combination of the two measurements produces a heat capacity measurement system capable of measuring to 2% accuracy and 0.07% resolution.

1. Introduction

Calorimetry allows the study of phase transitions and thermodynamics which in turn give a valuable insight into the fundamental properties of materials. The two main methods of measurement for heat capacity, both presently available through Oxford Instruments, are Adiabatic Calorimetry and Relaxation Calorimetry. The adiabatic method is accurate, but only allows relatively large samples to be measured (of order 1g). The relaxation technique is also rather accurate though the resolution is limited at high temperatures due to the time taken for each step and by the size of the temperature steps required. Smaller samples can be measured using the relaxation technique, of order 10 mg though they must be relatively good thermal conductors. Both techniques are limited by measurement speed which is low at high temperatures, and is fundamentally limited in temperature resolution by the size of the temperature steps required.

In 1967 Ac. Calorimetry was developed by Sullivan and Siedel to offer an alternative to the previous two techniques. The principle behind this technique is that a heater and thermometer are mounted on the sample and connected by a weak thermal link to a bath. An ac. power is applied to the heater and the ac. temperature variation detected on the thermometer, usually by using a lockin amplifier. The frequency of the oscillation must satisfy the criteria described by

$$\tau_2 << \omega^{-1} << \tau_1$$

where τ_1 is the sample to bath time constant, τ_2 is the chip to sample time constant and $\omega = 4\pi f$. If this frequency criteria is satisfied then equation 1 shows how the heat capacity of a sample can be determined from this measurement where f is the frequency of oscillation of the heater, V_0 is the heater voltage, R_H is the heater resistance, I_{Therm} is the current driving the thermometer, V_{LIA} is the rms. voltage read from the thermometer, dR/dT is the sensitivity of the thermometer and δ is a correction as defined in equation 2.

$$C = \frac{\sqrt{2}}{8.\pi.f}.\frac{(V_0)^2}{R_H}.\frac{I_{Therm}}{V_{LIA}}.\frac{dR}{dT}.(1-\delta) \tag{1}$$

$$\delta = \left\{1 + \left(\frac{1}{2\omega\tau_1}\right)^2 + (2\omega\tau_2)^2\right\}^{-\frac{1}{2}} \tag{2}$$

If the heater voltage is driven using the lockin amplifier's sinusoidal voltage output of $V_{OUT} = V_0\sin(\omega t)$ then the thermometer response is determined from considering the heating or cooling produced about the mean heater power, as indicated by the shading (red indicating heating and blue indicating cooling) in Figure 1. This only holds when the sample and chip are well thermally isolated from the bath.

It is worth noting here the difference between the Sulliven and Siedel paper and our case with regard to the phase angle. In their paper α is defined as the phase angle between the power and the temperature oscillations and is 90 degrees. In our experiments we measure the angle between a 2f reference signal and the temperature oscillations, giving a phase angle of 180 degrees when the criteria are satisfied, Figure 1.

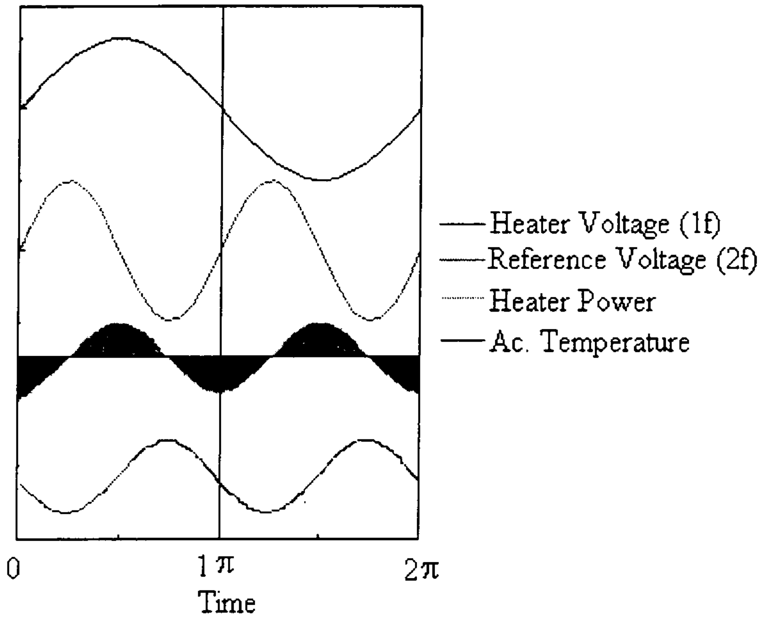

Figure 1 **Ac. response of the power and temperature to the heater voltage.**

The correction term δ can be determined from the phase angle measurement as τ_1 is known from the relaxation measurement and therefore τ_2 can be determined using equation 3.

$$\alpha - 90 = \sin^{-1}\left[1+\left\{\frac{1}{2\omega\tau_1} - (2\omega\tau_2)^2\right\}^2\right]^{-\frac{1}{2}} \qquad (3)$$

Where α is the phase angle measured on the lockin amplifier. If the frequency criteria do not hold, then the phase angle will be significantly different from 180 degrees and the data unreliable. For angles less than 5 degrees the δ correction is less than 2% and will be neglected.

The other criteria derivable from equation 1 is that at a fixed temperature, the relation between heater power and ac. temperature should be linear, i.e. a plot of V_{LIA} vs. $(V_0)^2$ should be linear. The deviation from linearity is caused by the dc. heating effect of the ac. heater power raising the temperature and hence changing the heat capacity.

The advantage of the ac. method is that it gives a continuous measurement of heat capacity, and at high temperatures, gives a better resolution both in temperature and in heat capacity than the relaxation technique. The absolute value of the heat capacity measured is not as accurate as the relaxation and adiabatic measurements, but the relative values obtained from the ac. measurement can be used in conjunction with either of the accurate absolute measurements to give correct absolute values with improved resolution.

2. Experimental setup

The ac. system uses the same probe as the relaxation system, i.e. a Heliox with the heat capacity cell mounted on the ^{3}He pot in vacuum. The wiring of both the heat capacity cell and the Heliox required no modification to allow ac. measurements to be made, with the measurement electronics being connected at the Fischer connector on the top of the Heliox. A schematic of the wiring used for the low temperature measurements is shown in Figure 2.

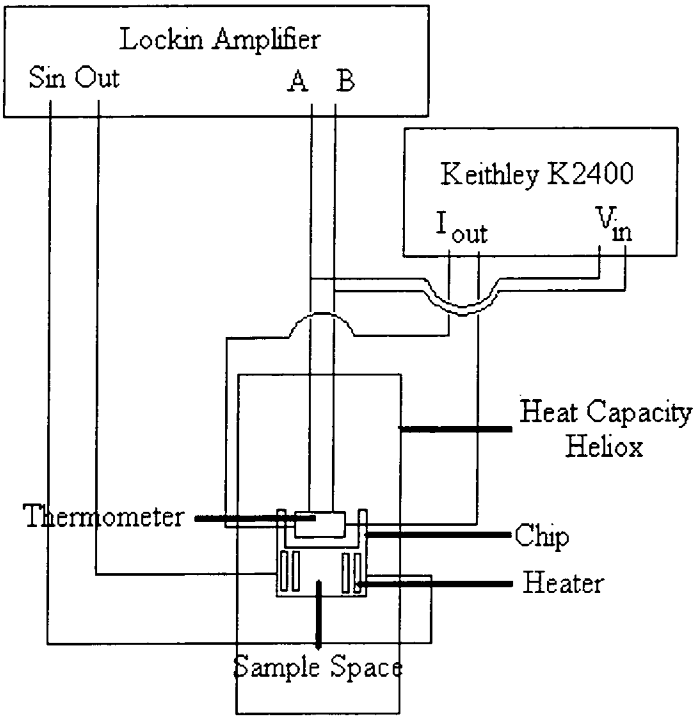

Figure 2 Low temperature measurement electronics schematic.

The Heliox is operated at low temperature as normal, with the ITC being used to sweep the temperature, either through heating the sorb or directly heating the ^{3}He pot. For the high temperature measurements, the temperature was set above the region of interest, then the heater switched to a manual power that allowed for a very slow and steady temperature sweep as the probe cooled.

The sample, as for the relaxation measurement, must be small in size, with dimensions approximately 3 x 2 x 2 mm and have a large flat surface to allow good thermal contact with the chip. It is mounted identically for both relaxation and ac. measurements making the change from relaxation to ac. measurements quick and simple with no need to warm up the Heliox.

At higher temperatures it was discovered that the lockin amplifier was limiting the resolution of the measurement. It was decided to use the bridge circuit and amplifier within the existing heat capacity controller to allow the offsetting of the dc. thermometer voltage, followed by an amplification of 1000 to the remaining dc. signal and to the ac. signal. This produced an improvement in the signal to noise ratio, demonstrating that the lockin amplifier was the limiting factor. A schematic is shown in Figure 3 for the high temperature operation electronics.

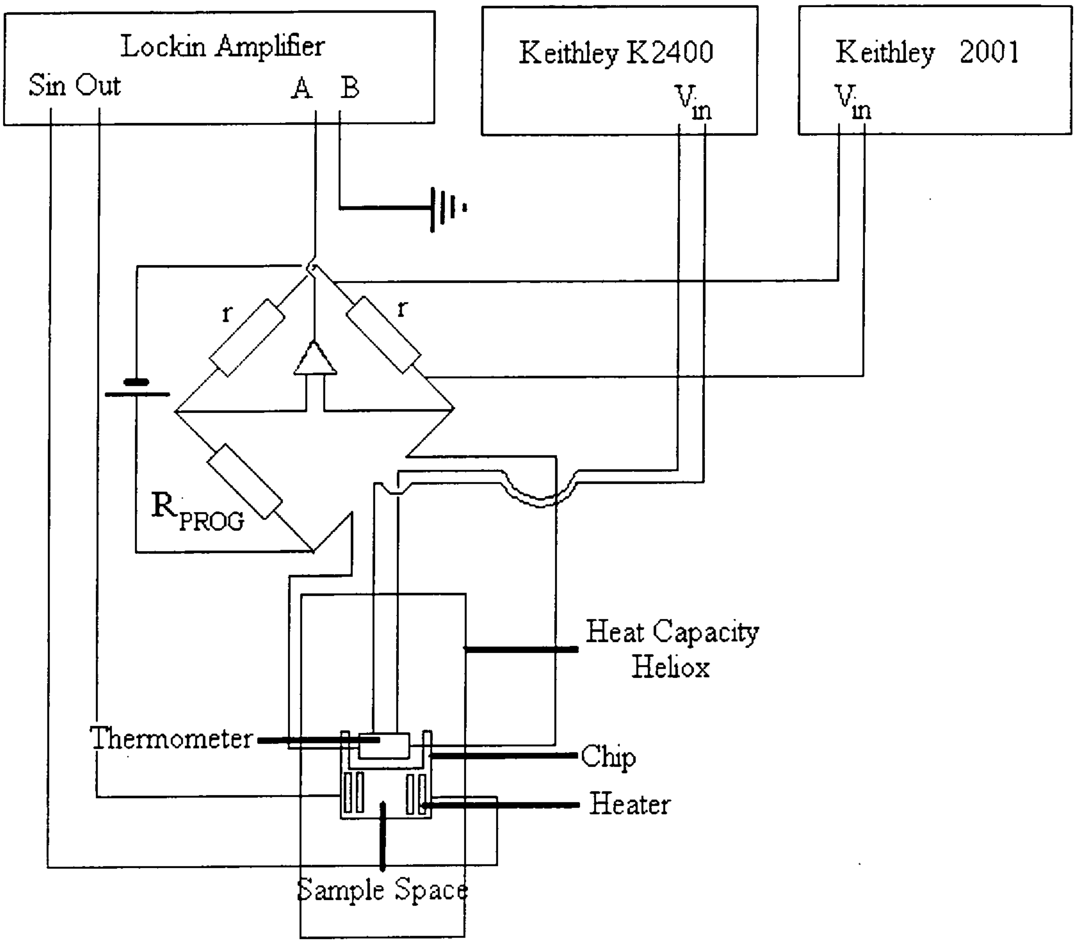

Figure 3 Schematic for the high temperature ac. measurement electronics.

The bridge formula, equation 4, reduces to $R_{ac} = 10.02\times V_{ac}$, where r = 100 kΩ, $R_{PROG} = 116\Omega$ and $V_{BRIDGE} = 10V$, for the experimental conditions used for these measurements.

$$R_{ac} = \frac{V_{ac}}{V_{BRIDGE}} \cdot \frac{(r + R_{PROG})^2}{r} \cdot \frac{1}{1000} \tag{4}$$

3. Measurements

i) Bare Chip

The first data taken was a relaxation measurement of the bare chip, to be used as an addendum for the following work, Figure 4.

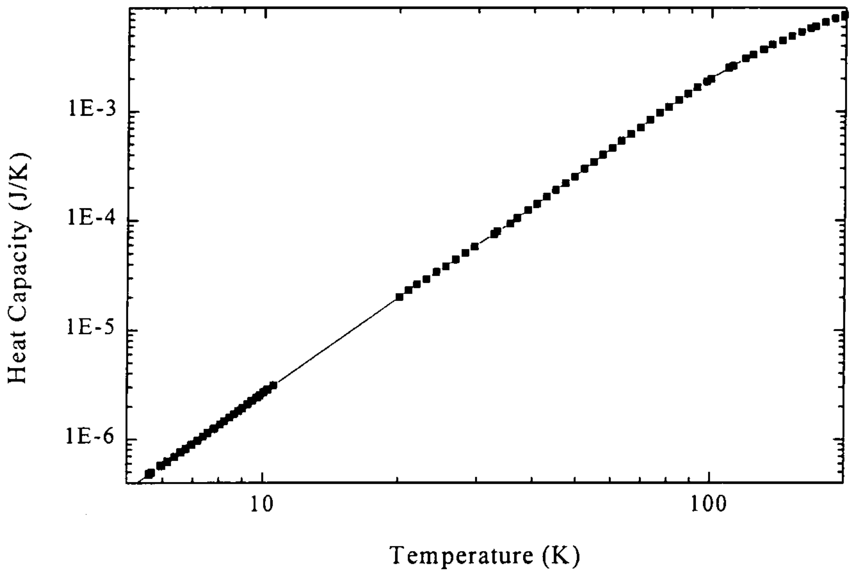

Figure 4 **Heat Capacity of the chip determined using relaxation measurements.**

ii) Tin

The sample was made from tin of purity 99.995%, shaped to the appropriate size, with a mass of 33 mg. The sample was mounted and a relaxation measurement was performed to determine the absolute value of the heat capacity, Figure 5.

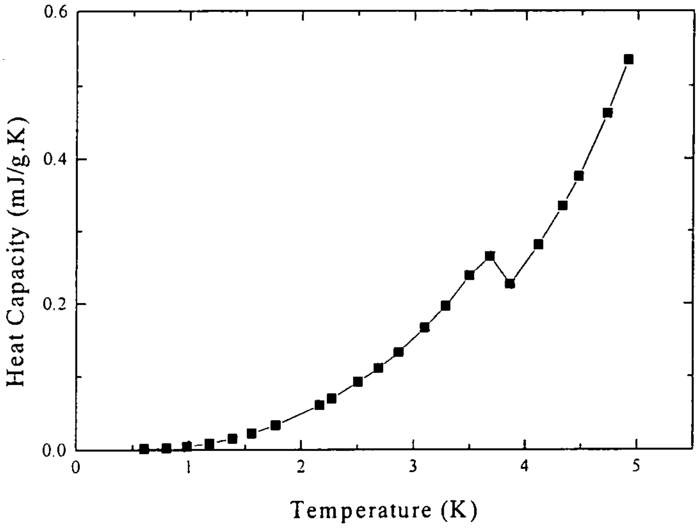

Figure 5 **A relaxation measurement of the superconducting transition in tin.**

The sample was then measured using the ac. technique to determine the frequency range and power range appropriate for this sample at 4K. The results are shown in Figure 6 and Figure 7.

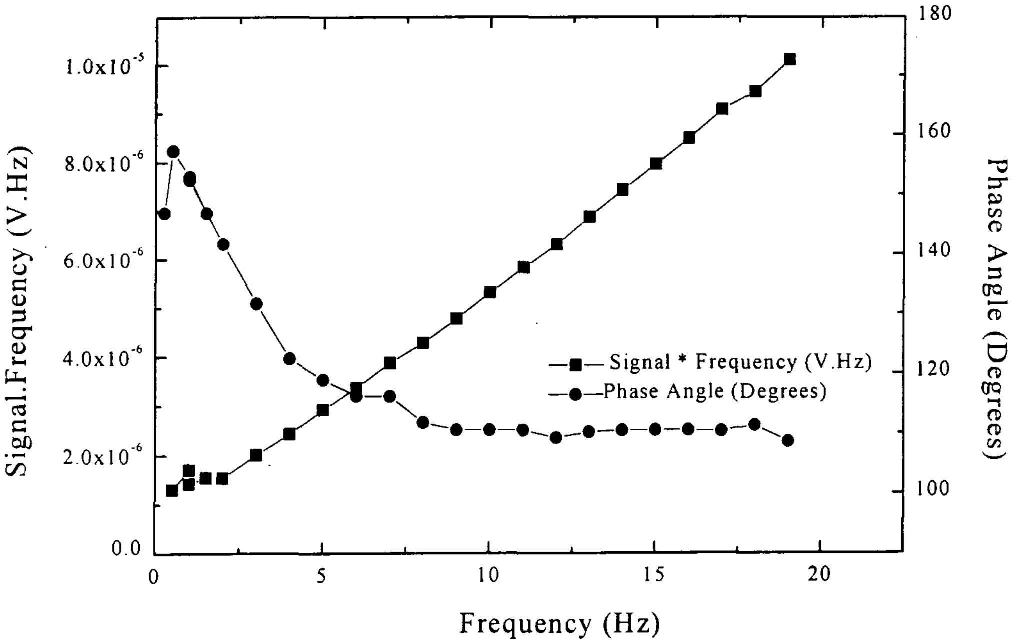

Figure 6 **The frequency response of the tin sample to determine the appropriate frequency.**

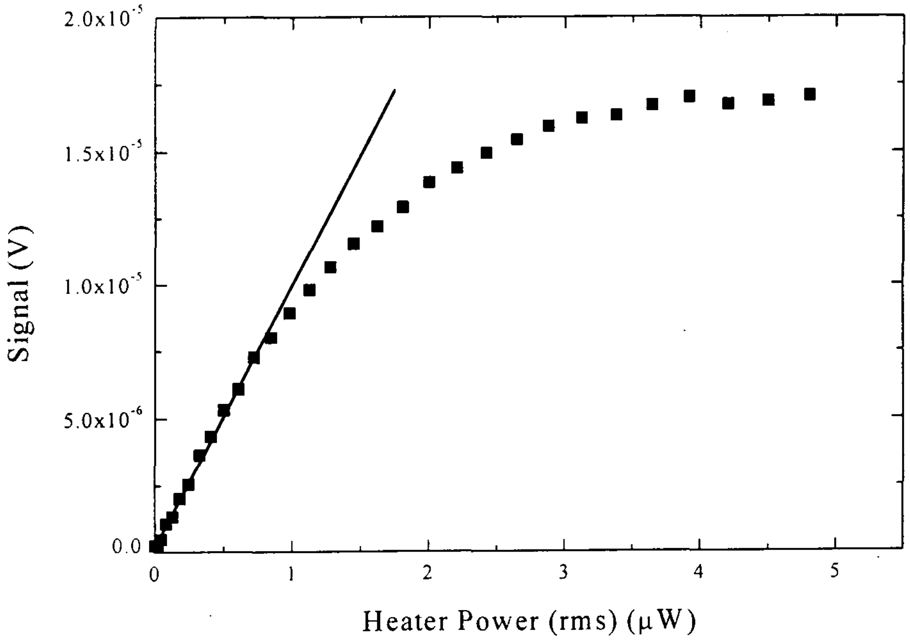

Figure 7 **The power response of the tin sample to determine the appropriate heater power at 1 Hz.**

The phase angle measurement, Figure 6 shows that at low frequencies the phase angle goes through a maximum at 0.5 Hz and then decreases. It is known from the relaxation measurements that τ_1 is 2 seconds which for $\omega^{-1} << \tau_1$ implies that $f > 0.4$ Hz is required, however above 0.5 Hz the phase angle is already increasing, meaning that the frequency is now too fast compared to τ_2 and the sample and chip are becoming decoupled. If the sample to chip thermal contact can be improved then this problem could be removed. This means that with this thermal link, both of the frequency criteria cannot be satisfied by a single frequency. The frequency response, signal * frequency in Figure 6, shows an almost constant level between 0.5 and 2 Hz, which increases at higher frequencies, corresponding to a decrease in measured heat capacity due to the sample and chip decoupling.

The power response is as expected, and has a linear region between 0 and 0.75 μW, corresponding to a maximum heater voltage of 25 mV. This corresponds to an ac. temperature oscillation of approximately 50 mK. From these data, a frequency of 1 Hz and a power of 0.75 μW were chosen to best fulfill the criteria for the mathematics given the problems with time constants. Using these values, a variable temperature measurement was performed and is compared to the relaxation measurement in Figure 8.

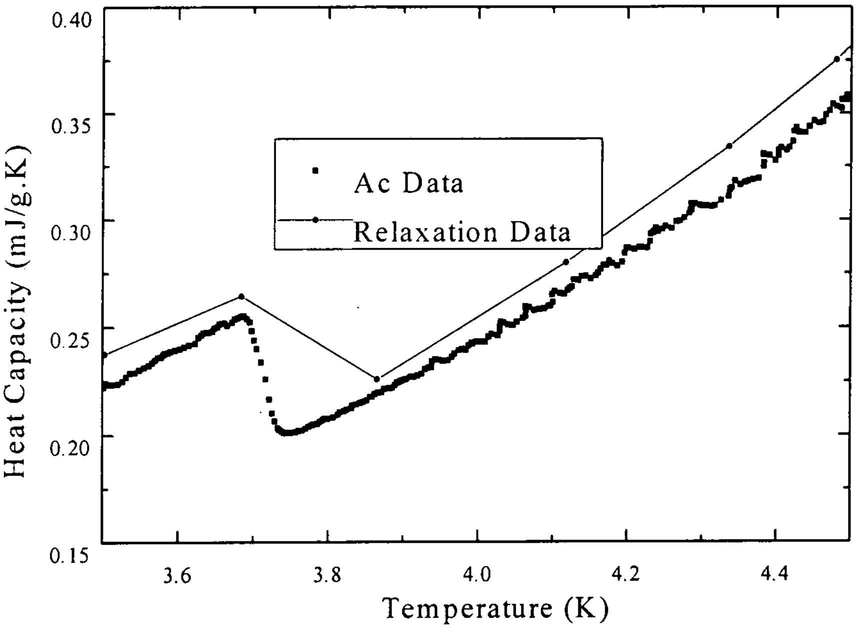

Figure 8 **A comparison between ac and relaxation measurements on tin**

The advantage of the ac. method can clearly be seen with the transition being much better resolved in temperature than is possible using the relaxation method with a minimum resolvable ΔT of 10 mK. Tin is a type I superconductor and hence the transition should be a vertical drop in heat capacity at T_c which is shown by the ac. measurement. The noise level on the heat capacity is 2μJ/g.K around the transition though the absolute value is only coincidentally correct around the transition however, as the value is dependent on frequency as seen later, Figure 9.

The importance of the frequency and power chosen was then investigated to determine how critical each was to the measurement of a sample.

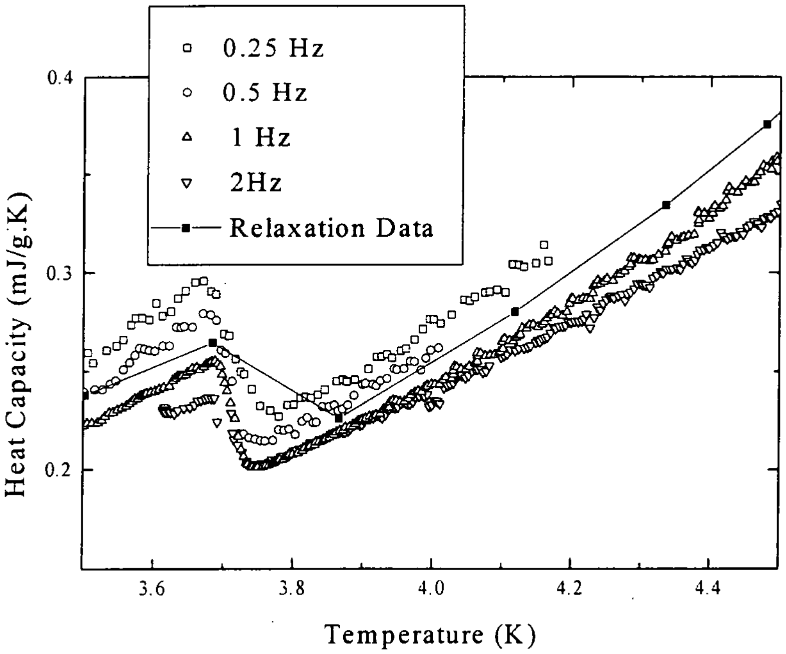

Figure 9 **The effect of a variation of heater frequency on the ac. measurement for tin**

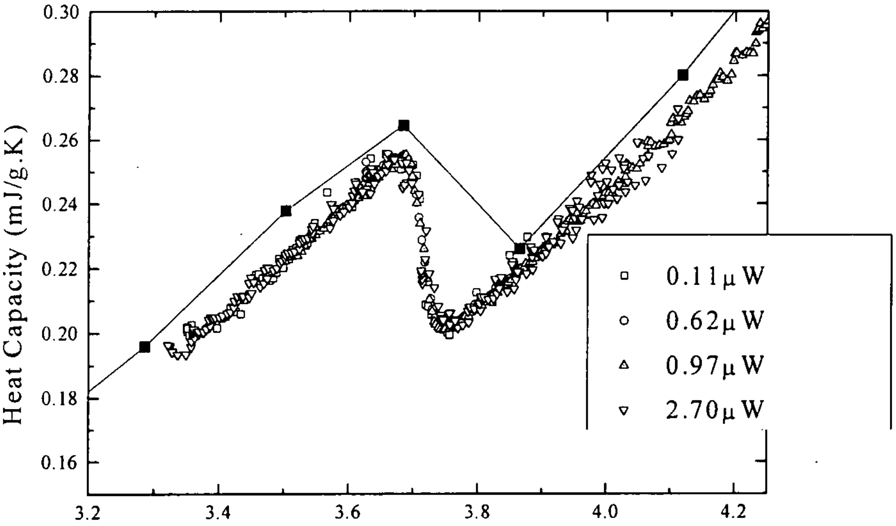

Figure 10 **The effect of a variation of rms. heater power on the ac. measurement for tin at 1Hz**

The results are quite sensitive to the frequency of measurement as expected, with 1 Hz being the optimum value for this sample at this temperature. The power criterion does not appear to be critical to the measurement as a power four times greater than the maximum determined, gives no significant change in the data.

Measurements Cont^d

iii) High Temperature Superconductor

A single crystal of YBCO, mass 11 mg, was provided by G. Yang from Birmingham University, with a T_c of approximately 92K as measured by ac. susceptibility. This was mounted on to the chip as it would be for the usual relaxation method measurements and a "quick" relaxation measurement performed in the temperature region of interest. This data is shown in Figure 13 and although described as a quick measurement, took more than seventy two hours to perform. This also gave a value for τ_1 of 130 second which means that f > 4 mHz. Hence a study was done between 0.01 and 10 Hz and between 0 and 1.25 mW for heater frequency and power respectively, at 90K.

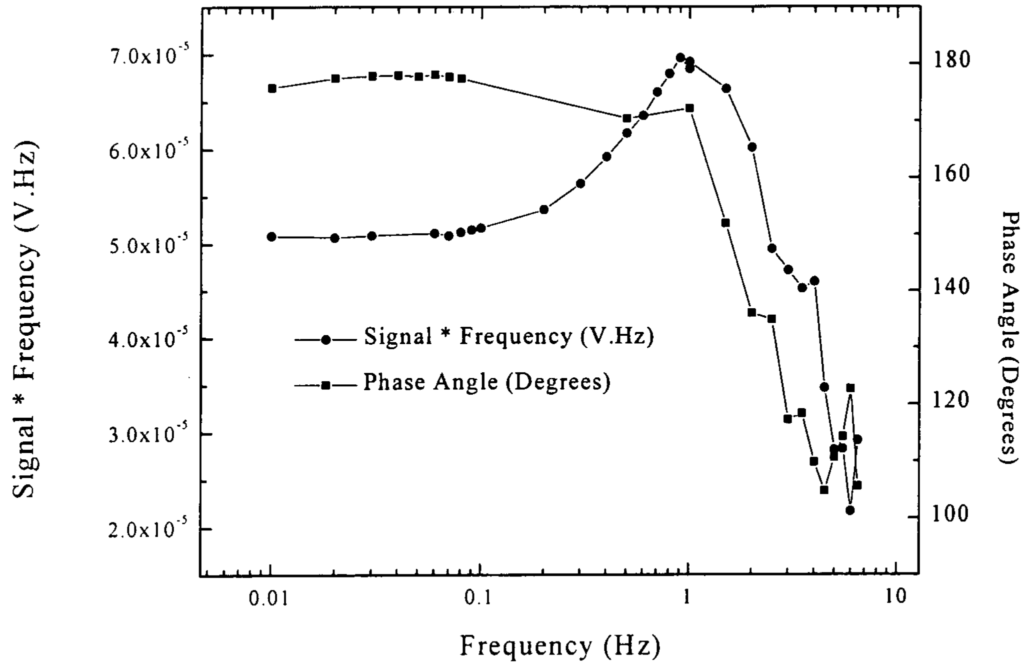

Figure 11 **The frequency response of the YBCO sample to determine the appropriate frequency**

From Figure 11 it can be seen that for a phase angle of 180 degrees, a frequency of less than 0.1 Hz is required. The fall off in signal at higher frequencies, above 1 Hz is attributed to the thermometer and the heater becoming thermally decoupled. To maximise the signal to noise ratio a frequency of 0.01 Hz was chosen, however this does limit the rate at which data can be taken. The temperature ramp rate is determined by the number of points per Kelvin required. The lockin amplifier has a time constant of 100s, i.e. one point is taken every 100s implying that a ramp rate of 5mK/min. gives one point approximately every 10 mK. This is an improvement on the relaxation technique which takes approximately 1500s per point at 90K. The power measurement, Figure 12 shows that a power of up to 0.3 mW was possible at this temperature which corresponds to approximately 250 mK ac. temperature oscillations.

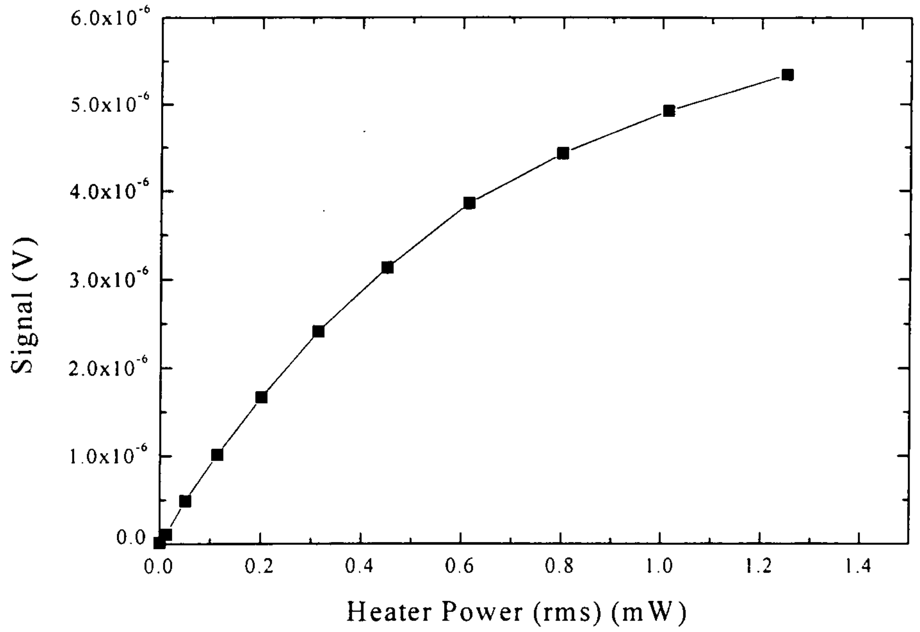

Figure 12 **The power response of the YBCO sample to determine the appropriate power**

Using these parameters, the ac. measurement was performed around the expected transition temperature of 92K. The temperature ramp rate was approximately 5 mK/min, using 0.01 Hz and 30 mW for the heater frequency and power respectively. Figure 13 shows a comparison between the relaxation and ac. measurements with the difference being approximately 40%. The phase angle delta correction is less than 2% and the internal time constant τ_2 was calculated to be approximately 1s.

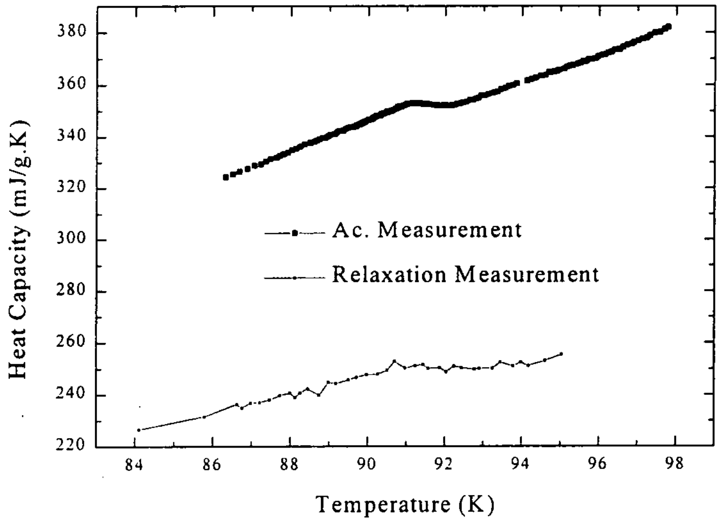

Figure 13 **A Comparison between ac and relaxation measurement on YBCO**

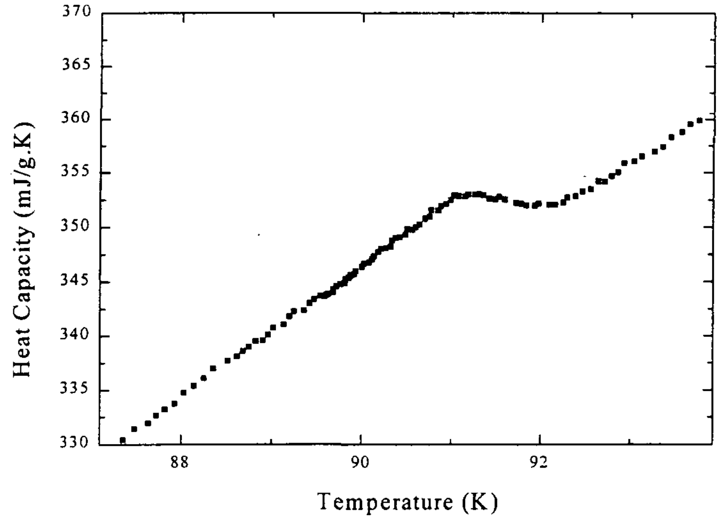

Figure 14 **Ac. heat capacity measurement of the superconducting transition in YBCO**

In Figure 15 the transition is very clear and well resolved in temperature, with a standard deviation of 0.07% about the underlying trend in heat capacity. This compares favourably with literature values for high quality measurements on YBCO [2, 3], where using an adiabatic technique, a noise level of 0.01% and an accuracy of 0.5% is obtained. The accuracy available using the relaxation measurement is of order 2%, so combining the two techniques in Oxford will give data that is accurate to 2%, with a standard deviation noise of 0.07%.

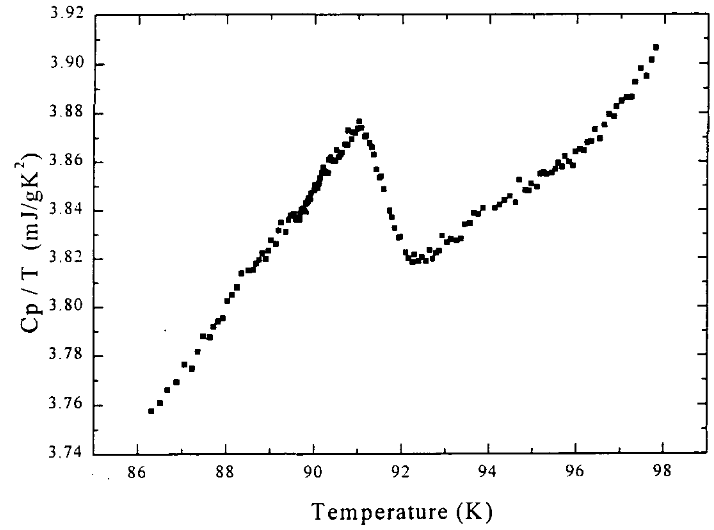

Figure 15 **Ac. measurement of Cp / T against temperature**

Figure 15 shows the transition plotted as heat capacity divided by temperature against temperature, emphasising the transition.

4. Conclusion

An ac. calorimeter has been developed and used to measure the superconducting transition in tin ($T_c = 3.72$ K) and YBCO ($T_c \approx 92$K). It requires only a lockin amplifier and a small amount of additional wiring to modify the standard relaxation measurement system.
In the low temperature regime it appears that it is not possible to satisfy the criteria for the frequency of heater oscillations, though data can still be taken, comparable to that obtained with the relaxation measurement.

Measurements at 90 K	Accuracy	Temperature Resolution	Heat Capacity Resolution
Relaxation Measurement	~2%	1%	1%
Ac. Measurement	50%	0.1%	0.07%
Best Published Data (Adiabatic) [2,3]	0.5%	0.2%	0.01%

Table 1 **A Comparison of heat capacity measurement systems**

The real advantage of the ac. measurement comes at high temperatures where the relaxation measurement becomes very slow and poorly resolved. The speed of measurement has been increased to 100s per point giving improved temperature resolution. A comparison of the two techniques is presented in Table 1 along with some recent high quality data published on YBCO. A combination of the ac. and relaxation techniques produces data with an absolute accuracy of 2% and a noise level of 0.07%, which compares very favourably with the best data in the literature.

Acknowledgments

The authors would like to thank Dr. Damian Hampshire from Durham University and Dr. Michael de Podesta from Birkbeck College, London, for their advice on ac. heat capacity measurements and all the members of the measurement systems group for their help and encouragement throughout this project.

References

[1] Sullivan P F and Siedel G, Physical Review 137 (1968) 679-685
[2] Junod A, Roulin M, Genoud J Y et al. Physica C 275 (1997) 245-258.
[3] Junod A, Wang K Q Janod E et al. Physica B 194-196 (1994) 1495-1496